UNIVERSIDAD POLITÉCNICA DE MADRID
Escuela Técnica Superior de Ingenieros Industriales

Numerical Methods and Algorithms for Phase-Field Fracture Modeling

D O C T O R A L T H E S I S

Submitted for the degree of Doctor by:

Miguel Castillón de Miguel
Master in Mechanical Engineering

Madrid, 2026

UNIVERSIDAD POLITÉCNICA DE MADRID
Escuela Técnica Superior de Ingenieros Industriales

Doctoral Degree in Mechanical Engineering

Numerical Methods and Algorithms for Phase-Field Fracture Modeling

D O C T O R A L T H E S I S

Submitted for the degree of Doctor by:

Miguel Castillón de Miguel
Master in Mechanical Engineering

Under the supervision of:
Dr. Ignacio Romero Olleros
Dr. Javier Segurado Escudero

Madrid, 2026

Title: Numerical Methods and Algorithms for Phase-Field Fracture Modeling

Author: Miguel Castillón de Miguel

Doctoral Programme: Mechanical Engineering

Thesis Supervision:

Dr. Ignacio Romero Olleros. Catedrático de Universidad, Escuela Técnica Superior de Ingenieros Industriales. (Supervisor)

Dr. Javier Segurado Escudero. Catedrático de Universidad, Escuela Técnica Superior de Ingenieros de Caminos, Canales y Puertos. (Supervisor)

External Reviewers:

Thesis Defense Committee:

Thesis Defense Date:

This thesis has been partially supported by the Spanish Ministry of Science and Innovation through the FPI grant PRE2020-092051 (MCIN/AEI/10.13039/501100011033).

A Lorenza, per la sua presenza costante
e il suo sostegno incondizionato.

Acknowledgements

I am deeply grateful to my supervisors, Ignacio and Javier, for their guidance and sustained support throughout this work. Their expertise and encouragement have been invaluable in shaping the direction of this research and in overcoming the challenges encountered along the way.

I would like to thank the IMDEA Materials Institute for its scientific excellence and for the professional support, which I am confident will open many future opportunities. I am grateful to my colleagues at IMDEA for several valuable years of collaboration, and I extend my appreciation to my colleagues at UPM.

My three-month stay at the Simula Research Laboratory (Oslo, Norway) was a valuable experience and an important milestone for this thesis. I am especially grateful to Jørgen for his guidance and direct help with several implementation aspects of the code, and to Thomas for insightful discussions—both of which greatly contributed to the development and exposition of the Latent Variable Proximal Point (LVPP) method discussed in this thesis. I extend my warmest thanks to everyone at Simula for their kindness and hospitality.

I gratefully acknowledge the financial support of the Spanish Ministry of Science and Innovation through the FPI grant PRE2020-092051 (MCIN/AEI/10.13039/501100011033).

On a personal note, I am deeply grateful to my partner, Lorenza, for her unwavering support and encouragement throughout the challenges of this research.

Furthermore, I am grateful to my friends, especially Antonio. Having started and finished our PhD journeys around the same time, he has been a constant source of support and encouragement, providing me with the motivation to persevere.

Finally, my deepest, heartfelt thanks go to my parents and my brother, whose unconditional love and support made all of this a reality.

Abstract

Fracture mechanics is essential for predicting the failure of materials and structures. The Phase-Field Fracture (PFF) method has emerged as a powerful computational tool, overcoming the limitations of classical discrete approaches by modeling cracks as diffuse damage bands. This formulation eliminates the need for explicit crack tracking and naturally handles complex topologies like branching and merging. However, despite its success, the method faces significant numerical and physical challenges, particularly regarding the robust enforcement of inequality constraints in some regularization models, the accurate measurement of geometric quantities distorted by strain localization, and the high computational cost of cycle-by-cycle fatigue simulations.

The computational challenge of fatigue—where phase-field fracture approaches typically rely on cycle-by-cycle simulations to accumulate damage over thousands of cycles, leading to prohibitive computational costs—is addressed in this thesis through a framework that enables fatigue analysis using only monotonic loading. This is made possible by a specialized energy-controlled solver designed to robustly track the complete crack equilibrium path, capturing instabilities such as snap-back. By performing a single quasi-static simulation, the method numerically extracts the compliance rate of the structure with respect to the crack area, which is then used to bridge the results with Linear Elastic Fracture Mechanics (LEFM) and integrate Paris' law. This allows for the prediction of fatigue life with drastically reduced computational effort while maintaining the topological flexibility of the phase-field method.

To ensure the accuracy of the geometric quantities extracted from these simulations, the work addresses the issue of crack area overestimation caused by numerical strain localization, which also affects the force and displacement values returned by the simulations. The Double Gradient Correction Method (DGCM) is proposed, founded on the principle of energy equipartition, where the energy contributions from the phase-field and its gradient are equal as the length-scale parameter approaches zero. Since numerical artifacts primarily affect the phase-field term while leaving the gradient term largely unperturbed, the crack area can be accurately approximated as twice the gradient-dependent energy. This method is inherently mesh-independent and readily applicable to the entire domain, including 3D simulations.

Finally, to enhance the robustness of constrained phase-field models beyond standard formulations, the Latent Variable Proximal Point (LVPP) algorithm is presented. In phase-field fracture simulations, the phase-field variable must remain within an admissible range typically between 0 (undamaged) and 1 (fully damaged) and satisfy an irreversibility condition to ensure damage does not decrease. While some standard models naturally respect the phase-field interval constraint, other regularizations require these physical constraints to be explicitly and robustly imposed. To address this, the LVPP framework reformulates these inequality-constrained problems as a sequence of unconstrained saddle-point problems via an auxiliary latent variable. This allows for the use of efficient Proximal Galerkin discretizations, providing a rigorous and robust solution that avoids the parameter sensitivity and convergence issues associated with traditional penalty methods.

All methodologies developed in this thesis are implemented in *PhaseFieldX*, an open-source software package designed to ensure reproducibility and to facilitate future research in the field.

Resumen

La mecánica de fractura es esencial para predecir el fallo de materiales y estructuras. El método de Fractura por Campo de Fase (PFF) ha emergido como potente herramienta computacional, modelando las grietas como bandas de daño difuso y superando limitaciones de enfoques discretos clásicos. Esta formulación elimina el seguimiento explícito de grietas y maneja topologías complejas como ramificación y fusión. Pese a su éxito, enfrenta importantes retos numéricos y físicos, especialmente en la imposición de restricciones de desigualdad en algunos modelos, la medición precisa de cantidades geométricas distorsionadas por la localización de deformaciones, y el alto coste computacional de simulaciones de fatiga ciclo a ciclo.

Para abordar el desafío computacional de la fatiga —donde las simulaciones ciclo a ciclo imponen costes prohibitivos—, esta tesis introduce un marco de análisis de fatiga usando solo carga monótona. Mantiene la flexibilidad topológica del método empleando un solucionador especializado controlado por energía que traza la trayectoria completa de equilibrio de la grieta, capturando inestabilidades como el *snap-back*. Con una única simulación cuasi-estática, se extrae numéricamente la tasa de flexibilidad de la estructura respecto al área de la grieta, conectando los resultados con la Mecánica de Fractura Elástica Lineal (LEFM) e integrando la ley de Paris. Esto permite predecir la vida a fatiga reduciendo drásticamente el esfuerzo computacional.

Para garantizar la precisión de las cantidades geométricas extraídas, se aborda la sobreestimación del área de grieta debida a la localización numérica de deformaciones, que también afecta a fuerzas y desplazamientos. Se propone el Método de Corrección de Doble Gradiente (DGCM), basado en la equipartición de energía, donde las contribuciones de energía del campo de fase y su gradiente se igualan cuando el parámetro de escala tiende a cero. Como los artefactos numéricos afectan principalmente al campo de fase, dejando inalterado al gradiente, el área se aproxima con precisión como el doble de la energía del gradiente. Este método es independiente de la malla y aplicable a todo el dominio, incluyendo problemas en 3D.

Finalmente, para mejorar la robustez de los modelos de campo de fase con restricciones, se presenta el algoritmo de Punto Proximal de Variable Latente (LVPP). En simulaciones PFF, el campo de fase debe acotarse, típicamente entre 0 (sin daño) y 1 (completamente dañado), y cumplir una condición de irreversibilidad para que el daño no disminuya. Aunque algunos modelos estándar respetan sus márgenes de manera natural, otras regularizaciones exigen que estas restricciones se impongan de forma explícita. El marco LVPP reformula estos problemas de minimización con restricciones de desigualdad como una secuencia de problemas de punto de silla sin restricciones usando una variable latente auxiliar. Esto permite usar discretizaciones de Proximal Galerkin, aportando una solución rigurosa y robusta que evita la sensibilidad y falta convergencia de los métodos de penalización.

Todas las metodologías desarrolladas en esta tesis se han implementado en *PhaseFieldX*, un paquete de software de código abierto diseñado para garantizar la reproducibilidad y facilitar la investigación futura en el campo.

Table of Contents

List of Figures

List of Tables

Notation

Abbreviations

PFF	Phase-Field Fracture
FEM	Finite Element Method
XFEM	Extended Finite Element Method
LEFM	Linear Elastic Fracture Mechanics
CSDF	Crack Surface Density Functional
AT1	Ambrosio-Tortorelli type 1 model (finite support)
AT2	Ambrosio-Tortorelli type 2 model (infinite support)
DGCM	Double Gradient Correction Method
LVPP	Latent Variable Proximal Point
SIF	Stress Intensity Factor
JOSS	Journal of Open Source Software
PDE	Partial Differential Equation
ASTM	American Society for Testing and Materials
MPI	Message Passing Interface

Symbols

Ω	Solid body domain
$V(\boldsymbol{u}, \Gamma_{\mathbf{sharp}})$	Total potential energy of a body with a sharp crack
$\mathcal{E}(\boldsymbol{u}, \phi)$	Total potential energy functional
$\mathcal{E}_{\mathbf{ext}}(\boldsymbol{u})$	Potential energy of external forces
$\Gamma_{\mathbf{sharp}}$	Sharp crack surface (discrete)
$\Gamma(\phi)$	Crack surface density functional (diffuse)
Γ_{ϕ}	Crack surface density functional: Phase-field term
$\Gamma_{\nabla\phi}$	Crack surface density functional: Gradient term
$\gamma(\phi, \nabla\phi)$	Crack surface density function
ϕ	Phase-field variable (0: no damage, 1: totally damaged)

$\dot{\phi}$ Rate of change of the phase-field variable

l Regularization length scale parameter

$\alpha(\phi)$ Geometric crack function

c_0 Normalization constant for the crack surface density functional

$g(\phi)$ Degradation function

$\boldsymbol{u}$ Displacement vector field

$\boldsymbol{\epsilon}$ Infinitesimal strain tensor

$\boldsymbol{\sigma}$ Cauchy stress tensor

ψ Strain energy density

ψ_a, ψ_b Active (tensile) / inactive (compressive) strain energy density

$\boldsymbol{\sigma}_a, \boldsymbol{\sigma}_b$ Active / inactive parts of the stress tensor

E Young's modulus

ν Poisson's ratio

λ, μ Lamé elastic parameters

κ Bulk modulus

G_c Critical energy release rate (fracture toughness)

K_c Critical stress intensity factor

a Crack length; or the half-length of the one dimensional bar, as dictated by the context.

B Specimen thickness

W Characteristic specimen width

P Applied force (load)

ΔP Cyclic force range

C Structural compliance (u/P)

$C(a)$ Structural compliance as a function of crack length

G Energy release rate

K Stress intensity factor

ΔK Stress intensity factor range

$f(a/W)$ Dimensionless geometry factor

N	Number of load cycles
$\mathrm{d}a/\mathrm{d}N$	Crack growth rate per cycle
$C_{\mathbf{Paris}}, n$	Paris' law material constants
$\mathrm{d}C/\mathrm{d}a$	Compliance derivative with respect to crack length
Λ	Lagrange multiplier (energy-controlled solver)
τ	Energetic control parameter
$\Delta\tau$	Energetic control parameter increment
c_1, c_2	Numerical parameters for energy-controlled solver constraints
η, ζ	Scaling/conversion factors for variational/energy-controlled solvers
$\mathcal{F}$	Crack area correction factor
$\Gamma_{\mathbf{sl}}$	Numerically computed crack area (with strain localization)
ξ	Auxiliary latent variable
β	Proximal variable
ρ	Penalty parameter
h	Finite element mesh size
N_a	Finite element shape function associated to node a

Chapter 1

INTRODUCTION

Fracture mechanics plays a critical role in engineering, as structural failure can lead to catastrophic economic and safety consequences. Among the various failure mechanisms, fatigue—damage accumulation under cyclic loading—is responsible for the vast majority of mechanical failures in service. Predicting the life of components under these conditions is therefore a primary goal in design and maintenance.

Over the years, significant advancements have been made in modeling and simulating fracture processes. While classical approaches like Linear Elastic Fracture Mechanics (LEFM) have been successful for simple geometries, they struggle with complex crack topologies, branching, and merging. In this context, the Phase-Field Fracture (PFF) method has emerged as a powerful and versatile computational tool. By regularizing the sharp crack interface into a diffuse damage band, PFF eliminates the need for explicit tracking of the crack path, offering a flexible framework to simulate complex failure scenarios.

However, despite its theoretical elegance, the practical application of PFF to fatigue and advanced fracture problems faces significant hurdles. High-cycle fatigue simulations are often computationally prohibitive due to the need to resolve millions of load cycles. Furthermore, the accuracy of the method depends heavily on the resolution of the diffuse crack profile, often leading to numerical artifacts that distort energy and geometric measurements. Finally, the robust enforcement of physical constraints—such as irreversibility and the interval constraint of the damage variable—remains a numerical challenge in many advanced formulation variants.

This thesis addresses these limitations by proposing new methods within both the analytical and numerical frameworks that enhance the efficiency, accuracy, and robustness of PFF simulations.

1.1 PFF background

Among the different models available to simulate failure, the PFF model has received significant attention in the last decade. To understand its advantages, it is useful to first consider the classical discrete approach. As illustrated in Figure 1.1, classical mechanics models a crack as a sharp geometric discontinuity, denoted as Γ_{sharp}, within the solid domain Ω. Figure 1.1(a) shows the idealized mathematical model where the crack is treated as an internal boundary, while Figure 1.1(b) depicts a schematic of a real-world fractured

plate. While physically intuitive, this sharp-interface representation poses significant numerical challenges: the crack path is an unknown boundary that must be explicitly tracked and updated as it propagates, making the handling of complex topologies like branching or merging computationally difficult.

The phase-field method addresses these difficulties by regularizing the sharp discontinuity into a diffuse band. As shown in Figure 1.1(c), the sharp interface is replaced by a region where a continuous scalar variable, $\phi \in [0, 1]$, varies smoothly from intact material ($\phi = 0$) to fully damaged material ($\phi = 1$). Figure 1.1(d) illustrates the diffuse representation of the crack, depicting the warped phase-field profile for visualization purposes. Rooted in the variational formulation proposed by [1] and further developed by [2, 3], this framework eliminates the need for explicit crack tracking. Consequently, the crack is treated not as a geometric boundary but as a region of localized damage, allowing the fracture problem to be solved as a coupled system of partial differential equations on a fixed mesh.

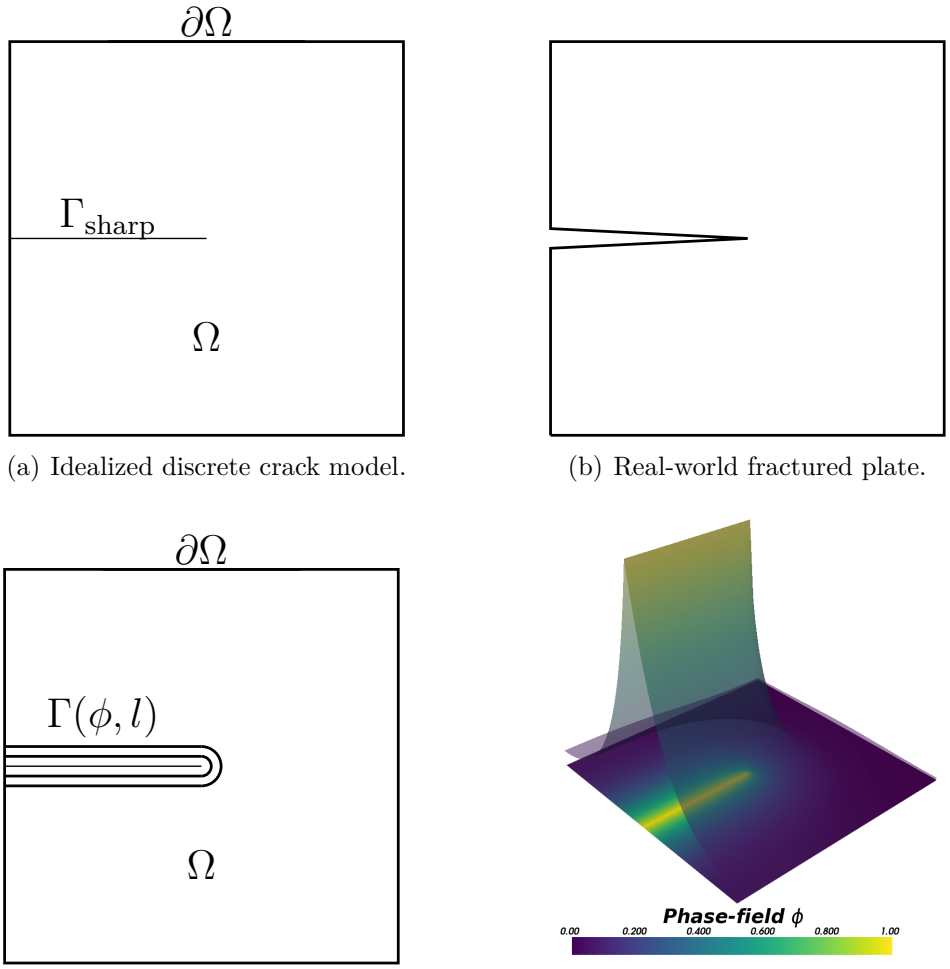

(a) Idealized discrete crack model.

(b) Real-world fractured plate.

(c) Schematic of regularized crack $\Gamma(\phi, l)$.

(d) Numerical phase-field result.

Figure 1.1: Comparison of fracture representations. Top: Discrete crack approach showing (a) an idealized mathematical crack and (b) a real-world fractured plate. Bottom: Phase-field approach showing (c) the diffuse interface regularization $\Gamma(\phi, l)$ and (d) a numerical result of the phase-field profile ϕ.

1.1.1 A modular framework

The extensive body of literature on PFF reveals that the method is best understood as a modular framework rather than a single, unified theory. A complete model is constructed by selecting a specific formulation for each of four fundamental components. The variety of choices available for each component allows for numerous combinations, enabling researchers to tailor models to specific materials, loading conditions, and fracture phenomena. The four core components are: (1) the crack surface density functional (CSDF), (2) the degradation function, (3) the strain energy split, and (4) the irreversibility condition. Each of these is discussed below.

The first component, the **CSDF**, approximates the sharp crack topology using a length-scale parameter that controls the width of the diffuse crack representation. Among the most common formulations are the Ambrosio-Tortorelli type 1 (AT1) and Ambrosio-Tortorelli type 2 (AT2) models, named after [4]. A significant distinction between these models lies in their ability to respect the physical constraints of the damage variable. The AT2 model, with its quadratic nature, inherently ensures that the phase-field variable does not take negative values. In contrast, the AT1 model and other regularization forms, such as the one proposed by Wu [5], do not naturally satisfy this interval constraint; consequently, an explicit constraint must be enforced numerically to prevent non-physical values [6, 7]. Regardless of this difference, a crucial property shared by all these functionals is their Γ-convergence to the sharp crack energy.

The second component is the **degradation function**, which couples the elastic response to the phase-field variable by reducing the material's stiffness as damage accumulates. Several degradation functions exist in the literature. Among them, a quadratic function is a common choice, widely adopted in works such as [2, 3]. Other alternatives, such as cubic and quartic functions, have also been analyzed in [8].

The third component is the **effective strain energy decomposition** (or energy split), which separates the strain energy into a part that drives crack growth and a part that does not. This split is essential for capturing the different responses of materials to tension and compression. Prominent decomposition methods include the spectral decomposition by [3] and the volumetric-deviatoric split by [9].

The fourth and final component is the enforcement of **crack irreversibility**. This fundamental physical constraint dictates that a crack, once formed, cannot heal. To ensure realistic simulations, this condition must be incorporated into the model. This characterizes the PFF formulation as an inequality-constrained minimization problem.

1.1.2 Numerical solution strategies

Numerical implementation of PFF models presents three primary challenges that must be addressed to ensure robust and accurate simulations.

First, the interval constraint of the phase-field variable ($\phi \in [0, 1]$) is not naturally guaranteed in all formulations. Specifically, while the AT2 model with a quadratic degradation function inherently confines ϕ to physical values, other models such as AT1 may violate this constraint. To enforce this constraint, techniques such as Lagrange multipliers or penalty methods are commonly employed [6, 7].

Second, the irreversibility condition ($\dot{\phi} \geq 0$) must be strictly enforced, as cracks physically

cannot heal. This is typically achieved using a history variable approach, where the maximum historical strain energy is used to drive damage, as presented in [3], or through penalty terms in the variational formulation, as done by [6]. Each approach involves trade-offs between implementation simplicity and variational scheme consistency.

Regarding these aspects, the novel Latent Variable Proximal Point (LVPP) algorithm, introduced in [10] and applied to several examples in [11], handles the PFF inequality-constrained problem in a robust manner, avoiding the use of history variables or penalty methods. This is achieved by reformulating the inequality-constrained optimization problem into a sequence of saddle-point problems involving latent variables, which rigorously enforce the physical bounds of the phase-field variable and naturally incorporate the irreversibility condition into the minimization process. The LVPP algorithm ensures that each iteration respects the constraints of the damage variable while maintaining numerical stability and convergence.

Third, the total energy functional is non-convex with respect to both displacement $\boldsymbol{u}$ and phase-field ϕ simultaneously. Consequently, solving the system in a monolithic scheme using standard Newton-Raphson procedures often leads to convergence issues or entrapment in local minima. To overcome this, staggered schemes (or alternate minimization) are widely used [3, 2]. These schemes solve for $\boldsymbol{u}$ and ϕ sequentially, providing robust unconditional stability but often at the cost of high computational expense due to the large number of iterations required.

Standard displacement-controlled algorithms are generally insufficient for capturing unstable crack propagation, which is characterized by *snap-back* phenomena in the load-displacement response. In these regimes, both the load and the displacement must decrease to maintain equilibrium as the crack advances dynamically. To trace these equilibrium paths quasi-statically, advanced control schemes are required, commonly referred to as **equilibrium path tracking algorithms**. While arc-length methods [12, 13] and crack-length control techniques [14] exist, they often introduce significant complexity. As detailed in the contributions of this thesis, a novel energy-controlled solver that robustly handles these instabilities using a single scalar constraint is proposed, facilitating the efficient simulation of complex fracture processes.

1.1.3 Considerations and mesh effects

In PFF modeling, the regularization is governed by a length-scale parameter, denoted as l, that controls the width of the diffuse crack representation. A central challenge in the finite element implementation of these models lies in the conflicting requirements placed on l and the characteristic mesh size, h.

On the one hand, the mesh must be fine enough to resolve the phase-field profile. A common guideline, particularly for the widely used AT2 model [15] within the Finite Element Method (FEM) framework with linear elements, is to maintain a ratio of $l/h \geq 2$. This ensures that the numerical solution can accurately capture the diffuse crack interface. On the other hand, to approximate the sharp-crack limit of fracture mechanics, l must be sufficiently small. However, this requirement is complicated by a numerical artifact known as *strain localization* [1, 16]. This phenomenon causes the phase-field variable to artificially saturate at $\phi = 1$ across entire finite elements, distorting the ideal diffuse profile and leading to a significant overestimation of the crack surface area. As demonstrated in

this dissertation and presented in [17], this overestimation systematically compromises the accuracy of simulation outputs by artificially scaling key quantities such as displacements, forces, and energy-related quantities.

Several strategies have been developed to mitigate this overestimation. One approach is the correction factor proposed in [1] for the AT2 crack surface regularization, which scales the effective energy release rate as a function of the ratio h/l and leads to $G_c^{\text{eff}} = G_c(1 + h/2l)$. However, instead of correcting the crack surface area directly, this formulation modifies G_c. In this thesis, the correction is applied directly to the crack area, because G_c is a material parameter that should remain unchanged. This interpretation is more closely aligned with the physical behavior of the problem and with the numerical artifact being corrected. While simple, the effectiveness of this correction relies on the ratio h/l approaching zero, which requires computationally expensive mesh refinement. Furthermore, it is derived under idealized one-dimensional assumptions and relies on a fixed element size around the crack tip, an assumption that can be unreliable for unstructured meshes or complex crack paths. Alternative post-processing techniques, such as skeletonization algorithms [18], estimate the crack area by thresholding the computed phase-field, for example by identifying regions where $\phi > 0.9$. Although effective for 2D simulations, their accuracy is sensitive to the chosen threshold and mesh quality. Moreover, these methods are computationally intensive, and their extension to 3D is complex. As a result, two competing requirements arise. To approach the sharp-crack limit, the length-scale parameter l must be small. However, the mesh size h must be fine enough to resolve the phase-field profile, while also remaining small relative to l to minimize the strain localization error, which is proportional to h/l. This often leads to computationally prohibitive mesh densities, highlighting the need for more robust and efficient correction methods.

Another significant artifact in PFF simulations is the presence of a non-physical peak force at the onset of crack initiation, a phenomenon not observed in experimental results [14, 12, 13]. This force overshoot is a numerical artifact linked to the nucleation process, where the phase-field variable evolves from an undamaged state ($\phi = 0$) to a fully damaged state ($\phi = 1$). This issue is addressed by existing correction methods with varying degrees of success. The Bourdin correction, being a constant scaling factor dependent on mesh size and length scale, reduces the magnitude of the peak force but does not eliminate the overshoot itself. In contrast, skeletonization-based methods, which measure the crack length by thresholding the phase-field (e.g., considering only regions where $\phi > 0.95$), effectively bypass the nucleation phase and thus remove the peak force from the corrected results. However, this approach has its own limitations: its accuracy depends on the chosen threshold and image processing techniques, and its application to complex crack topologies, such as multiple interacting cracks or three-dimensional problems, is not straightforward.

1.2 Fatigue analysis within PFF framework

The extensions of PFF to model fatigue crack propagation are relatively recent [19, 20, 21, 22, 23]. A common ingredient of most of the proposed models, as in [19], is the introduction of a fatigue degradation function that reduces fracture toughness according to a cumulative history variable, where the simulation progress is tracked by a pseudotime. This history variable typically monitors quantities such as accumulated plastic strain or energy dissipation, effectively capturing the material's fatigue history. In these models,

fatigue crack growth is simulated by incrementally applying cyclic loads and updating the history variable at each cycle. From a fundamental viewpoint, this framework is of significant interest since the parametrization of the history dependence of the damage is independent of the classical Paris law parameters and therefore allows the application of non-uniform cycles and loading conditions during propagation. Moreover, it has been shown that this law can be recovered as a result of cycle-by-cycle simulations. However, from a practical viewpoint, Paris law parameters have been experimentally determined for many materials, and their use in a linear fatigue simulation is convenient because it avoids expensive ad-hoc experimental campaigns and allows comparability with the results of other techniques. Another limitation of this cycle-by-cycle modeling approach is its computational cost, especially for high-cycle fatigue scenarios, as it requires resolving each individual load cycle within the phase-field simulation. This is particularly prohibitive, and the computational burden becomes even more significant in three-dimensional simulations, where the number of degrees of freedom and the complexity of crack evolution increase substantially. Although some techniques have been proposed to accelerate these simulations, such as cycle-jumping or cycle-skipping strategies [24, 25], the cost is still inherently high since it is fundamentally based on following the loading history, thus requiring a full set of simulations during loading.

In classical linear elastic fatigue frameworks, crack propagation is typically modeled using Paris-type laws, which provide the crack growth rate and direction as a function of the Stress Intensity Factors (SIF) at the crack tip. These SIFs are well defined within LEFM theory and can be derived as a function of the specimen's stiffness for a given crack length. While analytical expressions exist for simple cases, most modern fatigue simulation frameworks rely on the numerical evaluation of these factors using the J-integral within the FEM. To simulate the complete process of crack growth, numerical techniques such as the Extended Finite Element Method (XFEM) [26] or remeshing strategies [27] are commonly employed. These methods model crack propagation incrementally, either by enriching the finite element space (as in XFEM) or by explicitly modifying the mesh to accommodate the advancing crack. Criteria such as the Maximum Tangential Stress [28] and the Maximum Energy Release Rate [29] are often used to predict the direction of crack propagation. However, both approaches are computationally intensive, as they require frequent updates to the mesh connectivity and repeated assembly and factorization of the stiffness matrix at each propagation step.

In this work, a novel framework, presented in [17], combines PFF simulations with Paris-law integration and enables efficient fatigue crack propagation analysis without cycle-by-cycle computation. The method is validated against analytical and experimental benchmarks.

1.2.1 Software and reproducibility

The software landscape for phase-field fracture includes both commercial and open-source options. One route is to extend commercial platforms such as ABAQUS with subroutines [16, 30, 31, 32], which offer flexibility but are not open source. Another option is to rely on open-source frameworks such as RACCOON [33], a parallel finite-element environment specialized in PFF simulations.

Beyond these fracture-oriented tools, several platforms support phase-field modeling more broadly. Examples include FEniCS [34] and COMSOL, which can be used to implement

phase-field formulations but are often adapted to specific problems rather than provided as general-purpose fracture environments. Other noteworthy packages include SymPhas [35], a general-purpose platform for phase-field, phase-field crystal, and reaction-diffusion simulations; OpenPhase [36], which enables three-dimensional simulations of microstructural evolution using the multiphase-field method; and PRISMS-PF [37], a general framework for phase-field modeling based on a matrix-free finite-element approach.

A central contribution of this thesis is the development of ***PhaseFieldX***, the open-source package that implements the PFF models and numerical methods presented throughout this work. *PhaseFieldX* serves as the computational backbone of the thesis, providing a common implementation platform for the fatigue, DGCM, and LVPP methodologies developed here. To ensure scientific rigor and reproducibility, it has been peer-reviewed and published in the *Journal of Open Source Software* (JOSS) [38], which supports the quality, usability, and transparency of the code. By releasing the source code, documentation, and example problems, this thesis enables independent verification and extension of the computational results. The design, structure, and validation of *PhaseFieldX* are detailed in Chapter 6.

1.3 Objectives

The primary motivation of this doctoral thesis is to advance the predictive capabilities and computational efficiency of PFF mechanics. Despite the success of the method as a diffuse interface approach, significant limitations persist. Simulations of high-cycle fatigue are often computationally prohibitive due to the need to track individual cycles, while the accuracy of energy calculations is frequently compromised by strain localization artifacts. Additionally, robustly enforcing the physical constraints of the phase-field variable—such as irreversibility and its interval constraint—remains a challenge. Common techniques like penalty methods often introduce numerical parameters that affect accuracy and stability, which this work seeks to avoid and which constitute a central motivation of this research.

Addressing these challenges requires a unified approach that bridges rigorous theoretical formulations with efficient numerical algorithms. Consequently, the main objective of this dissertation is to develop advanced numerical frameworks that, while taking into account the characteristics of the theoretical formulations, enhance the efficiency, accuracy, and versatility of PFF simulations. The work also evaluates the validity and limitations of the proposed frameworks in a rigorous manner. To achieve this, the following specific objectives are defined:

- **Comprehensive review and analysis:** Conduct a detailed review of existing PFF models, highlighting their theoretical foundations and deriving the relationships between different formulations, such as isotropic and anisotropic models, different crack-surface regularizations (e.g., AT2 and AT1), and strategies to handle irreversibility from a theoretical point of view. This includes a specific analysis of the derivation and implementation details of these models.
- **Unified numerical framework:** Develop a general and modular framework capable of handling various PFF models and solvers within a unified architecture.
- **Robust equilibrium path tracking:** Develop a simplified crack path tracking algorithm capable of handling "snap-back" and "snap-through" instabilities. The

goal is to implement an energy-controlled solver using a single scalar constraint within a monolithic framework, allowing the tracking of unstable crack propagation during the simulation.

- **Novel fatigue approach:** Propose a new methodology for simulating fatigue crack propagation that bridges Phase-Field and LEFM. The aim is to overcome the high computational cost of cycle-by-cycle methods in high-cycle fatigue scenarios by extracting Paris-law parameters directly from quasi-static phase-field simulations.
- **Crack area correction method:** Develop an automatic and geometry-independent method to correct the overestimation of crack surface area caused by strain localization. This method should provide accurate predictions of crack growth and be directly extensible to three-dimensional simulations.
- **Analysis of length-scale effects:** Investigate the influence of the length-scale parameter (l) on simulation metrics and its relationship with the mesh size (h). Theoretical and numerical analyses will be conducted to establish recommended guidelines for mesh resolution to mitigate strain localization effects.
- **Robust constraint enforcement:** Develop a numerical strategy to rigorously enforce the physical constraints of the phase-field variable, specifically its interval constraint ($\phi \in [0, 1]$) and irreversibility ($\dot{\phi} \geq 0$). The aim is to overcome the limitations of standard penalty or history-variable methods by adopting a robust algorithmic framework that ensures stability without compromising accuracy.
- **Open-source software development:** Develop all the solvers and methodologies presented in this work within an open-source software package, ensuring reproducibility and accessibility to the scientific community. This includes comprehensive documentation and reproducible examples for each implemented method.

1.4 Outline

In order to achieve the objectives presented, this thesis is structured into seven chapters, organized as follows.

Chapter 2 provides a comprehensive review of PFF mechanics, detailing the evolution of the models and presenting several benchmark examples. It highlights the motivation for adopting phase-field methods, their advantages over traditional fracture mechanics approaches, and the challenges that remain in their numerical implementation.

Chapter 3 proposes a novel methodology for simulating fatigue crack propagation more efficiently. To address the computational cost of direct cycle-by-cycle simulations, a crack-path-controlled solver is presented. This approach allows for the accurate extraction of fracture parameters from quasi-static simulations, which are then used to integrate a Paris-law model, bridging the gap between phase-field and LEFM.

Chapter 4 introduces the DGCM to address the overestimation of crack surface area caused by strain localization. Based on the principle of energy equipartition, where the energy contributions from the phase-field and its gradient are equal as the length-scale parameter approaches zero, this method provides a geometry-independent correction factor. The chapter details the derivation and validation of the method, demonstrating that the definition of the correction factor is mesh-independent and readily applicable to the

entire domain, including 3D simulations.

Chapter 5 presents the application of the LVPP algorithm to PFF problems, implemented within a finite element framework known as the Proximal Galerkin method. The LVPP method is introduced as a robust and efficient solver that naturally handles the physical constraints of the phase-field variable, such as its interval constraint and irreversibility. Theoretical foundations, implementation derivation, and numerical examples demonstrating its effectiveness in simulating crack initiation and propagation are provided.

Chapter 6 discusses the development of the custom open-source software package *PhaseFieldX*, tailored for PFF simulations. It outlines the design principles and architecture of the software, which facilitates the implementation of the advanced numerical methods proposed in this thesis. The capabilities of the package are demonstrated through a series of benchmark problems and case studies.

Finally, Chapter 7 summarizes the key contributions and findings of this research. It discusses the impact of the proposed models and methodologies on the field of computational fracture mechanics and outlines potential directions for future research.

The organization of this dissertation reflects the scientific contributions and publications derived from this thesis. A total of four publications are directly related to the content presented herein: two have been published, and the others are currently under review. Chapter 2 provides the fundamental background and state-of-the-art review that serves as the basis for all subsequent chapters. Chapter 3 is directly based on the publication [17], where the proposed fatigue model is introduced and validated (published). The chapters 4 and 5 correspond to works that have been submitted. Chapter 6 describes the open-source software developed during this dissertation, *PhaseFieldX*, which is detailed in [38] (published). It is important to emphasize that *PhaseFieldX* contains the implementation of all methods and algorithms developed in this thesis. Furthermore, each scientific publication associated with this work includes a dedicated repository containing the specific scripts and example files required to reproduce the results, all of which are built upon the *PhaseFieldX* package.

The structure of the thesis and the interrelationships between chapters are visually summarized in Figure 1.2. While the thesis is presented in a linear sequence, the technical chapters are interconnected through the central theme of PFF. Chapter 2 serves as the foundational pillar. Chapters 3, 4, and 5 expand upon this foundation in distinct directions: fatigue analysis, geometric accuracy correction, and robust constraint enforcement, respectively. Specifically, the DGCM in Chapter 4 builds upon the energy-controlled solvers discussed in Chapter 3, addressing the crack surface overestimation issues identified therein. Meanwhile, the LVPP method in Chapter 5 provides a general solver framework that validates the robustness of the phase-field formulation itself. Finally, Chapter 6 unifies these contributions through their implementation in the *PhaseFieldX* package.

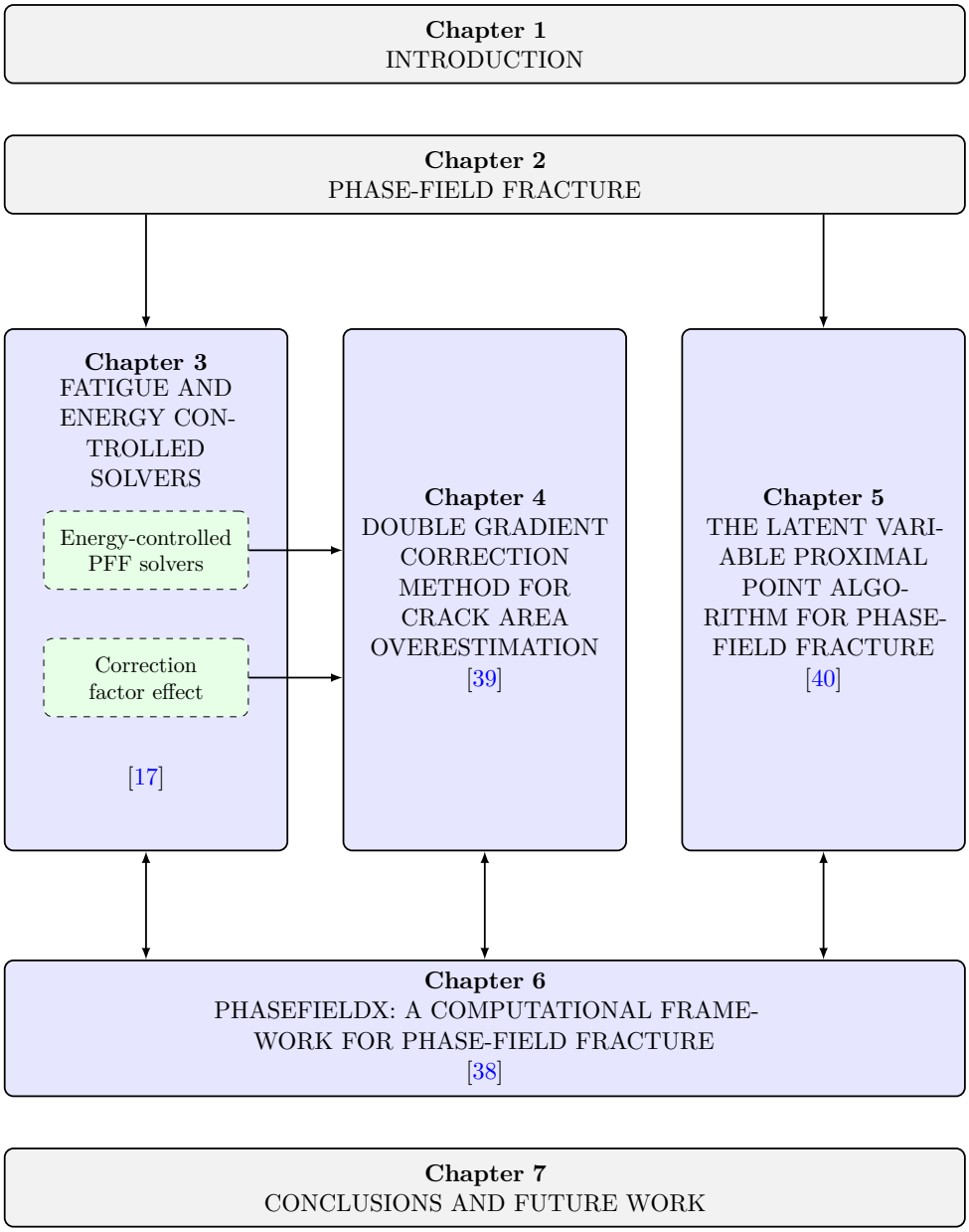

Figure 1.2: Structural organization of the thesis and interdependencies between chapters.

Chapter 2

PHASE-FIELD FRACTURE

The variational approach to fracture mechanics is fundamentally based on the principle of minimizing the total potential energy of a solid body containing a crack. This total potential energy comprises the elastic strain energy stored in the bulk material and the surface energy associated with the crack. In this formulation, the crack discontinuity set Γ_{sharp} is treated as an unknown of the problem, determined such that it minimizes the energy functional. This classical formulation is expressed in Eq. (2.1):

$$V(\boldsymbol{u}, \Gamma_{\text{sharp}}) = \underbrace{\int_{\Omega \setminus \Gamma_{\text{sharp}}} \psi(\boldsymbol{\epsilon}(\boldsymbol{u}))\, \mathrm{d}\boldsymbol{x}}_{\text{Elastic strain energy}} + \underbrace{G_c \int_{\Gamma_{\text{sharp}}} \mathrm{d}S}_{\text{Fracture surface energy}} - \mathcal{E}_{\text{ext}}(\boldsymbol{u}), \tag{2.1}$$

where $\boldsymbol{u}$ is the displacement field, $\boldsymbol{\epsilon}$ is the strain tensor, $\psi(\boldsymbol{\epsilon}(\boldsymbol{u}))$ represents the strain energy density, G_c denotes the critical energy release rate, Γ_{sharp} represents the sharp discontinuity or crack surface, and $\mathcal{E}_{\text{ext}}(\boldsymbol{u})$ refers to the potential energy of the external forces.

A major challenge in the classical formulation is that the crack set Γ_{sharp} is an unknown in the problem. To address this, [1, 2] reformulated the problem within a variational framework where the sharp discontinuity is approximated by a continuous auxiliary variable, the phase-field. This field varies smoothly from $\phi = 0$ (not damaged) to $\phi = 1$ (fully damaged), representing the crack transition. This method was further developed by authors such as [3]. The resulting regularization permits solving the fracture problem via a minimization principle that represents cracks using a continuous scalar field ϕ, eliminating the need for explicit crack-tracking algorithms and naturally handling complex crack topologies such as branching and merging.

The PFF method models crack propagation through the minimization of a total potential energy functional. Similar to Eq. (2.1), this functional is composed of the effective elastic strain energy, the fracture surface energy, and the work done by external forces. However, in this case, the unknown discontinuity is not explicitly present; instead, a new continuous variable ϕ is introduced to represent the crack. The total potential energy functional in the phase-field fracture framework is given by:

$$\mathcal{E}(\boldsymbol{u}, \phi) = \underbrace{\int_{\Omega} \left(g(\phi) \underbrace{\psi_a(\boldsymbol{\epsilon}(\boldsymbol{u})) + \psi_b(\boldsymbol{\epsilon}(\boldsymbol{u}))}_{\psi(\boldsymbol{\epsilon}(\boldsymbol{u}))} \right) \mathrm{d}\boldsymbol{x}}_{\Psi(\boldsymbol{\epsilon}(\boldsymbol{u}),\phi)\text{Effective elastic strain energy}} + \underbrace{G_c \underbrace{\int_{\Omega} \gamma(\phi, \nabla\phi)\, \mathrm{d}\boldsymbol{x}}_{\Gamma(\phi)}}_{\text{Fracture surface energy}} - \mathcal{E}_{\text{ext}}(\boldsymbol{u}), \tag{2.2}$$

where $\boldsymbol{\epsilon}(\boldsymbol{u}) = \frac{1}{2}(\nabla \boldsymbol{u} + (\nabla \boldsymbol{u})^T)$ is the symmetric strain tensor and ϕ is the phase-field variable. Here,

$$\psi(\boldsymbol{\epsilon}) = \frac{1}{2}\lambda(\mathrm{tr}(\boldsymbol{\epsilon}))^2 + \mu \mathrm{tr}(\boldsymbol{\epsilon}^2) \tag{2.3}$$

represents the strain energy density, with λ and μ denoting the Lamé parameters. These are defined in terms of Young's modulus E and Poisson's ratio ν as $\lambda = \frac{E\nu}{(1+\nu)(1-2\nu)}$ and $\mu = \frac{E}{2(1+\nu)}$. The strain energy is decomposed into an active part ψ_a, which is affected by the degradation function $g(\phi)$, and an inactive component ψ_b, which remains undegraded. This decomposition distinguishes between the energy that drives crack evolution (ψ_a) and the energy that does not (ψ_b). This separation enables the model to capture physically realistic behaviors, such as allowing damage under tensile loading while preventing it under compression. Different types of energy splits exist in the literature; each is covered in detail in Section 2.1.2.

The degradation function $g(\phi)$ quantifies the reduction in material stiffness as damage evolves. In general, the most widely used function takes a quadratic form

$$g(\phi) = (1-\phi)^2, \tag{2.4}$$

though other functional forms have been proposed in the literature [8].

The term $G_c \int_\Omega \gamma(\phi, \nabla\phi)\, \mathrm{d}\boldsymbol{x}$ represents the fracture surface energy, where G_c is the critical energy release rate and $\gamma(\phi, \nabla\phi)$ is the crack surface density function. This term is directly related to the diffuse representation of the crack, and several forms can be considered, as will be detailed in Section 2.2. Furthermore, this component can be analyzed as a problem depending only on the phase-field variable. The integral $\Gamma(\phi) = \int_\Omega \gamma(\phi, \nabla\phi)\, \mathrm{d}\boldsymbol{x}$ defines the Crack Surface Density Functional (CSDF), which governs the geometric regularization. This functional must not be confused with the local crack surface density function, $\gamma(\phi, \nabla\phi)$, which refers to the integrand. It is important to note that, in contrast to the previous sharp interface formulation, this energy depends on the phase-field variable ϕ and its gradient $\nabla\phi$, and it is defined as an integral over the whole domain, rather than over the crack surface as in Eq. (2.1).

The term $\mathcal{E}_{\mathrm{ext}}(\boldsymbol{u})$ represents the potential energy of the external forces given by

$$\mathcal{E}_{\mathrm{ext}}(\boldsymbol{u}) = \int_\Omega \boldsymbol{f} \cdot \boldsymbol{u}\, \mathrm{d}\boldsymbol{x} + \int_{\partial\Omega_t} \boldsymbol{t} \cdot \boldsymbol{u}\, \mathrm{d}S, \tag{2.5}$$

where $\boldsymbol{f}$ is the body force per unit volume and $\boldsymbol{t}$ is the traction applied on the Neumann boundary $\partial\Omega_N$. This term remains consistent between both the discrete and diffuse formulations, as it depends solely on the displacement field and external forces, and does not involve the crack representation.

Given the fundamental differences between the discrete (sharp) and the diffuse (phase-field) variational formulations, it is useful to establish a clear relationship between their respective terms to clarify the concepts. Table 2.1 presents a side-by-side comparison of the energetic components in both formulations. As seen in the table, the effective elastic strain energy in the phase-field formulation is modulated by the degradation function $g(\phi)$, which accounts for the damage state of the material. The fracture surface energy in the phase-field approach is represented as an integral over the entire domain, involving a crack surface density function $\gamma(\phi, \nabla\phi)$. The external energy term remains consistent

Table 2.1: Comparison between PFF (diffuse) and discrete (sharp) variational formulations (transposed).

	Diffuse (phase-field)	**Discrete (sharp)**
Unknowns	$\boldsymbol{u},\ \phi$	$\boldsymbol{u},\ \Gamma_{\text{sharp}}$
Elastic strain energy	$\int_\Omega g(\phi)\left(\psi_a(\boldsymbol{\epsilon}(\boldsymbol{u})) + \psi_b(\boldsymbol{\epsilon}(\boldsymbol{u}))\right) \mathrm{d}\boldsymbol{x}$	$\int_{\Omega\setminus\Gamma_{\text{sharp}}} \psi(\boldsymbol{\epsilon}(\boldsymbol{u}))\, \mathrm{d}\boldsymbol{x}$
Fracture surface energy	$G_c \int_\Omega \gamma(\phi, \nabla\phi)\, \mathrm{d}\boldsymbol{x}$	$G_c \int_{\Gamma_{\text{sharp}}} \mathrm{d}S$
External energy	$\mathcal{E}_{\text{ext}}(\boldsymbol{u})$	$\mathcal{E}_{\text{ext}}(\boldsymbol{u})$

between both formulations, as it depends solely on the displacement field and external forces.

To provide a clear roadmap of the PFF method, it is useful to view it as a modular framework rather than a monolithic theory. As illustrated in Figure 2.1, the formulation is constructed around distinct pillars that collectively define a specific model and its numerical implementation. This figure serves as a structural guide for the subsequent sections, where each of the highlighted components — Effective Elastic Strain Energy, Fracture Surface Energy, Irreversibility Enforcement, and Solution Strategy — is analyzed in detail.

As an introduction, these pillars are briefly described here, and they are analyzed in detail in the following sections:

1. **Effective elastic strain energy:** This term defines the material's response to deformation. Key modeling choices include the degradation function $g(\phi)$ (e.g., quadratic, cubic) and the energy decomposition method (isotropic or anisotropic) required to capture tension-compression asymmetry.
2. **Fracture surface energy:** This component governs the energy dissipated during crack propagation, defined by the critical energy release rate G_c and the specific crack surface density function. While integral to the coupled PFF problem, this functional can be analyzed as an independent variational problem—represented by the dashed workflow branches in Figure 2.1 to rigorously study the geometric regularization and the role of the length scale parameter l.
3. **Irreversibility enforcement:** To ensure thermodynamic consistency, the formulation must guarantee that cracks do not heal and that the phase-field variable remains within the interval constraint ($\phi \in [0, 1]$). This is typically enforced via history-field variables or penalty methods.
4. **Solution strategy:** The resulting problem is a constrained, non-convex minimization. Robust numerical schemes are required, such as staggered (operator-split) solvers for stability or monolithic solvers for efficiency, typically combined with Newton-Raphson linearization.

2.1 Effective elastic strain energy

The effective elastic strain energy describes the stored energy in the body, accounting for stiffness degradation due to damage. As presented in Eq. (2.2), the effective elastic strain

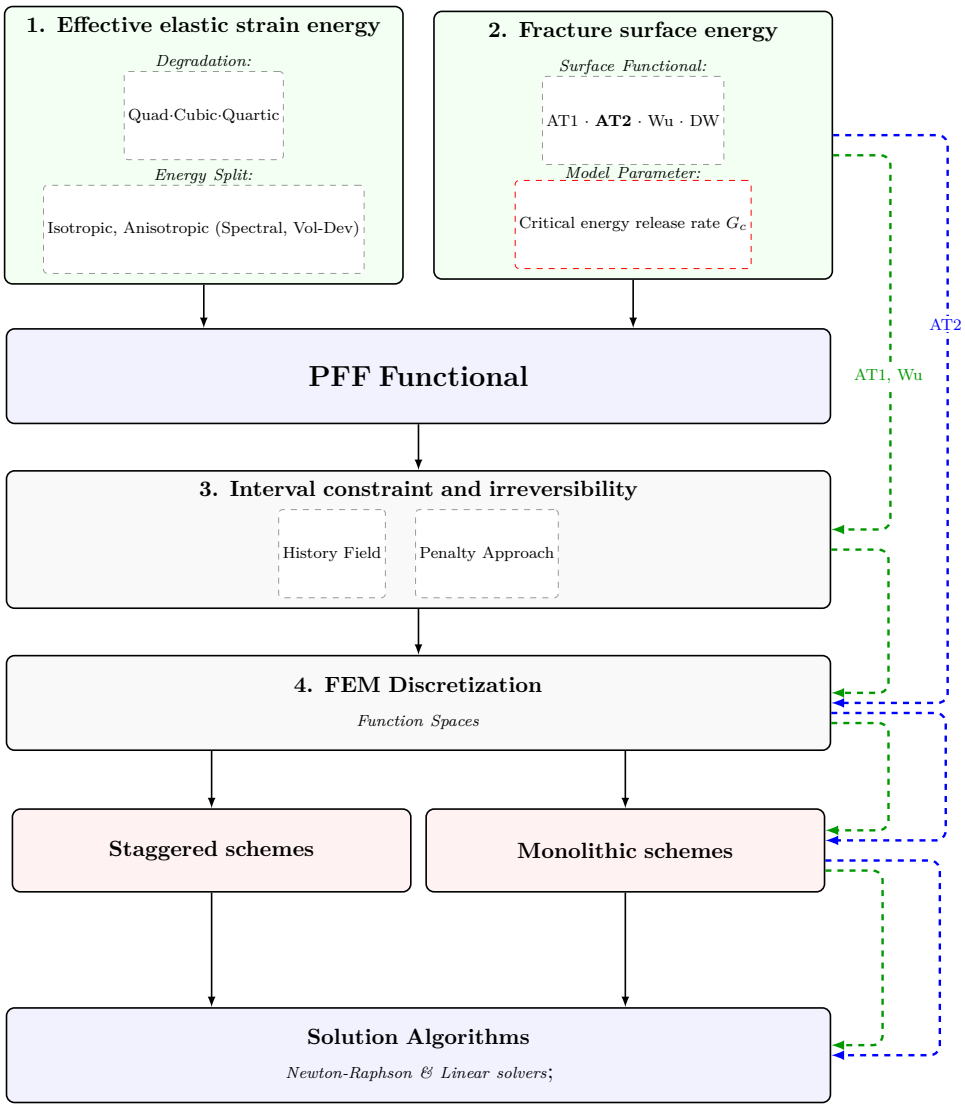

Figure 2.1: PFF modular framework: overview of the key components and numerical strategies. The dashed lines highlight the AT2 branch (blue) and the AT1/Wu branches (green), which can be analyzed independently by considering the CSDF separately from the full PFF problem.

energy is defined as:

$$\Psi(\boldsymbol{\epsilon}(\boldsymbol{u}),\phi) = \int_\Omega \Big(g(\phi) \underbrace{\psi_a(\boldsymbol{\epsilon}(\boldsymbol{u})) + \psi_b(\boldsymbol{\epsilon}(\boldsymbol{u}))}_{\psi(\boldsymbol{\epsilon}(\boldsymbol{u}))} \Big) \, \mathrm{d}\boldsymbol{x}. \tag{2.6}$$

Here, two main aspects are significant: first, the degradation function $g(\phi)$ modulates the strain energy density $\psi(\boldsymbol{\epsilon})$; second, the energy is decomposed into an active part ψ_a, which is affected by the degradation function $g(\phi)$, and an inactive component ψ_b, which is not. The strain energy density Eq. (2.3) is thus split as $\psi(\boldsymbol{\epsilon}) = \psi_a(\boldsymbol{\epsilon}) + \psi_b(\boldsymbol{\epsilon})$.

Several formulations for both the degradation function and the energy split exist in the literature; they are each addressed in the subsections below.

2.1.1 Degradation functions

The degradation function $g(\phi)$, as explained in detail in [41], plays a fundamental role in PFF models by quantifying the loss of material stiffness as damage accumulates. By modulating the elastic strain energy density, it effectively creates the coupling between the phase-field variable and the mechanical response.

To ensure a physically consistent representation of the damage process, $g(\phi)$ is required to satisfy the following properties, as outlined in [3]:

$$g(0) = 1, \quad g(1) = 0, \quad g'(1) = 0. \tag{2.7}$$

The first two conditions correspond to the states of intact material and complete failure, respectively. Thus, when damage is absent ($\phi = 0$), the degradation function equals 1 and does not affect the strain energy. Conversely, if damage is fully developed ($\phi = 1$), the degradation function equals 0, effectively eliminating the energy contribution. For intermediate values of the phase-field ($0 < \phi < 1$), the degradation function scales the energy by a factor between 0 and 1. The condition $g'(1) = 0$ ensures that the driving force for damage vanishes when the material is fully broken, preventing unphysical evolution in the fully damaged state.

While the quadratic form Eq. (2.4) is widely adopted due to its simplicity and robustness, as shown in [2], other functional forms have been proposed to tailor the softening behavior or to approximate specific cohesive laws. In this thesis, the standard quadratic degradation function is adopted as the primary choice for all analyses, providing a consistent basis for investigation. However, for completeness, other common alternatives, including cubic [42] and quartic [8] polynomials, are also presented here. Table 2.2 summarizes these common degradation functions along with their derivatives. Figure 2.2 shows the degradation function and its derivative with respect to the phase-field variable in the $[0, 1]$ range.

Having discussed the degradation function, the decomposition of the strain energy density into active and inactive parts is analyzed, which is crucial for controlling the conditions under which damage evolves.

2.1.2 Isotropic and anisotropic models

A central requirement in PFF modeling is to ensure that damage evolution is consistent with physical observations. Specifically, cracks should propagate under certain conditions;

Table 2.2: Summary of available degradation functions $g(\phi)$ and their derivatives.

Degradation Type	**Function** $g(\phi)$	**Derivative** $g'(\phi)$
Quadratic	$(1-\phi)^2$	$-2(1-\phi)$
Cubic	$3(1-\phi)^2 - 2(1-\phi)^3$	$-6\phi(1-\phi)$
Quartic	$4(1-\phi)^3 - 3(1-\phi)^4$	$-12(1-\phi)^2 + 12(1-\phi)^3$

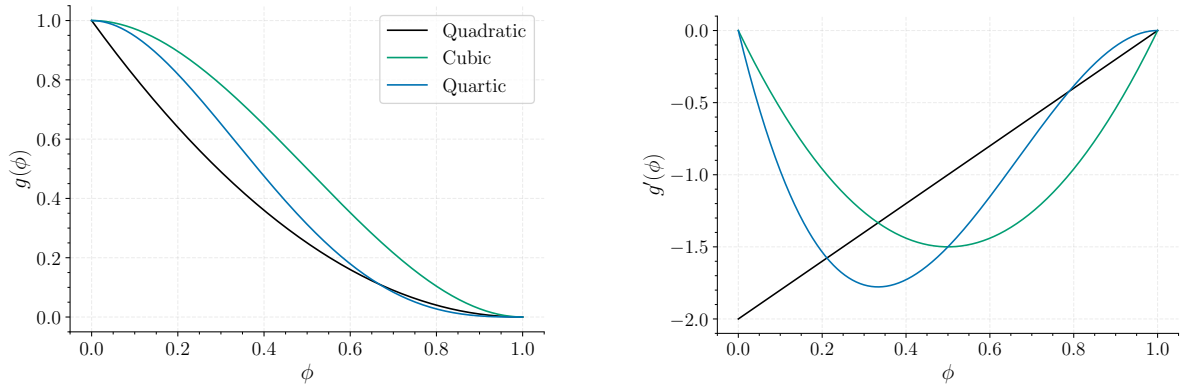

(a) Degradation function curves

(b) Derivative of degradation function curves

Figure 2.2: Comparison of different degradation functions: (a) degradation function $g(\phi)$ vs phase-field ϕ and (b) derivative of degradation function $g'(\phi)$ vs phase-field ϕ. The shape of $g(\phi)$ controls the softening behavior and the width of the fracture process zone.

for example, they should propagate under tension but not under compression. This is achieved by applying the degradation function exclusively to the energy contribution that can generate cracks, ψ_a, while leaving the inactive compressive component, ψ_b, undegraded. Various strategies have been developed to decompose the strain energy density into these contributions; these are collectively referred to as anisotropic formulations. Conversely, formulations that assume the degradation function acts on the total strain energy density are classified as isotropic.

Isotropic model

The simplest approach is the isotropic model, where degradation affects the entire strain energy density given in Eq. (2.3). In this framework, the entire strain energy density Eq. (2.3) is subject to degradation, so for the general representation presented in Eq. (2.2), the following terms are considered: $\psi_a = \psi(\boldsymbol{\epsilon})$ and $\psi_b = 0$. While computationally efficient, this model does not distinguish between tensile and compressive stress states, often leading to unrealistic crack patterns in compression-dominated regimes. To address the limitations of the isotropic model, anisotropic formulations aim to handle this aspect.

Anisotropic models

To accurately capture fracture behavior under complex loading conditions, anisotropic models decompose the strain energy density into active (energy capable of driving fracture) and inactive (energy not capable of driving fracture) parts. These energy decompositions

are based on two main considerations: 1) a kinematic decomposition of the strain tensor, and 2) the formulation of energy components based on the strain tensor as well as the split strain components. Two widely adopted methods in the literature are the spectral decomposition and the volumetric-deviatoric decomposition.

Spectral decomposition Proposed in [3], this method is based on the spectral decomposition of the strain tensor. The strain tensor $\boldsymbol{\epsilon}$ is diagonalized as $\boldsymbol{\epsilon} = \sum_{i=1}^{3} \epsilon^i \boldsymbol{n}^i \otimes \boldsymbol{n}^i$, where ϵ^i are the principal strains and $\boldsymbol{n}^i$ are the corresponding principal directions. Using Macaulay brackets,

$$\langle x \rangle_{\pm} = \frac{x \pm |x|}{2}, \tag{2.8}$$

the strain tensor is split into positive and negative contributions:

$$\boldsymbol{\epsilon}_{\pm} := \sum_{i=1}^{3} \langle \epsilon^i \rangle_{\pm} \boldsymbol{n}^i \otimes \boldsymbol{n}^i. \tag{2.9}$$

Accordingly, the strain energy density is decomposed into tensile (ψ_a) and compressive (ψ_b) parts:

$$\psi_a^{\text{spectral}}(\boldsymbol{\epsilon}) = \frac{1}{2}\lambda \langle \text{tr}(\boldsymbol{\epsilon}) \rangle_+^{\,2} + \mu \text{tr}(\boldsymbol{\epsilon}_+^2), \tag{2.10}$$

$$\psi_b^{\text{spectral}}(\boldsymbol{\epsilon}) = \frac{1}{2}\lambda \langle \text{tr}(\boldsymbol{\epsilon}) \rangle_-^{\,2} + \mu \text{tr}(\boldsymbol{\epsilon}_-^2). \tag{2.11}$$

This formulation provides a physically rigorous separation of tensile and compressive modes. Note that the term multiplying the Lamé parameter λ contributes entirely to either the active or the inactive part, depending on the sign of the strain tensor trace. In contrast, the term multiplying the shear modulus μ is split based on the positive and negative spectral components of the strain tensor, distributing energy between the degraded and undegraded parts.

Volumetric-Deviatoric decomposition Proposed in [9], this method is based on the volumetric (or spherical) and deviatoric parts of the strain tensor. The strain tensor is decomposed as:

$$\boldsymbol{\epsilon} = \boldsymbol{\epsilon}^S + \boldsymbol{\epsilon}^D, \qquad \boldsymbol{\epsilon}^S = \frac{1}{m}\text{tr}(\boldsymbol{\epsilon})\boldsymbol{I}, \qquad \boldsymbol{\epsilon}^D = \boldsymbol{\epsilon} - \boldsymbol{\epsilon}^S, \tag{2.12}$$

where m is the spatial dimension (1, 2, or 3). The energy split assumes that cracks form due to positive volumetric expansion and deviatoric deformations (shear). The energy components are defined as:

$$\psi_a^{\text{vol-dev}}(\boldsymbol{\epsilon}) = \frac{1}{2}\kappa \langle \text{tr}(\boldsymbol{\epsilon}) \rangle_+^{\,2} + \mu \text{tr}(\boldsymbol{\epsilon}^{D^2}), \tag{2.13}$$

$$\psi_b^{\text{vol-dev}}(\boldsymbol{\epsilon}) = \frac{1}{2}\kappa \langle \text{tr}(\boldsymbol{\epsilon}) \rangle_-^{\,2}, \tag{2.14}$$

where $\kappa = \lambda + \frac{2}{m}\mu$ is the bulk modulus.

Here again, the term multiplying the bulk modulus κ contributes entirely to either the active or the inactive part, depending on the sign of the trace of the strain tensor. In

contrast, the energy term multiplying the shear modulus μ is fully degraded, meaning it belongs entirely to the active energy component.

It is crucial to emphasize that while the nomenclature of anisotropic models typically refers to the kinematic decomposition of the strain tensor (the first ingredient), the physical behavior is ultimately determined by the definition of the active and inactive energy densities based on these tensor components (the second ingredient). Consequently, distinct models may share the same strain tensor decomposition but employ different energy splits. To illustrate this distinction, consider an alternative formulation based on the volumetric-deviatoric strain tensor split. Unlike the standard model presented above, this alternative defines the active energy solely through the deviatoric component, leaving the entire volumetric energy undegraded:

$$\psi_a^{\text{alternative vol-dev}}(\boldsymbol{\epsilon}) = \mu \text{tr}(\boldsymbol{\epsilon}^{D^2}), \tag{2.15}$$

$$\psi_b^{\text{alternative vol-dev}}(\boldsymbol{\epsilon}) = \frac{1}{2}\kappa \text{tr}(\boldsymbol{\epsilon})^2. \tag{2.16}$$

Summary of energy decompositions As seen before, both models rely on two main components: a kinematic decomposition of the strain tensor and a subsequent decomposition of the strain energy density. First, the strain tensor decompositions are outlined in Table 2.3. Subsequently, Table 2.4 summarizes the split components for both isotropic and anisotropic models. This includes the strain energy densities (ψ_a and ψ_b), the active and inactive stress tensors defined as the first derivatives of the energy with respect to the strain ($\boldsymbol{\sigma}_a = \frac{\partial \psi_a}{\partial \boldsymbol{\epsilon}}$ and $\boldsymbol{\sigma}_b = \frac{\partial \psi_b}{\partial \boldsymbol{\epsilon}}$), and the material tangent stiffness tensors computed as the second derivatives ($\mathbb{C}_a = \frac{\partial^2 \psi_a}{\partial \boldsymbol{\epsilon}^2}$ and $\mathbb{C}_b = \frac{\partial^2 \psi_b}{\partial \boldsymbol{\epsilon}^2}$). The split stress tensors will appear directly in the weak form of the governing equations of the PFF problem, while the material tangent stiffness tensors will be used to define the numerical framework and linearize the problem within a Newton-Raphson solution scheme, as will be presented in the following section.

Table 2.3: Strain tensor decomposition methods.

Spectral	**Volumetric-Deviatoric**
$\boldsymbol{\epsilon}_+ = \sum_{i=1}^{3} \langle \epsilon^i \rangle^+ \boldsymbol{n}^i \otimes \boldsymbol{n}^i$	$\boldsymbol{\epsilon}_S = \frac{1}{m}\text{tr}(\boldsymbol{\epsilon})\boldsymbol{I}$
$\boldsymbol{\epsilon}_- = \sum_{i=1}^{3} \langle \epsilon^i \rangle^- \boldsymbol{n}^i \otimes \boldsymbol{n}^i$	$\boldsymbol{\epsilon}_D = \boldsymbol{\epsilon} - \frac{1}{m}\text{tr}(\boldsymbol{\epsilon})\boldsymbol{I}$

Other anisotropic formulations have also been proposed in the literature. In particular, directional splits [44] introduce a crack-oriented decomposition of the driving energy based on a local crack orientation vector, enabling a consistent distinction between tensile and shear contributions and allowing for mode-dependent fracture behavior. Additionally, recent multi-cohesive anisotropic models [45] allow different cohesive lengths along the material directions, enabling independent control of the critical stresses governing crack nucleation in each direction. These formulations are relevant because they provide additional flexibility to represent crack nucleation and propagation under anisotropic conditions.

Table 2.4: Energy densities, stress tensors, and tangent tensors ($\mathbb{C}$) decompositions for isotropic and anisotropic models. Here, $\mathbb{J} = \boldsymbol{I} \otimes \boldsymbol{I}$, $\mathbb{I}^{\text{sym}}$ is the symmetric fourth-order identity, $\mathbb{Q} = \mathbb{I}^{\text{sym}} - \frac{1}{m}\mathbb{J}$ is the deviatoric projector, $\mathbb{P}_{\pm}$ are spectral projectors defined in [43], and $H(\cdot)$ is the Heaviside step function.

	Isotropic	**Anisotropic**	
		Spectral	**Volumetric-Deviatoric**
ψ_a	$\frac{1}{2}\lambda(\text{tr}(\boldsymbol{\epsilon}))^2 + \mu\text{tr}(\boldsymbol{\epsilon}^2)$	$\frac{1}{2}\lambda\langle\text{tr}(\boldsymbol{\epsilon})\rangle_+^{\,2} + \mu\text{tr}(\boldsymbol{\epsilon}_+^{\,2})$	$\frac{1}{2}\kappa\langle\text{tr}(\boldsymbol{\epsilon})\rangle_+^{\,2} + \mu\text{tr}(\boldsymbol{\epsilon}^{D\,2})$
ψ_b	0	$\frac{1}{2}\lambda\langle\text{tr}(\boldsymbol{\epsilon})\rangle_-^{\,2} + \mu\text{tr}(\boldsymbol{\epsilon}_-^{\,2})$	$\frac{1}{2}\kappa\langle\text{tr}(\boldsymbol{\epsilon})\rangle_-^{\,2}$
$\boldsymbol{\sigma}_a$	$\lambda\text{tr}(\boldsymbol{\epsilon})\boldsymbol{I} + 2\mu\boldsymbol{\epsilon}$	$\lambda\langle\text{tr}(\boldsymbol{\epsilon})\rangle_+\boldsymbol{I} + 2\mu\boldsymbol{\epsilon}_+$	$\kappa\langle\text{tr}(\boldsymbol{\epsilon})\rangle_+\boldsymbol{I} + 2\mu\boldsymbol{\epsilon}^D$
$\boldsymbol{\sigma}_b$	$\boldsymbol{0}$	$\lambda\langle\text{tr}(\boldsymbol{\epsilon})\rangle_-\boldsymbol{I} + 2\mu\boldsymbol{\epsilon}_-$	$\kappa\langle\text{tr}(\boldsymbol{\epsilon})\rangle_-\boldsymbol{I}$
$\mathbb{C}_a$	$\lambda\mathbb{J} + 2\mu\mathbb{I}^{\text{sym}}$	$\lambda H(\text{tr}(\boldsymbol{\epsilon}))\mathbb{J} + 2\mu\mathbb{P}_+(\boldsymbol{\epsilon})$	$\kappa H(\text{tr}(\boldsymbol{\epsilon}))\mathbb{J} + 2\mu\mathbb{Q}$
$\mathbb{C}_b$	$\boldsymbol{0}$	$\lambda H(-\text{tr}(\boldsymbol{\epsilon}))\mathbb{J} + 2\mu\mathbb{P}_-(\boldsymbol{\epsilon})$	$\kappa H(-\text{tr}(\boldsymbol{\epsilon}))\mathbb{J}$

2.2 Fracture surface energy

The fracture surface energy, as introduced in Eq. (2.2), is defined as the product of the critical energy release rate, G_c, and the CSDF, $\Gamma(\phi)$. Since G_c is a material constant, the primary component to analyze is the CSDF, $\Gamma(\phi)$, which approximates the sharp crack interface through a diffuse representation. As illustrated in the modular framework (Figure 2.1), this functional is a fundamental ingredient of the PFF method. To clearly understand the regularization mechanism, this functional is treated here as an independent problem, corresponding to the component highlighted by the green and blue dashed lines in Figure 2.1.

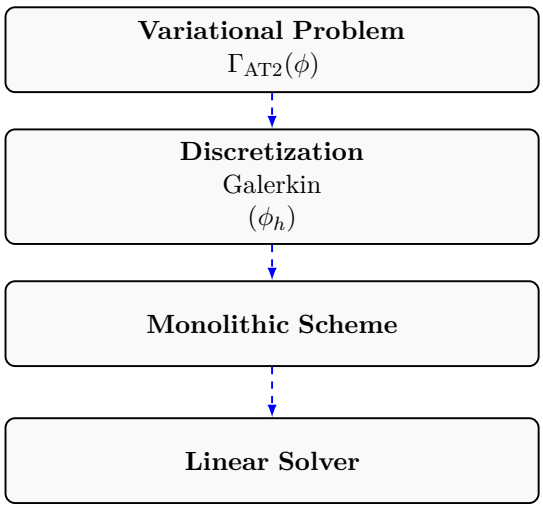

Figure 2.3: Numerical workflow for the AT2 CSDF: variational problem, discretization, monolithic scheme, and linear solver (centered).

In its general form, it is defined as:

$$\Gamma(\phi) = \int_\Omega \gamma(\phi, \nabla\phi)\,\mathrm{d}\boldsymbol{x}, \tag{2.17}$$

where $\gamma(\phi, \nabla\phi)$ is the crack surface density function per unit volume. A unified geometric approach for the crack surface density function, as detailed by [41], is given by:

$$\gamma(\phi, \nabla\phi) = \frac{1}{c_0}\left(\frac{1}{l}\alpha(\phi) + l|\nabla\phi|^2\right), \tag{2.18}$$

where l is the length scale parameter controlling the width of the transition zone, and $\alpha(\phi)$ is the geometric crack function, which satisfies $\alpha(0) = 0$ (not damaged) and $\alpha(1) = 1$ (fully damaged). The scaling constant $c_0 = 4\int_0^1 \sqrt{\alpha(\eta)}\, d\eta$ ensures that the energy dissipated during crack formation converges to the sharp fracture energy G_c as $l \to 0$.

While this general framework encompasses various models, this section focuses on the standard quadratic formulation known as the AT2 model. This corresponds to the dashed blue line presented in Figure 2.1 (other models are analyzed in detail in the following chapters) and is specifically presented in Figure 2.3, which outlines the specific numerical workflow for the AT2 model. In this model, the geometric function is defined as $\alpha(\phi) = \phi^2$ (implying $c_0 = 2$), yielding the specific CSDF:

$$\Gamma^{\mathrm{AT2}}(\phi) = \int_\Omega \left(\frac{1}{2l}\phi^2 + \frac{l}{2}|\nabla\phi|^2\right) \mathrm{d}\boldsymbol{x}. \tag{2.19}$$

Mathematically, this functional approximates the discrete crack surface area within the domain Ω. A rigorous understanding of this functional is essential, as it provides the theoretical basis for the length scale regularization parameter l.

For analytical purposes, it is useful to decompose $\Gamma^{\mathrm{AT2}}(\phi)$ into two distinct energy contributions: a term explicitly dependent on the phase-field variable, $\Gamma_\phi^{\mathrm{AT2}}$, and a term dependent on its gradient, $\Gamma_{\nabla\phi}^{\mathrm{AT2}}$:

$$\Gamma_\phi^{\mathrm{AT2}}(\phi) = \int_\Omega \frac{1}{2l}\phi^2 \,\mathrm{d}\boldsymbol{x}, \tag{2.20}$$

$$\Gamma_{\nabla\phi}^{\mathrm{AT2}}(\phi) = \int_\Omega \frac{l}{2}|\nabla\phi|^2 \,\mathrm{d}\boldsymbol{x}. \tag{2.21}$$

To illustrate the concept of crack regularization, consider a one-dimensional bar with a central crack, as shown in Figure 2.4. In a classical sharp interface approach (Figure 2.4(a)), the crack is represented as a discontinuity at a specific point. In the phase-field approach (Figure 2.4(b)), this discontinuity is represented by a phase-field variable distributed—or smeared—over the domain. The phase-field variable $\phi(\boldsymbol{x})$ transitions smoothly from $\phi = 0$ to $\phi = 1$. The width of this transition zone is controlled by the length scale parameter l.

The equilibrium equation for the phase-field is derived from the stationarity condition $\delta\Gamma^{\mathrm{AT2}} = 0$. Taking the first variation of Eq. (2.19) leads to the weak form:

$$\int_\Omega \left(\frac{1}{l}\phi\delta\phi + l\nabla\phi\cdot\nabla\delta\phi\right) \mathrm{d}\boldsymbol{x} = 0, \tag{2.22}$$

whose strong form is given by:

$$\frac{1}{l}\phi - l\Delta\phi = 0 \quad \text{in } \Omega, \tag{2.23}$$

with the Neumann boundary condition:

$$\nabla\phi\cdot\boldsymbol{n} = 0 \quad \text{on } \partial\Omega. \tag{2.24}$$

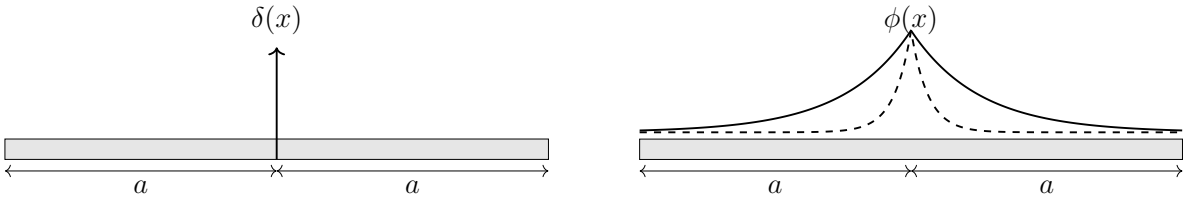

(a) Sharp crack representation.

(b) Phase-field approximation.

Figure 2.4: Bar with a central crack: (a) Sharp crack representation as a discontinuity at the center. (b) Phase-field approximation showing the smooth transition of $\phi(x)$. The solid line represents a larger length scale l, while the dashed line represents a smaller l, illustrating convergence to the sharp interface.

2.2.1 Analytical solution of the one-dimensional problem

To gain insight into the behavior of the phase-field variable ϕ and the role of the length scale parameter l, the one-dimensional case is first studied analytically. Consider a bar of half-length a with a central crack at $x = 0$, as illustrated in Figure 2.4. The equilibrium profile of the phase-field variable, $\phi(x)$, is governed by the following ordinary differential equation derived from Eq. (2.23):

$$\frac{1}{l}\phi(x) - l\phi''(x) = 0, \tag{2.25}$$

subject to the boundary conditions $\phi(0) = 1$ and, due to symmetry, $\phi'(\pm a) = 0$. The analytical solution is given by:

$$\phi_{\text{AT2}}(x) = e^{-|x|/l} + \frac{2\sinh\left(\frac{|x|}{l}\right)}{e^{\frac{2a}{l}} + 1}, \tag{2.26}$$

with its corresponding derivative:

$$\phi'_{\text{AT2}}(x) = \frac{-\text{sign}(x)}{l} e^{-|x|/l} + \frac{2\,\text{sign}(x)}{l} \frac{\cosh\left(\frac{|x|}{l}\right)}{e^{\frac{2a}{l}} + 1}, \tag{2.27}$$

where $\text{sign}(x)$ is the sign function. As the ratio $a/l \to \infty$, this solution converges to the well-known infinite domain solution, $\phi(x) = e^{-|x|/l}$, as presented by [3]. While [3] presents the solution referring to an infinite domain, here, it is interpreted as the solution for a finite domain where l is small enough that the second term in Eq. (2.26), which accounts for boundary effects, becomes negligible.

The total energy Γ can be decomposed into two contributions, as defined in Eqs. (2.20) and (2.21): the phase-field term, Γ_ϕ, and the gradient term, $\Gamma_{\nabla\phi}$. Substituting the analytical solution into these definitions yields the one-dimensional counterparts:

$$\Gamma_\phi^{\text{1D, AT2}} = \int_{-a}^{a} \frac{1}{2l}\phi(x)^2\,dx = \frac{1}{2}\tanh\left(\frac{a}{l}\right) + \frac{a}{2l}\left[1 - \tanh^2\left(\frac{a}{l}\right)\right], \tag{2.28}$$

$$\Gamma_{\nabla\phi}^{\text{1D, AT2}} = \int_{-a}^{a} \frac{l}{2}(\phi'(x))^2\,dx = \frac{1}{2}\tanh\left(\frac{a}{l}\right) - \frac{a}{2l}\left[1 - \tanh^2\left(\frac{a}{l}\right)\right]. \tag{2.29}$$

The total energy is the sum of these terms, which simplifies to:

$$\Gamma^{\text{1D, AT2}} = \Gamma_\phi^{\text{1D, AT2}} + \Gamma_{\nabla\phi}^{\text{1D, AT2}} = \tanh\left(\frac{a}{l}\right). \tag{2.30}$$

As $l/a \to 0$, the total energy converges to the sharp crack surface energy, and the contributions from the phase-field and gradient terms become equal, such that $\Gamma_{\phi}^{\text{1D, AT2}} = \Gamma_{\nabla\phi}^{\text{1D, AT2}}$. Recalling the comparison between the discrete variational problem and the PFF framework presented in Table 2.1, the energy approximation is given by:

$$G_c \int_{\Omega} \gamma(\phi, \nabla\phi)\, \mathrm{d}\boldsymbol{x} \approx G_c \int_{\Gamma_{\text{sharp}}} \mathrm{d}S. \tag{2.31}$$

As the length scale parameter l becomes sufficiently small, such that boundary effects are negligible, the total functional $\Gamma^{\text{1D, AT2}}$ converges to 1, which corresponds to the sharp crack surface in energy terms. This illustrates that the AT2 functional effectively regularizes the crack surface while ensuring convergence to the correct fracture energy as l approaches zero.

2.2.2 Numerical implementation and validation

Having defined and analytically studied the AT2 CSDF for a one-dimensional case, its numerical solution is now considered. This section presents the finite element discretization and validates the numerical framework by reproducing the analytical results.

Finite element discretization

The governing equations are discretized using the FEM. The phase-field variable ϕ is approximated within a standard Galerkin framework using nodal shape functions N_a. The discrete function space is defined as:

$$V = \left\{ \nu : \Omega \to \mathbb{R},\ \nu(\boldsymbol{x}) = \sum_{a=1}^{n_{\text{node}}} N_a(\boldsymbol{x})\, \nu_a \right\} \tag{2.32}$$

The continuous field and its variation are approximated as:

$$\phi_h(\boldsymbol{x}) = \sum_{a=1}^{n_{\text{node}}} N_a(\boldsymbol{x})\phi_a, \quad \delta\phi_h(\boldsymbol{x}) = \sum_{a=1}^{n_{\text{node}}} N_a(\boldsymbol{x})\delta\phi_a\ . \tag{2.33}$$

Substituting these approximations into the weak form given in Eq. (2.22) yields a system of algebraic equations. Since the variations $\delta\phi_a$ are arbitrary, the residual component at each node a, denoted by R_a^{ϕ}, must vanish. The global residual vector is obtained by assembling the elemental contributions:

$$\boldsymbol{R}^{\text{AT2}} = \mathop{\mathbf{A}}_{e} \left(R_a^{\text{AT2}} \right) = \mathbf{0}, \tag{2.34}$$

where $\mathbf{A}$ is the assembly operator, and the elemental residual contribution is given by:

$$R_a^{\text{AT2}} = \int_{\Omega_e} \left(\frac{1}{l}\phi_h N_a + l\nabla\phi_h \cdot \nabla N_a \right) \mathrm{d}\boldsymbol{x}. \tag{2.35}$$

The corresponding component of the elemental tangent stiffness matrix K_{ab}^{AT2}, defined as the derivative of R_a^{AT2} with respect to ϕ_b, is:

$$K_{ab}^{\text{AT2}} = \int_{\Omega_e} \left(\frac{1}{l} N_a N_b + l\nabla N_a \cdot \nabla N_b \right) \mathrm{d}\boldsymbol{x}. \tag{2.36}$$

Similar to the residual vector, the global tangent stiffness matrix is obtained by assembling the elemental contributions:

$$\boldsymbol{K}^{\mathrm{AT2}} = \mathop{\mathbf{A}}_{e} \left(K_{ab}^{\mathrm{AT2}} \right). \tag{2.37}$$

Standard references (e.g. [46, 47]) can be consulted for the details of these manipulations. It is worth noting that for the AT2 model, the tangent matrix is constant (independent of ϕ), which leads to a linear system of equations.

Validation of the phase-field profile and energy

To validate the numerical implementation and analyze the performance of the FEM, the same one-dimensional bar problem of half-length $a = 1\,\mathrm{mm}$ used in the analytical solution is considered. Exploiting symmetry, only half of the domain is modeled, with a Dirichlet boundary condition $\phi = 1$ applied at the symmetry plane ($x = 0$).

First, the numerical model is validated by comparing the computed crack surface representation and energy against the analytical solutions. For this analysis, a very fine, uniform mesh with element size $h = a/5000$ is employed to minimize discretization errors. The length scale parameter is varied from $l = 0.01\,\mathrm{mm}$ to $l = 2a$.

Figure 2.5 illustrates the normalized total energy Γ as a function of the length scale parameter l for the AT2 model. The numerical results demonstrate excellent agreement with the analytical solution across the entire range of l.

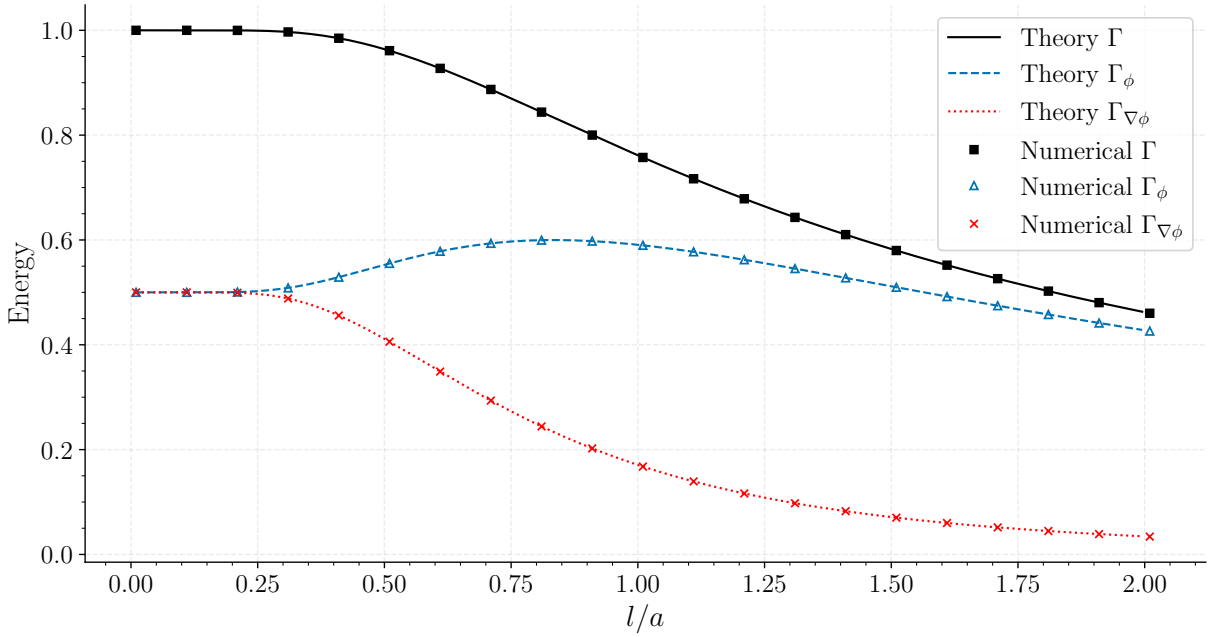

Figure 2.5: Validation of the normalized total energy Γ as a function of the length scale parameter l for the AT2 model. The numerical results demonstrate excellent agreement with the analytical solution.

Additionally, Figure 2.6 compares the numerical and theoretical phase-field variable $\phi(x)$ and its gradient $\nabla\phi(x)$ for different length scale parameters l. Results show good agreement between both solutions.

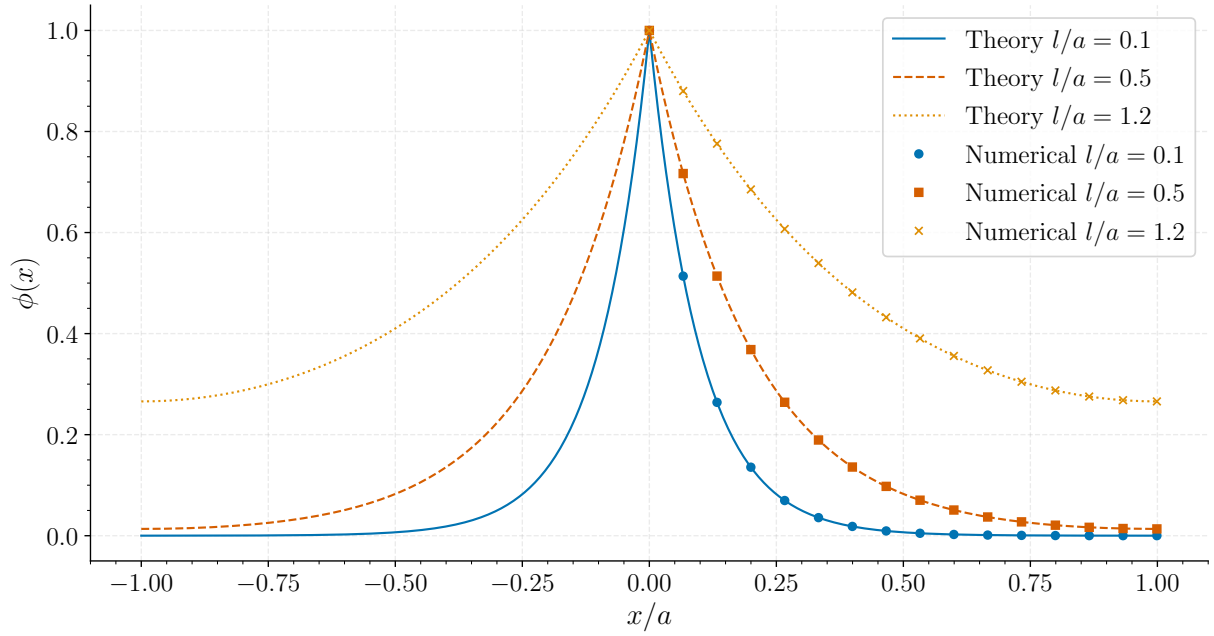

(a) Phase-field

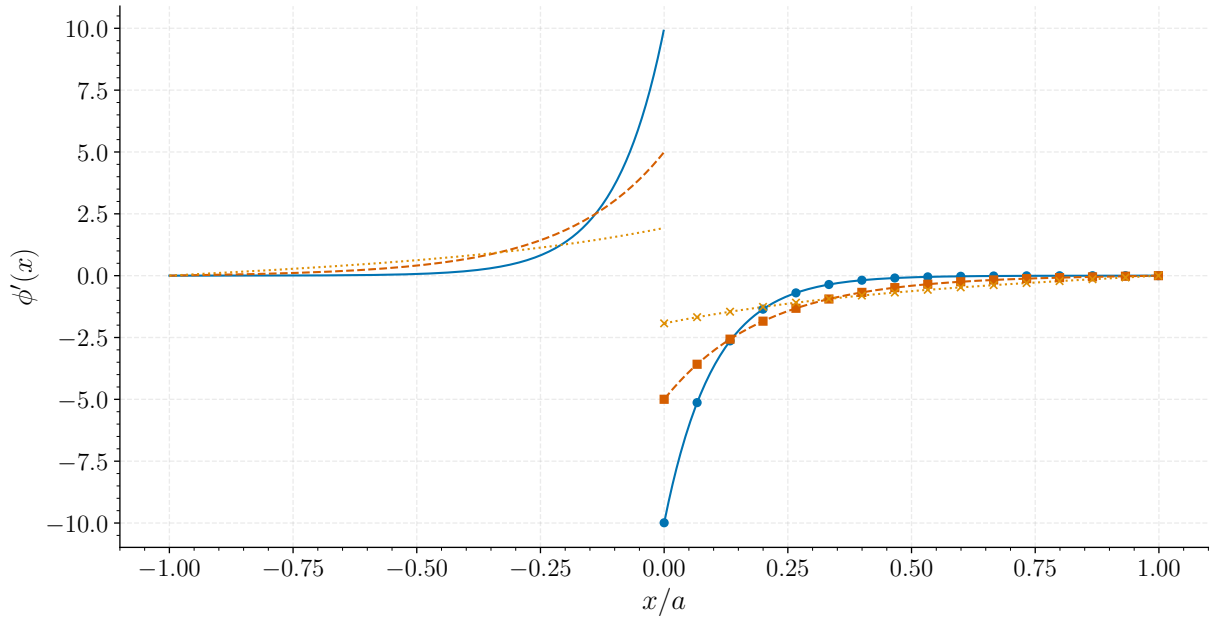

(b) Phase-field gradient

Figure 2.6: Comparison between numerical and analytical solutions for the AT2 model with $l/a = 0.1$: (a) Phase-field profile $\phi(x)$; and (b) Phase-field gradient $\nabla\phi(x)$.

Convergence analysis

Having validated the implementation with a fine mesh, a convergence analysis is performed to assess the accuracy of the numerical method with respect to the element size h using standard one-dimensional linear elements.

For this analysis, the length scale parameter is fixed at $l = 0.1\,\text{mm}$ ($l/a = 0.1$), resulting in a theoretical energy of $\Gamma \approx 1.0$. The number of elements is systematically increased from 1 to 100.

Figure 2.7 illustrates the convergence of the relative error of the total energy as a function of the l/h ratio.

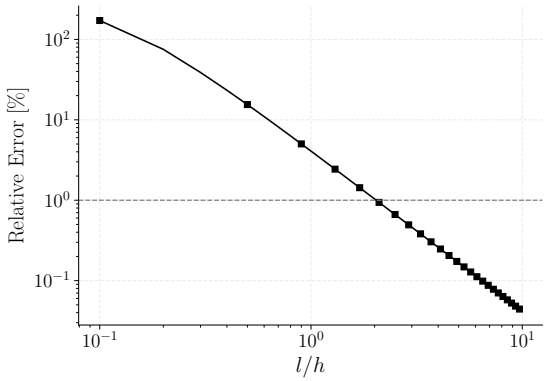

Figure 2.7: Convergence of the relative error in total energy for the one-dimensional problem using linear finite elements.

Notably, for linear elements, a ratio of $l/h > 2$ is sufficient to keep the relative error below 1%, which aligns with the recommendations in the literature [15].

2.3 Interval constraint and irreversibility

The PFF problem involves minimizing an energy functional subject to two fundamental physical constraints: the interval constraint on the damage variable and the irreversibility of crack growth.

The first constraint requires that the phase-field variable ϕ be constrained within the interval $[0, 1]$, representing the transition from a null-damage state ($\phi = 0$) to a fully damaged state ($\phi = 1$):

$$0 \leq \phi(\boldsymbol{x}, t) \leq 1 \quad \forall \boldsymbol{x} \in \Omega,\, \forall t. \tag{2.38}$$

This constraint is intrinsic to the definition of the CSDF, as discussed in Section 2.2, and must be strictly maintained throughout the evolution of the coupled fracture problem.

The second constraint enforces the thermodynamic consistency of the fracture process, ensuring that cracks do not heal; that is, damage is irreversible. Physically, the total crack surface area, approximated by the functional $\Gamma(\phi)$, must be non-decreasing over time. However, enforcing this condition only in a global sense is insufficient, as it could virtually allow for local healing provided that it is compensated by greater crack growth elsewhere in the domain.

To prevent such physical inconsistencies, the irreversibility condition is enforced locally. This implies that the crack surface density function $\gamma(\phi, \nabla\phi)$ must be non-decreasing at every material point:

$$\gamma(\phi(\boldsymbol{x}, t)) \geq \gamma(\phi(\boldsymbol{x}, s)) \quad \forall \boldsymbol{x} \in \Omega, \text{ for all } t \geq s. \tag{2.39}$$

This requirement naturally simplifies to the condition that the phase-field variable itself must be non-decreasing:

$$\phi(\boldsymbol{x}, t) \geq \phi(\boldsymbol{x}, s) \quad \forall \boldsymbol{x} \in \Omega, \text{ for all } t \geq s. \tag{2.40}$$

This condition guarantees that the damage state evolves monotonically, preventing any unphysical reduction in the phase-field value during the simulation.

2.4 Governing equations for the PFF problem

The governing equations are derived by enforcing the stationarity of the total potential energy functional Eq. (2.2) with respect to independent variations of the displacement field $\boldsymbol{u}$ and the phase-field ϕ. This variational procedure yields the following coupled weak forms:

$$\mathcal{E}'_{\boldsymbol{u}}(\boldsymbol{u}, \phi) := \int_\Omega \left[g(\phi)\boldsymbol{\sigma_a}(\boldsymbol{\epsilon}(\boldsymbol{u})) + \boldsymbol{\sigma_b}(\boldsymbol{\epsilon}(\boldsymbol{u})) \right] : \boldsymbol{\epsilon}(\delta\boldsymbol{u}) \, \mathrm{d}\boldsymbol{x} - \int_\Omega \boldsymbol{f} \cdot \delta\boldsymbol{u} \, \mathrm{d}\boldsymbol{x} - \int_{\partial\Omega_t} \boldsymbol{t} \cdot \delta\boldsymbol{u} \, dS = \boldsymbol{0}, \tag{2.41}$$

$$\mathcal{E}'_{\phi}(\boldsymbol{u}, \phi) := \int_\Omega g'(\phi)\psi_a(\boldsymbol{\epsilon})\delta\phi \, \mathrm{d}\boldsymbol{x} + \frac{G_c}{c_0} \int_\Omega \left(\frac{\alpha'(\phi)}{l}\delta\phi + 2l\nabla\phi \cdot \nabla\delta\phi \right) \mathrm{d}\boldsymbol{x} = 0. \tag{2.42}$$

where $\delta\boldsymbol{u}$ and $\delta\phi$ denote admissible variations, $g'(\phi)$ is the derivative of the degradation function with respect to ϕ detailed in Table 2.2, $\boldsymbol{\sigma_a} = \frac{\partial\psi_a}{\partial\boldsymbol{\epsilon}}$ and $\boldsymbol{\sigma_b} = \frac{\partial\psi_b}{\partial\boldsymbol{\epsilon}}$ are the active and inactive stress tensors corresponding to the energy split, as detailed in Table 2.4.

The corresponding strong form equations are given by:

$$\nabla \cdot [g(\phi)\boldsymbol{\sigma_a}(\boldsymbol{\epsilon}(\boldsymbol{u})) + \boldsymbol{\sigma_b}(\boldsymbol{\epsilon}(\boldsymbol{u}))] + \boldsymbol{f} = \boldsymbol{0} \quad \text{in } \Omega, \tag{2.43}$$

$$g'(\phi)\,\psi_a(\boldsymbol{\epsilon}(\boldsymbol{u})) + \frac{G_c}{c_0}\left(\frac{\alpha'(\phi)}{l} - 2l\Delta\phi \right) = 0 \quad \text{in } \Omega, \tag{2.44}$$

$$[g(\phi)\boldsymbol{\sigma_a}(\boldsymbol{\epsilon}(\boldsymbol{u})) + \boldsymbol{\sigma_b}(\boldsymbol{\epsilon}(\boldsymbol{u}))\cdot] \cdot \boldsymbol{n} = \boldsymbol{t} \quad \text{on } \partial\Omega_{\boldsymbol{t}}, \tag{2.45}$$

$$\nabla\phi \cdot \boldsymbol{n} = \boldsymbol{0} \quad \text{on } \partial\Omega. \tag{2.46}$$

Solving the problem defined by these governing equations requires addressing several critical aspects. First, the physical constraints—specifically the boundedness of the phase-field variable and the irreversibility of crack growth—must be enforced. Common strategies include penalty methods [6], which convert the inequality problem into an equality problem via a penalization term, and history variable approaches [3], which ensure irreversibility by driving the phase-field evolution with a non-decreasing energy quantity.

Second, once the approximated model is defined, the PDEs are solved numerically within a finite element framework. Due to the non-convexity of the total energy functional, the resulting complex coupled system requires robust numerical strategies. In the literature,

solution methods are generally categorized into staggered (operator-split) and monolithic approaches.

Figure 2.8 presents an overview of a typical framework. First, the variational problem with inequalities is approximated by an unconstrained problem (e.g., via a penalty or history-field method). Next, the resulting nonlinear PDE system is discretized using the FEM. Finally, the discrete system is solved using either a staggered (operator-split) or a monolithic scheme, typically linearized with the Newton–Raphson method. Each step addresses a specific challenge: the constraint method enforces boundedness and irreversibility, the FEM handles spatial discretization, and the iterative solver deals with the non-convexity of the energy functional in the discrete setting.

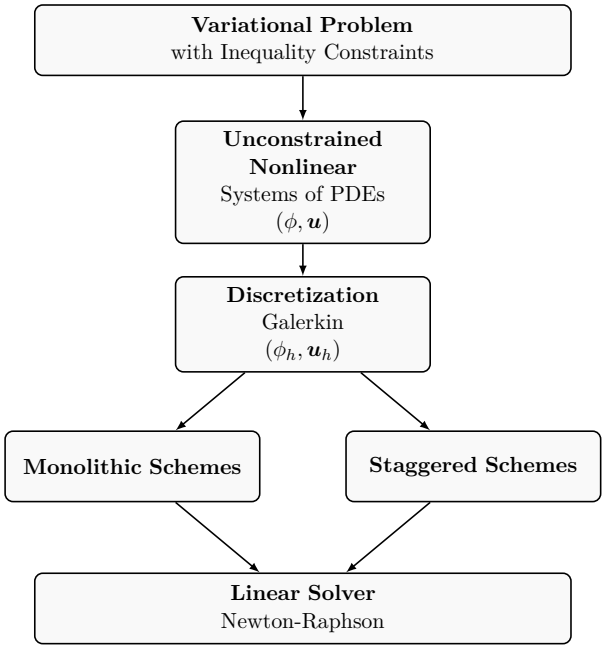

Figure 2.8: Flowchart illustrating the numerical strategy. The problem is first regularized to handle constraints, then discretized, and finally solved using iterative schemes.

2.5 Approximated continuous models

To ensure the thermodynamic consistency of the fracture process, the irreversibility condition—preventing crack healing—must be strictly enforced. This requirement necessitates specific modifications to the governing equations or the solution algorithm. Common strategies include the penalty methods proposed in [6] and the history field method proposed in [3]. Additionally, the phase-field variable ϕ must remain within the physical bounds $[0, 1]$.

This section introduces the modifications to the standard model required to handle these constraints. These modifications effectively transform the original constrained optimization problem into an approximated model suitable for numerical implementation. Two of the most common approaches, penalty formulations and the history field method, are discussed below.

2.5.1 Penalty formulations

The penalty method is a widely used strategy that transforms a constrained optimization problem into an unconstrained one by augmenting the potential energy functional. This is achieved by adding a penalty term that penalizes violations of the constraints, scaled by a sufficiently large penalty parameter ρ.

For the full PFF problem, the irreversibility condition requires that damage does not decrease over time, i.e., $\phi \geq \phi_{\text{prev}}$. Note that enforcing this condition implicitly satisfies the non-negativity constraint ($\phi \geq 0$), provided that the initial state is non-negative ($\phi_{\text{prev}} \geq 0$). By taking ϕ_{prev} from the previous time step as the reference, the total energy functional is defined by adding the penalization term to the original functional in Eq. (2.2), resulting in the augmented functional:

$$\mathcal{E}_{\text{penalty}}(\boldsymbol{u}, \phi) := \mathcal{E}(\boldsymbol{u}, \phi) + \frac{\rho}{2} \int_{\Omega} \langle \phi - \phi_{\text{prev}} \rangle_{-}^{2} \, \mathrm{d}\boldsymbol{x}. \tag{2.47}$$

Minimizing this functional with respect to the independent fields $\boldsymbol{u}$ and ϕ yields the coupled system of weak equations:

$$\mathcal{E}_{\text{penalty}}{}'_{\boldsymbol{u}}(\boldsymbol{u}, \phi) := \mathcal{E}'_{\boldsymbol{u}}(\boldsymbol{u}, \phi) = \boldsymbol{0}, \tag{2.48}$$

$$\mathcal{E}_{\text{penalty}}{}'_{\phi}(\boldsymbol{u}, \phi) := \mathcal{E}'_{\phi}(\boldsymbol{u}, \phi) + \rho \int_{\Omega} \langle \phi - \phi_{\text{prev}} \rangle_{-} \, \delta\phi \, \mathrm{d}\boldsymbol{x} = 0. \tag{2.49}$$

It should be noted that the penalty term depends exclusively on ϕ; therefore, the equilibrium equation for the displacement field Eq. (2.41) remains unaffected by this modification. Consequently, the equilibrium equation for the penalty formulation is obtained by adding the variation of the penalty term to the phase-field equation Eq. (2.42).

2.5.2 History field method

Another alternative is the history field method proposed by [3]. This approach introduces a local history variable $\mathcal{H}$ that captures the maximum tensile strain energy density experienced by the material at a point $\boldsymbol{x}$ over the entire loading history t. This variable is defined pointwise as:

$$\mathcal{H}(\boldsymbol{x}, t) = \max_{s \in [0,t]} \psi_a(\boldsymbol{\epsilon}(\boldsymbol{x}, s)). \tag{2.50}$$

In a numerical setting with time steps t_n, this is updated as:

$$\mathcal{H}(\boldsymbol{x}, t_n) = \begin{cases} \psi_a(\boldsymbol{\epsilon}(\boldsymbol{u})), & \text{if } \psi_a(\boldsymbol{\epsilon}(\boldsymbol{u})) > \mathcal{H}_{n-1}, \\ \mathcal{H}_{n-1}, & \text{otherwise}, \end{cases} \tag{2.51}$$

where $\mathcal{H}_n$ is the history field from the previous converged step.

In this formulation, the phase-field evolution is driven by the history field $\mathcal{H}$ rather than the instantaneous active energy ψ_a. Since $\mathcal{H}$ is non-decreasing by definition, the driving force for damage cannot decrease, thereby ensuring that ϕ does not decrease (crack healing is prevented).

The governing weak forms for the coupled problem are therefore modified. The momentum equation remains dependent on the current stress state with the chosen energy split, while

the phase-field weak form employs $\mathcal{H}$. The system of equations for an AT2 regularization is given by:

$$\mathcal{E}_{\text{Miehe}}{}'_{\boldsymbol{u}}(\boldsymbol{u},\phi) := \mathcal{E}'_{\boldsymbol{u}}(\boldsymbol{u},\phi) = \boldsymbol{0}, \tag{2.52}$$

$$\mathcal{E}_{\text{Miehe}}{}'_{\phi}(\boldsymbol{u},\phi) := \int_\Omega g'(\phi)\delta\phi\,\mathcal{H}\,\mathrm{d}\boldsymbol{x} + G_c\int_\Omega\left(\frac{1}{l}\phi\delta\phi + l\nabla\phi\cdot\nabla\delta\phi\right)\mathrm{d}\boldsymbol{x} \qquad = 0. \tag{2.53}$$

It should be noted that this approach loses the variational structure of the original problem, as the history field $\mathcal{H}$ is not derived from an energy functional but is introduced directly into the weak form for the phase-field variation.

This formulation handles the irreversibility condition, but not the interval constraint in $[0,1]$. However, it was originally presented for the AT2 regularization, where the phase-field variable satisfies the lower bound of 0 by definition. Therefore, it can be applied directly to this type of regularization. Another option is to use the history field for irreversibility and a penalization term only to impose the interval constraint. In that case, the penalization term is added to the previous penalization formulation, but with $\phi_{\text{prev}} = 0$ fixed, since irreversibility is already handled by the history field. The penalization term is then active only when ϕ becomes negative, which is unphysical. This approach will be discussed in more detail in the numerical implementation section, as it is a common strategy to handle both constraints simultaneously.

Hybrid formulation

A related approach is the hybrid formulation introduced in [48]. In this framework, starting from the original formulation in [3], the momentum equation is modified to incorporate the degradation function $g(\phi)$ applied to the total stress tensor $\boldsymbol{\sigma}(\boldsymbol{\epsilon})$ (the stress from the isotropic model). This adjustment ensures that the material stiffness is uniformly degraded in the presence of damage, regardless of the energy decomposition. The weak forms for the hybrid formulation are thus given by:

$$\mathcal{E}_{\text{Hybrid}}{}'_{\boldsymbol{u}}(\boldsymbol{u},\phi) := \int_\Omega g(\phi)\boldsymbol{\sigma}(\boldsymbol{\epsilon}(\boldsymbol{u})) : \boldsymbol{\epsilon}(\delta\boldsymbol{u})\,\mathrm{d}\boldsymbol{x} - \int_\Omega \boldsymbol{f}\cdot\delta\boldsymbol{u}\,\mathrm{d}\boldsymbol{x} - \int_{\partial\Omega_t}\boldsymbol{t}\cdot\delta\boldsymbol{u}\,\mathrm{d}S = \boldsymbol{0}, \tag{2.54}$$

$$\mathcal{E}_{\text{Hybrid}}{}'_{\phi}(\boldsymbol{u},\phi) := \mathcal{E}'_{\mathcal{H}\phi}(\boldsymbol{u},\phi) = 0. \tag{2.55}$$

The motivation for this approach is purely numerical: for example, when using a Newton–Raphson solver it is not necessary to compute tangent contributions associated with the energy-decomposition-based stress split. Only the tangent corresponding to the isotropic stress needs to be assembled, which can be computed once, thereby reducing computational cost.

2.6 Numerical models

This section outlines the numerical framework employed to solve the PFF problem. The solution methodology consists of two primary stages: the spatial discretization of the governing weak forms via the FEM, followed by the application of an iterative scheme to solve the resulting non-linear coupled system.

2.6.1 Finite element discretization

The governing equations are discretized using the FEM. Both the displacement field $\boldsymbol{u}$ and the phase-field ϕ are approximated within a standard Galerkin framework using the

same set of nodal shape functions N_a. The function space for the unknowns is defined as:

$$V = \left\{ \nu : \Omega \to \mathbb{R},\ \nu(\boldsymbol{x}) = \sum_{a=1}^{n_{\text{node}}} N_a(\boldsymbol{x})\, \nu_a \right\} \tag{2.56}$$

The continuous fields and their variations are then expressed as:

$$\boldsymbol{u}_h(\boldsymbol{x}) = \sum_{a=1}^{n_{\text{node}}} N_a(\boldsymbol{x})\boldsymbol{u}_a, \quad \delta\boldsymbol{u}_h(\boldsymbol{x}) = \sum_{a=1}^{n_{\text{node}}} N_a(\boldsymbol{x})\delta\boldsymbol{u}_a, \tag{2.57}$$

$$\phi_h(\boldsymbol{x}) = \sum_{a=1}^{n_{\text{node}}} N_a(\boldsymbol{x})\phi_a, \quad \delta\phi_h(\boldsymbol{x}) = \sum_{a=1}^{n_{\text{node}}} N_a(\boldsymbol{x})\delta\phi_a, \tag{2.58}$$

where $\boldsymbol{u}_a$ and ϕ_a denote the nodal displacement vector and nodal phase-field value, respectively, and n_{node} is the total number of nodes in the discretization.

Substituting these approximations into the weak form equations yields a system of non-linear algebraic equations. The requirement that the weak forms vanish for arbitrary variations $\delta\boldsymbol{u}_a$ and $\delta\phi_a$ leads to the definition of the global residual vectors at each node a:

$$\boldsymbol{R}_a^{\boldsymbol{u}} = \underset{e}{\mathbf{A}} \left(\boldsymbol{R}_a^{\boldsymbol{u},e}\right) = \mathbf{0} \quad \text{and} \quad R_a^{\phi} = \underset{e}{\mathbf{A}} \left(R_a^{\phi,e}\right) = 0 \tag{2.59}$$

where $\mathbf{A}$ represents the global assembly operator, and $\boldsymbol{R}_a^{\boldsymbol{u},e}$ and $R_a^{\phi,e}$ are the elemental contributions to the displacement and phase-field residuals, respectively.

The detailed definitions of the residuals and tangent stiffness matrices for the different formulations considered in this chapter are provided in the corresponding subsections below. Resolving this coupled non-linear system requires robust numerical strategies. Two main categories of solution schemes are commonly employed in the literature: monolithic schemes and staggered (or operator-split) schemes.

2.6.2 Monolithic schemes

In monolithic schemes, the displacement field $\boldsymbol{u}$ and the phase-field variable ϕ are solved simultaneously as a single coupled system. While this approach can be computationally efficient, it is generally less robust, as discussed in [48]. The non-convexity of the total energy functional renders the discrete system difficult to solve, and the standard Newton-Raphson method often fails to converge. Consequently, globalization strategies, such as line-search algorithms, are typically required to aid convergence.

Reference case

As a baseline for comparison, the monolithic solution of the standard phase-field model without explicitly enforcing the irreversibility constraint is first considered. In this case, assuming the AT2 regularization, the boundedness of the phase-field variable ($\phi \in [0, 1]$) is naturally satisfied by the model structure. This simplified formulation is applicable mainly to problems with monotonic loading paths where the crack driving force does not decrease, effectively satisfying irreversibility implicitly.

The elemental residual contributions are given by:

$$\mathbf{R}_a^{\boldsymbol{u}} = \int_{\Omega_e} \left[g(\phi_h)\, \boldsymbol{\sigma}_a(\boldsymbol{\epsilon}(\boldsymbol{u}_h)) + \boldsymbol{\sigma}_b(\boldsymbol{\epsilon}(\boldsymbol{u}_h)) \right] : \boldsymbol{\epsilon}(N_a)\, \mathrm{d}\boldsymbol{x} - \int_{\Omega_e} \boldsymbol{f} N_a\, \mathrm{d}\boldsymbol{x} - \int_{\partial\Omega_{t,e}} \boldsymbol{t} N_a\, \mathrm{d}S, \quad (2.60)$$

$$R_a^{\phi} = \int_{\Omega_e} g'(\phi_h)\psi_a(\boldsymbol{\epsilon}(\boldsymbol{u}_h)) N_a\, \mathrm{d}\boldsymbol{x} + \frac{G_c}{c_0} \int_{\Omega_e} \left(\frac{\alpha'(\phi_h)}{l} N_a + 2l \nabla\phi_h \cdot \nabla N_a \right) \mathrm{d}\boldsymbol{x}. \quad (2.61)$$

Note that for the standard AT2 model, $\alpha'(\phi) = 2\phi$ and $c_0 = 2$, recovering the familiar terms.

The global residual vector for the monolithic coupled system is obtained by assembling these elemental contributions:

$$\boldsymbol{R} = \mathop{\mathbf{A}}_{e} \begin{bmatrix} \mathbf{R}_a^{\boldsymbol{u}} \\ R_a^{\phi} \end{bmatrix}. \quad (2.62)$$

The corresponding components of the elemental tangent stiffness matrices are given by:

$$\mathbf{K}_{ab}^{\boldsymbol{uu}} = \int_{\Omega_e} \boldsymbol{\epsilon}(N_a) : \left[g(\phi_h)\mathbb{C}_a(\boldsymbol{\epsilon}(\boldsymbol{u}_h)) + \mathbb{C}_b(\boldsymbol{\epsilon}(\boldsymbol{u}_h)) \right] : \boldsymbol{\epsilon}(N_b)\, \mathrm{d}\boldsymbol{x}, \quad (2.63)$$

$$\mathbf{K}_{ab}^{\boldsymbol{u}\phi} = \int_{\Omega_e} \left[g'(\phi_h)\boldsymbol{\sigma}_a(\boldsymbol{\epsilon}(\boldsymbol{u}_h)) : \boldsymbol{\epsilon}(N_a) \right] N_b\, \mathrm{d}\boldsymbol{x}, \quad (2.64)$$

$$\mathbf{K}_{ab}^{\phi\boldsymbol{u}} = \int_{\Omega_e} \left[g'(\phi_h)\boldsymbol{\sigma}_a(\boldsymbol{\epsilon}(\boldsymbol{u}_h)) : \boldsymbol{\epsilon}(N_b) \right] N_a\, \mathrm{d}\boldsymbol{x}, \quad (2.65)$$

$$K_{ab}^{\phi\phi} = \int_{\Omega_e} g''(\phi_h)\psi_a(\boldsymbol{\epsilon}(\boldsymbol{u}_h)) N_a N_b\, \mathrm{d}\boldsymbol{x} + \frac{G_c}{c_0} \int_{\Omega_e} \left(\frac{\alpha''(\phi_h)}{l} N_a N_b + 2l \nabla N_a \cdot \nabla N_b \right) \mathrm{d}\boldsymbol{x}. \quad (2.66)$$

Similar to the residual vector, the global tangent stiffness matrix is obtained by assembling the elemental contributions:

$$\boldsymbol{K} = \mathop{\mathbf{A}}_{e} \begin{bmatrix} \mathbf{K}_{ab}^{\boldsymbol{uu}} & \mathbf{K}_{ab}^{\boldsymbol{u}\phi} \\ \mathbf{K}_{ab}^{\phi\boldsymbol{u}} & K_{ab}^{\phi\phi} \end{bmatrix}. \quad (2.67)$$

For the standard formulation, the coupled nonlinear system is solved using the Newton-Raphson method.

Penalization scheme

To address non-monotonic loading and enforce physical constraints strictly, the monolithic scheme can be augmented with penalty terms. In this approach, the weak forms corresponding to the penalized functional (introduced in Section 2.5.1) are solved simultaneously. The penalty terms incorporate the irreversibility condition ($\phi \geq \phi_{\text{prev}}$) and, if necessary, the boundedness constraints directly into the monolithic system.

The residuals and tangent stiffness matrices for the penalized monolithic scheme can be obtained by adding the corresponding penalty contributions to the standard phase-field equations. Specifically, the elemental phase-field residual R_a^{ϕ} is augmented by adding the following contribution:

$$R_a^{\phi,\text{pen}} = \rho \int_{\Omega_e} \langle \phi_h - \phi_{\text{prev}} \rangle_- N_a\, \mathrm{d}\boldsymbol{x}, \quad (2.68)$$

where $\rho > 0$ is a sufficiently large penalty parameter, and the phase-field tangent stiffness component $K_{ab}^{\phi\phi}$ is augmented by adding the corresponding derivative term:

$$K_{ab}^{\phi\phi,\text{pen}} = \rho \int_{\Omega_e} H(\phi_{\text{prev}} - \phi_h)\, N_a N_b\, \mathrm{d}\boldsymbol{x}, \quad (2.69)$$

where $H(\cdot)$ is the Heaviside step function.

2.6.3 Staggered schemes

Staggered schemes, also referred to as operator-splitting methods, decouple the solution procedure by solving for the displacement and phase-field variables sequentially rather than simultaneously. In a typical algorithmic step, the mechanical equilibrium equation is solved for the displacement field while holding the phase-field variable fixed. Subsequently, the phase-field evolution equation is solved using the updated displacement field. This alternating process is repeated until the coupled system satisfies the staggered convergence criteria.

A key advantage of staggered schemes is their robustness; by decoupling the fields, the resulting sub-problems are typically convex with respect to the variable being solved (assuming the other is fixed). This property simplifies the solution of the systems at each staggered step. Because the fields are solved sequentially rather than simultaneously, the off-diagonal coupling tangent blocks ($\mathbf{K}^{\boldsymbol{u}\phi}$ and $\mathbf{K}^{\phi\boldsymbol{u}}$) are neither computed nor assembled.

Penalization scheme

In the penalized staggered scheme, the displacement field is updated based on the phase-field from the previous iteration, and the phase-field is then updated using the new displacements. Within each uncoupled solver step, the residuals and independent tangent components match those presented in Section 2.6.2. The alternating sequence continues until the staggered convergence criteria are satisfied, as discussed in Section 2.6.3. The procedure is outlined in Algorithm 1 and shown in Figure 2.9.

Algorithm 1 Staggered Scheme with penalty method

Initialize: $t \leftarrow 0$, $step \leftarrow 0$, initial fields $\boldsymbol{u}_0, \phi_0$. Set $\phi_{\text{prev}} \leftarrow \phi_0$.
while $t < t_{\text{final}}$ **do**
  $t \leftarrow t + \Delta t$, $step \leftarrow step + 1$
  Update boundary conditions for the current time step.
  Initialize staggered iteration: $k \leftarrow 0$.
  Set $\boldsymbol{u}^{(0)} \leftarrow \boldsymbol{u}_{n-1}$, $\phi^{(0)} \leftarrow \phi_{n-1}$.
  while $(k < k_{\min}) \vee$ staggered convergence not satisfied **do**
    $k \leftarrow k + 1$
    Solve for displacement: Given $\phi^{(k-1)}$, find $\boldsymbol{u}^{(k)}$ such that $\boldsymbol{R}^{\boldsymbol{u}}(\boldsymbol{u}^{(k)}, \phi^{(k-1)}) = \mathbf{0}$.
    Solve for phase-field: Given $\boldsymbol{u}^{(k)}$, find $\phi^{(k)}$ such that $\boldsymbol{R}^{\phi}_{\text{penalty}}(\boldsymbol{u}^{(k)}, \phi^{(k)}) = \mathbf{0}$.
    Check staggered convergence (see Section 2.6.3)
  end while
  Update solutions: $\boldsymbol{u}_n \leftarrow \boldsymbol{u}^{(k)}$, $\phi_n \leftarrow \phi^{(k)}$.
  Update history field for next step: $\phi_{\text{prev}} \leftarrow \phi_n$.
end while

Figure 2.9 illustrates the general flowchart of the staggered scheme.

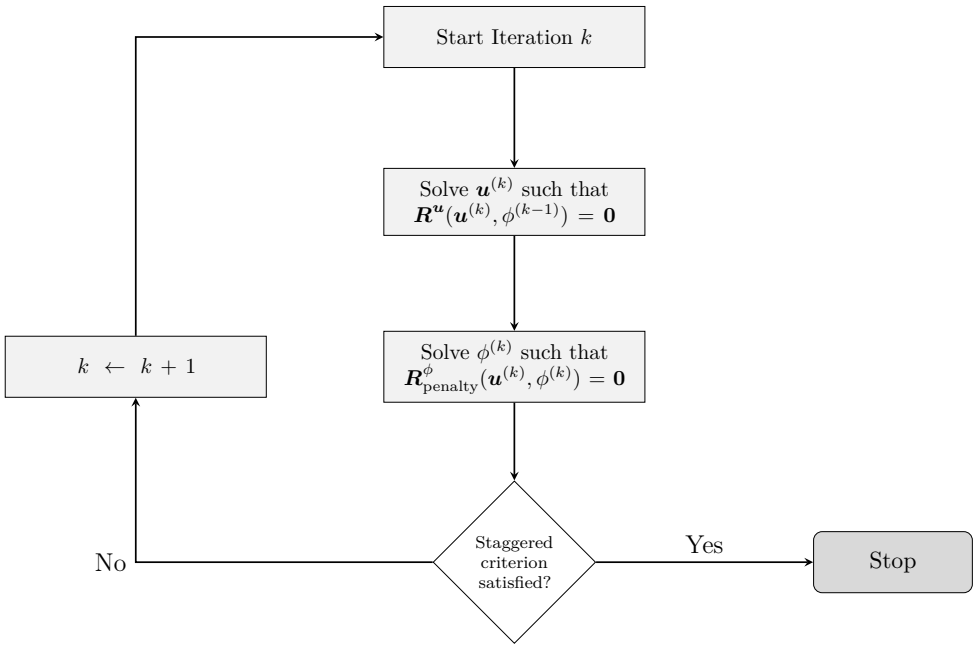

Figure 2.9: General flowchart of the staggered solution scheme.

History field method

The history field method, as formulated in [3], is naturally suited for staggered schemes. In this approach, irreversibility is enforced by driving the phase-field evolution with a history variable $\mathcal{H}$, which records the maximum tensile strain energy density over time.

Crucially, implementing this method requires careful handling of the history variable update. Within the staggered loop, the history variable $\mathcal{H}$ must be computed based on the active energy of the current iteration, updated against the maximum value stored from the previous time step.

The numerical residual associated with the displacement field coincides with Eq. (2.60). For the phase-field residual, the history field must be considered instead of the active energy density. Therefore, the residual is written as:

$$R^{\phi}_{a} = \int_{\Omega_e} g'(\phi_h)\mathcal{H}N_a \,\mathrm{d}\boldsymbol{x} + \frac{G_c}{c_0}\int_{\Omega_e}\left(\frac{\alpha'(\phi_h)}{l}N_a + 2l\nabla\phi_h\cdot\nabla N_a\right)\mathrm{d}\boldsymbol{x}. \tag{2.70}$$

Since this formulation is solved using a staggered scheme, the tangent block for the displacement field coincides with Eq. (2.63), while the phase-field tangent block is given by:

$$K^{\phi\phi}_{ab} = \int_{\Omega_e} g''(\phi_h)\mathcal{H}N_aN_b \,\mathrm{d}\boldsymbol{x} + \frac{G_c}{c_0}\int_{\Omega_e}\left(\frac{\alpha''(\phi_h)}{l}N_aN_b + 2l\nabla N_a\cdot\nabla N_b\right)\mathrm{d}\boldsymbol{x}. \tag{2.71}$$

The algorithm proceeds as follows:

1. Given the phase-field from the previous iteration, solve the mechanical equilibrium equation using $\mathbf{R}^{\boldsymbol{u}}$ and $\mathbf{K}^{\boldsymbol{uu}}$.
2. Compute the current active energy density, $V_c = \psi_a(\boldsymbol{\epsilon}(\boldsymbol{u}^{(k)}))$.

3. Update the local history field for the current iteration as $\mathcal{H} = \max(V_c, V_n)$, where V_n is the history variable from the previous converged time step.
4. Solve the phase-field evolution equation using the modified R^ϕ and $K^{\phi\phi}$, where the active energy term $\psi_a(\boldsymbol{\epsilon}(\boldsymbol{u}^{(k)}))$ is replaced by the updated history variable $\mathcal{H}$.

This procedure is summarized in Algorithm 2.

Algorithm 2 Staggered Scheme with History Field

Initialize: $t \leftarrow 0$, *step* $\leftarrow 0$, initial fields $\boldsymbol{u}_0, \phi_0$. Set $V_n \leftarrow \psi_a(\boldsymbol{\epsilon}(\boldsymbol{u}_0))$.
while $t < t_{\text{final}}$ **do**
  $t \leftarrow t + \Delta t$, *step* $\leftarrow$ *step* $+ 1$
  Update boundary conditions and loading for current t
  Initialize staggered iteration: $k \leftarrow 0$
  Set $\boldsymbol{u}^{(0)} \leftarrow \boldsymbol{u}_{n-1}$, $\phi^{(0)} \leftarrow \phi_{n-1}$
  while $(k < k_{\min} \vee \text{not converged}) \wedge (k < k_{\max})$ **do**
    $k \leftarrow k + 1$
    Displacement step: Given $\phi^{(k-1)}$, solve for $\boldsymbol{u}^{(k)}$
    Compute active energy: $V_c = \psi_a(\boldsymbol{\epsilon}(\boldsymbol{u}^{(k)}))$
    Update current history field: $\mathcal{H} = \max(V_c, V_n)$
    Phase-field step: Given $\boldsymbol{u}^{(k)}$ and $\mathcal{H}$, solve for $\phi^{(k)}$
    Check staggered convergence (see Section 2.6.3)
  end while
  Update: $\boldsymbol{u}_n \leftarrow \boldsymbol{u}^{(k)}$, $\phi_n \leftarrow \phi^{(k)}$
  Update stored history variable for next step: $V_n = \mathcal{H}$
end while

Staggered tolerance criteria

Establishing a robust convergence criterion is a critical aspect of any staggered scheme. Since the mechanical and phase-field sub-problems are solved sequentially, satisfying the equilibrium conditions for each field individually does not guarantee that the coupled system has reached a state of global equilibrium. Consequently, iterations are necessary to ensure that the solution properly captures the interaction between the displacement and phase-field variables.

Several approaches are commonly employed in the literature to determine when to terminate this iterative process. One method involves monitoring the evolution of the total energy of the system (elastic strain energy plus fracture energy), assuming convergence when the energy change between iterations becomes negligible. A more direct approach checks the variation of the solution fields themselves, typically by examining the norms of the solution increments between consecutive staggered iterations. However, the most rigorous criterion involves quantifying the global residuals of the governing equations to ensure they fall below a specified tolerance, thereby guaranteeing that the coupled equations are satisfied simultaneously.

The following sections summarize three of the most common strategies found in the literature: using a fixed number of iterations, monitoring solution increment norms, and applying residual-based convergence criteria.

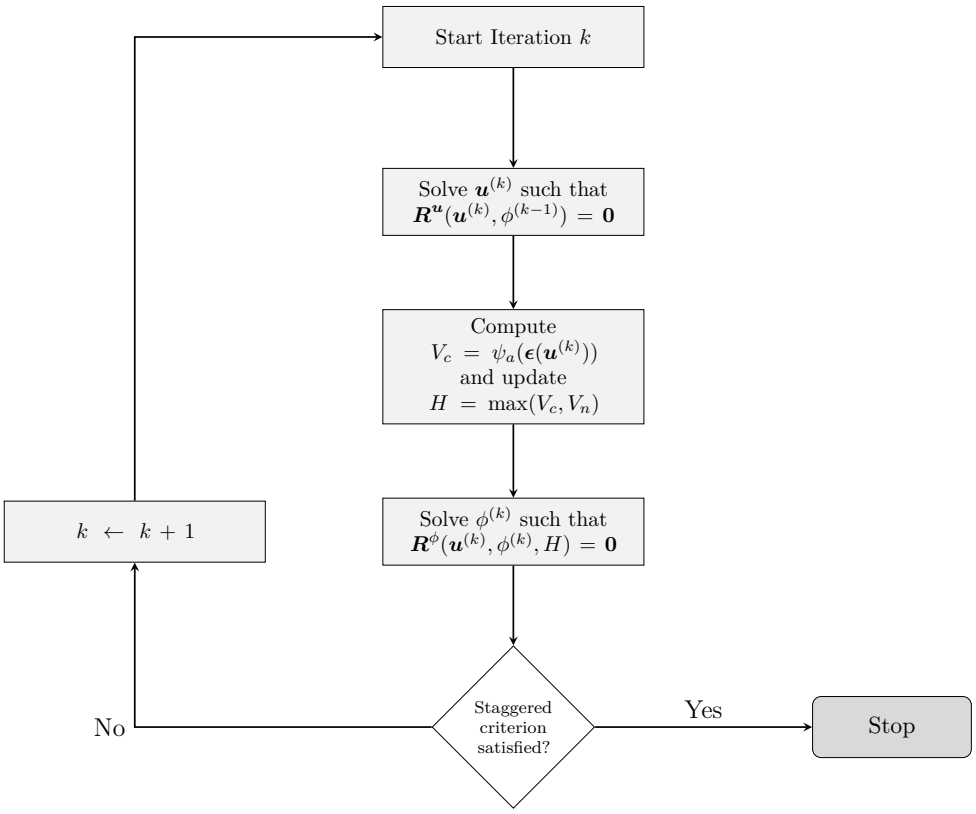

Figure 2.10: Flowchart of the staggered scheme with history field.

Fixed number of iterations In some implementations, such as the one described in [3], no explicit convergence criterion is defined for the staggered loop. Instead, a fixed number of staggered iterations is performed per time step. To mitigate the resulting splitting error, extremely small time steps are typically required. While this approach ensures that the individual sub-problems (displacement and phase-field) are solved to equilibrium, it does not guarantee that the coupled system reaches global equilibrium simultaneously within the step. Although computationally efficient per step, this method may lead to drift from the true equilibrium path and inaccuracies.

Solution increment norms A widely used convergence criterion assesses the relative change in the solution fields between consecutive staggered iterations. Convergence is assumed when the normalized L^2 norms of the solution increments fall below a user-defined tolerance:

$$\text{error}_{\boldsymbol{u}} = \frac{\| \boldsymbol{u}^{(k)} - \boldsymbol{u}^{(k-1)} \|_{L^2}}{\| \boldsymbol{u}^{(k)} \|_{L^2}} < \text{tol}, \tag{2.72}$$

$$\text{error}_{\phi} = \frac{\| \phi^{(k)} - \phi^{(k-1)} \|_{L^2}}{\| \phi^{(k)} \|_{L^2}} < \text{tol}. \tag{2.73}$$

While this method indicates that the solution has stabilized, it does not strictly enforce the satisfaction of the governing equations' residuals. Furthermore, although the criteria shown above evaluate the increments of both fields, alternative implementations may monitor only one of them, most commonly the phase-field increment. Additionally, while the L^2 norm is standard, other metrics are also employed; for instance, [49] considers

the unnormalized L^∞ norm for the phase-field increment, whereas [2] applies it to the displacement increment.

Residual-based staggered convergence criterion A more rigorous convergence criterion for the staggered scheme involves directly monitoring the global residuals of the governing equations. The fundamental objective of this scheme is to obtain a specific pair of solution fields, $(\boldsymbol{u}, \phi)$, that simultaneously satisfy both equilibrium conditions at the end of the time step.

Conveniently, when the uncoupled sub-problems are solved using the Newton–Raphson method, this evaluation occurs naturally. The initial residual (evaluated at iteration 0, prior to any nodal updates) explicitly measures whether the fields entering the sub-problem already satisfy the corresponding governing equation. If this initial residual falls below the prescribed tolerance, the current variables are deemed adequate, and no further Newton iterations or staggered steps are required.

Based on this property, the termination of the staggered loop follows an efficient "early exit" logic, as illustrated in Figure 2.11. Because the equations are solved sequentially, the initial residual of the phase-field equation can be evaluated immediately after solving for the displacement field. If this initial residual satisfies the tolerance, the staggered loop terminates, as the displacement field has just been solved to equilibrium and the phase-field inherently satisfies its respective condition.

Symmetric logic applies if the solving sequence is reversed: if the initial residual of the displacement field falls below the prescribed tolerance immediately after solving the phase-field equation, the staggered loop terminates. This robust approach guarantees that the final solution fields strictly satisfy the coupled problem.

Ultimately, this criterion provides a direct global measure of equilibrium. It should be noted that at least one complete staggered iteration must be performed to initialize the cycle. Ideally, the staggered tolerance should match the tolerance imposed on the individual Newton–Raphson schemes, ensuring that the residual equations satisfy the required accuracy bounds both individually and globally. Finally, it is crucial that the variables accepted as the final time-step solution are precisely those satisfying the initial residual condition, ensuring strict enforcement of the coupled governing partial differential equations (PDEs).

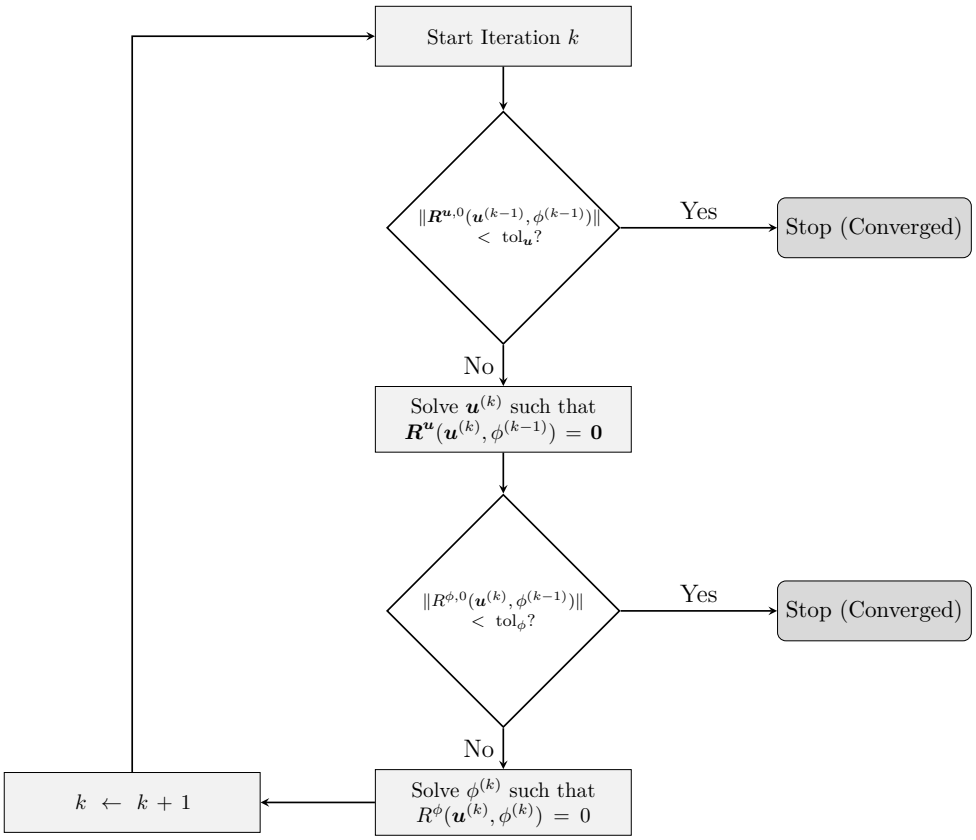

Figure 2.11: Flowchart of the staggered scheme with "early exit" residual-based convergence checks. The condition $\boldsymbol{R}^{\boldsymbol{u},0}$ and $R^{\phi,0}$ refers to the residual of the first Newton-Raphson iteration.

2.7 Examples

After presenting the different solution schemes and formulations, this section provides well-known PFF examples to illustrate their application.

2.7.1 One-element local damage model

To validate the numerical implementation, a simplified benchmark is considered in which a specimen is subjected to uniaxial loading. As shown in Figure 2.12, all degrees of freedom are constrained except for the vertical displacement at the top boundary, where the load is applied. In this setup, it is assumed that the gradient term in the phase-field equation vanishes, reducing the problem to a local damage model. This assumption is consistent with the solution of a finite element problem using a single element, where the discretization naturally renders the gradient of the phase-field variable zero, effectively making the problem local.

In this case, a linear finite element is considered to reproduce the exact solution since the stress state is uniform under this setup. This simplification permits the derivation of an analytical solution for the phase-field variable, displacements, strains, and stresses, thus providing a clear benchmark for validating the numerical implementation.

The test can be posed in 1D, 2D (quadrilateral element), or 3D (hexahedral element). Figure 2.12 illustrates the 1D and 2D discretizations. While previous studies focused on isotropic formulations [30], the present analysis also examines anisotropic energy splits (Section 2.1.2) and compares different numerical solution strategies: the monolithic penalty formulation (Section 2.6.2), the staggered penalty formulation (Section 2.6.3), and the staggered history-field formulation (Section 2.6.3).

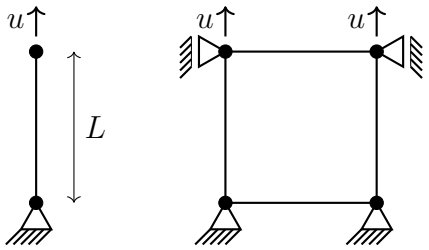

(a) 1D element. (b) 2D quadrilateral element.

Figure 2.12: Schematic representation of the single-element models used for validation: (a) 1D bar element; and (b) 2D quadrilateral element.

Under the single-element assumption, the governing equations simplify. With $g(\phi) = (1-\phi)^2$ and using the AT2 crack-surface regularization (Section 2.2), the balance equations reduce to

$$\nabla \cdot \Big[(1-\phi)^2 \boldsymbol{\sigma_a}(\boldsymbol{\epsilon}(\boldsymbol{u})) + \boldsymbol{\sigma_b}(\boldsymbol{\epsilon}(\boldsymbol{u}))\Big] + \boldsymbol{f} = \boldsymbol{0} \quad \text{in } \Omega, \tag{2.74}$$

$$-2(1-\phi)\,\psi_a(\boldsymbol{\epsilon}(\boldsymbol{u})) + G_c\left(\frac{1}{l}\phi \cancel{- l\Delta\phi}\right) = 0 \quad \text{in } \Omega, \tag{2.75}$$

where the Laplacian term vanishes because $\nabla\phi = \boldsymbol{0}$. The algebraic phase-field equation

can be rearranged to obtain the closed-form expression

$$\phi = \frac{2\,\psi_a(\boldsymbol{\epsilon}(\boldsymbol{u}))}{\dfrac{G_c}{l} + 2\,\psi_a(\boldsymbol{\epsilon}(\boldsymbol{u}))}, \tag{2.76}$$

which is manifestly non-negative and bounded by one.

However, the analytical solution above does not inherently account for the irreversibility condition, meaning ϕ could theoretically decrease during unloading. This condition must be enforced explicitly, for instance, by tracking the maximum value of ϕ over time:

$$\phi_t = \max\left(\phi, \phi_{t-1}\right). \tag{2.77}$$

Alternatively, considering the original formulation presented in Section 2.6.3, the phase-field variable for the history field method is given by:

$$\phi_{\mathcal{H}} = \frac{2\mathcal{H}}{\frac{G_c}{l} + 2\mathcal{H}}. \tag{2.78}$$

In this local problem where the gradient term is null, both approaches for enforcing irreversibility are equivalent. The total stress is then given by:

$$\boldsymbol{\sigma}(\boldsymbol{u}, \phi) = (1-\phi)^2 \boldsymbol{\sigma_a}(\boldsymbol{\epsilon}(\boldsymbol{u})) + \boldsymbol{\sigma_b}(\boldsymbol{\epsilon}(\boldsymbol{u})). \tag{2.79}$$

The effective stresses are identical for both formulations in this local (single-element) problem, whether irreversibility is enforced through the phase-field variable or through a history field.

For the uniaxial tests considered here, the only non-zero strain component in a two-dimensional description is ϵ_{yy}. The strain energy density and stresses follow from the decompositions listed in Table 2.4.

For convenience, the element length is set to $L = 1\,\text{mm}$ so that the engineering strain equals the applied displacement (small-strain assumption): $\epsilon = \Delta L/L = u_{\text{applied}}$.

The material and simulation parameters used in the reference calculations (taken from [30]) are listed in Table 2.5. Several cases are analyzed to validate the numerical implementation, to verify the enforcement of irreversibility, and to assess the behavior of anisotropic models.

Table 2.5: Material and simulation parameters for the reference case.

Parameter	**Symbol**	**Value**
Young's modulus	E	210 kN/mm^2
Poisson's ratio	ν	0.3
Critical energy release rate	G_c	0.005 kN/mm
Length scale	l	0.1 mm

Reference case: effect of irreversibility

Two loading protocols are considered to assess the implementation and the irreversibility treatment: (i) monotonic displacement loading up to a prescribed maximum; and (ii) a

loading-unloading-reloading cycle that activates the irreversibility condition. The imposed displacement histories are shown in Figure 2.13.

The comparison includes: the staggered-history-field implementation (Section 2.6.3), the staggered-penalty implementation (Section 2.6.3), and the monolithic-penalty implementation (Section 2.6.2).

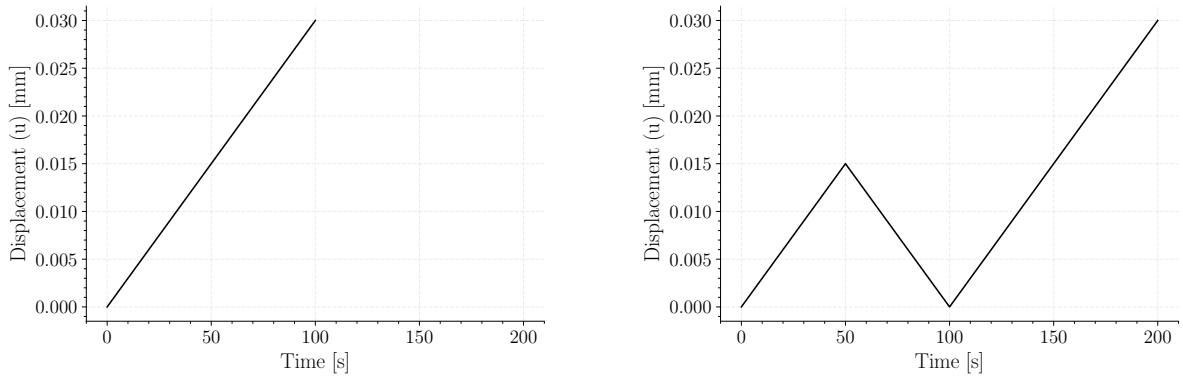

(a) Monotonic loading.

(b) Loading-unloading-reloading.

Figure 2.13: Prescribed displacement histories for the reference cases: (a) monotonic loading; (b) loading-unloading-reloading cycle.

Figure 2.14 compares the numerical solutions obtained with the history-field and penalty approaches against the analytical solution for the monotonic case. Figure 2.14(a) shows the reaction force versus applied displacement and the expected softening behavior as damage develops. Figure 2.14(b) shows the evolution of the phase-field variable with applied displacement.

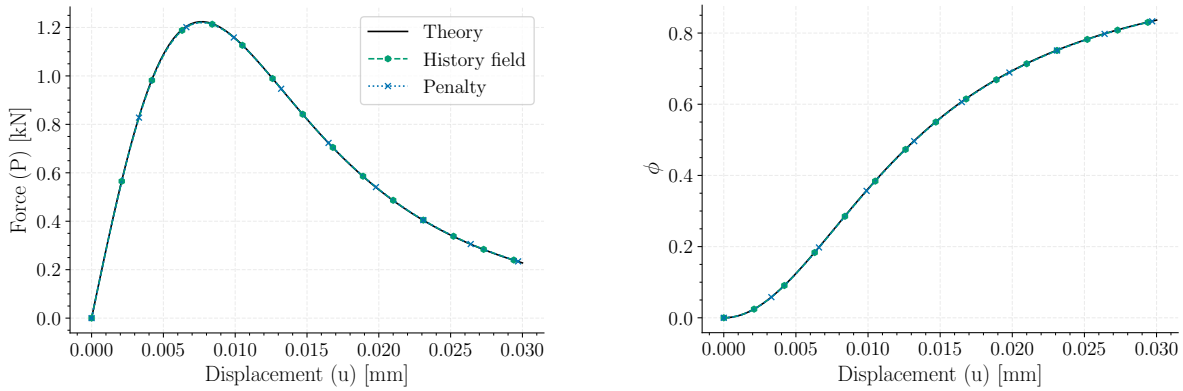

(a) Force vs. displacement (monotonic).

(b) Phase-field vs. displacement (monotonic).

Figure 2.14: Monotonic loading results: (a) reaction force versus applied displacement; (b) evolution of ϕ with applied displacement.

Figure 2.15 reports the solution for the same models under a loading–unloading cycle. During unloading (Figure 2.15(b)), the phase-field remains constant (no healing), and the force returns toward zero along a linear path. During reloading, damage progresses only after the previous peak is exceeded.

The numerical results agree with the analytical expressions, confirming the correctness of the implementation and the irreversibility enforcement.

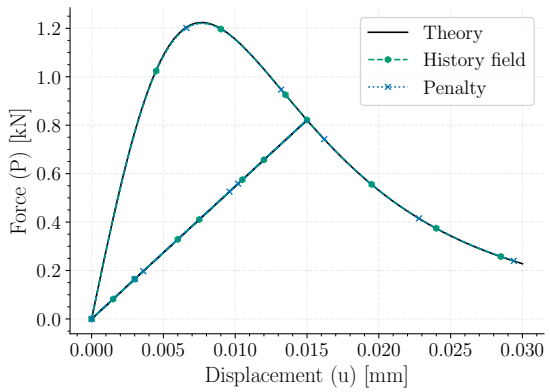

(a) Force vs. displacement (cycle).

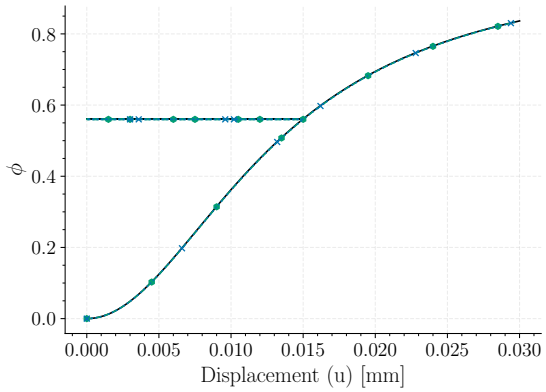

(b) ϕ vs. displacement (cycle).

Figure 2.15: Loading–unloading results demonstrating irreversibility: (a) force–displacement response; (b) phase-field evolution.

Anisotropic model: spectral decomposition

To assess anisotropic formulations, an initial compressive displacement (Figure 2.16) is applied and then reversed to tension. The case is simulated with both the staggered-history-field scheme and the monolithic-penalty scheme. Figure 2.17 compares numerical and analytical responses. Figure 2.17(a) shows the force as a function of applied displacement. Under initial compression (negative displacement) the anisotropic model predicts no damage and a linear force–displacement response; upon reversal to tension damage initiates and the force–displacement curve softens, as shown by the phase-field evolution in Figure 2.17(b).

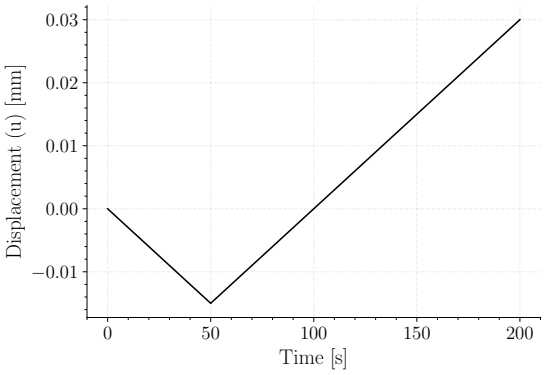

Figure 2.16: Applied displacement versus time for the anisotropic compression–tension test.

Pure shear case

A pure shear single-element test is used to examine the models' response under shear conditions with anisotropic formulations. A square element is subjected to opposing horizontal displacements at the top and bottom edges (Figure 2.18), producing a shear strain ϵ_{xy}, with $2\epsilon_{xy} = u/L$ for $L = 1, \text{mm}$. The staggered history-field solver is used for these simulations.

Figure 2.19 summarizes the results. For the volumetric–deviatoric decomposition, the

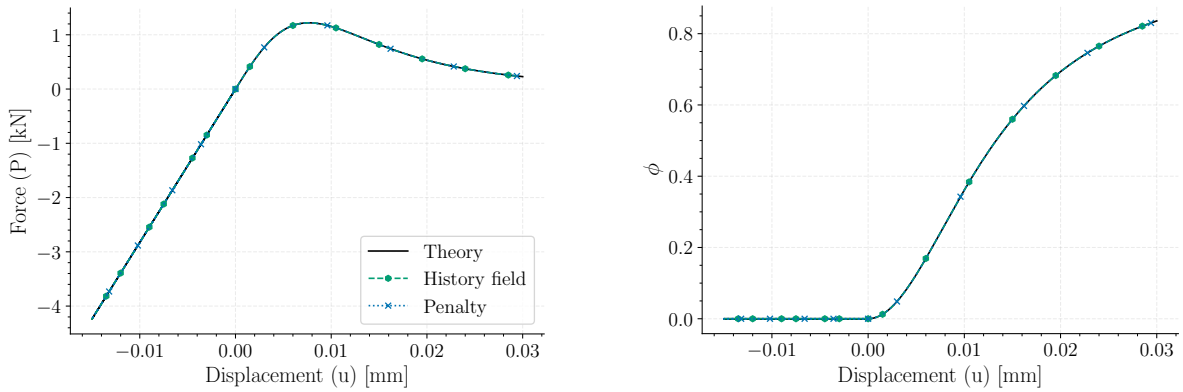

(a) Force vs. displacement.

(b) Phase-field vs. displacement.

Figure 2.17: Anisotropic spectral decomposition: comparison of numerical and analytical results for compression–tension loading.

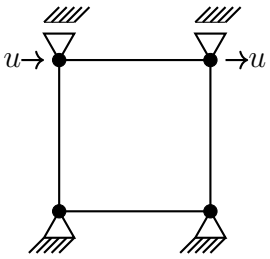

Figure 2.18: Schematic representation of the single-element model for the pure shear case.

reaction force tends to zero as damage localizes. In contrast, the spectral decomposition exhibits a different trend: although the phase-field variable evolves (see Figure 2.19(b)), the reaction force continues to increase because the undegraded energy component still contributes to load transfer. These observations are consistent with expected behavior and highlight the importance of carefully selecting an energy split.

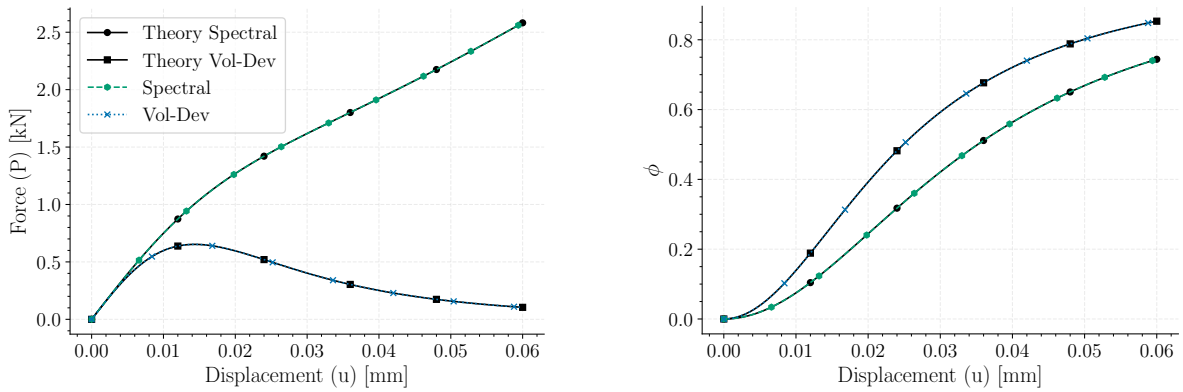

(a) Force vs. displacement.

(b) Phase-field vs. displacement.

Figure 2.19: Pure shear results: (a) shear reaction versus applied displacement; (b) evolution of the phase-field variable.

2.7.2 Single edge notched tension test

This section analyzes the single edge notched tension test, a benchmark problem described in [3]. The problem involves a square plate with a horizontal notch extending from the left edge to the center, located halfway up the specimen. The bottom edge is fully constrained, while the top edge is subjected to a vertical displacement. The geometry and boundary conditions are depicted in Figure 2.20. The specimen has a width $2W = 1.0\,\text{mm}$ and height $2W = 1.0\,\text{mm}$, with an initial notch length of $a = 0.5\,\text{mm}$.

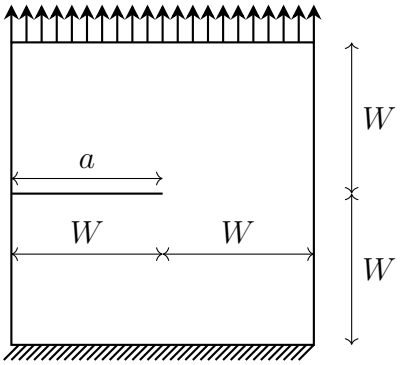

Figure 2.20: Single edge notched tension test: geometry, dimensions, and boundary conditions.

The material properties are listed in Table 2.6: Young's modulus $E = 210\,\text{kN/mm}^2$, Poisson's ratio $\nu = 0.3$, and critical energy release rate $G_c = 0.0027\,\text{kN/mm}$. The length scale parameter is $l = 0.015\,\text{mm}$. The domain is discretized with quadrilateral elements and locally refined in the region where crack propagation is expected. In the refined zone, the element size is $h = 0.002\,\text{mm}$, giving a resolution ratio of $l/h = 7.5$. The mesh used for the simulation is illustrated in Figure 2.21; it consists of 25724 quadrilateral elements and 25827 nodes. Since there is one degree of freedom for the phase-field variable and two for the displacement at each node, the total number of degrees of freedom is 77481.

Table 2.6: Material parameters for the single edge notched tension test.

Parameter	**Symbol**	**Value**
Young's modulus	E	$210\,\text{kN/mm}^2$
Poisson's ratio	ν	0.3
Critical energy release rate	G_c	$0.0027\,\text{kN/mm}$
Length scale parameter	l	$0.015\,\text{mm}$
Element size (refined zone)	h	$0.002\,\text{mm}$

This example is used to evaluate different solution schemes and models.

Results using staggered scheme with history field

The benchmark settings proposed in [3] are used as a starting point. Two length-scale values are considered for sensitivity: $l_1 = 0.015\,\text{mm}$ and $l_2 = 0.0075\,\text{mm}$. The loading is applied in increments of $\Delta u = 2.5 \times 10^{-5}\,\text{mm}$ for the first 500 steps and reduced to $\Delta u = 1.0 \times 10^{-6}\,\text{mm}$ thereafter until failure. The anisotropic spectral decomposition ([3])

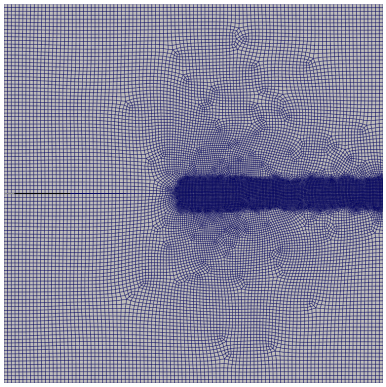

Figure 2.21: Finite element mesh for the single edge notched tension test, showing local refinement in the expected crack propagation zone.

is used for these simulations, and the staggered scheme with the history-field irreversibility is employed as the primary solution strategy.

The original implementation [3] used a single staggered iteration per time step and compensated for the lack of a restrictive staggered tolerance by reducing the time-step size [3]. For a more robust comparison, this study performs two staggered iterations per time step; the effect of using more (or fewer) inner iterations is discussed in the comparison with the penalized schemes.

After the simulations, the reaction force is examined as a function of applied displacement. Figures 2.22(a) and 2.22(b) show the reaction-force results for both length scales, demonstrating good agreement with the reference results in [3].

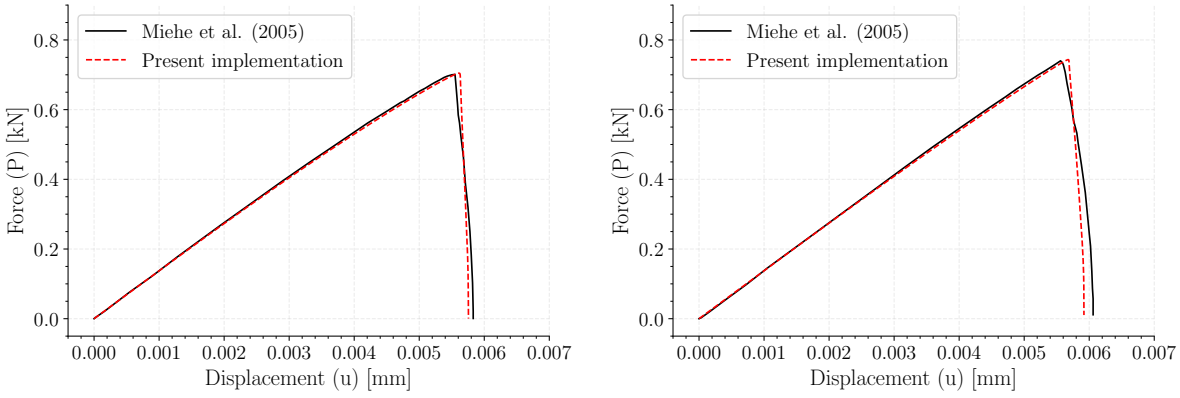

(a) Length scale $l = 0.015\,\text{mm}$.

(b) Length scale $l = 0.0075\,\text{mm}$.

Figure 2.22: Single edge notched tension test: reaction force vs. applied displacement using the staggered scheme with history field and anisotropic model with spectral decomposition.

Comparison: history field vs. penalization method

This section compares the staggered scheme with the history field to the staggered scheme with the penalization method. An isotropic model is used for both simulations, with the same material parameters and geometry as presented above.

The number of staggered iterations is determined by the increment in the L^2 norm between fields, as described in Section 2.6.3. A stricter tolerance permits larger time steps while ensuring solution accuracy with a tolerance of 10^{-8}. For the comparison, loading increments of $\Delta u = 1.0 \times 10^{-4}$ mm are used until failure and a length-scale $l_1 = 1.5 \times 10^{-2}$ mm is adopted for both methods. The penalized implementation follows the formulation in [6] and serves as an independent check against the staggered-history-field results.

Figure 2.23(a) presents the reaction-force curves for both solution schemes and Figure 2.23(b) reports the number of staggered iterations per time step. The reaction-force curves show excellent agreement between the history-field and penalization treatments, confirming that both methods produce consistent results when properly converged.

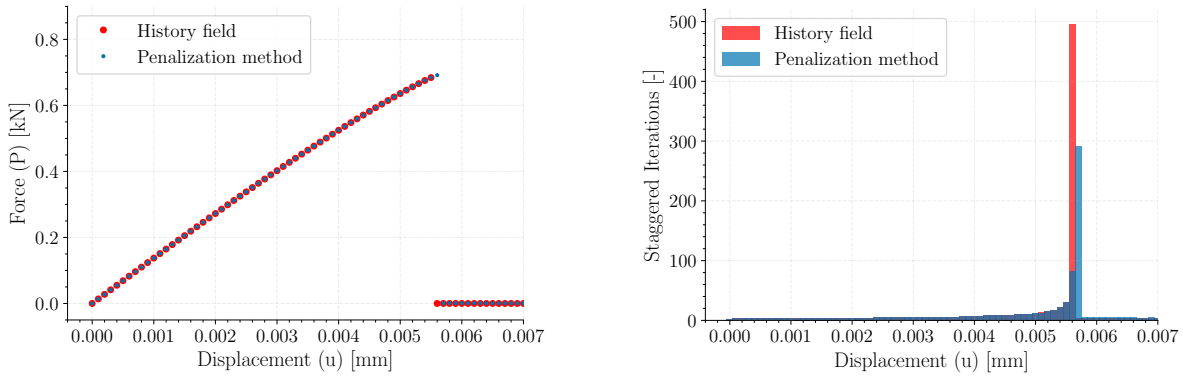

(a) Reaction force.

(b) Staggered iterations.

Figure 2.23: Comparison between history field and penalization method: (a) Reaction force vs. applied displacement; (b) Number of staggered iterations.

Figures 2.24(a) and 2.24(b) show the final phase-field evolution for both solution schemes. In this case, the phase-field crack pattern is the same for both methods and matches the expected results due to the symmetry of the problem. However, it can be seen that the simulation performed with the history-field method presents a wider profile of the phase-field variable, while the penalization method shows a sharper profile. This difference can be attributed to the nature of the irreversibility enforcement. Here, and in the following, the phase-field colorbar follows the same convention as presented in Figure 1.1(d).

As discussed in Section 2.6.3, there are several strategies to handle the convergence criterion of the staggered scheme. Here, the initial residual criterion was also considered for the penalty approach simulation. In this case, it has been verified that with a tolerance of 10^{-10}, the same number of staggered iterations is obtained as with the previous scheme.

2.7.3 Single edge notched pure shear test

This section analyzes the single edge notched shear test, a benchmark problem subjected to shear loading. The problem setup follows the description in [3, 50]. The specimen consists of a square plate with a central notch, subjected to shear deformation.

The geometry and boundary conditions are depicted in Figure 2.25. The specimen has a width $2W = 1.0\,\text{mm}$, a height $2H = 1.0\,\text{mm}$, and an initial notch of length $2a = 0.5\,\text{mm}$. As illustrated in Figure 2.25, the bottom edge is fully constrained. The top edge is constrained vertically, while the lateral edges are constrained horizontally. A horizontal

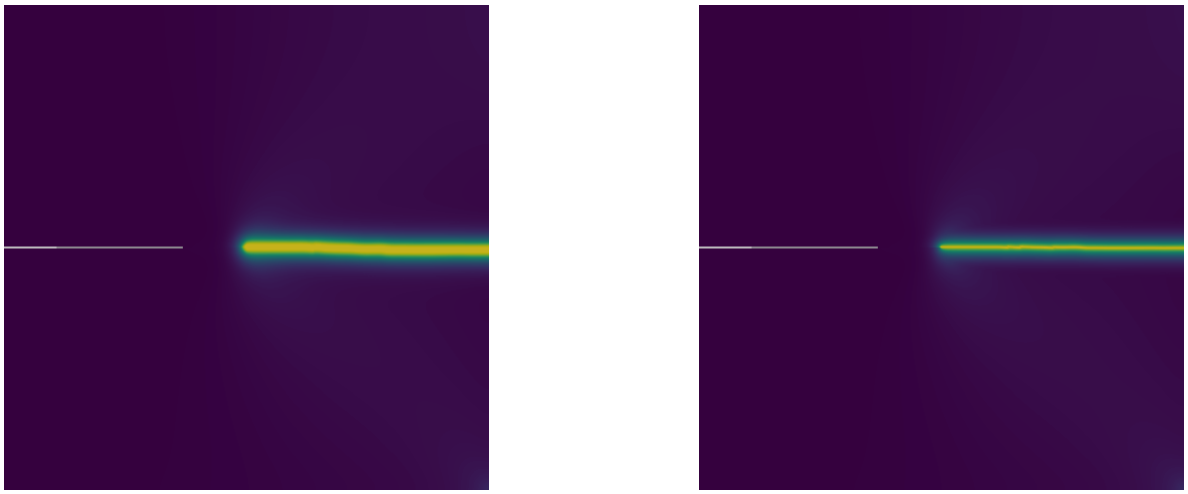

(a) History field method. (b) Penalization method.

Figure 2.24: Final phase-field profile: comparison between (a) history field method and (b) penalization method.

displacement is applied to the top edge in increments of $\Delta u = 10^{-5}\,\text{mm}$.

The material parameters are identical to those in the tension test: Young's modulus $E = 210\,\text{kN/mm}^2$, Poisson's ratio $\nu = 0.3$, and critical energy release rate $G_c = 0.0027\,\text{kN/mm}$. A length scale parameter of $l = 0.015\,\text{mm}$ is adopted. The finite element mesh used for the simulation is illustrated in Figure 2.26; it consists of 85556 quadrilateral elements and 85635 nodes. Since there is one degree of freedom for the phase-field variable and two for the displacement at each node, the total number of degrees of freedom is 256905.

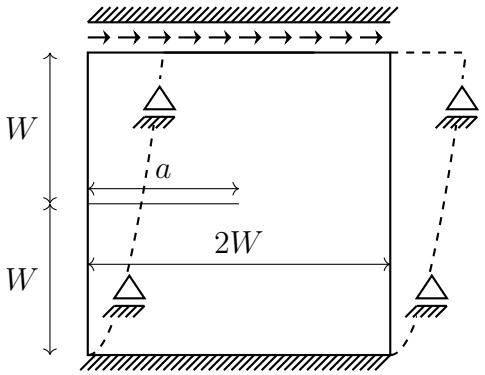

Figure 2.25: Shear test specimen with a central notch, showing dimensions and loading configuration.

Results using the staggered scheme with history field

The benchmark settings in [3] are adopted for the shear test. Simulations are carried out for both the spectral anisotropic split ([3]) and the volumetric–deviatoric split ([9]). Results are obtained with the staggered-history-field solver (two inner staggered iterations per time step, unless otherwise noted). Figure 2.27(a) compares the reaction force as a function of applied displacement with the results obtained by [3], and Figure 2.27(b) shows the results for the volumetric–deviatoric split.

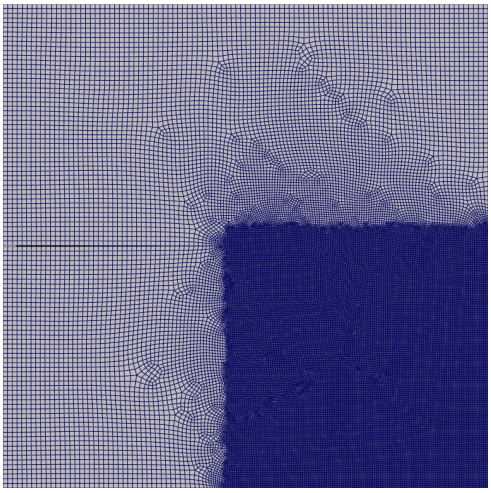

Figure 2.26: Finite element mesh for the single edge notched shear test, showing local refinement in the expected crack propagation zone.

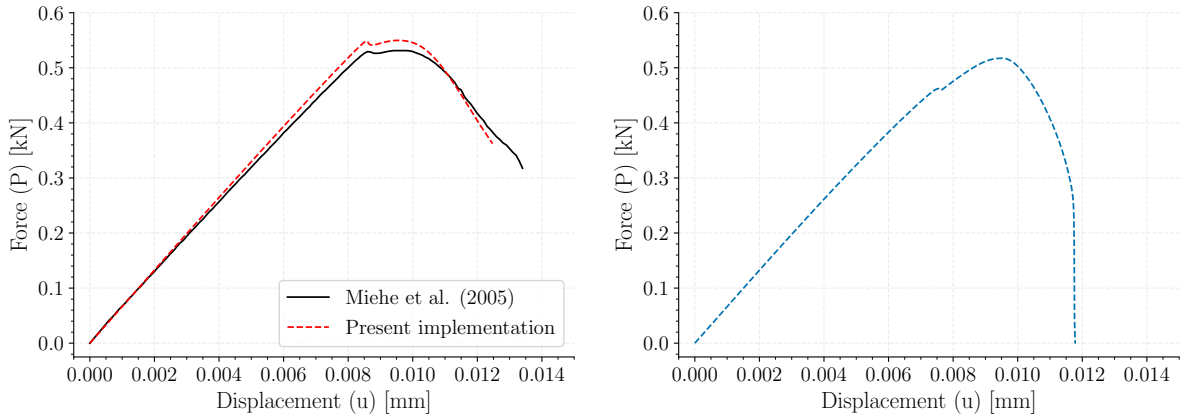

(a) Spectral decomposition.

(b) Volumetric-Deviatoric decomposition.

Figure 2.27: Single edge notched shear test: Reaction force versus applied displacement. Comparison between (a) Spectral decomposition and (b) Volumetric-Deviatoric decomposition (penalization method).

The phase-field profiles at the end of the simulation are shown in Figures 2.28(a) and 2.28(b) for the spectral and volumetric–deviatoric splits, respectively.

Penalization method

The penalty approach is also applied to the anisotropic model in both spectral and volumetric–deviatoric variants. For the penalized simulations, the staggered loop runs until an initial residual tolerance criterion of 10^{-5} is reached, with a safeguard limit of 5000 inner iterations to avoid excessive computational cost. The final phase-field profiles (Figure 2.30) and the reaction-force curves (Figure 2.29(a)) show that both solution schemes recover crack paths consistent with those obtained with the history field method. Figure 2.29(b) reports the number of staggered iterations required per step for the penalized runs.

Here, it must be noted that in the spectral decomposition solution, the reaction force con-

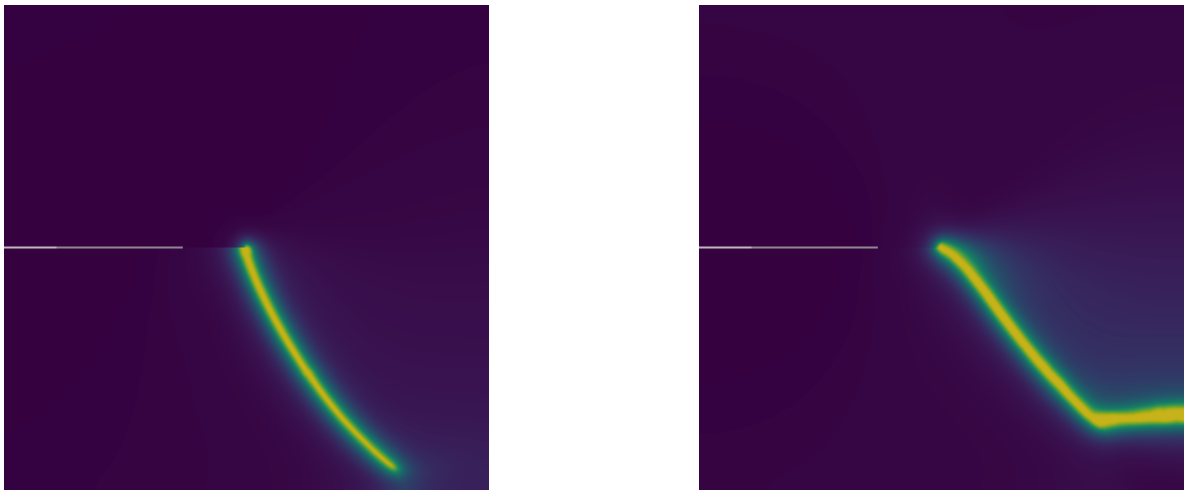

(a) Spectral. (b) Volumetric deviatoric.

Figure 2.28: Final phase-field profile using the history field method with 2 staggered iterations: (a) Spectral decomposition; and (b) Volumetric-deviatoric decomposition.

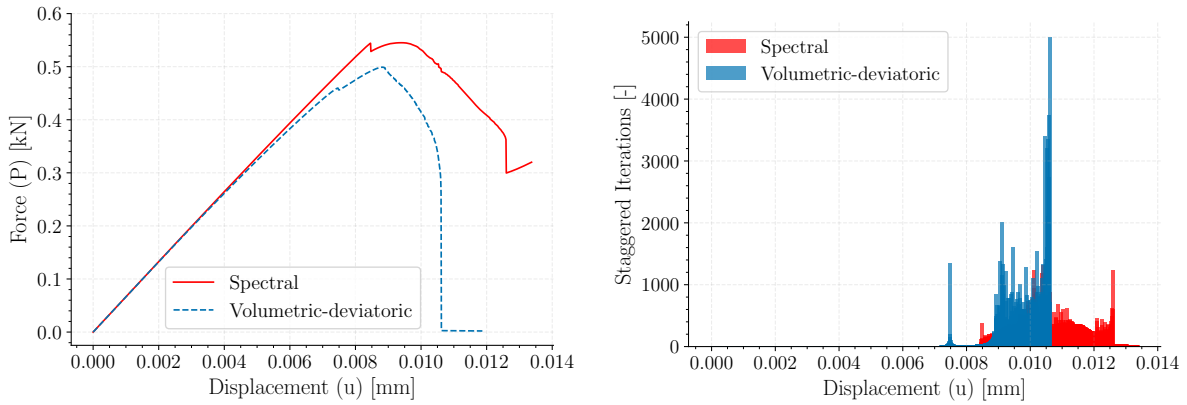

(a) Force-displacement. (b) Staggered iterations.

Figure 2.29: Comparison of solution schemes for the shear test: (a) Reaction force vs. applied displacement; (b) Number of staggered iterations.

tinues to grow, although the crack has completely propagated, as shown in 2.30(a). This occurs because the undegraded component in the spectral decomposition still contributes to load transfer, as discussed in Section 2.7.1. In contrast, the volumetric–deviatoric decomposition shows a clear drop in reaction force as the crack propagates, consistent with the expected behavior for this energy split. It must also be noted that the choice of energy split has a significant impact on the force response under shear loading, and this example highlights the importance of carefully selecting the appropriate model for the specific loading conditions being analyzed.

2.8 Conclusions

This chapter has presented a comprehensive overview of the phase-field approach to fracture, framing it not as a monolithic theory, but as a flexible modular system. This perspective allows for the clear identification of the distinct roles played by each compo-

(a) Spectral. (b) Volumetric deviatoric.

Figure 2.30: Final phase-field profile using the penalization method with a residual tolerance of 10^{-5}: (a) Spectral decomposition; and (b) Volumetric-deviatoric decomposition.

nent in the physical and numerical representation of cracks. By dissecting the method into its fundamental pillars—the fracture surface energy, the effective elastic energy, the irreversibility constraint, and the solution algorithm—a robust basis for modeling complex fracture phenomena is established.

The key findings and contributions derived from this modular analysis are summarized as follows:

- **Geometric regularization (fracture surface energy):** The analytical and numerical analysis of the AT2 model provided a rigorous verification of the regularization properties. A specific contribution of this work is the derivation of the analytical solution for the finite 1D domain, which accounts for boundary effects often neglected in infinite-domain solutions. This study confirmed that the total energy converges to the sharp fracture energy as $l \to 0$ and highlighted the mesh resolution requirement, showing that a ratio of $l/h > 2$ is sufficient to maintain relative errors below 1% when using linear elements.
- **Physical modeling (effective elastic energy):** The comparison between isotropic and anisotropic formulations verifies that the choice of energy split is critical for capturing tension–compression asymmetry. While isotropic models are efficient, they fail to prevent damage under compression. Conversely, anisotropic models (such as spectral or volumetric–deviatoric decompositions) effectively handle this asymmetry but can yield distinct crack paths and force responses under complex loading conditions.. It is concluded that, while the energy splits analyzed in this work are not universally applicable, understanding their specific kinematic and energetic implications is essential for accurate modeling.
- **Constraint enforcement (approximated continuous models):** The investigation into irreversibility enforcement demonstrated that both the history-field method and the penalty formulation yield consistent results when properly converged. While both approaches provide similar outcomes, the history-field method disrupts the variational formulation of the problem. In contrast, the penalty approach preserves

this variational structure, facilitating a rigorous analysis of how the approximated model converges to the original problem via the penalty parameter.

- **Numerical robustness (solution strategy):** A critical contribution of the numerical framework addresses the non-convexity of the phase-field fracture problem, which causes convergence issues in monolithic schemes. To overcome this, a robust staggered scheme is employed, with the option of considering staggered convergence through the proposed rigorous residual-based convergence criterion. Unlike standard checks on solution increments, the proposed "initial residual" check ensures that the coupled system strictly satisfies the global equilibrium equations at every step. This criterion prevents the numerical drift often observed in operator-split schemes and guarantees the reliability of the solution without excessive computational cost.

In conclusion, the careful integration of these four pillars—geometric regularization, physical energy splitting, constraint enforcement, and robust numerical solvers—defines the success of the phase-field method. Furthermore, all models have been validated against the analytical solution for the 1D problem (CSDF), single-element benchmarks, and results from the literature. These insights provide the necessary theoretical and numerical foundation for the advanced developments in fatigue and path-following solvers addressed in the subsequent chapters.

Chapter 3

FATIGUE AND ENERGY CONTROLLED SOLVERS

This chapter presents a novel, robust and efficient framework for fatigue crack-propagation that combines the principles of LEFM with PFF. Contrary to cycle-by-cycle PFF approaches, this method employs a quasistatic, monotonic process to predict fatigue life from a single simulation, and uses standard crack propagation models such as Paris' law for the material response, simplifying its parametrization.

The core of the methodology is the numerical evaluation of the derivative of the specimen's compliance with respect to the crack area ($\mathrm{d}C/\mathrm{d}a$). To retrieve this compliance, the framework relies on a PFF-FEM simulation, controlled by imposing monotonic crack growth. This control of the loading process is achieved by a new crack-control scheme which allows for robustly tracing the complete equilibrium path of a crack, capturing complex instabilities such as snap-back. The specimen's compliance obtained from the PFF simulation enables the integration of Paris' law to predict fatigue life without simulating individual cycles.

The proposed methodology is first validated through a series of benchmarks with analytical solutions to demonstrate its accuracy. The framework is then applied to more complex geometries where the crack path is unknown, showing very good agreement with experimental results for both crack paths and fatigue life.

3.1 Introduction

Fracture mechanics and fatigue analysis are two fundamental theories for understanding the failure of materials and structures. Fracture mechanics provides a theoretical framework to study the conditions for quasistatic crack propagation, while fatigue analysis focuses on the behavior of materials under cyclic loading conditions.

To overcome the challenges identified thus far in the models reviewed, a new method is proposed to model fatigue. This method resembles conventional crack propagation models, relying on the effective Stress Intensity Factor (SIF) during crack growth to integrate a Paris-law model for life prediction. In contrast, both the stress intensity and crack path here are derived from a single PFF simulation.

The method is based on obtaining the compliance rate with respect to the crack area using the PFF model, combined with novel energy-controlled techniques. In this form, the effective SIF is obtained at each stage of crack propagation and is used to integrate a Paris type law to provide the crack path evolution with the corresponding number of cycles at stage in a single simulation. With the modeling approach presented, it is not necessary to simulate cycle by cycle propagation, enabling the simulation of cases with millions of steps without increasing the computational cost. Moreover, contrary to X-FEM or re-meshing techniques, the use of PFF eliminates the need of recomputing and factorizing the stiffness matrix at each crack propagation step also strongly reducing the computational cost.

The key point of this approach is the development of a novel energy-controlled equilibrium path solver, formulated in both variational and non-variational forms. These solvers robustly trace the complete equilibrium path — including snap-back and snap-through instabilities — by adding only a single scalar unknown to the system, resulting in a simple and efficient implementation. In the variational scheme, this scalar is a true Lagrange multiplier, whereas in the non-variational scheme, it is a parameter that plays a similar role but is not derived from the stationarity of a functional. Alternative equilibrium path tracking methods have been proposed in the literature, such as crack-length control techniques [14], arc-length methods integrated with fracture energy control [12], and arc-length control for staggered phase-field schemes [13]. While these approaches also address the challenge of tracing unstable equilibrium paths, the method presented here stands out for its simplicity: only one additional scalar unknown is added to the system, and the implementation is straightforward within a monolithic framework. This enables efficient and robust simulation of quasi-static crack growth and provides direct access to the rate of compliance with respect to the crack area, which is essential for subsequent fracture and fatigue analysis.

This chapter is organized as follows. Section 3.2 reviews the theoretical foundations of LEFM and Paris' law. Section 3.3 establishes scaling relationships that enable the transformation of mechanical responses between problems with different fracture toughness values. Section 3.4 introduces the variational and non-variational energy-controlled solvers and explains the computation of key quantities, such as the compliance derivative ($\mathrm{d}C/\mathrm{d}a$). Section 3.5 details the numerical implementation, including the adaptive solution strategy and methods for correcting the overestimation of the crack area and its resulting effects. Section 3.6 provides a comprehensive validation of the framework. It begins with the three-point bending test (Section 3.6.1), where the equivalence of the proposed solvers is validated and the results are compared against analytical solutions. It then analyzes the center-cracked specimen (Section 3.6.2) to investigate numerical aspects-such as the length scale parameter and crack measurement corrections-and validates the fatigue life prediction by comparing the results with theoretical benchmarks. Once the approach is validated, Section 3.7 demonstrates the framework's capabilities on a complex example, analyzing the unknown crack paths in a modified compact tension specimen with multiple holes. Finally, Section 3.8 summarizes the findings.

3.2 Theoretical background and key concepts in LEFM

This section establishes the theoretical foundation of LEFM that underpins the proposed methodology. While these concepts are well-established, a succinct presentation is essen-

tial as this work demonstrates that combining fundamental fracture mechanics principles with energy-controlled phase-field models can achieve remarkable accuracy and computational efficiency.

The SIF, K, is a fundamental parameter in LEFM that quantifies the intensity of the stress field in the vicinity of a crack tip. For a given specimen geometry and loading configuration, it is expressed as:

$$K = \frac{P}{B\sqrt{W}} f(a/W), \tag{3.1}$$

where P is the applied force, B is the specimen thickness, W is a characteristic dimension (typically the specimen width), a is the crack length, and $f(a/W)$ is a dimensionless geometry factor that depends on the specimen configuration and loading conditions.

Fracture is predicted to occur when the SIF reaches a critical value, the fracture toughness K_c, which is an intrinsic material property. The critical force P_c required to initiate fracture is determined by setting $K = K_c$:

$$P_c = \frac{B\sqrt{W}\, K_c}{f(a/W)}. \tag{3.2}$$

In cases involving mixed-mode fracture, the critical parameter is the equivalent SIF, K_{eq}, which accounts for the combined effects of all active fracture modes. Specifically, K_{eq} is a function of the individual mode contributions.

The precise form of $K_{\text{eq}} = f(K_I, K_{II}, K_{III})$ depends on the material and loading conditions, and it enables a unified treatment of fracture processes where multiple modes are present simultaneously.

Under cyclic loading conditions, crack growth is commonly described by Paris' law, which relates the crack growth rate per cycle, $\mathrm{d}a/\mathrm{d}N$, to the equivalent SIF range ΔK_{eq}:

$$\frac{\mathrm{d}a}{\mathrm{d}N} = C_{\text{Paris}}(\Delta K_{\text{eq}})^n, \tag{3.3}$$

where C_{Paris} and n are empirical material constants determined experimentally. The equivalent SIF range accounts for all active fracture modes and is calculated from the cyclic loading conditions. This reduces to:

$$\Delta K = \frac{\Delta P}{B\sqrt{W}} f(a/W), \tag{3.4}$$

where $\Delta P = P_{\max} - P_{\min}$ is the cyclic force range. The fatigue life of a component can be calculated by integrating Paris' law employing Eqs. (3.3) and (3.4):

$$N_f = N_i + \frac{1}{C_{\text{Paris}}\left(\frac{\Delta P}{B\sqrt{W}}\right)^n} \int_{a_i}^{a_f} \frac{\mathrm{d}a}{[f(a/W)]^n}\ , \tag{3.5}$$

where N_i and N_f are the initial and final cycle numbers, and a_i and a_f are the corresponding crack lengths. This equation enables fatigue life calculations based on material properties (C_{Paris}, n), applied loading (ΔP), specimen geometry (B, W), and calculations from LEFM ($f(a/W)$).

An alternative, yet equivalent, formulation in LEFM is based on the energy release rate, G, which represents the energy dissipated per unit of newly created crack surface area. For a body under an applied force P, the energy release rate is related to the compliance derivative as:

$$G = \frac{P^2}{2B}\frac{\mathrm{d}C}{\mathrm{d}a}, \tag{3.6}$$

where C is the structural compliance and a is the crack length. For linear elastic materials, the energy release rate and equivalent SIF are related through:

$$G = \frac{K_{\mathrm{eq}}^2}{E'}, \tag{3.7}$$

where E' is the effective Young's modulus, defined as $E' = E$ for plane stress conditions and $E' = E/(1-\nu^2)$ for plane strain conditions, with E being Young's modulus and ν Poisson's ratio. Notably, the energy release rate G intrinsically incorporates the effects of all fracture modes, as it is defined in terms of the equivalent SIF K_{eq}, which aggregates the contributions from Modes I, II, and III. This ensures that G provides a unified energetic criterion for crack propagation regardless of the mode mixity.

The relationship between the applied force P and the energy release rate G can be expressed by rearranging Eq. (3.6):

$$P = \sqrt{\frac{2BG}{\mathrm{d}C/\mathrm{d}a}}\ . \tag{3.8}$$

Fracture is predicted to occur when the energy release rate G reaches its critical value G_c. The critical force, P_c, is therefore determined by substituting $G = G_c$ into Eq. (3.8). This expression provides a method for fracture prediction based on the rate of compliance with respect to the crack area, which can be determined experimentally or numerically.

The energetic framework can be extended to fatigue analysis. Substituting the relationship $\Delta K = \sqrt{E'}\ \Delta\sqrt{G}$ into Paris' Law (Eq. (3.3)) yields an expression for crack growth in terms of the energy release rate range, $\Delta\sqrt{G}$:

$$\frac{da}{dN} = C_{\mathrm{Paris}}\left(\sqrt{E'}\Delta\sqrt{G}\right)^n. \tag{3.9}$$

Integrating from the initial crack length a_i to the final crack length a_f gives the fatigue life:

$$N_f = N_i + \frac{1}{C_{\mathrm{Paris}}(E'/(2B))^{n/2}(\Delta P)^n}\int_{a_i}^{a_f}\frac{\mathrm{d}a}{(\mathrm{d}C/\mathrm{d}a)^{n/2}}. \tag{3.10}$$

This equation is equivalent to Eq. (3.5) and demonstrates that fatigue life can be predicted directly from compliance evolution.

It is important to note that while Eq. (3.10) contains the effective Young's modulus E', the fatigue behavior described by Paris' law depends fundamentally on the material constants C_{Paris} and n. The term E' appears because compliance C is inversely proportional to E'. The derivative can be expressed as:

$$\frac{\mathrm{d}C}{\mathrm{d}a} = \frac{1}{E'}\frac{\mathrm{d}\bar{C}}{\mathrm{d}a}, \tag{3.11}$$

where $\bar{C}$ is a normalized compliance depending only on geometry. Substituting this into Eq. (3.10), one confirms that the E' terms cancel out and that fatigue life prediction is independent of elastic modulus, consistent with the physical nature of Paris' law.

The direct relationship between the geometry factor and compliance derivative can be established by combining Eqs. (3.1), (3.6), and (3.7):

$$f(a/W) = \sqrt{\frac{E'BW}{2}\frac{\mathrm{d}C}{\mathrm{d}a}}. \tag{3.12}$$

This equivalence confirms that, within the framework of LEFM, both stress-based and energy-based approaches are consistent and interchangeable. The choice between them depends on whether the geometry factor or compliance evolution is more convenient to work with, for a given problem. For complex geometries or unknown crack paths, calculating compliance evolution numerically via phase-field simulations offers a powerful and versatile method for fracture and fatigue analysis in the linear elastic regime.

3.3 Scaling relationships for different critical energy release rates

The critical energy release rate G_c does not influence the structural compliance of the specimen, which depends solely on geometry and elastic properties. This fundamental property enables the establishment of scaling relationships between problems with different G_c values but identical geometric and elastic properties.

For two problems with critical energy release rates G_{c1} and G_{c2}, the Griffith criterion gives:

$$G_{c1} = \frac{P_1^2}{2B}\frac{dC}{da}, \quad G_{c2} = \frac{P_2^2}{2B}\frac{dC}{da} \tag{3.13}$$

Since dC/da is identical (same geometry and elastic properties), the scaling factor $\zeta = \sqrt{G_{c2}/G_{c1}}$ yields:

$$P_2 = \zeta P_1, \quad u_2 = \zeta u_1, \quad \psi_2 = \zeta^2 \psi_1 \tag{3.14}$$

where displacement scaling follows from $u = C \cdot P$ and strain energy for linear elasticity applies $\psi_{\mathrm{le}} = \frac{1}{2}Pu$. These relationships enable efficient transformation of mechanical responses between simulations with different fracture toughness values.

3.4 Energy-controlled PFF solvers

Traditional solution strategies for PFF, such as force or displacement control as presented in Chapter 2, often fail to capture the complete equilibrium path when the structural response overcomes critical points such as snap-back or snap-through behavior. In these cases, displacement-controlled solvers may jump between stable equilibrium points, missing critical portions of the response, while force-controlled schemes may be unable to trace the path entirely.

To overcome these limitations, this section introduces two novel energy-controlled schemes. These are designed to robustly trace the complete equilibrium path during crack propagation by controlling the simulation with a monotonically increasing energetic parameter.

This ensures monotonic crack propagation even in the presence of instabilities, allowing for an accurate characterization of the system's compliance throughout the entire fracture process.

As the main objective of this chapter is to present the fatigue framework, the simplest PFF formulation is considered: a quadratic degradation function, $g(\phi) = (1-\phi)^2$, without an energy split, so an isotropic model is used; additionally, an AT2 regularization is adopted. However, the extension to other, more general models, such as an anisotropic formulation or the AT1 crack surface regularization, is straightforward.

3.4.1 Variational scheme

The first approach is a variational scheme in which the simulation is driven by an energetic control function, $\tau(t)$. This is accomplished by introducing a constraint that equates $\tau(t)$ to a weighted combination of the crack surface energy and the work done by external forces. A Lagrange multiplier, Λ, is employed to enforce this constraint. The constraint equation is defined as:

$$c_1 \int_\Omega \left(\frac{1}{2l}\phi^2 + \frac{l}{2}|\nabla\phi|^2 \right) \mathrm{d}\boldsymbol{x} + c_2 \int_{\partial\Omega_t} \boldsymbol{t}\cdot\boldsymbol{u}\,\mathrm{d}S = \tau(t). \tag{3.15}$$

Here, c_1 and c_2 are numerical parameters introduced to improve solver convergence and ensure dimensional consistency in the constraint. Their values can be chosen to appropriately scale the contributions of the crack surface energy and the external work, respectively. For example, if c_1 is assigned the same units as the critical energy release rate G_c (energy per unit length), then c_2 becomes dimensionless, and $\tau(t)$ has units of energy. Alternatively, if c_1 is dimensionless, then c_2 must have units of compliance (length per force), and $\tau(t)$ will have units of area, in this case the algorithm can be referred to as a crack area controlled algorithm. In practice, these parameters are selected to balance the terms in the constraint and facilitate numerical stability.

In this formulation, a force is applied in a prescribed direction $\boldsymbol{n}$, while the actual load magnitude is determined as part of the solution through the Lagrange multiplier. This multiplier emerges naturally from the constrained optimization, ensuring that the equilibrium path is traced by enforcing the energy balance and is determined simultaneously with the phase-field and displacement fields by the solver, as an unknown of the problem, in such a way that the energetic constraint is satisfied. Concurrently, the displacement field evolves to satisfy the equilibrium equations under the imposed energy constraint. The augmented functional for this constrained system, V, is defined as:

$$\begin{aligned} V(\boldsymbol{u},\phi,\Lambda) = &\int_\Omega g(\phi)\psi(\boldsymbol{\epsilon}(\boldsymbol{u}))\,\mathrm{d}\boldsymbol{x} + G_c \int_\Omega \left(\frac{1}{2l}\phi^2 + \frac{l}{2}|\nabla\phi|^2 \right) \mathrm{d}\boldsymbol{x} - \int_{\partial\Omega_t} \boldsymbol{t}\cdot\boldsymbol{u}\,\mathrm{d}S \\ &+ \Lambda \left[c_1 \int_\Omega \left(\frac{1}{2l}\phi^2 + \frac{l}{2}|\nabla\phi|^2 \right) \mathrm{d}\boldsymbol{x} + c_2 \int_{\partial\Omega_t} \boldsymbol{t}\cdot\boldsymbol{u}\,\mathrm{d}S - \tau(t) \right]. \end{aligned} \tag{3.16}$$

The equilibrium equations are obtained by enforcing stationarity, $\delta V = 0$. The resulting weak form is:

$$\int_\Omega g(\phi)\boldsymbol{\sigma}(\boldsymbol{\epsilon}(\boldsymbol{u})) : \boldsymbol{\epsilon}(\delta\boldsymbol{u})\,\mathrm{d}\boldsymbol{x} - (1-\Lambda c_2)\int_{\partial\Omega_t} \boldsymbol{t}\cdot\delta\boldsymbol{u}\,\mathrm{d}S = 0, \tag{3.17}$$

$$\int_\Omega g'(\phi)\delta\phi\,\psi(\boldsymbol{\epsilon}(\boldsymbol{u}))\,\mathrm{d}\boldsymbol{x} + (G_c + \Lambda c_1)\int_\Omega \left(\frac{1}{l}\phi\delta\phi + l\nabla\phi\cdot\nabla\delta\phi \right) \mathrm{d}\boldsymbol{x} = 0, \tag{3.18}$$

$$\delta\Lambda \left[c_1 \int_\Omega \left(\frac{1}{2l}\phi^2 + \frac{l}{2}|\nabla\phi|^2 \right) \mathrm{d}\boldsymbol{x} + c_2 \int_{\partial\Omega_t} \boldsymbol{t}\cdot\boldsymbol{u}\,\mathrm{d}S - \tau(t) \right] = 0, \tag{3.19}$$

where $\delta\boldsymbol{u}, \delta\phi, \delta\Lambda$ are, respectively, the variations of the displacement field, the phase field, and the Lagrange multiplier. From the solution $(\boldsymbol{u}, \phi, \Lambda)$, the Lagrange multiplier provides key physical insights: the effective applied force magnitude is scaled by the factor $(1-\Lambda c_2)$, and the effective critical energy release rate becomes $G_c^{\text{eff}} = (G_c + \Lambda c_1)$.

A fundamental characteristic of the variational scheme is that the introduction of the Lagrange multiplier replaces the toughness G_c with a modified value G_c^{eff}. Consequently, the equations do not directly trace the physical response for a constant material toughness G_c. Nevertheless, the mathematical relationship detailed in Section 3.3 establishes the connection between two problems with different critical energy release rates.

Based on this, equivalence with a problem that has a constant G_c can be established by introducing a scaling factor, η.

$$\eta = \sqrt{\frac{G_c}{G_c^{\text{eff}}}} = \frac{1}{\sqrt{1 + \frac{\Lambda c_1}{G_c}}}\ . \tag{3.20}$$

The physical quantities for constant G_c can then be recovered from the variational simulation results using the following transformation equations:

$$P_{G_c} = \eta \cdot P_{\text{variational}} \tag{3.21}$$

$$u_{G_c} = \eta \cdot u_{\text{variational}} \tag{3.22}$$

$$\psi_{G_c} = \eta^2 \cdot \psi_{\text{variational}} \tag{3.23}$$

Here, $P_{\text{variational}}$, $u_{\text{variational}}$, and $\psi_{\text{variational}}$ are the reaction force, displacement, and strain energy density obtained from the variational solution, while P_{G_c}, u_{G_c}, and ψ_{G_c} are the corresponding quantities for a solution with a constant G_c. These transformations provide a systematic approach to reconstruct the physical quantities. The factor η depends on the instantaneous value of the Lagrange multiplier Λ and ensures that the recovered response corresponds to the true material behavior.

3.4.2 Non-variational scheme

As an alternative approach, a non-variational energy-controlled scheme is proposed that directly computes the physical equilibrium path for an effective constant $G_c^{\text{eff}} = G_c$ without requiring post-processing transformations. This formulation is achieved by modifying the weak form equations to ensure that the critical energy release rate, G_c, remains constant throughout the simulation, independent of Λ.

Derivation from the variational scheme

This section presents a formal derivation demonstrating that the non-variational scheme can be obtained from the variational formulation through a consistent change of variables.

The derivation begins with the weak form of the phase-field evolution equation from the variational scheme (Eq. (3.18)), where $\boldsymbol{u}$ is the displacement field obtained from

the variational solver. The scaling factor η from Eq. (3.20) is introduced, defined as $\eta^2 = G_c/(G_c + \Lambda c_1)$. Multiplying Eq. (3.18) by η^2 yields:

$$\eta^2 \int_\Omega g'(\phi)\delta\phi\, \psi(\boldsymbol{\epsilon}(\boldsymbol{u}))\, \mathrm{d}\boldsymbol{x} + G_c \int_\Omega \left(\frac{1}{l}\phi\delta\phi + l\nabla\phi\cdot\nabla\delta\phi\right)\, \mathrm{d}\boldsymbol{x} = 0. \tag{3.24}$$

Next, a change of variables for the displacement field is introduced. A new field is defined, $\boldsymbol{u}_{\text{phys}}$, representing the physical displacement corresponding to a constant toughness G_c. Based on the scaling relationships in Section 3.3, it follows that $\boldsymbol{u}_{\text{phys}} = \eta\boldsymbol{u}$, which implies $\psi(\boldsymbol{\epsilon}(\boldsymbol{u}_{\text{phys}})) = \eta^2\psi(\boldsymbol{\epsilon}(\boldsymbol{u}))$. Substituting this into the equation gives:

$$\int_\Omega g'(\phi)\delta\phi\, \psi(\boldsymbol{\epsilon}(\boldsymbol{u}_{\text{phys}}))\, \mathrm{d}\boldsymbol{x} + G_c \int_\Omega \left(\frac{1}{l}\phi\delta\phi + l\nabla\phi\cdot\nabla\delta\phi\right)\, \mathrm{d}\boldsymbol{x} = 0. \tag{3.25}$$

This equation is identical to the phase-field evolution equation of the non-variational scheme (Eq. (3.29)), with $\boldsymbol{u}_{\text{phys}}$ as the displacement unknown.

A similar transformation is applied to the momentum balance equation (Eq. (3.17)). Multiplying by η and using the change of variables $\boldsymbol{u}_{\text{phys}} = \eta\boldsymbol{u}$ and $\boldsymbol{t}_{\text{phys}} = \eta\boldsymbol{t}$ (where $\boldsymbol{t}$ is the prescribed traction vector in the variational scheme), the following expression is obtained:

$$\int_\Omega g(\phi)\boldsymbol{\sigma}(\boldsymbol{\epsilon}(\boldsymbol{u}_{\text{phys}})) : \boldsymbol{\epsilon}(\delta\boldsymbol{u}_{\text{phys}})\, \mathrm{d}\boldsymbol{x} - (1 - \Lambda c_2)\int_{\partial\Omega_t} \boldsymbol{t}_{\text{phys}}\cdot\delta\boldsymbol{u}_{\text{phys}}\, \mathrm{d}S = 0. \tag{3.26}$$

This result matches the momentum equation of the non-variational scheme (Eq. (3.28)).

Finally, the constraint equation (Eq. (3.19)) is transformed by applying the same change of variables:

$$\delta\Lambda\left[c_1\int_\Omega\left(\frac{1}{2l}\phi^2 + \frac{l}{2}|\nabla\phi|^2\right)\, \mathrm{d}\boldsymbol{x} + c_2\int_{\partial\Omega_t}\boldsymbol{t}_{\text{phys}}\cdot\boldsymbol{u}_{\text{phys}}\, \mathrm{d}S - \tau_{\text{phys}}(t)\right] = 0. \tag{3.27}$$

where $\tau_{\text{phys}}(t)$ is a new control parameter $\tau_{\text{phys}}(t) = \eta^p\tau(t)$, the constraint becomes structurally identical to that of the non-variational scheme (Eq. (3.30)). The exponent p depends on the units of the weighting factors: $p = 2$ if c_1 has units of energy per length and c_2 is dimensionless, and $p = 0$ if c_1 is dimensionless and c_2 has units of length per force. But as is a control parameter, defined in the solution procedure, the entire term $\tau_{\text{phys}}(t)$ can be directly imposing without explicitly defining p or η.

This derivation confirms that the non-variational formulation can be obtained from the variational one through a consistent change of variables. The resulting system directly solves for the physical quantities $(\boldsymbol{u}_{\text{phys}}, \phi, \Lambda)$ corresponding to a constant G_c, thereby avoiding the need for post-processing corrections. Although this formulation is no longer strictly variational (as it does not derive from the stationarity of a single energy functional), it produces the same physical results as those obtained from the variational scheme after applying its corresponding post-processing corrections.

Equations and formulation

The governing equations for this non-variational scheme are formulated as follows:

$$\int_\Omega g(\phi)\boldsymbol{\sigma}(\boldsymbol{\epsilon}(\boldsymbol{u})) : \boldsymbol{\epsilon}(\delta\boldsymbol{u})\, \mathrm{d}\boldsymbol{x} - (1 - \Lambda c_2)\int_{\partial\Omega_t}\boldsymbol{t}\cdot\delta\boldsymbol{u}\, \mathrm{d}S = 0, \tag{3.28}$$

$$\int_\Omega g'(\phi)\delta\phi\, \psi(\boldsymbol{\epsilon}(\boldsymbol{u}))\, \mathrm{d}\boldsymbol{x} + G_c\int_\Omega\left(\frac{1}{l}\phi\delta\phi + l\nabla\phi\cdot\nabla\delta\phi\right)\, \mathrm{d}\boldsymbol{x} = 0, \tag{3.29}$$

$$\delta\Lambda \left[c_1 \int_\Omega \left(\frac{1}{2l}\phi^2 + \frac{l}{2}|\nabla\phi|^2 \right) \mathrm{d}\boldsymbol{x} + c_2 \int_{\partial\Omega_t} \boldsymbol{t}\cdot\boldsymbol{u}\,\mathrm{d}S - \tau(t) \right] = 0. \tag{3.30}$$

The fundamental distinction of this formulation lies in the treatment of the scalar Λ, which — strictly speaking — is not a Lagrange multiplier but plays a similar role to Λ in Eqs. (3.17)-(3.19). This key difference ensures that the material toughness G_c remains constant throughout the simulation, thereby enabling the solver to directly trace the physical force-displacement curve without requiring post-processing corrections.

Despite their fundamentally different mathematical formulations, both energy-controlled solvers—the variational (with post-processing corrections) and non-variational schemes—are equivalent in that they trace the same physical equilibrium path. Regarding the parameters c_1 and c_2, their choice does not affect the physical results: these parameters are introduced solely for numerical purposes and to improve solver convergence. For the non-variational solver, the results are insensitive to their specific values. In the variational solver, the equivalence with the non-variational formulation ensures that different parameter choices lead to the same physical solution. In both energy-controlled approaches, the energy-based control parameter ensures a robust tracing of the complete equilibrium path, including complex instabilities such as snap-back and snap-through behavior.

3.4.3 Computation of compliance and its derivative

A key advantage of the proposed energy-controlled framework is the ability to directly compute essential LEFM parameters from phase-field simulation results. The structural compliance, as a function of crack length a, is defined as the ratio of the displacement at the loading point, u, to the corresponding reaction force, P:

$$C = \frac{u}{P}. \tag{3.31}$$

This compliance can also be calculated from the total elastic energy of the body, $\mathcal{U}$, using $\mathcal{U} = \frac{1}{2}Pu$. In the case of the PFF functional, this corresponds to the effective elastic energy presented in Eq. (2.6), so the following relation holds for the isotropic model employed here, which does not consider an energy split:

$$C = \frac{2\mathcal{U}}{P^2} = \frac{2}{P^2}\int_\Omega g(\phi)\psi(\boldsymbol{\epsilon}(\boldsymbol{u}))\,\mathrm{d}\boldsymbol{x}\ . \tag{3.32}$$

Similarly, an energetically consistent displacement, u_{energy}, is:

$$u_{\text{energy}} = \frac{2\mathcal{U}}{P} = \frac{2}{P}\int_\Omega g(\phi)\psi(\boldsymbol{\epsilon}(\boldsymbol{u}))\,\mathrm{d}\boldsymbol{x}\ . \tag{3.33}$$

This energy-based calculation provides a robust measure of displacement that is consistent with the variational principles of the model.

For the fatigue analysis methodology proposed in this work, it is critical to obtain the rate of change of compliance with respect to crack length, $\mathrm{d}C/\mathrm{d}a$. A significant benefit of this approach is that this quantity can be computed directly without resorting to numerical differentiation, thus avoiding the inaccuracies associated with finite difference approximations.

The calculation differs slightly depending on the solver used. For the non-variational solver, the energy release rate is always equal to the material's fracture toughness, G_c.

By rearranging the fundamental relationship from LEFM (Eq. (3.6)), the compliance derivative is computed directly as:

$$\frac{\mathrm{d}C}{\mathrm{d}a} = \frac{2BG_c}{P^2} \ , \tag{3.34}$$

where P is the reaction force obtained from the simulation.

For the variational solver, to ensure the result corresponds to the true material behavior, it is crucial to use the corrected physical force, P_{G_c}, as defined in Eq. (3.21). This ensures that the computed compliance evolution is consistent with a constant fracture toughness G_c.

3.5 Numerical implementation

Regarding the discretization and finite element implementation, the same discretization as presented in 2.6.1 is used. The solution procedure employs a monolithic Newton-Raphson scheme to solve the coupled system of equations. However, an additional unknown corresponding to the scalar Λ is present, which is treated as an additional global unknown.

Regarding the irreversibility of crack growth, in both solvers, the scalar field Λ enforces the constraint defined by the control parameter $\tau(t)$. Since $\tau(t)$ is prescribed to increase monotonically over time, the weighted sum of the energy quantities in the constraint is guaranteed to increase throughout the simulation. It should be noted that this global constraint does not strictly prevent local reversibility; for instance, in specimens with multiple cracks, one crack could theoretically retract while another extends, or energy could be redistributed between different parts of the domain. However, within the context of the solution strategy and the specific examples considered in this work, this behavior does not influence the results.

3.5.1 Adaptive solution strategy

The non-linear system is solved monolithically using the Newton-Raphson method. The prescribed dissipated energy τ, acting as the control parameter, is set proportional to a pseudo-time t. To improve numerical efficiency, instead of using a fixed time step, an adaptive time algorithm adjusts the time increment Δt, and consequently the value of $\Delta\tau$, based on convergence. If the solver converges quickly, $\Delta\tau$ increases; if not, it decreases. Failed steps are reverted and retried with a smaller $\Delta\tau$. The adaptive control-step algorithm used in this work is summarized in Algorithm 3, where Γ refers to the crack area calculated by integrating the phase-field crack surface density function, which, in this case with the AT2 regularization, is given by Eq. (2.19).

3.5.2 Correction of the simulated crack area

The accurate determination of crack surface area is crucial for reliable fatigue and fracture analyses. In the phase-field model, crack area is typically obtained by integrating the crack surface density function, $\Gamma = \int_\Omega \gamma(\phi, \nabla\phi)\,\mathrm{d}\boldsymbol{x}$, over the computational domain. However, this integral tends to systematically overestimate the true physical crack area.

Algorithm 3 Adaptive control-step algorithm for energy-controlled PFF simulation.

Initialize: solution state $(\boldsymbol{u}_c, \phi_c, \Lambda_c)$, control parameter τ, step size $\Delta\tau$
Set: min/max step sizes $\Delta\tau_{\min}, \Delta\tau_{\max}$, final control value τ_{final}
Set: golden ratio ≈ 0.618 for step size adaptation
while $\Gamma < \Gamma_{\text{final}}$ **do**
    $\tau \leftarrow \tau + \Delta\tau$ ▷ Attempt a new step
    num_iterations, converged $\leftarrow$ SolveNonlinearSystem(τ)
    if converged **then**
        // Step accepted
        UpdateState $(\boldsymbol{u}_c, \phi_c, \Lambda_c) \leftarrow (\boldsymbol{u}, \phi, \Lambda)$
        SaveResults()
        if num_iterations ≤ 2 **then**
            $\Delta\tau \leftarrow \min(\Delta\tau \times (1 + \text{golden\_ratio}), \Delta\tau_{\max})$ ▷ Increase step size
        end if
        step $\leftarrow$ step $+ 1$
    else
        // Step rejected
        $\tau \leftarrow \tau - \Delta\tau$ ▷ Revert control parameter
        RevertState $(\boldsymbol{u}, \phi, \Lambda) \leftarrow (\boldsymbol{u}_c, \phi_c, \Lambda_c)$
        $\Delta\tau \leftarrow \max(\Delta\tau \times \text{golden\_ratio}, \Delta\tau_{\min})$ ▷ Reduce step size
        if $\Delta\tau \leq \Delta\tau_{\min}$ **then**
            break ▷ Stop if step size is too small
        end if
    end if
end while

To address this limitation, several correction methods have been proposed in the literature. In general, the corrected crack area can be expressed as:

$$\Gamma_{\text{phys}} = \frac{\Gamma_{\text{sim}}}{\mathcal{F}} \tag{3.35}$$

where Γ_{phys} is the corrected crack area, Γ_{sim} is the area obtained from the phase-field simulation, and $\mathcal{F}$ is a correction factor that compensates for the overestimation caused by the diffuse crack representation.

One classical approach, introduced by Bourdin [51], applies a correction factor based on mesh resolution:

$$\mathcal{F}_{\text{Bourdin}} = 1 + \frac{h}{2l} \tag{3.36}$$

where h is the characteristic mesh size and l is the phase-field length scale parameter. This correction remains constant for a given mesh and length scale.

Crack length measurement via image post-processing and skeletonization algorithms

An alternative approach is the skeletonization or thresholding technique [18]. In this approach, crack area is measured directly from the finite element mesh by identifying regions where the phase-field variable exceeds a specified threshold (typically $\phi > 0.9$ or 0.95). The skeletonization algorithm then extracts the central path of the crack, representing it as a sequence of points with unit pixel length. To improve accuracy, especially for cracks propagating diagonally or with complex geometry, a spline is fitted through these points, and the crack length is calculated from the spline curve. This procedure accounts for sub-pixel crack propagation and avoids overestimation due to pixelation effects. Unlike the mesh-based correction, the correction factor in this method varies throughout the simulation and is computed at each step as:

$$\mathcal{F}_{\text{Skeleton}} = \frac{\Gamma_{\text{sim}}}{\Gamma_{\text{measured}}} \tag{3.37}$$

where Γ_{measured} is the crack area obtained through the thresholding and skeletonization procedure.

The crack area obtained by directly integrating the $\gamma(\phi, \nabla\phi)$ function systematically overestimates the true crack area. To address this limitation, an automated crack length measurement procedure is implemented using image post-processing and skeletonization algorithms from the scikit-image package [52], specifically employing the algorithm described in [53]. This skeletonization algorithm operates by iteratively removing pixels from object boundaries until a single-pixel-wide centerline representation of the crack is obtained.

The procedure automatically extracts and measures crack length from phase-field solutions stored in `.vtu` format through the following steps: (1) identification of cracked regions where $\phi > \phi_{\text{th}} = 0.95$; (2) generation of binary images with red zones indicating $\phi > \phi_{\text{th}}$ and black zones for $\phi < \phi_{\text{th}}$; (3) skeletonization to extract single-pixel-wide crack paths; (4) coordinate extraction from the single-pixel-wide path, where pixel coordinates are converted to real physical domain coordinates using the known pixel-to-domain mapping; (5) spline curve fitting to improve measurement accuracy by avoiding length mismeasurement that occurs when cracks follow diagonal paths; and (6) calculation of crack length from the fitted spline curves. Since the phase-field variable is not saved at every simulation step, quadratic interpolation is applied to obtain crack length at all time steps. Figure 3.1 illustrates this procedure.

This automated procedure significantly improves the accuracy of crack length measurements in phase-field simulations by eliminating the overestimation inherent in integrating the $\gamma(\phi, \nabla\phi)$ function, applying image processing and skeletonization techniques to extract the true crack path, and enabling direct mapping of image data to physical coordinates for precise measurements.

By combining the damage threshold ϕ_{th} with a coordinate mapping to the physical domain, the true crack extent is objectively isolated. A smoothing operation is subsequently applied during the spline fitting to mitigate artifacts stemming from the skeletonization process. The generated splines demonstrate excellent agreement with the diffuse phase-field damage patterns, yielding highly accurate crack lengths without numerical overestimation. As shown in Figure 3.1, the fitted curves reliably capture the continuous evolution of the crack trajectory throughout the simulation. Validated across 2D geometries, this approach provides a robust and reliable methodology for precise crack length measurement in PFF frameworks.

3.5.3 Transformation of simulated results to physical quantities

Once the correction factor $\mathcal{F}$ is determined, it is necessary to transform the simulated results into physically meaningful quantities. This ensures that the corrected values are consistent with the principles of LEFM. The basis for this transformation is the assumption that the structural compliance, a global property, is accurately captured by the simulation, i.e., $C_{\text{phys}} = C_{\text{sim}}$.

The relationship between the physical compliance derivative and the simulated one is established through the chain rule, using the corrected crack area. For 2D simulations under plane strain conditions, the crack area is computed as the product of the specimen thickness B and the crack length, i.e., $A = B \cdot a$. Since the correction factor $\mathcal{F}$ applies

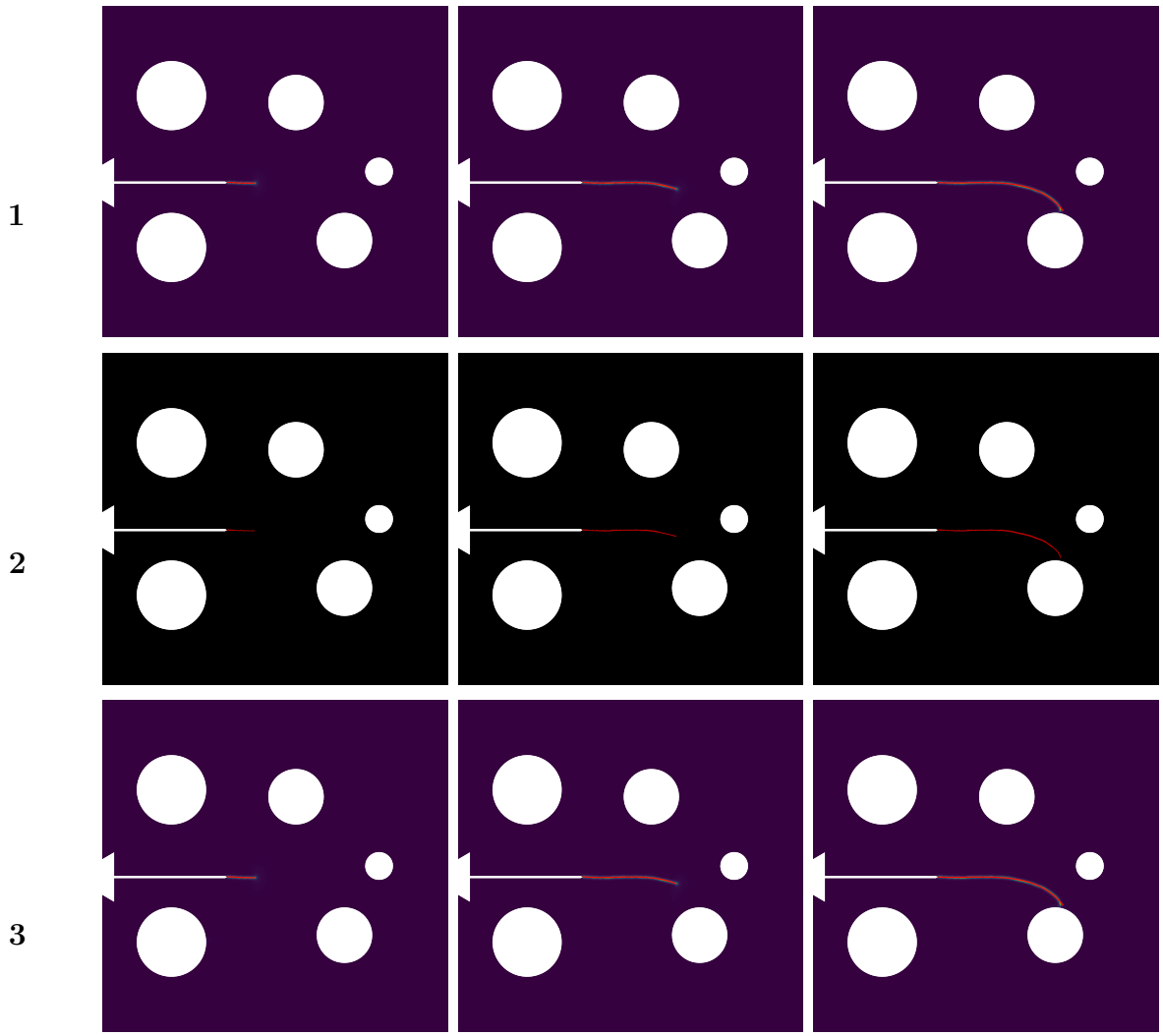

(a) $a = 3.94$ **mm** **(b)** $a = 13.58$ **mm** **(c)** $a = 19.07$ **mm**

Figure 3.1: Illustration of the automated crack length measurement procedure using image post-processing. The process is shown for three stages of crack growth (columns a, b, c). Row 1: The original phase-field solution (ϕ). Row 2: A binary image created by applying a threshold ($\phi > 0.95$) to isolate the cracked region. Row 3: The skeletonization algorithm extracts the crack's centerline from the binary image. A spline is fitted to the resulting points and overlaid on the original phase-field solution to visualize the measured crack path.

only to the crack length and not to the thickness, it follows that $a_{\text{phys}} = a_{\text{sim}}/\mathcal{F}$, and the correction factor remains unchanged regardless of the specimen thickness. Therefore, the derivative of compliance with respect to the physical crack area or crack length is:

$$\frac{\mathrm{d}C}{\mathrm{d}a_{\text{phys}}} = \frac{\mathrm{d}C}{\mathrm{d}a_{\text{sim}}}\frac{\mathrm{d}a_{\text{sim}}}{\mathrm{d}a_{\text{phys}}} = \frac{\mathrm{d}C}{\mathrm{d}a_{\text{sim}}}\mathcal{F} \ . \tag{3.38}$$

This direct computation approach does not require numerical differentiation, avoiding introducing the correction factor in the numerical derivative, and avoiding both the noise from the skeletonization-based crack measurements and the inherent inaccuracies of finite difference schemes.

It is important to note that when this term is corrected, Eq. (3.34) becomes physically inconsistent. Given that compliance does not require correction, it can be shown that both the force and displacement must be also corrected. This will be detailed in the following section, where the physical consistency of the correction factor application is discussed.

All quantities of interest are corrected by the factor $\mathcal{F}$, as summarized in Table 3.1. Note that, depending on the chosen methodology (e.g., the Bourdin or skeletonization-based approach), the correction factor $\mathcal{F}$ can be either a constant or a variable array affecting each simulation step differently.

Physical Quantity	**Transformation**
Crack Length	$a_{\text{phys}} = a_{\text{sim}}/\mathcal{F}$
Force	$P_{\text{phys}} = P_{\text{sim}}/\sqrt{\mathcal{F}}$
Displacement	$u_{\text{phys}} = u_{\text{sim}}/\sqrt{\mathcal{F}}$
Compliance Derivative	$\frac{\mathrm{d}C}{\mathrm{d}a_{\text{phys}}} = \frac{\mathrm{d}C}{\mathrm{d}a_{\text{sim}}} \cdot \mathcal{F}$
Compliance	$C_{\text{phys}} = C_{\text{sim}}$

Table 3.1: Transformations from simulated to physical quantities using the correction factor $\mathcal{F}$.

Physically consistent application of the correction factor

To clarify and align with alternative approaches addressing this phenomenon, it must be emphasized that the crack surface area is inherently overestimated by the phase-field approximation. This overestimation can also be interpreted as an effectively higher energy release rate. However, it is crucial to distinguish whether the crack surface is overestimated or the critical energy release rate is effectively higher than expected. Several considerations can be taken into account to correct all quantities of the phase-field fracture problem while satisfying the governing equations. In this context, three alternative, mathematically consistent schemes (**Scheme I**, **Scheme II**, and **Scheme III**) for transforming simulated results into physical quantities using the correction factor $\mathcal{F}$ are presented in Table 3.2. Each scheme applies the correction factor differently to the critical energy release rate, crack area, force, and displacement, while ensuring that the overall physical consistency of the model is maintained. Furthermore, the degraded strain energy, denoted as $\Psi(\boldsymbol{u}, \phi) = \int_\Omega g(\phi)\, \psi(\boldsymbol{\epsilon}(\boldsymbol{u}))\, \mathrm{d}\Omega$, and the specimen compliance are also considered. To illustrate these alternatives, consider the relationship for the critical energy release rate G_c, a fundamental material parameter in the PFF problem, defined as:

$$G_c = \frac{P^2}{2B}\frac{dC}{da}, \tag{3.39}$$

Using this definition, the relationship in Eq. (3.39) can be expressed for each scheme as follows:

- **Scheme I**: $G_c = \frac{(P/\sqrt{\mathcal{F}})^2}{2B}\left(\frac{\mathrm{d}C}{\mathrm{d}a} \cdot \mathcal{F}\right)$
- **Scheme II**: $G_c\mathcal{F} = \frac{(P\sqrt{\mathcal{F}})^2}{2B}\frac{\mathrm{d}C}{\mathrm{d}a}$

Physical Quantity	**Scheme I**	**Scheme II**	**Scheme III**
Critical energy release rate $G_{c,\text{phys}}$	$G_{c,\text{sim}}$	$G_{c,\text{sim}}\mathcal{F}$	$G_{c,\text{sim}}\mathcal{F}$
Crack length a_{phys}	$a_{\text{sim}}/\mathcal{F}$	a_{sim}	$a_{\text{sim}}/\mathcal{F}$
Force P_{phys}	$P_{\text{sim}}/\sqrt{\mathcal{F}}$	$P_{\text{sim}}\sqrt{\mathcal{F}}$	P_{sim}
Displacement u_{phys}	$u_{\text{sim}}/\sqrt{\mathcal{F}}$	$u_{\text{sim}}\sqrt{\mathcal{F}}$	u_{sim}
Compliance derivative $\frac{\mathrm{d}C}{\mathrm{d}a_{\text{phys}}}$	$\frac{\mathrm{d}C}{\mathrm{d}a_{\text{sim}}}\cdot\mathcal{F}$	$\frac{\mathrm{d}C}{\mathrm{d}a_{\text{sim}}}$	$\frac{\mathrm{d}C}{\mathrm{d}a_{\text{sim}}}\cdot\mathcal{F}$
Compliance C_{phys}	C_{sim}	C_{sim}	C_{sim}

Table 3.2: Three alternative mathematically consistent schemes (**Scheme I**, **Scheme II**, and **Scheme III**) for transforming simulated results into physical quantities using the correction factor $\mathcal{F}$. The scheme I is the one considered in this work, that refer to the presented table 3.1

- **Scheme III**: $G_c\mathcal{F} = \frac{P^2}{2B}\left(\frac{\mathrm{d}C}{\mathrm{d}a}\cdot\mathcal{F}\right)$

Simplifying these expressions shows that the fundamental relationship (3.39) is satisfied in all cases, confirming the thermodynamic consistency of the transformations. Another way to verify this aspect is by considering the dimensionless phase-field fracture scheme, where it can be shown that the PFF problem is defined by the Poisson's ratio ν and the dimensionless length scale parameter, as presented in [54].

As mentioned previously, the correction framework adopted in this work corresponds to **Scheme I**, motivated by the following considerations:

- The critical energy release rate G_c is an intrinsic material property; therefore, it should not be modified by a correction factor addressing a numerical artifact.
- Since the inaccuracy is directly related to the overestimation of the crack area, it is physically more intuitive to apply the correction to the crack length rather than the energy release rate.
- Force and displacement are global quantities that depend on the overall system response. Consequently, it is preferable to apply the correction only to the output quantities resulting from the simulations, rather than to the material input parameters, to accurately reflect the true physical behavior of the problem.
- In this manner, the exact physical parameter (the given G_c) is preserved, and the correction is systematically applied to the simulation outputs, namely the crack area, forces, and displacements.

However, it must be noted that all three cases are mathematically consistent. The choice of the correction scheme can ultimately depend on practical considerations, such as ease of implementation or the specific interpretability required for the results.

In the general literature, the correction is typically applied to G_c, which corresponds to **Scheme II** or **Scheme III**. However, this approach can lead to confusion, as modifying G_c can alter the force or the crack length, but not both simultaneously. Furthermore, the effect on displacement and the overall mathematical consistency of the system are rarely addressed. Concurrently correcting the force using **Scheme II** and the crack area using

Scheme III mixes assumptions and produces physically inconsistent results. For these reasons, the unambiguous methodology presented in **Scheme I** is preferred in this work.

3.6 Validation

In this section, different aspects involved in the proposed methodology will be analyzed and validated against closed form expressions and analytical results. For computational efficiency, several examples will take advantage of symmetry in the simulations. However, it is important to note that all graphs and theoretical solutions presented for comparison purposes will always refer to the complete model to ensure a clear and consistent validation.

3.6.1 Energy-controlled schemes validation

The proposed energy-controlled techniques are validated by comparing the variational and non-variational phase-field solvers with each other and with the analytical solution from LEFM for a classical three-point bending test. The simulations use identical material parameters, mesh resolution, and boundary conditions to ensure a direct and fair comparison.

The three-point bending specimen consists of a rectangular plate with a centrally located notch, supported at both ends, as shown in Figure 3.2(a).

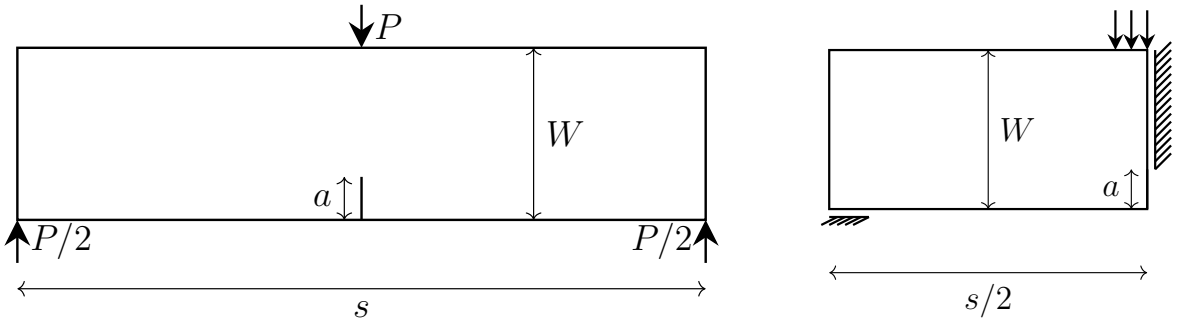

(a) Full specimen geometry

(b) Symmetric half-model

Figure 3.2: Geometry and boundary conditions for the three-point bending test. (a) Complete specimen geometry showing loads, supports, and dimensions. (b) Symmetric half-model with symmetry boundary conditions applied to the right edge.

According to LEFM theory [55], the SIF for a specimen with a span-to-width ratio of $s/W = 8$ is given by Eq. (3.1), where the geometric factor $f(a/W)$ is defined in Eq. (3.40) with an accuracy of 0.2% for $a/W \leq 0.6$.

$$f(a/W) = \frac{3\sqrt{\pi}(s/W)\sqrt{a/W}}{2} \times \left[1.106 - 1.552\left(\frac{a}{W}\right) + 7.71\left(\frac{a}{W}\right)^2 - 13.53\left(\frac{a}{W}\right)^3 + 14.23\left(\frac{a}{W}\right)^4\right] \tag{3.40}$$

The specimen's compliance, $C(a)$, can be determined by combining Eqs. (3.6) and (3.7). Integrating the resulting expression with respect to the crack length yields the compliance

for a specimen of thickness B:

$$C(a) = \frac{C_{a_0}}{B}\left[1 + \frac{1}{C_{a_0}}\frac{2}{E'BW}\int_{a_0}^{a}\left[f\left(\frac{a}{W}\right)\right]^2 da\right], \tag{3.41}$$

where C_{a_0} is the initial compliance per unit thickness, for a crack length a_0 and a specimen under plane strain conditions and unit thickness $B = 1\,\text{mm}$. In the case of an uncracked specimen ($a_0 = 0\,\text{mm}$), the initial compliance can be calculated using beam theory as

$$C_0 = \frac{s^3}{48E'I}, \tag{3.42}$$

where $I = BW^3/12$ is the area moment of inertia of the beam's cross-section.

The critical force P_c that the specimen can withstand before fracture can be determined either from the critical SIF K_{Ic} using Eq. (3.2) or from the critical energy release rate considering G_c in the Eq. (3.8). With the compliance $C(a)$ and critical force $P_c(a)$ known, the full force-displacement equilibrium path, including snap-back, can be constructed. The force-displacement curve initially follows a linear behavior governed by the compliance $C(a_0)$ until the critical force $P_c(a_0)$ is reached. Subsequently, the system follows the equilibrium path defined by $u(a) = C(a)P_c(a)$ as the crack propagates.

For the numerical validation, a specimen with a span of $s = 8.0$ mm, a width of $W = 1.0$ mm, and a thickness of $B = 1.0$ mm was modeled, matching the $s/W = 8$ ratio. Figure 3.2(b) shows the symmetric half-model used to improve computational efficiency. The boundary conditions consist of a fixed vertical displacement over a small area ($A_{\text{surface}} = 0.075$ mm^2) at the lower-left support and an applied downward vertical force over an equal area at the top center. The symmetry plane is constrained horizontally. Although a contact problem for the support must be considered to perfectly match the problem with the analytical solution, this configuration provides a good approximation due to the large span-to-width ratio, and the initial stiffness of the FEM model matches the analytical solution, due to the specific surface value considered. For other configurations, the initial compliance from the FEM model should be used for accurate comparison.

All simulations were performed with an initial crack of $a_0 = 0.2$ mm on a regular 400×100 grid of square elements with a size of $h = 0.01$ mm. The material properties were set to $G_c = 0.0005$ kN/mm, $E = 20.8$ kN/mm^2, and $\nu = 0.3$. The phase-field length scale was $l = 0.03$ mm, resulting in a ratio of $l/h = 3$. The applied traction vector was $\boldsymbol{t} = (0, -1/A_{\text{surface}})$. For the variational solver, the control parameters were $c_1 = 35.0$ kN/mm and $c_2 = 1.0$, while for the non-variational solver, they were $c_1 = 1.0$ kN/mm and $c_2 = 1.0$. An initial $\Delta\tau = 0.001$ kN·mm was used for both solvers.

For the variational solver, the resulting force-displacement and Lagrange multiplier-displacement curves are shown in Figures 3.3(a) and 3.3(b), respectively. It should be noted that this solution does not correspond to a constant G_c, as equilibrium is achieved by modifying the effective critical energy release rate, as explained in Section 3.4.1. To recover the solution for a constant G_c, Eqs. (3.21) and (3.22) must be applied.

Figure 3.4(a) compares the force-displacement curves from both solvers with the LEFM solution. The non-variational solver directly computes the physical response for a constant G_c, while the variational solver's output yields identical results after applying the

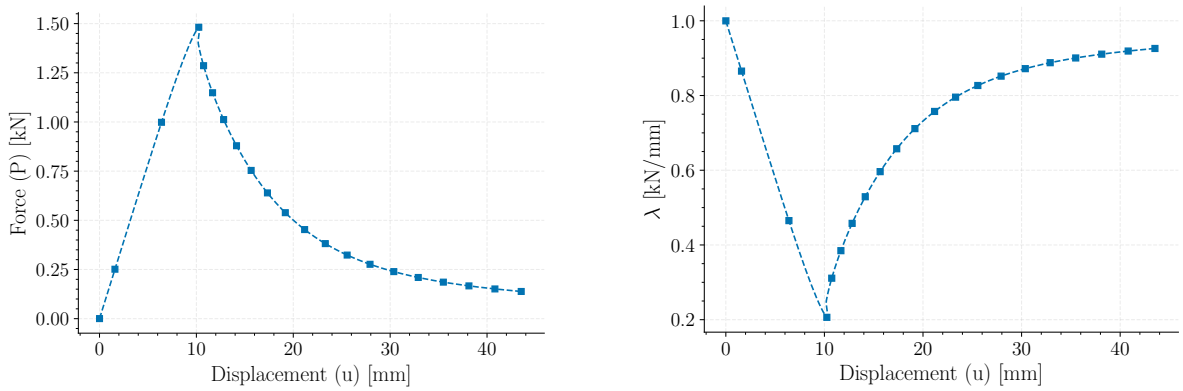

(a) Force-displacement response

(b) Lagrange multiplier evolution

Figure 3.3: Results from the variational energy-controlled solver for the three-point bending test: (a) force-displacement curve; (b) evolution of the Lagrange multiplier with displacement.

necessary correction. Both solvers show excellent agreement with each other, confirming their equivalence. However, the simulated peak force for the phase-field solvers is higher than the LEFM prediction. This is a known artifact attributed to the diffuse crack representation in phase-field models, which leads to an effective overestimation of crack area, as explained in Section 3.5.2.

To address this, the scaling relationships from Section 3.5.2 are applied using the correction factor $\mathcal{F} = 1 + 2h/(2l)$ from [1]. The factor of 2 multiplying the element size h accounts for the symmetry boundary condition used in the simulation, as referenced in [16]. As shown in Figure 3.4(b), applying this correction to the force and displacement, brings the force-displacement curves into close agreement with the analytical LEFM solution. Furthermore, the evolution of the phase-field variable during the simulation is depicted in Figure 3.5, illustrating the progressive damage localization and crack growth.

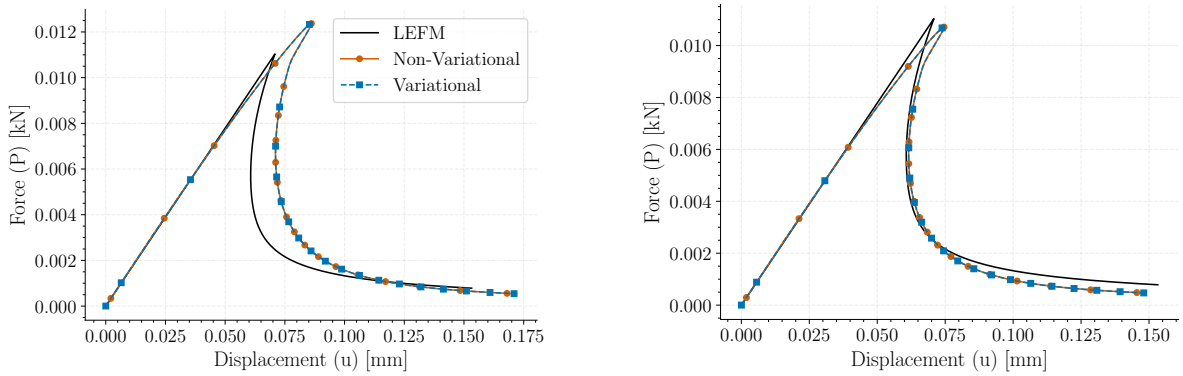

(a) Force–displacement curves for both solvers compared with LEFM theory.

(b) Corrected force–displacement curves showing improved agreement with LEFM.

Figure 3.4: Comparison of the phase-field solvers with LEFM theory for the three-point bending test. (a) Original results from the energy-controlled solvers. (b) Corrected methodology showing improved agreement with LEFM predictions.

In summary, this benchmark demonstrates that both energy-controlled schemes are equivalent and capable of robustly tracing the complete equilibrium path, including snap-back

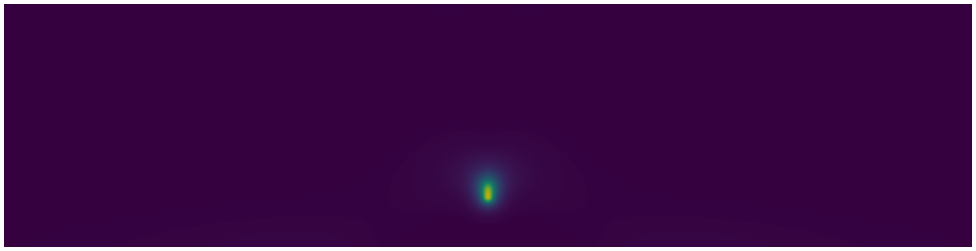

(a) Phase-field distribution at $a = 0.2807$ mm

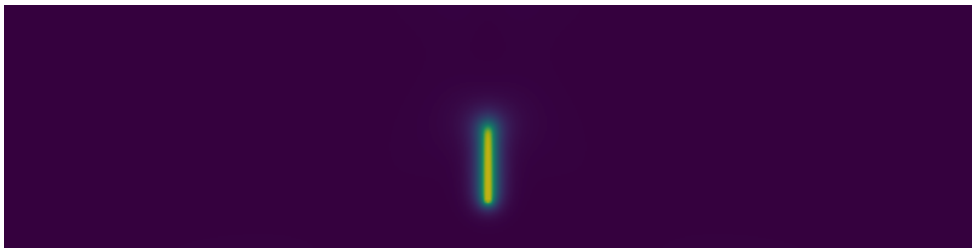

(b) Phase-field distribution at $a = 0.5163$ mm

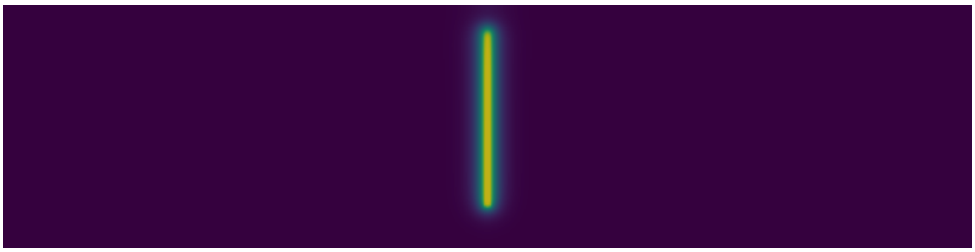

(c) Phase-field distribution at $a = 0.9366$ mm

Figure 3.5: Evolution of the phase-field variable ϕ during crack propagation in the three-point bending test. The sequence shows progressive damage localization and crack growth: (a) initial crack extension at $a = 0.2807$ mm, (b) intermediate stage at $a = 0.5163$ mm, and (c) advanced crack propagation at $a = 0.9366$ mm. The measurements are obtained by applying the Bourdin correction factor to account for overestimation in the crack length. The phase-field approach successfully captures crack initiation, propagation, and damage localization without explicit crack tracking.

behavior. The validation confirms the accuracy of the proposed methodology and its potential for reliable fracture analysis, if the overestimation of the crack length and the critical energy release rate are taken properly into account.

3.6.2 Validation of fatigue crack propagation: the center cracked test specimen

This section evaluates the method's ability to predict the critical force and fatigue life for a center-cracked tension specimen. Similar to the three-point bending test, this example is particularly relevant because the crack path and geometric factor are well-known, allowing for a direct comparison with analytical solutions. First, the analytical LEFM solution is presented. Subsequently, to validate the LEFM solution numerically, a series of pure linear elastic simulations are performed by explicitly defining the crack in the mesh. Finally, a comprehensive analysis of the phase-field method is conducted. This includes investigating

the influence of the length scale parameter l, the resulting compliance, and the correction factor used to address the overestimation of crack length. A fatigue analysis is then performed using Paris' law to demonstrate the framework's ability to predict fatigue life.

The center-cracked tension specimen, shown in Figure 3.6(a), is a rectangular plate with a centrally located crack subjected to uniform tensile loading. The specimen has a total width of $2W = 2.0\,\text{mm}$, a total height of $2H = 6.0\,\text{mm}$, and an initial crack of total length $2a$. According to [55], for the chosen aspect ratio of $H/W = 3$, the plate can be approximated as an infinite strip, which implies that the test yields equivalent results under both force- and displacement-controlled loading. The material properties are provided in Table 3.3.

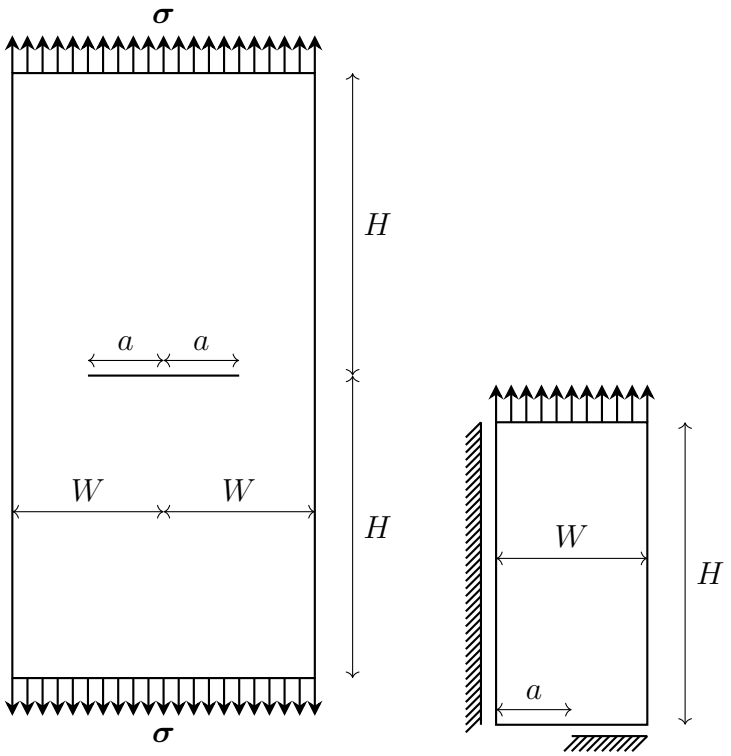

(a) Center-cracked tension specimen geometry and loading.

(b) Quarter-symmetry FEM model with boundary conditions.

Figure 3.6: Schematic of the center-cracked tension test specimen. (a) Full geometry, showing dimensions and loading configuration. (b) Quarter-symmetry finite element model, illustrating the applied boundary conditions for efficient simulation.

According to LEFM theory [55], the SIF for this specimen is given by Eq. (3.1), where the geometric factor $f(a/W)$ is given in Eq. (3.43). This expression provides an accuracy within 0.1% for any value of a/W.

$$f(a/W) = \sqrt{\frac{\pi a}{4W}\sec\left(\frac{\pi a}{2W}\right)}\left[1.0 - 0.025\left(\frac{a}{W}\right)^2 + 0.06\left(\frac{a}{W}\right)^4\right] \tag{3.43}$$

From this expression, the critical force P_c required for fracture can be determined by

Parameter	**Value**	**Units**
Young's Modulus (E)	210	$\mathrm{kN/mm^2}$
Poisson's Ratio (ν)	0.3	–
Critical Energy Release Rate (G_c)	0.0027	kN/mm
Paris Exponent (n)	2.5	–
Fatigue Constant (C_{Paris})	10^{-9}	$\frac{mm^{\frac{2+3n}{2}}}{cycle\ kN^n}$

Table 3.3: Material parameters for the center-cracked tension test specimen.

combining Eq. (3.7) and the critical SIF K_{Ic}:

$$P_c = \frac{B\sqrt{W}\sqrt{E'G_c}}{f(a/W)}. \tag{3.44}$$

Additionally, the specimen's compliance can be obtained by integrating the relationship between the energy release rate and the compliance derivative (Eqs. (3.6) and (3.7)):

$$C(a) = \frac{C_{a_0}}{B}\left[1 + \frac{1}{C_{a_0}}\frac{4}{E'BW}\int_{a_0}^{a}\left[f\left(\frac{a}{W}\right)\right]^2 da\right], \tag{3.45}$$

where C_{a_0} is the initial compliance per unit thickness, for a crack length a_0 and a specimen under plane strain conditions and unit thickness $B = 1\,\mathrm{mm}$. For an uncracked specimen ($a_0 = 0\,\mathrm{mm}$), the initial compliance is given by the theoretical expression $C_0 = \frac{H}{E'W}$.

By knowing the compliance $C(a)$ and critical force $P_c(a)$ as functions of crack length, the force-displacement equilibrium path ($G = G_c$) can be constructed for any initial crack length. Figure 3.7(a) shows the force-displacement response calculated with LEFM theory for different initial crack lengths. While a larger initial crack reduces specimen stiffness, the equilibrium paths converge to a single trajectory once propagation begins. Figure 3.7(b) illustrates the effect of the critical energy release rate, G_c, for a fixed initial crack length of $a_0 = 0.5$ mm. As detailed in section 3.3, a higher G_c increases the critical force but does not alter the post-peak curve, since stiffness is independent of fracture toughness.

FEM elasticity validation

To assess the validity of the LEFM expressions of stiffness and critical force in the case considered here, these values were compared with the results of an elastic finite element model of the specimen under both force- and displacement-controlled loading. The quarter-symmetry model shown in Figure 3.6(b) was used to improve computational efficiency. The crack was explicitly defined in the mesh, and appropriate boundary conditions were applied as shown in Figure 3.8: the bottom edge was constrained in the vertical direction, except for the region representing the initial crack, while the left edge was fixed in the horizontal direction to enforce symmetry. Simulations were performed for crack lengths ranging from $a = 0.0$ to $0.95\,\mathrm{mm}$. The mesh consisted of quadrilateral elements with a size of $h = 0.005\,\mathrm{mm}$.

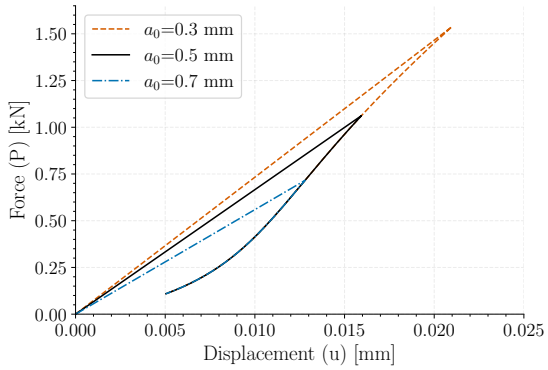

(a) Effect of initial crack length a_0 on force-displacement response.

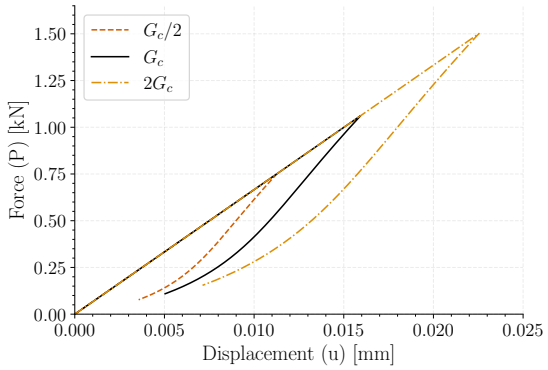

(b) Effect of critical energy release rate G_c on force-displacement response.

Figure 3.7: LEFM analytical force-displacement curves for the center-cracked specimen. (a) Shows that a larger initial crack length a_0 leads to lower initial stiffness, but the equilibrium paths converge upon crack propagation. (b) Illustrates that a higher G_c increases the peak force but does not affect the specimen's stiffness.

It is instructive to relate this elastic analysis to the general variational formulation of fracture (see Eq. (2.1)). The boundary value problem solved here effectively minimizes the same total potential energy functional, but with a fundamental distinction: the discontinuity set Γ_{sharp} is not an unknown to be determined. Instead, the crack geometry is explicitly imposed as a fixed boundary within the domain. Consequently, the problem reduces to minimizing the elastic potential energy for a predetermined crack configuration.

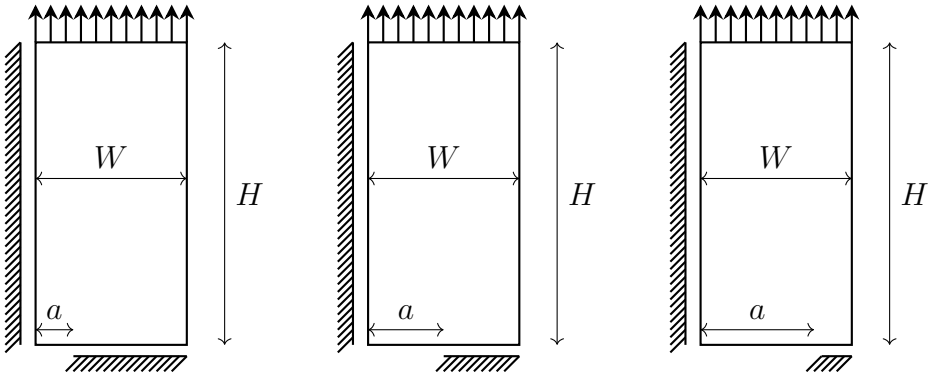

(a) $a = 0.25$ mm (b) $a = 0.5$ mm (c) $a = 0.75$ mm

Figure 3.8: Quarter-symmetry finite element models used to improve computational efficiency. Symmetry boundary conditions are applied along the left and bottom edges. By systematically varying the crack length a, the specimen structural compliance $C(a)$ is determined. The subfigures illustrate the model setup and boundary condition evolution for three distinct crack lengths.

Figure 3.9(a) compares the specimen stiffness as a function of crack length from FEM simulations (under both force and displacement control) with the LEFM analytical solution. Figure 3.9(b) shows the corresponding critical force. For the FEM results, the compliance derivative, dC/da, was obtained by numerical differentiation. The excellent

agreement between the numerical and analytical predictions for both stiffness and critical force confirms the reliability of the FEM approach.

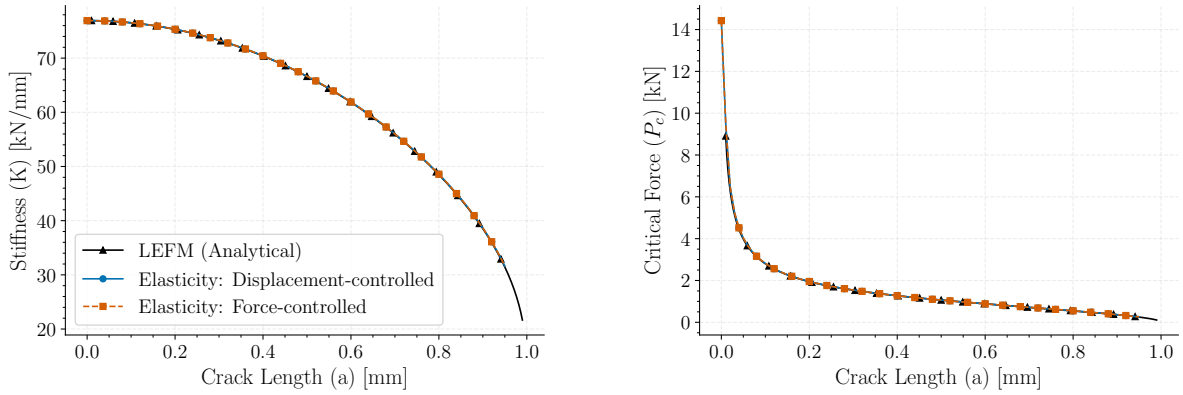

(a) Stiffness vs. crack length.

(b) Critical force vs. crack length.

Figure 3.9: Validation of stiffness and critical force for the center-cracked specimen. The results from both displacement- and force-controlled FEM simulations show excellent agreement with the analytical LEFM solutions, confirming the accuracy of the numerical model.

PPF: length scale influence

Next, the phase-field approach is applied to the center-cracked specimen to investigate the influence of the length scale parameter l and the initial crack length a_0. A series of simulations were performed with three initial crack lengths ($a_0 = 0.3, 0.5, 0.7$ mm) and two length scale parameters ($l_1 = 0.025$ mm and $l_2 = 0.0025$ mm), as summarized in Table 3.4. The material properties are identical to those in the LEFM analysis (Table 3.3).

The mesh size h was refined proportionally to the length scale parameter l, ensuring a consistent resolution ratio of $l/h = 2.5$ across all simulations.

Simulation	**Initial Crack Length (a_0)**	**Length Scale (l)**	**Mesh Size (h)**
1	0.3 mm	0.025 mm	0.01 mm
2	0.3 mm	0.0025 mm	0.001 mm
3	0.5 mm	0.025 mm	0.01 mm
4	0.5 mm	0.0025 mm	0.001 mm
5	0.7 mm	0.025 mm	0.01 mm
6	0.7 mm	0.0025 mm	0.001 mm

Table 3.4: PFF simulations for the center-cracked tension test specimen. Three different initial crack lengths are considered, each with two different length scale parameters. The mesh size is refined proportionally to the length scale parameter to ensure accurate resolution of the diffuse crack interface.

Figure 3.10(a) and Figure 3.10(b) show the force-displacement curves for the larger (l_1) and smaller (l_2) length scales, respectively. For a given length scale, the equilibrium

paths converge after sufficient crack propagation, becoming independent of the initial crack length a_0. It is also observed that simulations with a smaller length scale parameter (l_2) yield a higher peak force. Additionally, Figure 3.11 depicts the evolution of the crack phase-field variable at different stages of propagation for simulation 1 referenced in Table 3.4.

Furthermore, for the larger length scale (l_1), the initial part of the force-displacement curve deviates from the linear elastic response, indicating damage initiation before the peak load. This effect is diminished for the smaller length scale (l_2), which aligns more closely with the expected elastic behavior.

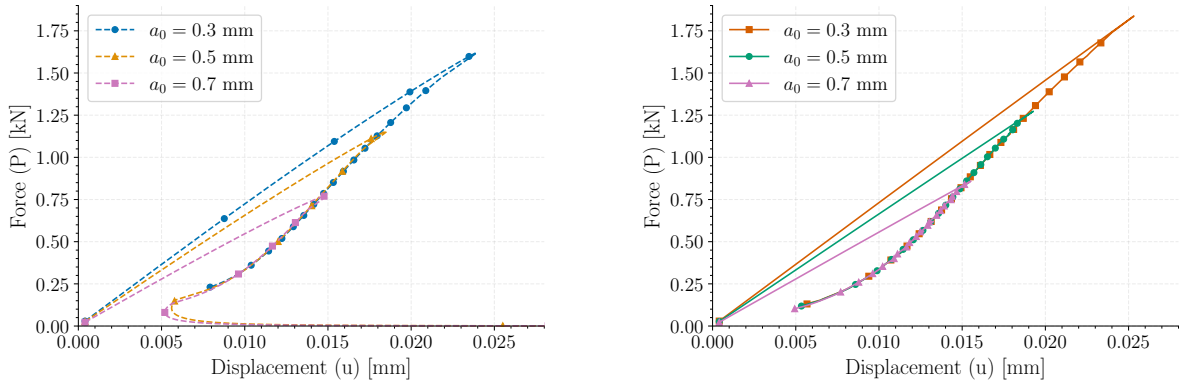

(a) Length scale $l_1 = 0.025$ mm.

(b) Length scale $l_2 = 0.0025$ mm.

Figure 3.10: Force-displacement curves for three initial crack lengths under two phase-field length scales: (a) $l_1 = 0.025$ mm and (b) $l_2 = 0.0025$ mm. For each length scale, the curves converge after crack propagation, indicating that the equilibrium path becomes independent of the initial crack length.

PFF: correction factor and length scale effect

To facilitate a direct and faithful comparison with the LEFM solution, the results from the phase-field simulations have been adjusted. As detailed in Section 3.5.2, raw phase-field models tend to overestimate the critical force. To counteract this, a constant Bourdin correction factor has been applied to the simulated force and displacement values. This straightforward scaling brings the numerical results into much closer alignment with the analytical predictions.

Figures 3.12(a) and 3.12(b) show the corrected force-displacement and stiffness-displacement curves, respectively, for an initial crack of $a_0 = 0.3$ mm, comparing two length scales ($l_1 > l_2$) against the LEFM solution. The corrected force-displacement curves show excellent agreement with LEFM. However, the stiffness plots reveal that the phase-field simulations still exhibit a gradual reduction prior to fracture, a sign of premature damage accumulation not present in the ideal LEFM case. This effect is more pronounced for the larger length scale (l_1), confirming that the simulation with the smaller length scale (l_2) more accurately captures the expected linear elastic behavior.

A critical aspect of the analysis is the measurement of crack length and its impact on key fracture metrics. To evaluate this, the analytical LEFM solution is compared with phase-field results (for a simulation with $a_0 = 0.3$ mm and $l = 0.0025$ mm) using three

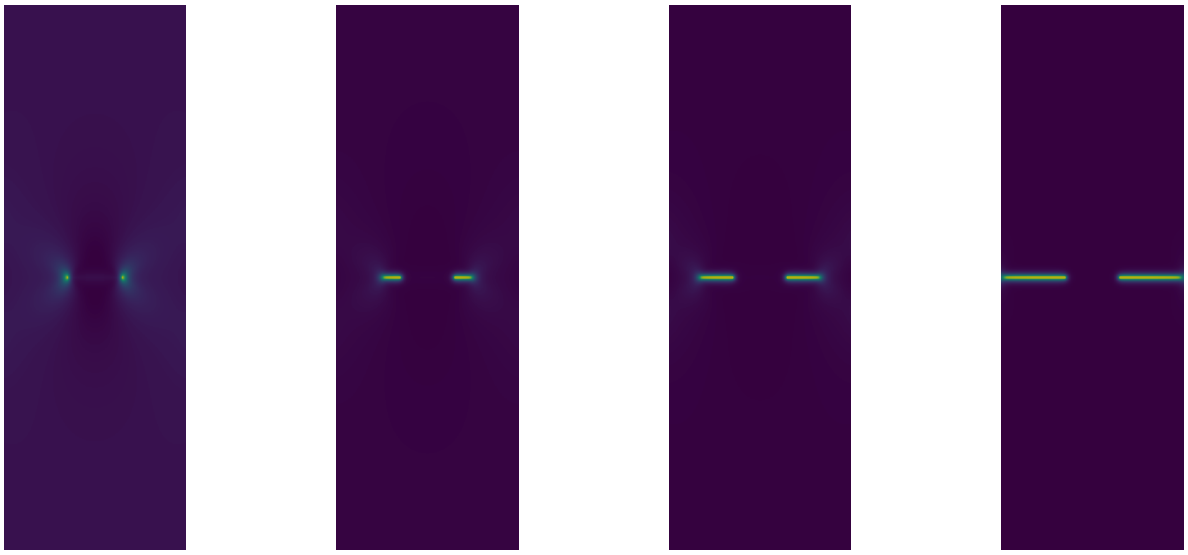

(a) Phase-field distribution at $a = 0.3843\,\text{mm}$

(b) Phase-field distribution at $a = 0.5602\,\text{mm}$

(c) Phase-field distribution at $a = 0.7341148\,\text{mm}$

(d) Phase-field distribution at $a = 1.0372\,\text{mm}$

Figure 3.11: Evolution of the phase-field variable ϕ for the center-cracked specimen at different stages of crack propagation. The sequence shows progressive damage localization and crack growth. The phase-field approach successfully captures crack initiation, propagation, and damage localization without explicit crack tracking.

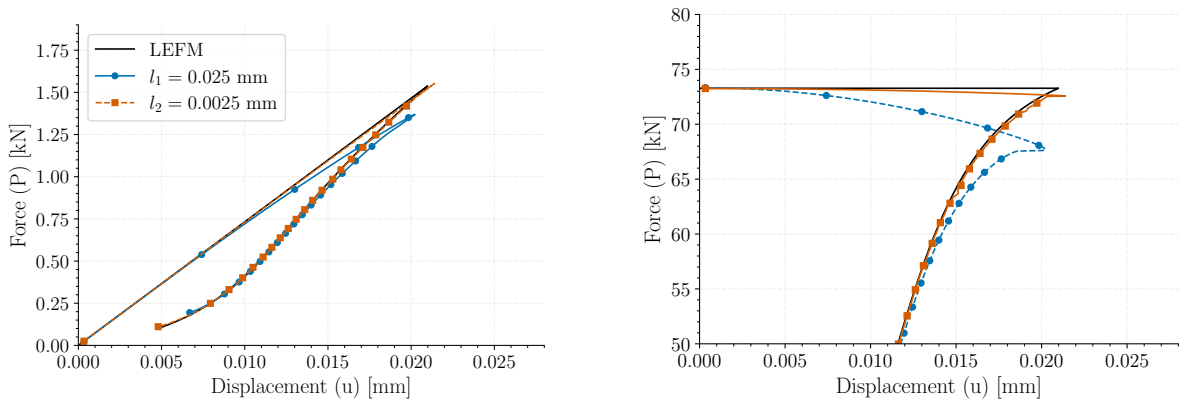

(a) Force vs. displacement.

(b) Stiffness vs. displacement.

Figure 3.12: Comparison of force-displacement (a) and stiffness-displacement (b) curves for an initial crack of $a_0 = 0.3$ mm. The results for two phase-field length scales are compared with the LEFM solution. The simulation with the smaller length scale (l_2) shows better agreement with the linear elastic behavior predicted by LEFM. The Bourdin correction has been applied to the phase-field results.

different crack length definitions: direct integration of the crack surface density function $\gamma(\phi, \nabla\phi)$, the Bourdin correction, and the skeletonization measurement technique.

Figure 3.13(a) illustrates the resulting relationship between stiffness and crack length, while Figure 3.13(b) shows the corresponding critical force. Together, these figures demonstrate the performance of each correction method in aligning the phase-field predictions

with the analytical solution.

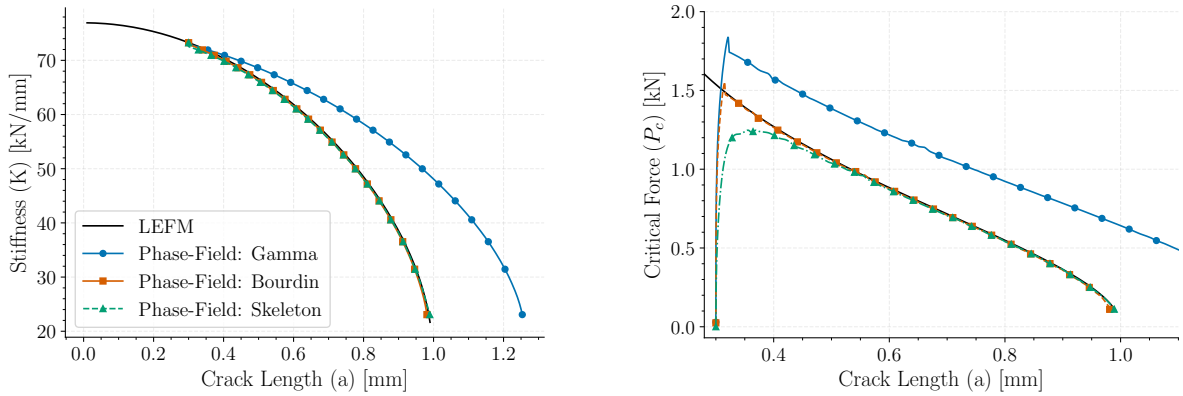

(a) Stiffness vs. crack length.

(b) Critical force vs. crack length.

Figure 3.13: Validation of stiffness and critical force for the center-cracked specimen. The results from both displacement- and force-controlled FEM simulations show excellent agreement with the analytical LEFM solutions, confirming the accuracy of the numerical model.

Fatigue life prediction

A fatigue analysis was conducted to predict the crack propagation life of the center-cracked specimen. The analysis employed the Paris' law parameters specified in Table 3.3 and subjected the specimen to a cyclic load range of $\Delta P = 33$ kN (from $P_{\min} = 0$ kN to $P_{\max} = 33$ kN). The simulation tracked crack growth from an initial length of $a = 0.4$ mm until complete failure.

Figure 3.14 presents the results, plotting the number of cycles to failure against the corresponding crack length. The figure provides a comprehensive comparison of fatigue life predictions obtained from various approaches. It includes the phase-field simulation results with $l = 0.0025$ mm and $a_0 = 0.3$ mm (referring to simulation 2 in Table 3.4), considering the fatigue analysis starting from $a = 0.4$ mm. The results are shown for crack lengths measured directly via the integration of $\gamma(\phi, \nabla\phi)$, those corrected using the Bourdin gamma correction, and those adjusted with the skeleton correction. Additionally, the figure displays the results from the elasticity FEM analysis under force controlled conditions, where the crack was explicitly imposed through boundary conditions as explained in 3.6.2, and the predictions derived from the analytical LEFM solution. This comparative assessment highlights the accuracy and differences among the methods.

The results indicate that the FEM simulation with an explicit crack representation in the mesh geometry aligns most closely with the LEFM reference solution. This suggests that the most accurate predictions from the phase-field model are achieved when its behavior approaches that of the pure elastic case. Notably, without applying a correction for the inherent overestimation of crack length in the phase-field model, the predicted number of cycles is significantly overestimated. However, when correction factors derived from skeletonization or Bourdin's method are applied, the phase-field predictions show excellent agreement with the theoretical solution, validating the approach proposed in the case of a straight crack path.

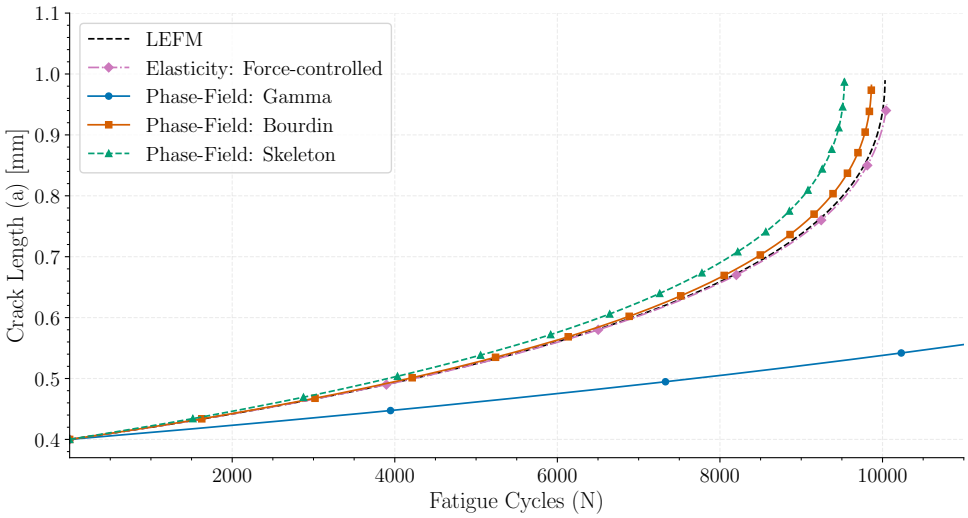

Figure 3.14: Comparison of fatigue life predictions for the center-cracked specimen. The plot shows the number of cycles to failure as a function of crack length, comparing the phase-field model (with and without correction), the elastic simulation, and the analytical LEFM solution.

Extraction of the geometric factor from the compliance derivative

It is worth noting that once the compliance derivative dC/da is obtained from the phase-field simulations, the geometry factor $f(a/W)$ can be calculated using the relationship between the energy release rate and the compliance derivative (Eqs. (3.6) and (3.7)). This allows for a direct comparison of the geometry factor derived from the phase-field model with the analytical expression given in Eq. (3.43). Such a comparison serves as an additional validation of the ability of the phase-field approach to capture the correct fracture mechanics behavior of this specific specimen.

Figure 3.15 presents the geometric factor calculated from the LEFM analytical expression (Eq. (3.43)) alongside the values obtained from phase-field simulations. These results correspond to the simulations using the smallest length scale parameter (l_2) with three different initial crack lengths, as detailed in Table 3.4 and previously shown in Figure 3.10(b). It can be observed that the results from simulations with different initial crack lengths collapse onto a single curve as the crack propagates. Specifically, the curve corresponding to a smaller initial crack length perfectly aligns with that of a larger initial crack as soon as the propagating crack reaches the larger initial size. Moreover, all three numerical curves exhibit excellent agreement with the theoretical LEFM result. The initial deviation, where the value starts from infinity, is due to the initial loading phase and the transition from the initial diffuse crack topology. These results demonstrate that the phase-field model accurately captures the geometry factor throughout the crack propagation process, further validating the proposed framework.

Displacement-controlled scheme

To further demonstrate the advantages of the energy-controlled approach, Simulation 3, as detailed in Table 3.4, was repeated using a standard displacement-controlled scheme. This comparison employed a staggered solver with a residual convergence criterion (refer to Section 2.6.3) set to a tolerance of 10^{-10}.

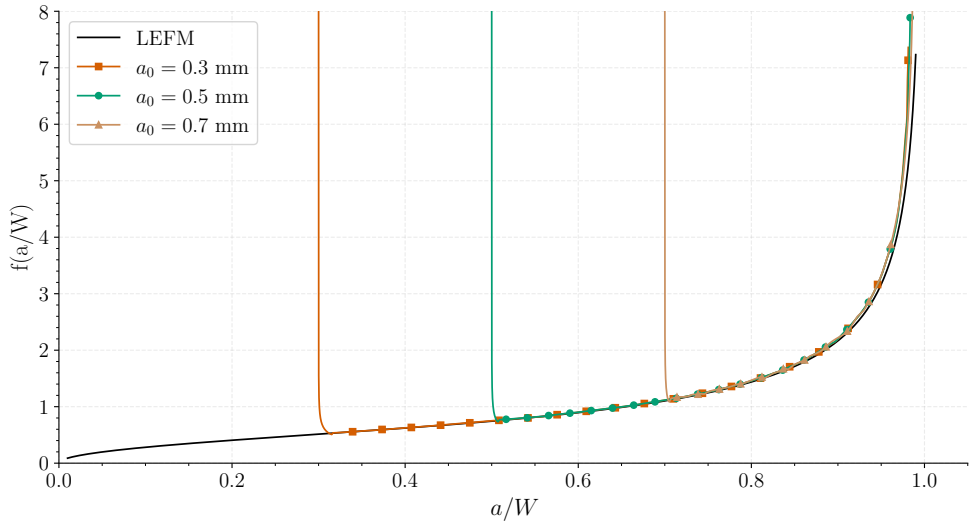

Figure 3.15: Evolution of the geometry factor $f(a/W)$ for the center-cracked specimen as a function of crack length. The curves derived from phase-field simulations with different initial crack lengths match the analytical LEFM solution perfectly.

Figure 3.16(a) presents the resulting force-displacement curves. Theoretically, for this specific specimen geometry, force- and displacement-controlled conditions yield equivalent results up to the point of instability. Consequently, the curves coincide perfectly until the peak load is reached. However, beyond this point, the energy-controlled solver successfully traces the unstable equilibrium path, capturing the complete softening branch and the snap-back behavior essential for accurate fracture characterization. In contrast, the displacement-controlled scheme fails to capture the post-peak response, snapping directly to failure because it cannot track equilibrium paths where a decrease in displacement is required to maintain stability.

Figure 3.16(b) illustrates the evolution of the crack area, Γ, as a function of displacement (note that without a correction factor, the normalized crack length exceeds unity due to the overestimation inherent in the diffuse interface approximation). While the energy-controlled scheme captures a progressive and smooth evolution of the crack area, the displacement-controlled simulation exhibits a sudden, discontinuous jump. These results underscore the necessity of employing an energy-controlled scheme to robustly capture the entire crack propagation process, particularly in the presence of structural instabilities such as snap-back.

3.7 Results and validation on complex geometries

This section aims to evaluate the capability of the proposed methodology to predict fatigue life in complex scenarios with unknown crack paths. To this aim modified compact tension (CT) specimens with different initial cracks and containing internal voids are analyzed, serving as a challenging benchmark due to their geometric complexity and non-trivial crack propagation. The results of the proposed modeling approach for curvilinear paths will be compared with the results of the experimental campaign performed by [56, 57] on the same modified CT specimens.

The specimen geometry is based on the ASTM-E647 standard and modified by introduc-

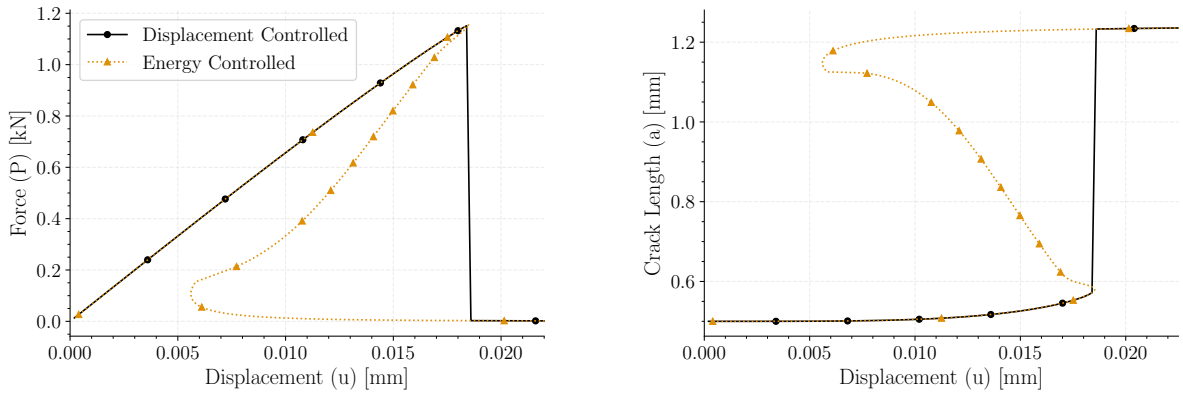

(a) Force vs. displacement.

(b) Crack area (Γ) vs. displacement.

Figure 3.16: Comparison between displacement-controlled and energy-controlled schemes for the center-cracked specimen. (a) Force-displacement curves show that the displacement-controlled solver fails to capture the snap-back instability. (b) The crack area evolution demonstrates the smooth propagation captured by the energy-controlled solver versus the sudden failure in the displacement-controlled case.

ing three additional circular holes and varying the initial crack tip position, denoted by the parameter H. The overall geometry is illustrated in Figure 3.17. All dimensions, proportional to the specimen width $W = 40$ mm, are listed in Table 3.5. The material is a Haynes 230 nickel-based superalloy and the properties used for this material are given in Table 3.7. Among these values, the elastic parameters E and ν were characterized in the publications of the experimental campaign [56, 57]. In contrast, fatigue related parameters were not reported and are taken from literature or estimated. The Paris' law exponent is assumed to be independent of the particular material condition and is taken from [58]. On the other hand, the prefactor has been adjusted so that the fatigue life of a simple specimen approximately matches the lifetimes reported in [56, 57]. It is important to note that the value obtained is in the order of magnitude of the ones provided in other studies [58]. Finally, the critical energy release rate (G_c) is obtained from [59], although this parameter does not influence the fatigue life predictions in the proposed framework.

The geometric complexity, particularly the additional holes, induces curvilinear crack growth, posing a significant challenge for traditional fracture models. In contrast, the phase-field method is well-suited to this problem, as it naturally predicts complex crack trajectories without remeshing. This study investigates the influence of the initial crack position through a parametric analysis of multiple configurations, each with a different value of H, as specified in Table 3.6. The proposed energy-controlled approach enables the direct computation of the rate of change of the compliance with respect to crack length, $\mathrm{d}C/\mathrm{d}a$, providing the necessary inputs for the subsequent fatigue life analysis using Paris' law. The objective is to demonstrate the model's ability to capture how small variations in geometry can significantly alter crack paths and fatigue life predictions.

Once the compliance-crack length relationship is established for each specimen, the fatigue life is predicted by integrating Paris' law. For the standard compact tension specimen (without holes), the analytical LEFM solution is used as a reference, since closed-form expressions for the geometry factor and compliance are available. For the modified specimens with additional holes—where analytical solutions are not possible due to the complex

crack paths—the fatigue life predictions from the numerical phase-field simulations are directly compared with experimental data reported in [57].

To ensure a meaningful comparison with the experimental data, the numerical fatigue analysis meticulously replicates the experimental loading protocol. The experiments involved first the generation of an initial pre-crack of approximately 3.5 mm, followed by a fatigue test where the SIF range increased exponentially. Following the ASTM-E647 standard, the variable-amplitude loading is defined by:

$$\Delta K(a) = (1-R)K_0 e^{\theta(a-a_i)} \tag{3.46}$$

where the initial SIF is $K_0 = 0.474$ kN/mm$^{3/2}$, the load ratio is $R = 0.1$, the scaling parameter is $\theta = 0.04$ mm^{-1}, and a_i is the initial crack length including the pre-crack.

Since the standard fatigue life calculation (Eq. (3.10)) was derived for constant amplitude loading, it must be adapted to the variable loading applied here. The resulting expression for the number of cycles to failure, N_f, is given by:

$$N_f = N_i + \frac{1}{C_{\text{Paris}}(E'/(2B))^{n/2}((1-R)P_0)^n} \int_{a_i}^{a_f} \frac{\mathrm{d}a}{(\mathrm{d}C/\mathrm{d}a)^{n/2}\, e^{n\theta(a-a_i)}}. \tag{3.47}$$

Here, the initial force, P_0, is calculated from the initial SIF, K_0, by first converting it to the energy release rate, G, using Eq. (3.7), and then applying Eq. (3.8). This calculation uses the compliance derivative, $\mathrm{d}C_i/\mathrm{d}a_i$, corresponding to the initial crack length, a_i, which includes the pre-crack. The fatigue analysis employs the Paris law constant, C_{Paris}, and exponent, n, from Table 3.7. It is important to note that while the load ratio, R, influences the crack growth rate, the crack path is primarily determined by the stress state at peak load.

3.7.1 Standard compact tension test specimen

First, as a baseline for comparison, the standard CT specimen without additional holes is analyzed. This corresponds to Specimen 1 in Table 3.6, where the initial crack is centered ($H = L$), resulting in a symmetric configuration. For this case, the theoretical crack path is straight, and an analytical expression for the geometry factor $f(a/W)$ is available in the literature [55, 60]. The SIF is given by Eq. (3.1), with the geometry factor for the standard CT specimen defined as:

$$f(a/W) = \frac{2+\frac{a}{W}}{\left(1-\frac{a}{W}\right)^{\frac{3}{2}}}\left[0.886 + 4.64\left(\frac{a}{W}\right) - 13.32\left(\frac{a}{W}\right)^2 + 14.72\left(\frac{a}{W}\right)^3 - 5.60\left(\frac{a}{W}\right)^4\right] \tag{3.48}$$

which is accurate to within 0.5% for $a/W > 0.2$.

Following the approach from the previous section, the specimen's compliance is obtained using LEFM with the expression:

$$C(a) = \frac{C_{a_0}}{B}\left[1 + \frac{1}{C_{a_0}}\frac{2}{E'W}\int_{a_0}^{a}\left[f\left(\frac{a}{W}\right)\right]^2 da\right], \tag{3.49}$$

where C_{a_0} is the initial compliance per unit thickness, for a crack length a_0 and a specimen under plane strain conditions and unit thickness $B = 1$ mm. Since an analytical expression for C_{a_0} is not available, it is calculated numerically via an elastic finite element analysis.

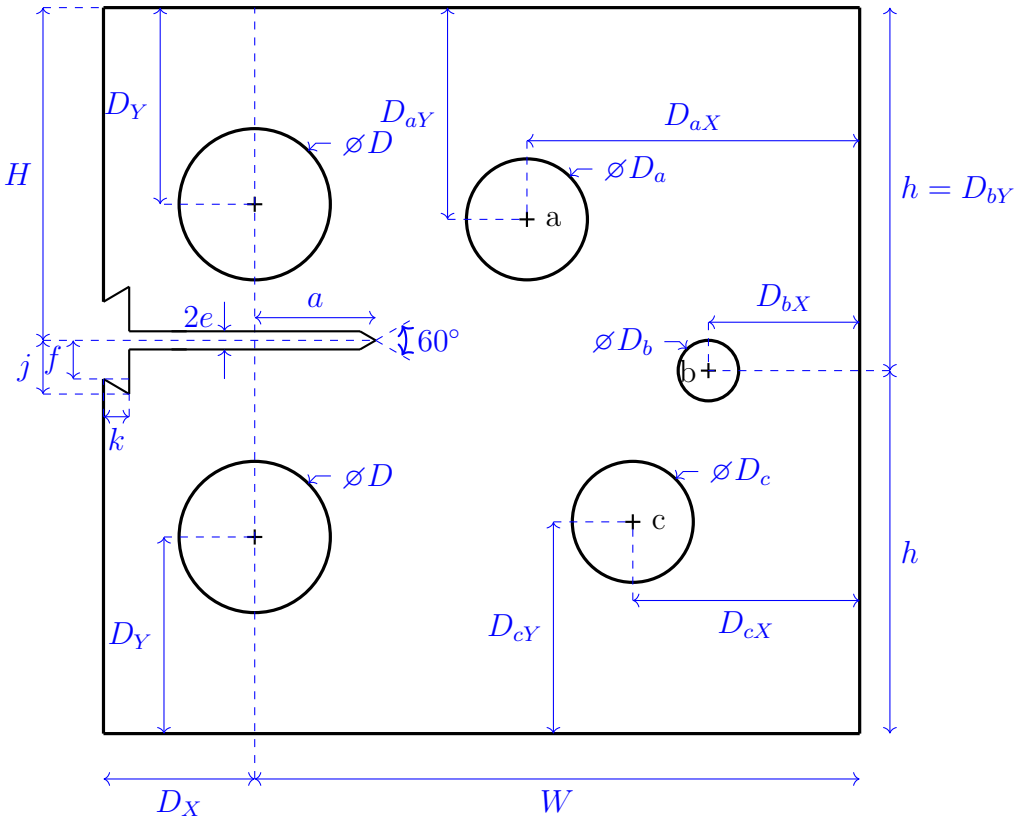

Figure 3.17: Compact tension specimen geometry with modified design featuring three circular holes. All dimensions are proportional to the base width $W = 40$ mm. The specimen includes a notched crack region positioned at distance H from the top edge and three circular holes (labeled a, b, and c) that disrupt the specimen symmetry and influence crack propagation patterns.

Guided by the analysis in [61], the boundary conditions were chosen to ensure close agreement with established LEFM solutions. As illustrated in Figure 3.18, these conditions involve constraining the lower half of the bottom loading hole in all directions and applying a distributed vertical force to the upper half of the top loading hole. To validate the chosen boundary conditions, a series of linear elastic finite element analyses were performed. This involved generating multiple meshes, each with an explicitly defined crack of length a, ranging from an initial length of $a_0 = 0.2W = 8.0$ mm up to $0.95W = 38.0$ mm in increments of $\Delta a = 0.5$ mm. For each mesh, a single force-controlled linear elastic analysis was conducted to compute the structural compliance. For instance, Figure 3.18(a) depicts the schematic with an initial crack length of $a_0 = 8.0$ mm, whereas Figure 3.18(b) presents the configuration for a crack length of $a = 30.0$ mm. This process established a numerical compliance-crack length relationship, $C(a)$, which was then compared with the analytical LEFM solution to verify the accuracy of the simulation setup.

The linear elastic finite element model employs quadrilateral elements with a characteristic size of $h = 0.001W = 0.04$ mm in the central region, ensuring consistency with the mesh refinement used in subsequent phase-field simulations. The Young's modulus E and Poisson's ratio ν for these simulations are specified in Table 3.7.

For the phase-field simulation a length scale parameter of $l = 0.0025W = 0.1$ mm is chosen, resulting in a ratio of $l/h = 2.5$. The simulation is performed with the same

Parameter	Value	Description
W	40 mm	Specimen width (reference dimension)
H	Variable	Initial crack tip vertical position
L	$0.6\,W = 24$ mm	Half specimen height
a	$0.2\,W = 8$ mm	Initial crack length
D	$0.25\,W = 10$ mm	Loading hole diameter
D_X	$0.25\,W = 10$ mm	Notch horizontal offset
D_Y	$0.325\,W = 13$ mm	Notch mouth vertical offset
$\varnothing D_a$	$0.2\,W = 8$ mm	Diameter of hole a
$\varnothing D_b$	$0.1\,W = 4$ mm	Diameter of hole b
$\varnothing D_c$	$0.2\,W = 8$ mm	Diameter of hole c
D_{aX}	$0.55\,W = 22$ mm	Horizontal position of hole a (from right edge)
D_{aY}	$0.35\,W = 14$ mm	Vertical position of hole a (from specimen top edge)
D_{bX}	$0.25\,W = 10$ mm	Horizontal position of hole b (from right edge)
D_{bY}	$0.6\,W = 24$ mm	Vertical position of hole b (from specimen top edge)
D_{cX}	$0.375\,W = 15$ mm	Horizontal position of hole c (from right edge)
D_{cY}	$0.35\,W = 14$ mm	Vertical position of hole c (from specimen bottom edge)
f	$0.06375\,W = 2.55$ mm	Vertical half-width of the crack mouth opening
j	$0.08875\,W = 3.55$ mm	Vertical half-width of the notch throat section
k	$0.04250\,W = 1.70$ mm	Horizontal depth of the notch throat indentation
e	$0.00375\,W = 0.15$ mm	Half-height of the crack tip region
B	$0.08\,W = 3.2$ mm	Specimen thickness

Table 3.5: Geometric parameters for the compact tension specimen with additional holes and notched crack geometry. All dimensions are given as functions of the reference width $W = 40$ mm. The table summarizes the main specimen dimensions, hole locations and sizes, and crack notch geometric parameters used in the simulations.

Specimen	H (Crack Position)	Holes Considered
Specimen 1	$H = 0.60W = 24.0$ mm	No holes
Specimen 2	$H = 0.56W = 22.4$ mm	With holes
Specimen 3	$H = 0.58W = 23.2$ mm	With holes
Specimen 4	$H = 0.64W = 25.6$ mm	With holes

Table 3.6: Specimen configurations with different initial crack positions H and hole presence. The first specimen represents the standard compact tension specimen with the crack positioned in the middle and no holes, while specimens 2-4 include three additional holes and have the crack positioned off-center.

boundary conditions as the linear elastic simulations. The non-variational phase-field solver is employed with constants $c_1 = 1.0$ kN/mm and $c_2 = 1.0$ (dimensionless). The applied traction force is $\boldsymbol{t} = (0, 1/\text{surface})$ kN, where "surface" is the area over which the force is applied (the upper half of the top circle).

Figure 3.19 compares the final crack path predicted by the phase-field simulation with

Parameter	**Value**	**Units**
Young modulus (E)	211	$\mathrm{kN/mm}^2$
Poisson ratio (ν)	0.3	–
Critial energy release rate (G_c)	0.073	kN/mm
Paris exponent (n)	2.08	–
Fatigue constant (C_{Paris})	2.129×10^{-5}	$\frac{mm^{\frac{2+3n}{2}}}{cycle\ kN^n}$

Table 3.7: Material properties for the Haynes 230 nickel-based superalloy. Elastic constants taken from [57]. The Paris law exponent n is obtained from [58], while the Paris constant C_{Paris} is calibrated from experiments. The critical energy release rate G_c, which does not influence fatigue life in the proposed model, is taken from [59].

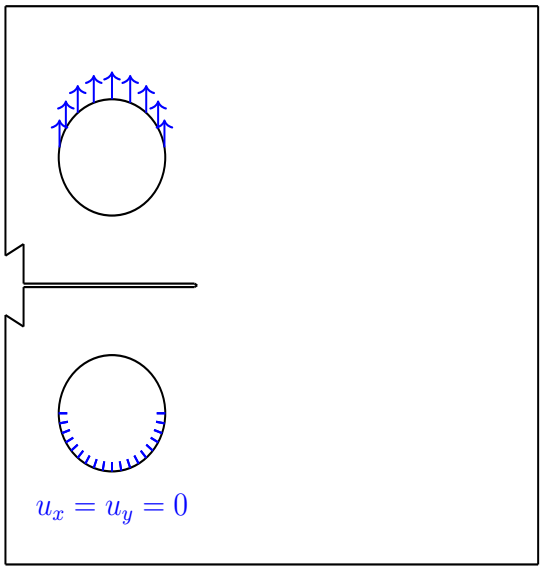

(a) Theoretical crack path based on geometry and loading conditions

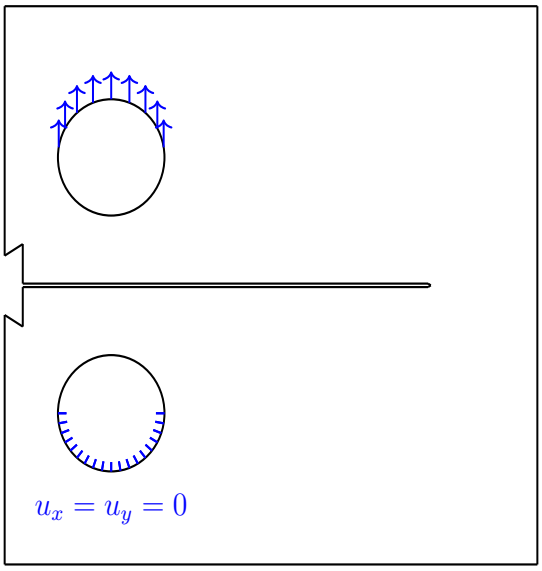

(b) Theoretical crack path based on geometry and loading conditions

Figure 3.18: Boundary conditions for the compact tension specimen (Specimen 1). The lower half of the bottom loading hole is fixed in all directions ($u_x = u_y = 0$), while a distributed vertical force is applied to the upper half of the top loading hole.

the theoretical straight path. The left panel shows the phase-field variable ϕ at the final step, while the right panel shows the theoretical crack path. The simulation accurately captures the straight crack propagation, demonstrating the method's ability to predict crack evolution without prior knowledge of the path. A slight upward deviation at the beginning of the crack path is observed, which can be attributed to mesh effects.

Figure 3.20(a) compares the stiffness results from the phase-field simulation, using crack lengths measured by both the Bourdin and skeleton methods, against the analytical LEFM solution and linear elastic finite element simulations. Similarly, Figure 3.20(b) highlights the relationship between the rate of change of compliance with respect to crack area ($\mathrm{d}C/\mathrm{d}a$) and the crack length, a key parameter for fatigue analysis.

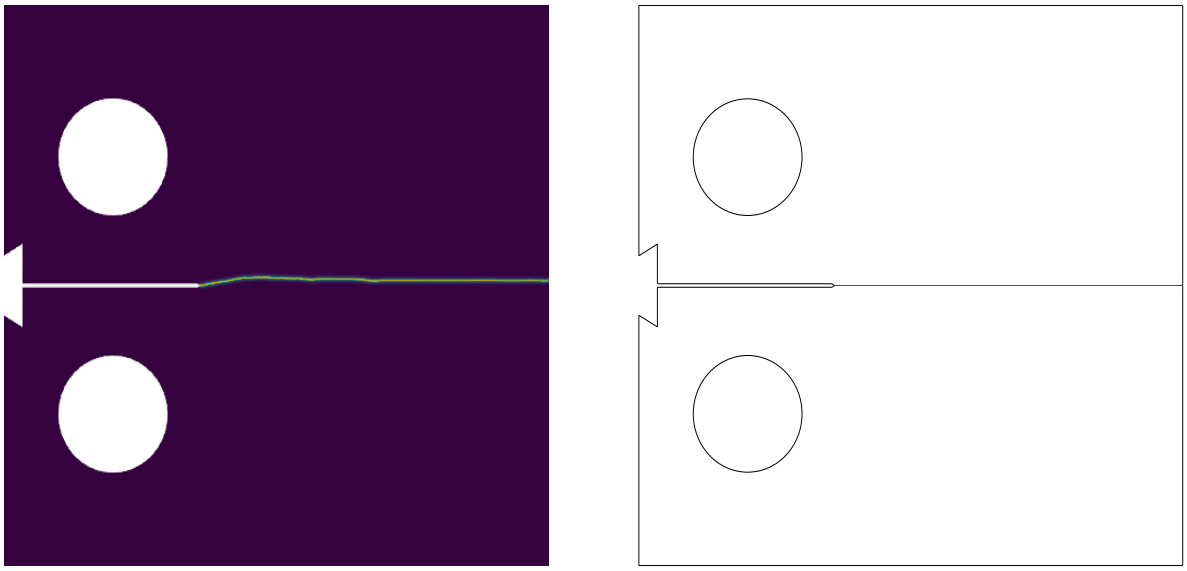

(a) Final phase-field simulation results showing the crack path at the last step of the simulation

(b) Theoretical crack path based on geometry and loading conditions

Figure 3.19: Comparison of phase-field simulation results with theoretical predictions for the standard compact tension (CT) specimen without additional holes. (a) The phase-field simulation accurately captures the straight crack propagation path. (b) Theoretical crack path based on the specimen's geometry and loading conditions.

From these results, it is concluded that for an unstructured mesh where the crack does not propagate exactly along a symmetry plane, the skeleton crack length measurement provides results closer to the theoretical solution than the Bourdin correction. Therefore, the skeleton algorithm is used for all subsequent analyses. The elastic simulation also shows good correlation with the theoretical one, despite minor differences.

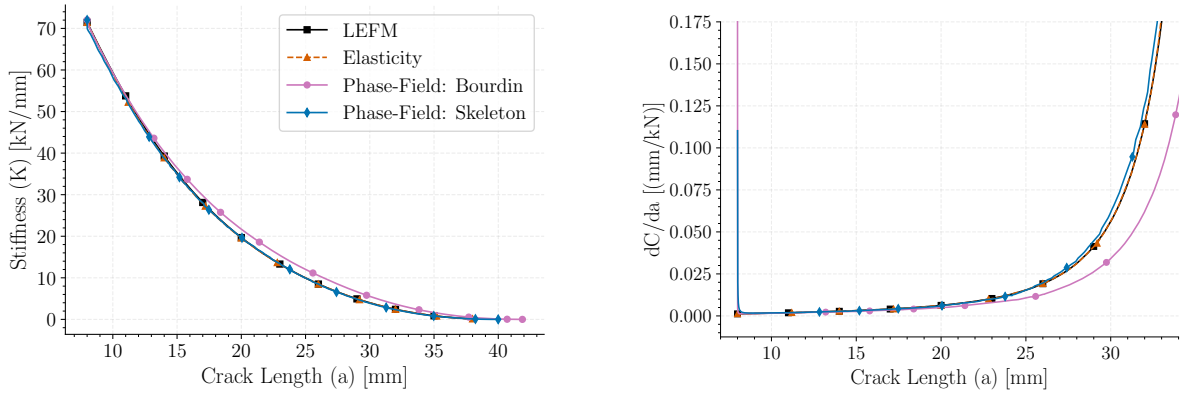

(a) Stiffness versus crack length, validating the phase-field simulation against analytical and numerical linear elastic solutions.

(b) Compliance derivative ($\mathrm{d}C/\mathrm{d}a$) as a function of crack length, comparing phase-field simulation results with analytical and numerical solutions.

Figure 3.20: Validation results for the standard compact tension specimen: (a) Stiffness versus crack length, validating the phase-field simulation against analytical and numerical linear elastic solutions; (b) Compliance derivative ($\mathrm{d}C/\mathrm{d}a$) as a function of crack length, demonstrating the phase-field method's accuracy in capturing compliance evolution.

With the compliance derivative, $\mathrm{d}C/\mathrm{d}a$, established for each method (Figure 3.20(b)), the

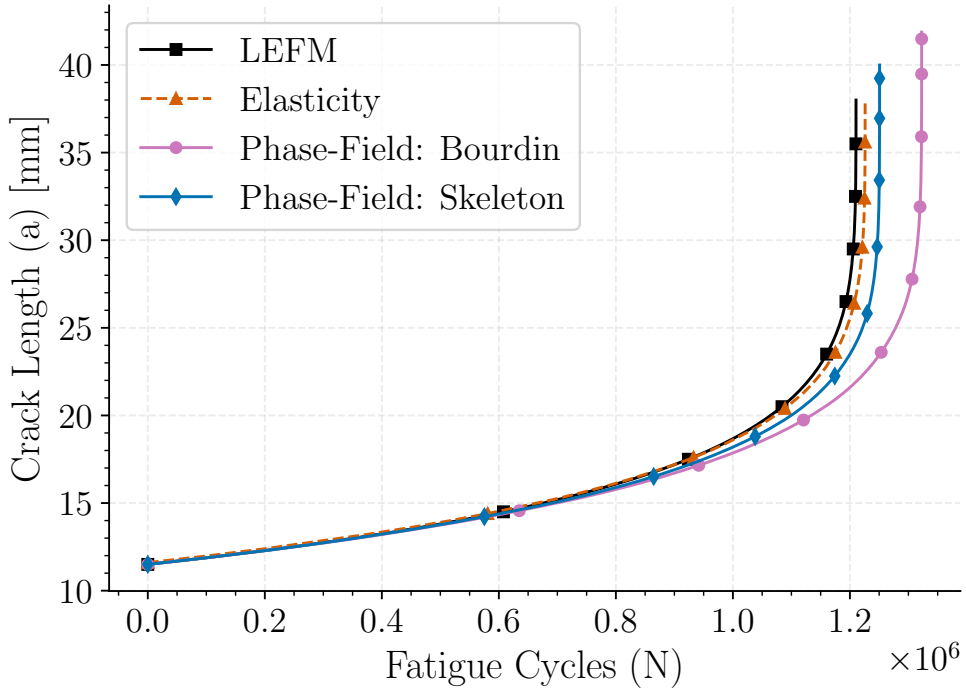

Figure 3.21: Fatigue life prediction using Paris' law, highlighting the phase-field method's accuracy in fatigue analysis.

fatigue life is calculated using Eq. (3.47). The analysis begins from an initial crack length of $a_i = 11.5$ mm to ensure consistency with the experimental data presented later.

Figure 3.21 compares the fatigue life predictions from the theoretical LEFM solution, the elasticity simulation, and the phase-field model (with both Bourdin and skeleton corrections). While the underlying stiffness and $\mathrm{d}C/\mathrm{d}a$ curves show strong agreement, the resulting fatigue life predictions exhibit more pronounced differences. These discrepancies are primarily due to the amplification of small variations in $\mathrm{d}C/\mathrm{d}a$ by the Paris exponent, n. Furthermore, the phase-field simulation shows a slight upward crack deviation not present in the other models, which increases the total crack length and affects the life prediction. Consequently, the skeleton-corrected phase-field results align more closely with the LEFM and elasticity solutions than the Bourdin-corrected results.

3.7.2 Specimens with holes

This section validates the methodology on modified CT specimens with internal voids, replicating the experimental work presented in [56, 57]. Three configurations with varying initial crack positions (H) are analyzed: Specimen 2 ($H = 0.56W$), Specimen 3 ($H = 0.58W$), and Specimen 4 ($H = 0.64W$). The material properties, boundary conditions, and solver settings are identical to those used for the standard CT specimen. Figure 3.22 illustrates the finite element meshes for specimens 2, 3, and 4. These meshes are carefully generated to provide sufficient resolution in the regions where crack initiation and propagation are expected.

Figure 3.23 compares the predicted crack paths with experimental results. The simulations show excellent agreement for Specimen 2 (Figure 3.23(a)) and Specimen 4 (Figure 3.23(c)), where the crack correctly propagates to holes 'a' and 'c', respectively, match-

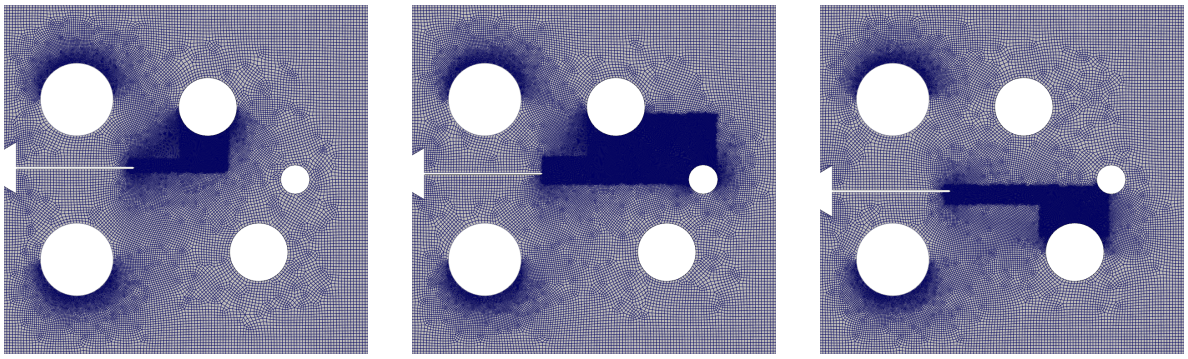

(a) Specimen 2 ($H = 0.56W = 22.4$ mm) (b) Specimen 3 ($H = 0.58W = 23.2$ mm) (c) Specimen 4 ($H = 0.64W = 25.6$ mm)

Figure 3.22: Finite element meshes for compact tension specimens: (a) Specimen 2, (b) Specimen 3, (c) Specimen 4. Meshes use quadrilateral elements with $h = 0.001W = 0.04$ mm in crack regions.

ing the experimental observations. However, for Specimen 3 (Figure 3.23(b)), the simulation predicts a path toward hole 'a', deviating from the experimental observation where the crack terminates at hole 'b'. This case is particularly complicated because the initial crack is placed more centered with respect to the upper and lower holes, so the results for this configuration have a higher sensitivity to the conditions of the simulation, as also reported in [56]. This indicates the presence of an instability in the crack propagation, which is likely also present experimentally. It is also interesting to note that other numerical fracture approaches provide larger differences in this case with respect to the other two geometries [57, 56]. Therefore, the particular details of the PFF model chosen (energy decomposition, characteristic length, etc.) might have a strong influence on the crack path, whereas in more stable cases, such as the other two, these choices produce minimal changes.

The fatigue life predictions are presented in Figure 3.24. For Specimens 2 and 4, where the crack paths were accurately predicted, the fatigue life curves show excellent agreement with the experimental data, with a final life prediction error of less than 4%. For Specimen 3, the incorrect crack path naturally leads to a deviation in the predicted fatigue life.

Regarding a qualitative comparison with cycle-by-cycle simulation, for specimen 4, the predicted fatigue life is on the order of 10^6 cycles. In the simulation using the adaptive algorithm, approximately 9,000 steps were required. In contrast, a cycle-by-cycle simulation would require at least 4 points per cycle to capture the cyclic behavior, resulting in $4 \times 10^6 = 4,000,000$ steps—a reduction of more than 400 times in the number of steps required. If 8 points per cycle are used, the number of steps increases to $8 \times 10^6 = 8,000,000$, yielding a reduction of over 800 times. For 3D problems or cases with even longer fatigue life, these differences become even more significant. Additionally, with the proposed approach, it is possible to consider different Paris' law parameters without repeating the simulations, allowing for efficient analysis of materials with varying fatigue lives at the same computational cost.

To further exploit the results of the proposed technique, the static force-displacement curve obtained under a crack-controlled experiment is computed and represented in Figure 3.25(a) for the specimen without holes and in Figure 3.25(b) for the other cases. The

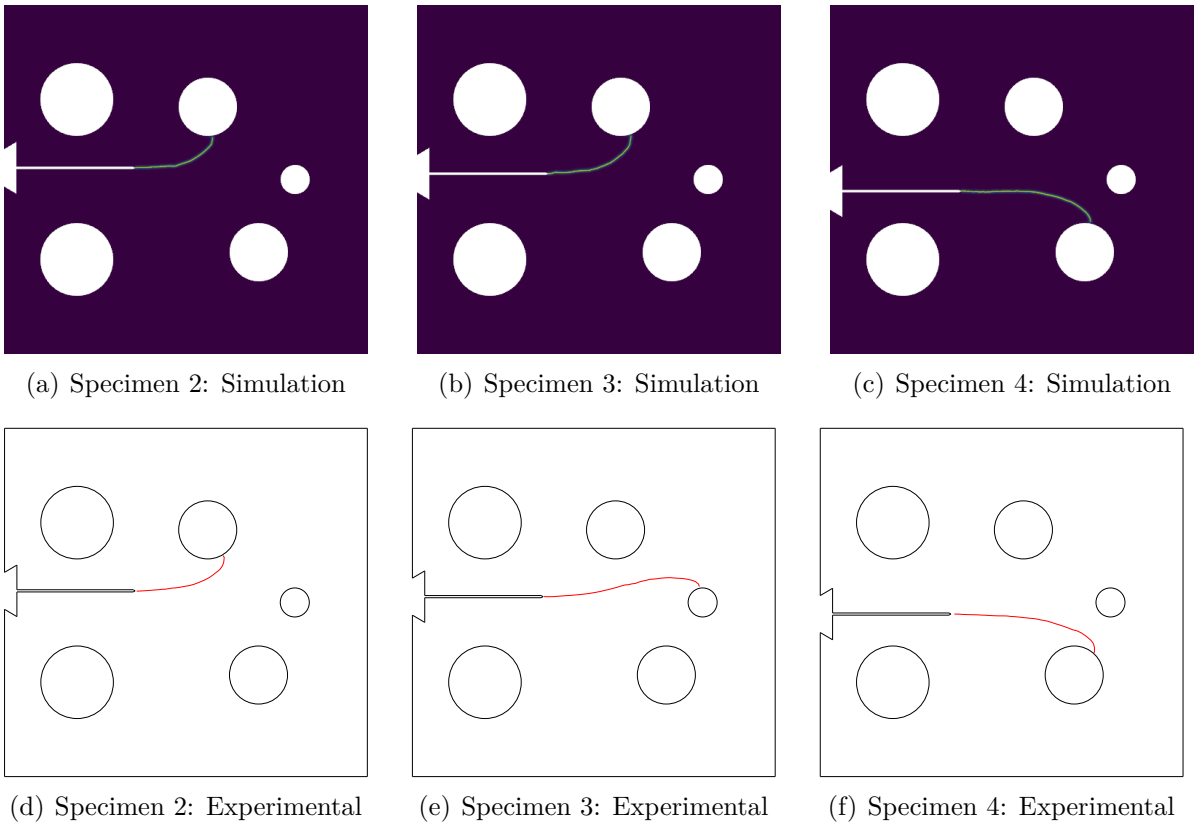

(a) Specimen 2: Simulation (b) Specimen 3: Simulation (c) Specimen 4: Simulation

(d) Specimen 2: Experimental (e) Specimen 3: Experimental (f) Specimen 4: Experimental

Figure 3.23: Comparison of phase-field simulation (top row) and experimental (bottom row) crack paths for the modified compact tension specimens. From left to right: Specimen 2, Specimen 3, and Specimen 4. The phase-field simulation accurately predicts the crack trajectory for Specimens 2 and 4, while a deviation is observed for Specimen 3.

results in both figures incorporate the skeleton correction. The specimens with holes exhibit snap-back behavior in the final part of their curves, which occurs as the crack approaches a hole. This snap-back implies a strong reduction in the energy dissipated during monotonic crack propagation, due to the reduction in crack length. To ascertain whether this snap-back response and its corresponding reduction in energy dissipation correlate with fatigue performance, the fatigue crack evolution is represented in Figure 3.26. As expected, the specimen without holes exhibits the longest fatigue life. Specimen 2 has the shortest fatigue life, followed by Specimen 3, which shows a similar life despite its crack path differing from experimental results. Specimen 4, where the simulated crack terminates at the bottom hole, has the longest fatigue life among the specimens with holes. These results establish a clear qualitative correlation between the fatigue life of the specimen and the crack length (or total dissipated energy) under monotonic crack growth in a static experiment.

In summary, the proposed framework successfully predicted both the complex crack paths and fatigue lives for two of the three modified specimens with a high degree of accuracy. The results validate the methodology's capability to handle complex geometries and unknown crack trajectories using a single quasi-static simulation, without any case-specific parameter tuning. It is possible that specific choices of parameters related to boundary conditions or mesh sensitivity could lead to better agreement. However, these factors must be accounted for when evaluating these models. Since the objective is to evalu-

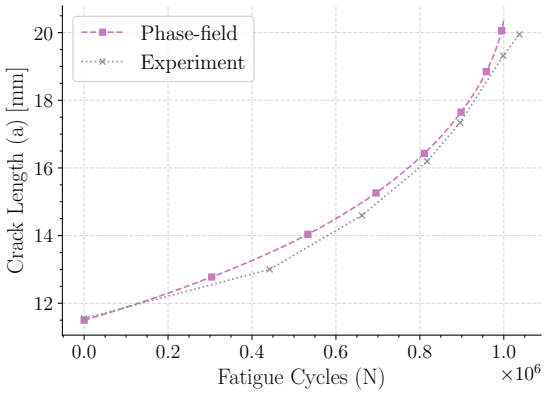

(a) Specimen 2

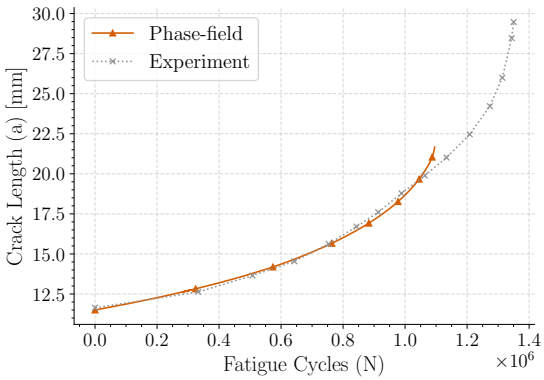

(b) Specimen 3

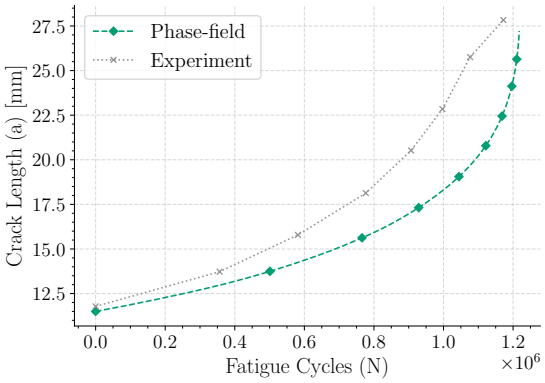

(c) Specimen 4

Figure 3.24: Comparison of predicted fatigue life from phase-field simulations with experimental results for modified compact tension specimens: (a) Specimen 2, (b) Specimen 3, and (c) Specimen 4. The simulation results show excellent agreement with the experimental data for specimens 2 and 4.

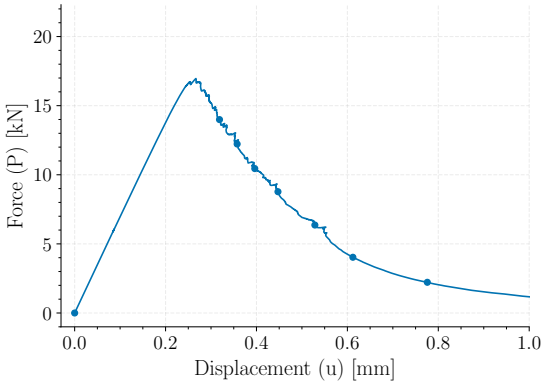

(a) Force-displacement curve for the standard compact tension specimen without holes.

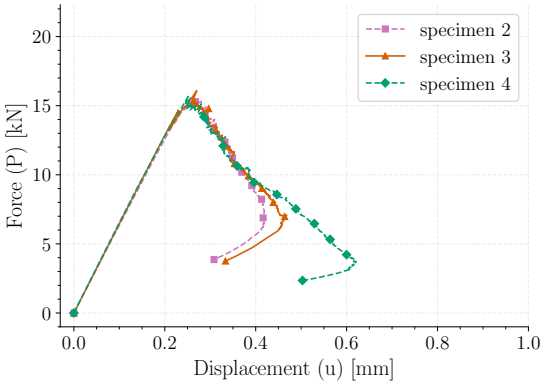

(b) Force-displacement curves for the compact tension specimens with additional holes.

Figure 3.25: Force-displacement curves for the compact tension specimens. (a) Response of the standard specimen without holes. (b) Response of the specimens with holes, showing snap-back behavior as the crack approaches a hole.

ate the model's predictive capacity under consistent conditions, no parametric study was

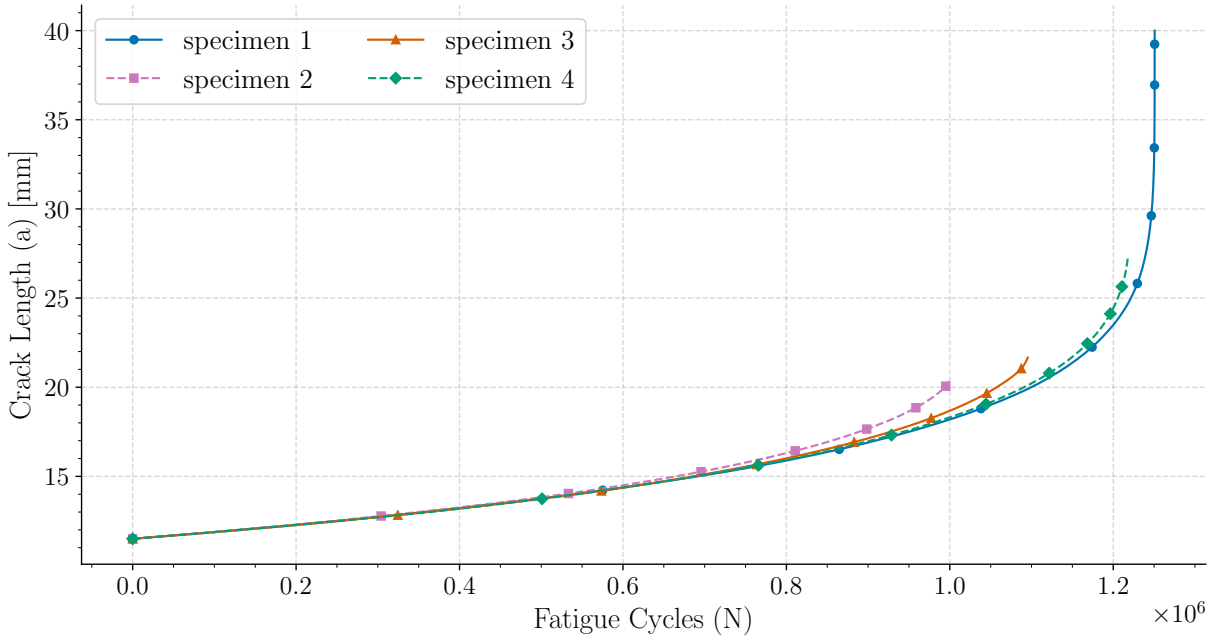

Figure 3.26: Comparison of fatigue life predictions for all compact tension specimens. The plot shows the number of cycles versus crack length for the standard specimen (without holes) and the three modified specimens.

conducted to optimize the parameters for reproducing this specific crack path.

3.8 Conclusions

In this chapter, a novel approach for the simulation of fatigue crack propagation based on the phase-field framework has been presented. This methodology is founded on a unified and computationally efficient framework that combines the principles of LEFM and Paris' law with PFF static simulations. The core of the methodology lies in the development of novel energy (crack length)-controlled solvers that robustly trace the complete quasi-static equilibrium path of a cracked body, including complex snap-back instabilities, in a single simulation.

From an experimental viewpoint, the new approach does not require specific parametrization, unlike other PFF-based fatigue models, since it relies directly on Paris' law parameters fitted in standard experiments. From a numerical and computational perspective, the current approach does not rely on cycle-by-cycle simulation, unlike other phase-field fatigue approaches, making it possible to simulate High Cycle Fatigue (HCF) or Ultra High Cycle Fatigue (UHCF) cases with the same cost as Low Cycle Fatigue (LCF). Secondly, in comparison with classic methods for crack propagation, remeshing or element enhancing on-the-fly is not necessary, and the computation reduces to a single monotonic simulation.

The main contributions and findings of this study can be summarized as follows:

1. Two equivalent energy-controlled schemes were developed. It was shown that both methods are capable of handling complex structural instabilities with the addition

of only a single Lagrange multiplier. The choice between them relates to computational aspects, such as the symmetry of the variational solver in a Newton-Raphson approach versus obtaining physical parameters directly.

2. The proposed framework leverages the energy-controlled simulation to directly compute the evolution of the specimen's compliance and its derivative with respect to the crack area, $\mathrm{d}C/\mathrm{d}a$. This avoids the need for computationally expensive cycle-by-cycle simulations, as the fatigue life can be directly integrated using Paris' law from the compliance data of a single quasi-static analysis. This significantly reduces computational cost compared to cycle-by-cycle methods and avoids extensive calibration work required by other phase-field fatigue models.

3. An important limitation to consider is the typical overestimation of the crack length when measured via the integration of the γ function. A systematic procedure for correcting this inherent overestimation was implemented and validated. By applying correction factors based on either mesh parameters or image skeletonization, the simulation results show excellent agreement with analytical LEFM predictions for standard benchmarks.

4. The framework's predictive power was demonstrated on a complex modified compact tension specimen with multiple holes, where the crack path is not known a priori. The model successfully predicted intricate, curvilinear crack trajectories in most cases, which were in good agreement with experimental data from the literature, showcasing its utility for analyzing realistic engineering components. However, one case presented a completely different crack path than that reported in other simulations and experiments. This discrepancy could be attributed to mesh dependency, the need for a smaller length-scale parameter, or the possibility that the isotropic energy degradation model was insufficient for that specific case.

5. This methodology enables a rigorous and transparent assessment of its limitations. It allows for a clear evaluation of factors such as the non-linear trend in initial stiffness due to damage accumulation, overestimation of crack length, differences in crack path arising from isotropic versus anisotropic models, mesh dependency, and the influence of the length scale parameter. Although these limitations exist, it is shown that their influence can be studied in detail to account for them comprehensively.

In conclusion, the proposed methodology offers a powerful and practical tool for fracture and fatigue analysis. By combining the descriptive power of phase-field models with the foundational principles of LEFM, it provides a computationally tractable approach for life prediction in complex engineering structures.

Chapter 4

DOUBLE GRADIENT CORRECTION METHOD FOR CRACK AREA OVERESTIMATION

PFF models are known to overestimate crack area, a discrepancy that compromises the accuracy of fracture predictions. This issue stems from the diffuse crack representation and numerical artifacts, such as strain localization, where the phase-field variable artificially saturates across finite elements.

Existing correction strategies, including mesh-dependent factors and skeletonization algorithms, have significant limitations. Mesh-based corrections are often unreliable for unstructured meshes, while skeletonization can be complex and inaccurate for intricate crack topologies, especially in three dimensions.

This chapter introduces a novel and robust framework to correct this overestimation. The approach presented in this work is founded on the equipartition principle of the fracture energy components. This theoretical result demonstrates that the energy contributions from the phase field and its gradient are equal when the length scale parameter approaches zero, or strictly speaking, when the phase-field variable has enough space to develop without the influence of boundary conditions or other cracks. Since numerical artifacts primarily affect the phase-field term while leaving its gradient largely unperturbed, it is proposed that the crack area can be accurately approximated as twice the gradient-dependent energy. The definition of this correction method is inherently mesh-independent and readily applicable to the entire domain, including 3D simulations.

To provide a comprehensive understanding, the multidimensional demonstration of energy equipartition is first presented. Subsequently, the classical one-dimensional analytical solution of the crack surface density functional regularization model is used as an illustrative example to clarify the underlying mechanisms, including the strain localization effect. The insights gained from this analysis inform the development of the correction method, which is designed to be applicable to more complex, multi-dimensional problems. The proposed methodology is validated against benchmarks with analytical solutions and compared with established methods like skeletonization to demonstrate its accuracy. It is then applied

to complex geometries with curvilinear crack paths and evaluated in a three-dimensional simulation.

Another significant artifact in phase-field fracture simulations is the presence of a non-physical peak force at the onset of crack initiation, a phenomenon not observed in experimental results [14, 12, 13]. This force overshoot is a numerical artifact linked to the nucleation process, where the phase-field variable evolves from an undamaged state ($\phi = 0$) to a fully damaged state ($\phi = 1$). This issue is addressed by existing correction methods with varying degrees of success. The Bourdin correction, being a constant scaling factor dependent on mesh size and length scale, reduces the magnitude of the peak force but does not eliminate the overshoot itself. In contrast, skeletonization-based methods, which measure the crack length by thresholding the phase-field (e.g., considering only regions where $\phi > 0.95$), effectively bypass the nucleation phase and thus remove the peak force from the corrected results. However, this approach has its own limitations: its accuracy depends on the chosen threshold and image processing techniques, and its application to complex crack topologies, such as multiple interacting cracks or three-dimensional problems, is not straightforward.

Regarding the numerical framework, the standard AT2 PFF model with an isotropic energy decomposition is employed (refer to Section 2.1.2). To ensure stable crack propagation and capture the complete equilibrium path, including potential snap-back instabilities, the non-variational energy-controlled scheme derived in Chapter 3 (specifically Section 3.4) is utilized. This solver is crucial for the present analysis as it enables tracing the evolution of energy quantities throughout the entire fracture process.

This chapter is organized as follows. Section 4.1 establishes the theoretical background, emphasizing the energy equipartition concept. Section 4.2 analyzes the strain localization effect and its influence on crack area overestimation. Section 4.3 introduces the framework for correcting this overestimation, focusing on the element size-based Bourdin correction, and Section 4.4 presents the proposed Double Gradient Correction Method (DGCM). Section 4.5 provides a comparative summary of the different correction techniques. Section 4.6 examines the influence of finite element discretization error. Section 4.7 validates the proposed framework through several benchmarks, including complex curvilinear crack paths. Section 4.8 discusses the extension of the method to general phase-field formulations. Finally, Section 4.9 summarizes the main findings.

4.1 Theoretical background

This section establishes the theoretical background for the proposed crack area correction method. It briefly recalls the relevant components of the PFF theory detailed in Chapter 2. Specifically, the focus is on the AT2 model formulation defined in Section 2.2 and the associated CSDF.

The core concept of this correction factor is based on the components of the CSDF. As introduced in Eq. (2.2), the fracture surface energy is given by $\Gamma(\phi) = \int_\Omega \gamma(\phi, \nabla\phi)\, \mathrm{d}\boldsymbol{x}$. In the standard AT2 model, this density corresponds to the integrand of the functional defined in Eq. (2.19).

In the general multidimensional case, in the limit where the length scale parameter l approaches zero, the diffuse crack representation converges to a sharp crack without bound-

ary influence. Under these conditions, the total accumulated energy converges to the theoretical fracture area Γ_{sharp}. Crucially, as the regularization parameter vanishes, the energy contributions from the phase-field term (Γ_ϕ) and the gradient term ($\Gamma_{\nabla\phi}$) equilibrate:

$$\Gamma_\phi = \Gamma_{\nabla\phi}. \tag{4.1}$$

This **equipartition of energy** is a fundamental property of the CSDF and forms the physical basis for the correction method proposed in this work.

Consequently, the energy components present in the phase-field CSDF (Eqs. (2.20) and (2.21)) that depend on the phase-field variable and its gradient are analyzed.

4.1.1 Equipartition of the fracture energy

A key result for the remainder of the chapter is the *equipartition* of the fracture energy. This result, which is proven next, says that the two terms of the fracture energy contribute equally in the limit $l \to 0$. For simplicity, the focus is placed on the three-dimensional problem with the AT2 model.

To start, it should be noted that the phase-field function ϕ belongs to $H^1(\Omega)$, the space of functions defined on the domain Ω that are square-integrable and have square-integrable (weak) derivatives. These functions satisfy Young's inequality

$$\int_\Omega |\phi|\,|\nabla\phi|\,d\Omega \leq \int_\Omega \left[\frac{|\phi|^2}{2\epsilon^2} + \frac{\epsilon^2}{2}|\nabla\phi|^2\right] d\Omega\ , \tag{4.2}$$

for all $\epsilon \neq 0$. Moreover, the equality is verified only if $|\phi|/\epsilon = \epsilon|\nabla\phi|$ almost everywhere. Next, it is observed that the left side of this inequality can be written as

$$\int_\Omega |\phi|\,|\nabla\phi|\,d\Omega = \frac{1}{2}\int_\Omega |\nabla(\phi^2)|\,d\Omega\ , \tag{4.3}$$

and the right-hand integral is known as the *total variation* of ϕ^2.

Consider now a fracture problem with a crack $\mathcal{C}$ of area $|\mathcal{C}|$. The trace of the phase field ϕ would be 1 on the crack and 0 far from it. Then, define coordinates (ξ_1, ξ_2, ξ_3) for Ω such that the first two are surface coordinates of the crack and the third one is normal to $\mathcal{C}$. The set Ω can then be split into three regions: one with positive ξ_3 denoted Ω^+; a second one, Ω^- with negative ξ_3, and a third one where the coordinates (ξ_1, ξ_2, ξ_3) are not well-defined due to the singularity of the crack edge. Then, since the normal to the crack corresponds with the ξ_3 direction, a bound for the total variation of ϕ^2 can be evaluated as

$$\int_\Omega |\nabla(\phi^2)|\,d\Omega \geq \int_{\Omega^+\cup\Omega^-} |\nabla(\phi^2)|\,d\Omega = \int_{\mathcal{C}}\int \left|\frac{\partial}{\partial\xi_3}(\phi^2)\right| d\xi_3\,d\xi_1\,d\xi_2 = 2\,|\mathcal{C}|\ , \tag{4.4}$$

where the area of the crack surface must be counted twice since the integral must be performed on Ω^+ and Ω^-. From the Modica-Mortola theory, it is known that the fracture energy satisfies

$$\lim_{l\to 0} G_c \int_\Omega \left[\frac{\phi^2}{2l} + \frac{l}{2}|\nabla\phi|^2\right] d\Omega = G_c\,|\mathcal{C}|\ . \tag{4.5}$$

Then, using Eq. (4.2) with $\epsilon = \sqrt{l}$, and Eqs. (4.4)-(4.5), it follows that

$$G_c\,|\mathcal{C}| = \lim_{l\to 0} G_c \int_\Omega \left[\frac{\phi^2}{2l} + \frac{l}{2}|\nabla\phi|^2\right] d\Omega\ \geq \frac{G_c}{2}\int_\Omega |\nabla(\phi^2)|\,d\Omega \geq G_c\,|\mathcal{C}|\ . \tag{4.6}$$

For these identities to hold, the inequalities must be equalities, which occurs only if

$$\lim_{l\to 0}\int_\Omega \frac{\phi^2}{2l}\,d\Omega = \lim_{l\to 0}\int_\Omega \frac{l}{2}|\nabla\phi|^2\,d\Omega, \tag{4.7}$$

which is precisely the equipartition result.

It is noted that the equipartition of the fracture energy only happens in the limit $l \to 0$ when the Modica-Mortola functional converges to the crack area and the total variation of ϕ^2 can be evaluated.

4.2 Strain localization artifact

A common numerical artifact in PFF simulations is strain localization, as analyzed in [16]. In this phenomenon, the phase-field variable artificially saturates to $\phi = 1$ across an entire element of size h, leading to an overestimation of the crack surface area when the latter is measured from the fracture energy functional. Figure 4.1 illustrates how the ideal phase-field profile is distorted by this effect.

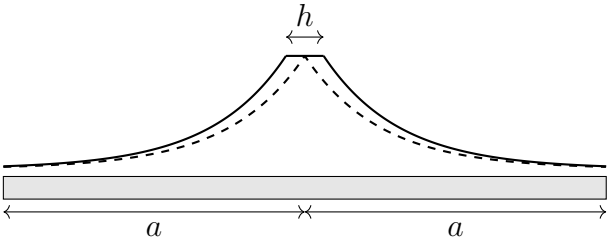

Figure 4.1: Illustration of the phase-field profile distortion caused by strain localization. The ideal profile (dashed line) is artificially flattened to $\phi = 1$ over an element of size h (solid line), leading to an overestimation of the crack surface energy.

Within the localized element, the phase-field is constant ($\phi = 1$), and its gradient is zero. Figure 4.2(a) and 4.2(b) illustrate this for the phase field and its gradient, respectively. This alters the energy calculation. The total energy, accounting for the strain localization effect, is denoted as Γ_{sl}, and can be obtained by modifying the integral in Eq. (2.19) to account for the localized region:

$$\Gamma_{\text{sl}}(\phi,\nabla\phi) = \int_{-a}^{+a}\left(\frac{1}{2l}\phi^2 + \frac{l}{2}(\phi')^2\right)dx + \int_0^h\left(\frac{1}{2l}(1)^2 + \frac{l}{2}(0)^2\right)dx. \tag{4.8}$$

As a result, the energy contributions are modified. The phase-field term, Γ_ϕ, increases due to the contribution from the localized region, whereas the gradient term, $\Gamma_{\nabla\phi}$, remains unchanged because the gradient vanishes where ϕ is constant:

$$\Gamma_{\phi,\text{sl}} = \Gamma_\phi^{\text{AT2}} + \frac{h}{2l}, \tag{4.9}$$

$$\Gamma_{\nabla\phi,\text{sl}} = \Gamma_{\nabla\phi}^{\text{AT2}}, \tag{4.10}$$

where Γ_ϕ^{AT2} and $\Gamma_{\nabla\phi}^{\text{AT2}}$ correspond to the analytical energy components defined in Eqs. (2.28) and (2.29), respectively. The total energy with strain localization becomes:

$$\Gamma_{\text{sl}} = \Gamma_{\phi,\text{sl}} + \Gamma_{\nabla\phi,\text{sl}} = \tanh\left(\frac{a}{l}\right) + \frac{h}{2l}. \tag{4.11}$$

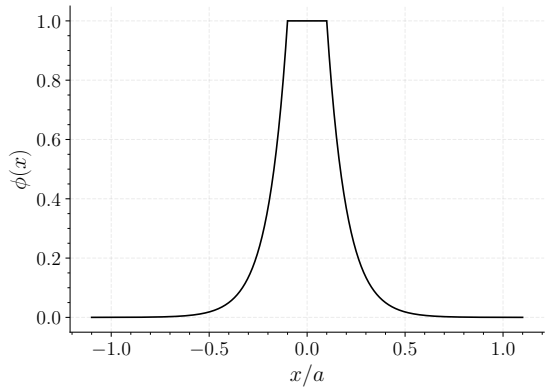

(a) Phase-field profile $\phi(x)$ with strain localization.

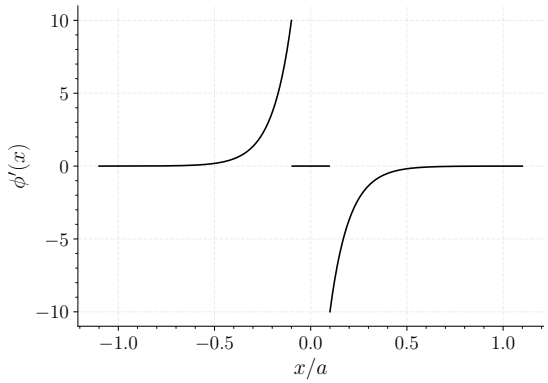

(b) Phase-field gradient profile $\phi'(x)$ with strain localization.

Figure 4.2: Effect of strain localization on the phase-field profile and its gradient for a ratio $l/a = 0.1$. The profiles exhibits a plateau of width h where $\phi = 1$ and $\phi' = 0$, deviating from the ideal analytical profile.

This shows that strain localization introduces an additive error of $h/(2l)$ to the total crack surface energy in the one-dimensional case. This error is directly proportional to the element size h and inversely proportional to the length scale l.

Figures 4.3(a) and 4.3(b) illustrate the impact of strain localization on the computed energies. These plots show the total energy and the phase-field energy component, respectively, for various h/a ratios. As the element size h decreases, the additional energy introduced by strain localization diminishes, and the computed energies converge toward the theoretical values. In contrast, the gradient-dependent energy component remains unaffected by this artifact and therefore coincides with the theoretical $\Gamma_{\nabla\phi}$ curve shown in Figure 2.5.

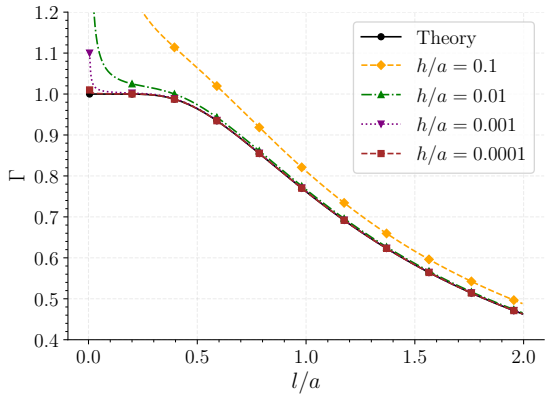

(a) Total energy Γ_{sl} vs. l/a ratio.

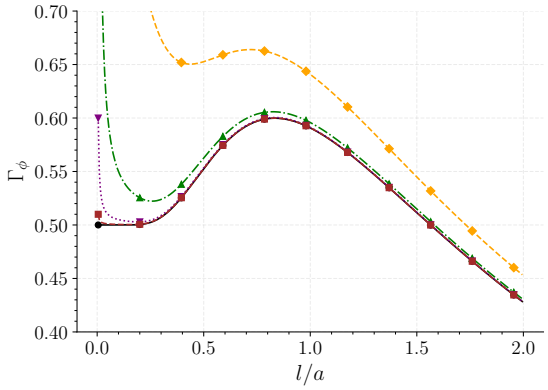

(b) Phase-field energy $\Gamma_{\phi,\text{sl}}$ vs. l/a ratio.

Figure 4.3: Effect of strain localization on energy contributions for different element sizes h. As h decreases, both the total energy (a) and the phase-field energy (b) converge to the ideal theoretical solution (solid black line).

4.3 Framework for correcting crack surface overestimation

Accurately measuring the crack surface area is a critical challenge in phase-field modeling. The standard approach of integrating the CSDF, $\Gamma(\phi)$, over the domain typically overestimates the true physical crack area. This discrepancy arises from numerical artifacts like strain localization, which artificially inflates the computed crack surface. As demonstrated in Section 3.5.2, this overestimation systematically affects all related simulation quantities—including forces and displacements—compromising the physical accuracy of the results even when the numerical solution satisfies the governing equations. To address this issue, existing strategies and a novel correction method are presented in the following sections.

Following the approach presented in Section 3.5.2, the physical crack area Γ, defined as the area that would be obtained in the absence of strain localization, is determined by scaling the simulated area Γ_{sl} (which includes the overestimation) by a correction factor $\mathcal{F}$:

$$\Gamma = \frac{\Gamma_{\text{sl}}}{\mathcal{F}}. \tag{4.12}$$

Here, $\mathcal{F}$ is a factor that quantifies the overestimation caused by the diffuse crack representation and numerical artifacts. Based on this relationship, the relative error introduced by the strain localization effect can be expressed in terms of the correction factor as:

$$\text{Relative Error} = \frac{|\Gamma - \Gamma_{\text{sl}}|}{|\Gamma|} = \frac{|\Gamma - \mathcal{F}\,\Gamma_{\text{sl}}|}{|\Gamma_{\text{sl}}|} = |1 - \mathcal{F}|. \tag{4.13}$$

The following sections introduce the Bourdin correction and the novel DGCM approach. In an idealized scenario, the correction factor should approach one as the mesh is refined (i.e., as the element size $h \to 0$), indicating that the overestimation effect vanishes with finer discretizations.

4.3.1 Element size-based correction method

This correction method is derived from the one-dimensional analytical solution. As detailed in Section 4.2, the presence of strain localization causes the computed total crack surface energy, Γ_{sl}, to be overestimated by an additive term directly proportional to the element size h:

$$\Gamma_{\text{sl}} = \Gamma + \frac{h}{2l}, \tag{4.14}$$

where Γ is the ideal energy without localization effects. The correction factor is designed to scale the simulated energy back to the theoretical value. Based on this, the factor can be defined as:

$$\mathcal{F}_{\text{elem}} = \frac{\Gamma_{\text{sl}}}{\Gamma} = \frac{\Gamma + \frac{h}{2l}}{\Gamma} = 1 + \frac{1}{\Gamma}\frac{h}{2l}. \tag{4.15}$$

A key limitation of this formulation is its dependence on Γ. In a phase-field simulation, the computed quantity is Γ_{sl}, which incorporates the strain localization effect. The objective is to correct this value to recover Γ, the physical crack area free from numerical artifacts. However, since Γ is unknown, it cannot be used directly. To proceed, it is standard to assume the idealized scenario of a one-dimensional crack in an infinite domain (or where boundary effects are negligible, i.e., $l/a \to 0$). In this limit, the theoretical energy Γ

converges to 1, as shown in Figure 2.5 and Eq. (2.30). By adopting this assumption, the correction factor simplifies to:

$$\mathcal{F}_{\text{Bourdin}} = 1 + \frac{h}{2l}. \tag{4.16}$$

This expression is the well-known Bourdin correction, also presented before in Section 3.5.2, a foundational method for mitigating crack area overestimation in phase-field models [51]. It directly addresses the numerical artifact of strain localization by introducing a correction factor that is constant throughout the simulation, as it depends only on the mesh size h and the length scale parameter l.

The effectiveness of this method is highest when the mesh is regular in the damaged regions. As the mesh is refined ($h/l \to 0$), the correction factor approaches 1, indicating that the overestimation effect diminishes. However, a key limitation is that its derivation assumes $\Gamma \approx 1$. This assumption is only valid when the boundaries are sufficiently large compared to the length scale (i.e., $a/l \to \infty$).

This method's effectiveness is highest for straight cracks propagating perpendicular to mesh edges, a scenario that mirrors the idealized one-dimensional case from which it is derived. Furthermore, the factor does not account for boundary effects which can influence the energy term Γ. Despite these limitations, its simplicity has made it a widely adopted choice for correcting phase-field results.

It is important to note that for simulations employing symmetry boundary conditions, where only half of the crack is modeled, the theoretical energy Γ in Eq. (4.15) is effectively halved (i.e., $\Gamma \approx 0.5$). This implies that the Bourdin correction factor for symmetric cases becomes:

$$\mathcal{F}_{\text{Bourdin,sym}} = 1 + \frac{h}{l}. \tag{4.17}$$

This result is consistent with the correction presented in [16], and introduced in the previous chapter, where the factor 2 explanation arises because the strain localization occurs over a full element width h, but this contribution is scaled relative to the energy of only half the crack.

4.4 DGCM

The DGCM is founded on the principle that while strain localization artifacts significantly overestimate the phase-field energy term (Γ_ϕ), the gradient energy term ($\Gamma_{\nabla\phi}$) remains largely unperturbed. As discussed in Section 4.2, strain localization causes the phase-field profile to artificially saturate at $\phi = 1$ within an element. Consequently, the gradient $\nabla\phi$ becomes zero in that region, but the overall integral of the gradient term is less affected than the phase-field term.

This disparity is key. As proven in Section 4.1.1, the phase-field model demonstrates a crucial property in the sharp-crack limit: the energy contributions from the phase-field and its gradient are equal. This equipartition of energy, where $\Gamma_\phi = \Gamma_{\nabla\phi}$, is a fundamental feature of the regularized model when the phase field has sufficient space to develop.

Since the gradient energy $\Gamma_{\nabla\phi}$ provides a more robust measure, it is proposed that the true physical crack area can be accurately approximated by doubling this term:

$$\Gamma \approx 2\Gamma_{\nabla\phi}. \tag{4.18}$$

This approximation effectively replaces the overestimated phase-field energy with its more reliable gradient-based counterpart. Based on this principle, a dynamic correction factor is defined by comparing the standard simulated area, $\Gamma_{\text{sl}} = \Gamma_{\text{sl},\phi} + \Gamma_{\text{sl},\nabla\phi}$, which incorporates the strain localization energy, with the proposed approximation. Recognizing that the gradient energy term is unaffected by strain localization (i.e., $\Gamma_{\text{sl},\nabla\phi} = \Gamma_{\nabla\phi}$), the factor is given by:

$$\mathcal{F}_{\text{DGCM}} = \frac{\Gamma_{\text{sl}}}{\Gamma} = \frac{\Gamma_{\text{sl},\phi} + \Gamma_{\nabla\phi}}{2\Gamma_{\nabla\phi}} = \frac{1}{2}\left(1 + \frac{\Gamma_{\text{sl},\phi}}{\Gamma_{\nabla\phi}}\right). \tag{4.19}$$

This approach can be directly applied to PFF problems, where the parameters in the correction factor are computed as integrals over the domain, obtained from the finite element solution at each simulation step. Since the gradient term is not affected by strain localization, whereas the phase-field term is, the correction factor —being a function of these known quantities— enables the correction of the overestimation effect. Therefore, the correction factor can be generalized to two or three dimensions, following the same rationale as the extension of the Bourdin correction to higher dimensions, as follows:

$$\mathcal{F}_{\text{DGCM}} = \frac{1}{2}\left(1 + \frac{\int_\Omega \phi^2 \, \mathrm{d}\Omega}{l^2 \int_\Omega |\nabla\phi|^2 \, \mathrm{d}\Omega}\right). \tag{4.20}$$

The proposed DGCM correction offers several key advantages. Its definition is independent of the mesh size (h). Instead of being a global correction factor, it can be viewed as a local correction factor that adapts to the entire domain and evolves during the different time steps of a PFF simulation, making it robust for unstructured meshes and complex crack paths. Crucially, it extends directly to 3D simulations without modification, based on the same assumption discussed in Section 4.3.1.

4.5 Comparative summary of correction methods

The main correction methods for crack area overestimation in phase-field modeling can be grouped into three categories: (1) mesh-dependent corrections, such as the Bourdin factor, which scale the computed crack area based on the element size and length scale; (2) post-processing techniques like skeletonization (see Section 3.5.2), which estimate the crack area by thresholding the phase-field variable and extracting the crack path; and (3) energy-based approaches, such as the DGCM, which exploit the equipartition property of the phase-field model to provide a mesh-independent correction. These methods differ in their assumptions, implementation complexity, and applicability to complex geometries or three-dimensional problems. Table 4.1 summarizes the formulas for the correction factor, $\mathcal{F}$, for each method.

It should be noted that the application of the Bourdin correction requires that $\Gamma = 1$. Similarly, the proposed method DGCM requires that the equipartition of the phase-field and gradient energies holds; thus, the accuracy of this method hinges on the validity of this assumption. These two conditions are equivalent: if energy equipartition holds (i.e., the two energy components are equal), the condition $\Gamma = 1$ is satisfied, and *vice versa*. The relative error associated with the application of this correction factor is given by:

$$\text{Relative Error} = \frac{|2\Gamma_{\nabla\phi} - \Gamma|}{\Gamma} = \frac{a}{l}\frac{1 - \tanh^2(a/l)}{\tanh(a/l)}. \tag{4.21}$$

Table 4.1: Summary of correction factors for crack area overestimation.

Method	**Correction Factor ($\mathcal{F}$)**	**Type**
Bourdin	$\mathcal{F}_{\text{Bourdin}} = 1 + \dfrac{h}{2l}$	Constant
DGCM	$\mathcal{F}_{\text{DGCM}} = \dfrac{1}{2}\left(1 + \dfrac{\int_\Omega \phi^2 \, \mathrm{d}\Omega}{l^2 \int_\Omega \lvert\nabla\phi\rvert^2 \, \mathrm{d}\Omega}\right)$	Dynamic
Skeletonization	$\mathcal{F}_{\text{skeleton}} = \dfrac{\Gamma_{\text{sl}}}{\Gamma_{\text{measured}}}$	Dynamic

This error reduces rapidly as the a/l ratio increases; for instance, at $a/l = 5$, the error is less than 0.1%. This error expression is specific to the AT2 model, which has infinite support. For models with finite support (like AT1), the error is exactly zero provided the phase-field has sufficient space to develop without boundary interference.

Once determined, the correction factor $\mathcal{F}$ is applied to the raw simulation results (denoted by the subscript 'sl'), which include the effects of strain localization, to recover the physical quantities. These transformations refer to those presented in Table 3.1, which correspond to Scheme I presented in Table 3.2. However, for clarity and ease of reference, the definition is introduced in Table 4.2, which refers directly to the simulated crack area as Γ_{sl}.

Energy-related quantities, such as the crack area and the degraded strain energy ($\Psi = \int_\Omega g(\phi)\, \psi(\boldsymbol{\epsilon}) \, \mathrm{d}\Omega$), are scaled by $1/\mathcal{F}$. Consistent with this energy scaling, both force and displacement are scaled by $1/\sqrt{\mathcal{F}}$. Consequently, the stiffness—defined as the ratio of force to displacement—remains invariant under this correction.

Table 4.2: Transformations from simulated (sl) to physical quantities using the correction factor $\mathcal{F}$.

Physical Quantity	**Transformation**
Crack Area (Γ)	$\Gamma_{\text{phys}} = \Gamma_{\text{sl}}/\mathcal{F}$
Degraded Strain Energy (Ψ)	$\Psi_{\text{phys}} = \Psi_{\text{sl}}/\mathcal{F}$
Force (P)	$P_{\text{phys}} = P_{\text{sl}}/\sqrt{\mathcal{F}}$
Displacement (u)	$u_{\text{phys}} = u_{\text{sl}}/\sqrt{\mathcal{F}}$
Stiffness (K)	$K_{\text{phys}} = K_{\text{sl}}$

4.6 Finite element discretization error

Similar to the analysis in Section 2.2.2, the influence of finite element discretization error on the computed crack surface energy is examined here for a scenario where boundary effects are negligible. While the correction methods discussed previously—such as the DGCM—are designed to mitigate the overestimation caused by strain localization, they do not directly address errors arising from the numerical discretization of the phase-field profile itself. These discretization errors impact the energy components differently. Figure 4.4 presents the relative error in the total crack surface energy Γ, the phase-field energy component Γ_ϕ, and the gradient energy component $\Gamma_{\nabla\phi}$ obtained from a one-

dimensional finite element simulation, plotted as a function of the mesh resolution ratio l/h.

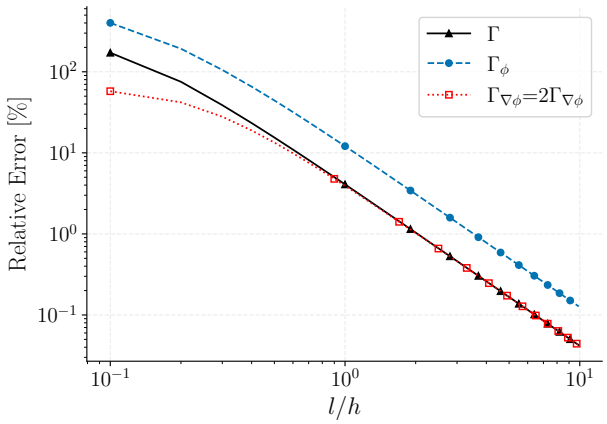

Figure 4.4: Relative error in the total crack surface energy Γ, phase-field energy component Γ_ϕ, and gradient energy component $\Gamma_{\nabla\phi}$ in a finite element one-dimensional simulation as a function of the mesh resolution ratio l/h.

In this scenario, where boundary effects are negligible, the energy equipartition condition holds ($\Gamma_\phi = \Gamma_{\nabla\phi}$). Consequently, the total energy can be approximated as twice the gradient energy ($2\Gamma_{\nabla\phi}$). By applying this approximation, the error in the total energy becomes dependent solely on the gradient energy term, which, as shown in the figure, exhibits a lower error than that obtained by directly summing the two numerical components.

Regarding the finite element discretization, Section 2.2.2 previously analyzed the energy error for a half-bar model. Although the specific discretization case where $\phi = 1$ at the element midpoint was not explicitly addressed there, the prevalence of strain localization in PFF simulations—where ϕ artificially saturates to 1 across entire elements—implies that the discretization error behaves similarly to the symmetric problem analyzed in that section.

4.7 Numerical examples and validation

To validate the proposed correction method for crack area overestimation, this section presents two benchmark examples to analyze the performance of the DGCM method and compare it against established approaches, specifically the Bourdin correction and the skeletonization technique. For this purpose, the center-cracked tension specimen and a modified compact tension specimen with internal voids are considered.

4.7.1 Center-cracked tension specimen

First, the proposed correction method is analyzed and compared with the Bourdin correction. The convergence of key quantities, such as crack length and peak force, is examined as a function of element size and the length scale parameter. Subsequently, the method's performance is evaluated in a three-dimensional context to demonstrate its applicability to 3D problems.

For this purpose, the center-cracked tension specimen introduced in Section 3.6.2 is utilized. To facilitate a direct comparison, the geometric dimensions and material parameters

are kept identical to those in the reference study (see Figure 3.6 and Table 3.3 in Chapter 3). Consequently, only the length scale parameter l and the mesh size h are varied in the present analysis. This test case is ideal for validation, as the crack path is known a priori and analytical reference solutions from LEFM (LEFM) are available.

The specimen geometry and loading configuration are shown in Figure 3.6(a). All simulations exploit the specimen's symmetry. Figure 4.5 shows the half-symmetry FEM model, which is used for the three-dimensional analysis in the following sections. Figure 3.6(b) depicts the quarter-symmetry model, which is first considered under plane strain conditions, with a specimen thickness of $B = 1$ mm. In this case the left edge is constrained in the horizontal direction, while the bottom edge is fixed vertically in the region where the initial crack is absent. The top edge is subjected to an upward traction force. The energy-controlled algorithm is employed, with the traction force direction set as $\boldsymbol{t} = (0, 1/A_{\text{surface}})$ kN, where A_{surface} is the area of the top surface where the traction is applied. The constants $c_1 = 1$ kN/mm and $c_2 = 1.0$ are used in the energy-controlled algorithm.

In this specimen, the crack propagates along a known straight horizontal path from the initial notch. This geometry allows for a straightforward characterization of boundary effects using the ratio H/l, where H is the distance to the top boundary. With a length scale of $l = 0.1$ mm and a half-height of $H = 3.0$ mm, this ratio is $H/l = 30$. Since $\tanh(30) \approx 1$, the influence of the boundary is negligible. Additionally, the presence of a single, isolated crack eliminates interactions with other fracture zones. Under these conditions, the assumptions underlying both the Bourdin correction and the proposed DGCM are fully satisfied, and the theoretical relative error for the DGCM (Eq. (4.21)) effectively vanishes. It is worth noting that while boundary effects may be slightly more pronounced during the initial nucleation phase, they become insignificant once the crack is fully developed and propagating parallel to the distant top and bottom boundaries.

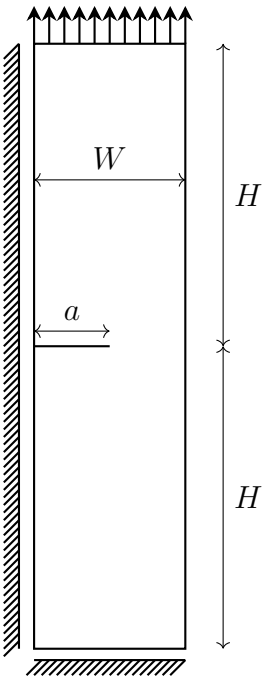

Figure 4.5: Schematic of the center-cracked tension test specimen. Half-symmetry finite element model.

This analysis investigates the influence of the length scale parameter l and the mesh size h. A critical aspect of this study is the ratio l/h, which can be realized through various combinations of these parameters. To systematically explore this relationship and facilitate comparison, the scaling factors ρ_1 and ρ_2 are introduced, defining the ratio as:

$$\frac{l}{h} = \frac{\rho_1 l_0}{\rho_2 h_0} \tag{4.22}$$

where $l_0 = 0.0125$ mm and $h_0 = 0.005$ mm represent the base values for the length scale and mesh size, respectively, corresponding to Simulation 1. The specific parameter sets used for this analysis, along with all performed simulations, are detailed in Table 4.3. Note that all l/h ratios are chosen to be greater than 2, ensuring that the phase-field profile is sufficiently resolved in accordance with the guidelines proposed by [3].

#	ρ_1	ρ_2	Length scale l (mm)	Mesh size h (mm)	l/h
1	1.0	1.0	0.012500	0.005000	2.5
2	0.2	0.2	0.002500	0.001000	2.5
3	0.1	0.1	0.001250	0.000500	2.5
4	0.05	0.05	0.000625	0.000250	2.5
5	1.0	0.6250	0.012500	0.003125	4.0
6	0.2	0.125	0.002500	0.000625	4.0
7	0.1	0.0625	0.001250	0.0003125	4.0
8	0.05	0.03125	0.000625	0.00015625	4.0
9	0.20000	0.1666	0.002500	0.000833	3.0
10	0.20000	0.1	0.002500	0.000500	5.0
11	0.20000	0.0833	0.002500	0.0004166	6.0

Table 4.3: Phase-field simulation parameters for the center-cracked tension specimen. Columns ρ_1 and ρ_2 list the scaling factors used to obtain l and h from base values.

Figure 4.6 presents the results of Simulation 8, comparing the reference solution, the solutions obtained after applying the post-processing correction methods, and the analytical LEFM solution. Figure 4.6(a) shows the force-displacement response. As observed, the results obtained with either the Bourdin correction or the proposed DGCM are in good agreement with the LEFM solution, whereas the uncorrected results deviate significantly. It is also important to note the presence of a peak force overshoot in the reference solution, a phenomenon reported by other authors [14, 12, 13]. This overshoot persists with the Bourdin correction, as it acts as a constant scaling factor. In contrast, the proposed DGCM effectively eliminates this artifact, acting as a regularization mechanism. Figure 4.6(b) displays the stiffness as a function of crack length. Again, the corrected solutions match the LEFM prediction well. A zoomed view of the initial crack propagation phase reveals that, in all cases, a loss of stiffness occurs due to damage accumulation during loading.

To rigorously analyze the convergence of the correction factors, two key quantities are examined: the peak force value and the crack length corresponding to a fixed stiffness. This analysis is conducted in two stages. First, the influence of the length scale parameter

l is investigated by decreasing l while maintaining a constant ratio l/h. Second, the effect of mesh refinement is isolated by varying the element size h while keeping the length scale parameter l constant.

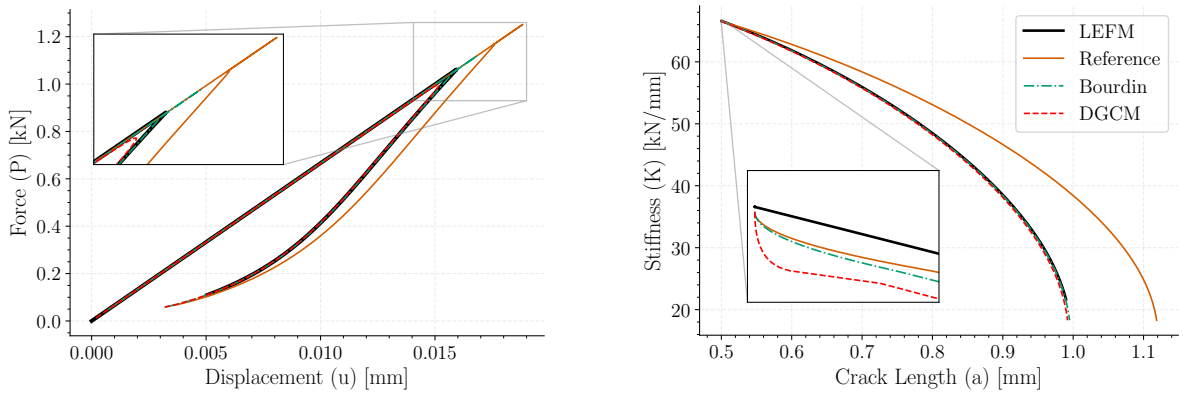

(a) Force-displacement response.

(b) Stiffness vs. crack length.

Figure 4.6: Comparison of numerical results with the analytical LEFM solution for the center-cracked specimen (Simulation 8). (a) Force-displacement response. (b) Stiffness degradation as a function of crack length.

Convergence analysis with respect to length scale l at constant mesh resolution l/h

First, the influence of the length scale parameter l is analyzed. This study is conducted using a fixed mesh resolution ratio of $l/h = 2.5$, ensuring that the phase-field profile remains well-resolved and that the element size scales proportionally with the length scale. The simulations corresponding to $l/h = 2.5$ are detailed in rows 1-4 of Table 4.3.

Before presenting the formal convergence analysis, several key curves are examined to provide an intuitive understanding of the model's behavior. Figure 4.7(a) illustrates the specimen stiffness as a function of the applied force using the proposed DGCM. As the length scale parameter decreases, the onset of damage during the initial loading phase is delayed, and the response converges toward a constant stiffness that matches the LEFM prediction. Furthermore, the graph demonstrates that as l decreases, the maximum force at crack initiation converges to a stable value, closely aligning with the theoretical prediction. Notably, the proposed method eliminates the force overshoot observed in both the uncorrected reference results and the Bourdin correction.

Figure 4.7(b) displays the DGCM correction factors as a function of the corrected crack length. Since these simulations share the same l/h ratio, the Bourdin correction factor remains constant across all cases; this is represented by a solid horizontal line on the graph. As the length scale is reduced, the initial transient region of the curve — associated with crack nucleation and the peak force overshoot — becomes sharper, eventually converging to a linear trend. This indicates that in the limit as $l \to 0$, the correction factor rapidly stabilizes.

Having analyzed the general trends of the correction factors, the convergence behavior of the peak force and the crack length corresponding to a fixed stiffness value is now examined. This analysis compares the uncorrected reference solution with results obtained using the Bourdin and DGCM correction methods.

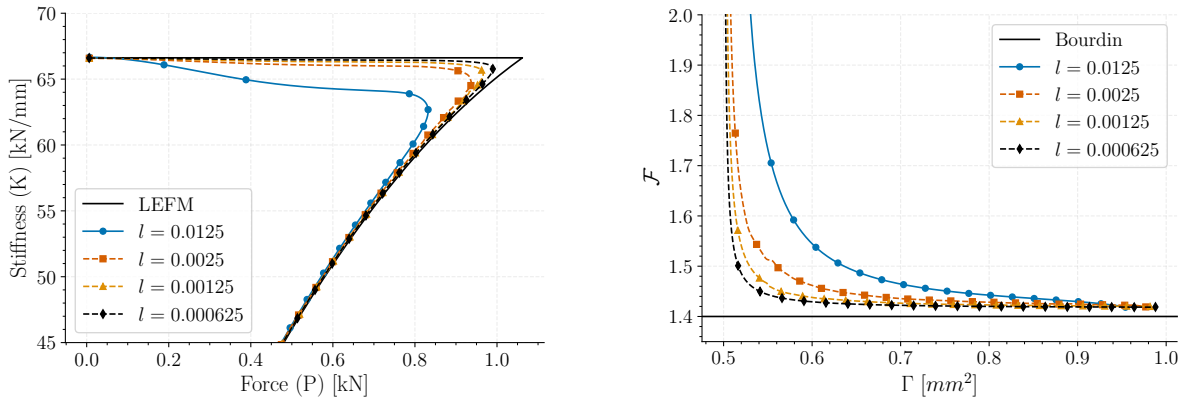

(a) Stiffness vs. applied force.

(b) Correction factor evolution vs. crack length.

Figure 4.7: Convergence analysis for a constant mesh resolution ratio $l/h = 2.5$. (a) Stiffness degradation as a function of applied force for decreasing length scales l, illustrating convergence toward the LEFM solution. (b) Evolution of the DGCM correction factor with crack length compared to the constant Bourdin factor.

Figure 4.8(a) depicts the peak force as a function of the length scale parameter l for the reference and corrected solutions. The uncorrected reference solution exhibits the highest force values, significantly inflated by the characteristic force overshoot. The Bourdin correction, acting as a constant scaling factor, reduces the peak force magnitude but fails to eliminate the overshoot artifact. In contrast, the proposed DGCM correction not only significantly reduces the peak force but also effectively suppresses the overshoot. As the length scale l decreases, the DGCM-corrected peak force converges toward the theoretical value predicted by LEFM (LEFM). Conversely, while the other methods show a decreasing trend with smaller l, they consistently overestimate the theoretical peak force.

Figure 4.8(b) illustrates the convergence of the crack length for a fixed stiffness value of 38.52514 kN/mm. The theoretical crack length corresponding to this stiffness is 0.9 mm. Since this measurement point is well beyond the initial crack nucleation phase and the associated force overshoot, both the Bourdin and DGCM corrections yield similar results. As the length scale parameter decreases, both methods converge toward the theoretical crack length.

In addition to the primary analysis with $l/h = 2.5$ (solid lines), Figures 4.8(a) and 4.8(b) also display results for a finer mesh resolution ratio of $l/h = 4.0$ (dashed lines). For the peak force, the finer mesh results in higher values for both correction methods compared to the coarser mesh. However, for the uncorrected solution, the peak force decreases with mesh refinement. It is worth noting that as the ratio $h/l \to 0$, the Bourdin correction factor approaches unity, causing the corrected and uncorrected solutions to coincide. A similar convergence behavior is observed for the crack length measurements.

Finally, Figure 4.9 shows the convergence of the DGCM correction factor evaluated at three distinct crack lengths: 0.55 mm, 0.75 mm, and 0.9 mm. Additionally, the Bourdin correction factor is plotted; since the ratio l/h is held constant in this analysis, this factor appears as a constant horizontal line. As the length scale parameter decreases, the DGCM correction factor drops rapidly, indicating that the relative overestimation of the crack area diminishes with finer length scales. Furthermore, at crack lengths far from the initial nucleation zone (e.g., 0.75 mm and 0.9 mm), the correction factors converge to

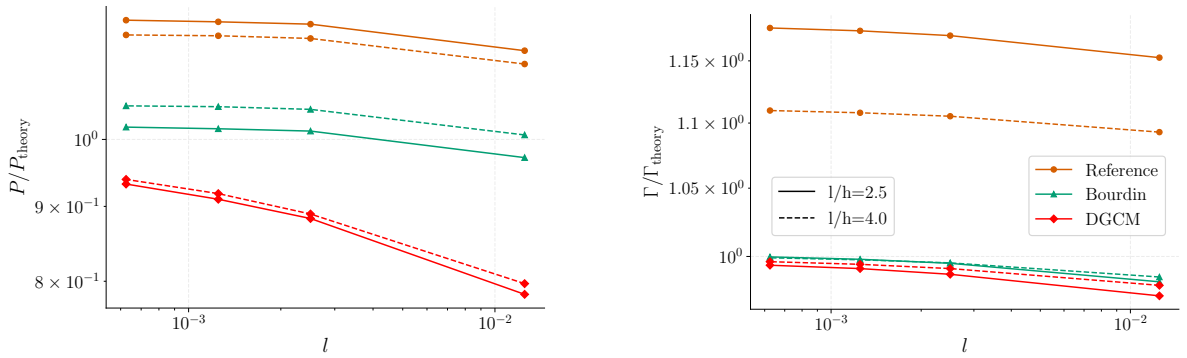

(a) Convergence of the peak force.

(b) Convergence of crack length at fixed stiffness ($K \approx 38.5$ kN/mm).

Figure 4.8: Convergence analysis with respect to the length scale parameter l for constant mesh resolution ratios ($l/h = 2.5$ and $l/h = 4.0$). (a) Peak force convergence toward the LEFM limit. (b) Crack length convergence for a specific stiffness value.

similar values, as the influence of the initial peak force overshoot dissipates.

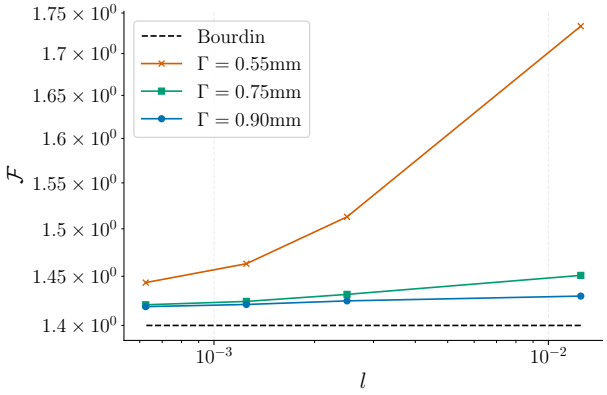

Figure 4.9: Convergence of the DGCM correction factor as a function of the length scale parameter l for different crack lengths.

Convergence analysis with respect to mesh size h at constant length scale l

In this case, the length scale parameter is fixed at $l = 0.0025$ mm, while the mesh size h is varied to study the influence of mesh refinement. The simulations corresponding to this analysis are detailed in rows 2, 6, 9, 10, and 11 of Table 4.3.

Figure 4.10(a) shows the evolution of the peak force as a function of mesh size h for a fixed length scale $l = 0.0025$ mm. As the mesh is refined (i.e., h decreases), the Bourdin correction factor approaches 1, causing the Bourdin-corrected solution to converge toward the uncorrected result. Notably, the uncorrected solution exhibits a decreasing trend in peak force with mesh refinement, while the Bourdin-corrected peak force increases as the mesh size becomes smaller. This indicates a tendency for the peak force to increase with decreasing mesh size when the Bourdin correction is applied. In contrast, the proposed DGCM correction consistently yields a lower and more stable peak force, effectively eliminating the artificial peak observed in standard phase-field simulations. Furthermore, the DGCM-corrected peak force demonstrates reduced sensitivity to mesh refinement, indi-

cating improved robustness and convergence with respect to mesh size. It is also observed that, as the mesh is refined, both the uncorrected and Bourdin-corrected results converge toward a common value that lies between them, with the DGCM-corrected result closely matching this converged value.

Figure 4.10(b) illustrates the convergence of the crack length for a fixed stiffness value of 38.52514 kN/mm as the mesh is refined. Similar to the previous analysis, both the Bourdin and DGCM corrections yield comparable results for this measurement point, which is well beyond the initial crack nucleation phase. As the mesh size decreases, both correction methods converge toward the theoretical crack length of 0.9 mm.

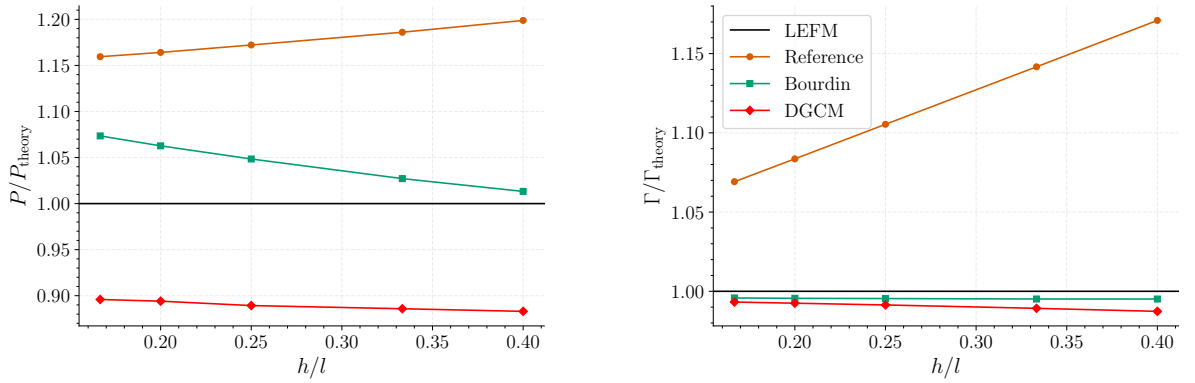

(a) Convergence of the peak force.

(b) Convergence of crack length at fixed stiffness ($K \approx 38.5$ kN/mm).

Figure 4.10: Convergence analysis with respect to mesh size h for a constant length scale $l = 0.0025$ mm. (a) Peak force convergence. (b) Crack length convergence for a specific stiffness value.

Figure 4.11 shows the convergence of the Bourdin and DGCM correction factors as a function of mesh size h, evaluated at a crack length of 0.9 mm. As the mesh is refined (i.e., as h decreases), both correction factors decrease and approach unity, indicating that the overestimation effect diminishes with finer meshes.

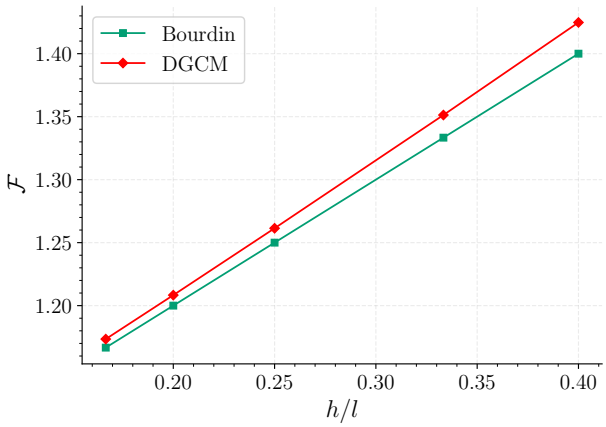

Figure 4.11: Convergence of the Bourdin and DGCM correction factors as a function of mesh size h, evaluated at a crack length of 0.9 mm.

Extension to 3D

To demonstrate the applicability and robustness of the DGCM in three-dimensional scenarios, the analysis is extended to a 3D version of the center-cracked tension specimen. The half-symmetry model shown in Figure 4.5, with an assigned thickness of $B = 0.05$ mm, is employed. The boundary conditions are defined as follows: the left face is constrained horizontally to enforce symmetry, and the bottom face is constrained in the vertical and out-of-plane directions. The mesh consists of tetrahedral elements with a characteristic size of $h \approx 0.0025$ mm in the expected crack propagation zone. A length scale of $l = 0.00625$ mm is used, resulting in a mesh resolution of $l/h \approx 2.5$. The simulation utilizes the non-variational energy-controlled scheme with constants $c_1 = 1.5$ kN/mm and $c_2 = 1.0$, keeping material properties consistent with the 2D analysis.

This validation is particularly significant because 3D simulations often involve complex, unstructured meshes where methods like skeletonization are challenging to implement. Although it might be possible to approximate the crack area in this specific example by applying skeletonization to one of the external faces, the proposed DGCM provides a direct measurement without such complexities. Furthermore, the Bourdin correction is typically evaluated for one-dimensional or two-dimensional quadrilateral elements, implying a straightforward extension to hexahedral elements in 3D. In contrast, the assumption underlying the proposed method applies universally to all element types in one, two, or three dimensions without requiring additional considerations.

The evolution of the crack front is visualized in Figure 4.12, which displays the isosurfaces where the phase-field variable $\phi > 0.95$ at different stages of the simulation.

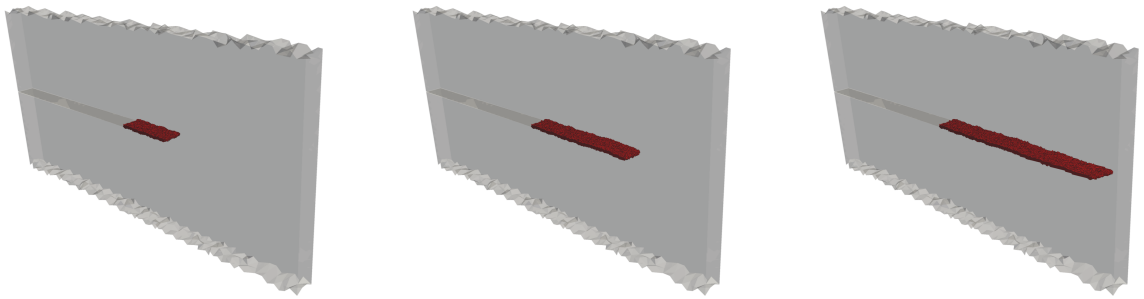

(a) Initial propagation (b) Mid-propagation (c) Final stage

Figure 4.12: Crack propagation in the 3D center-cracked tension specimen. The images show the isosurface of the phase-field variable for $\phi > 0.95$ at three different stages of the simulation, illustrating the evolution of the crack front.

Table 4.4 presents the crack area obtained using the different correction methods at three distinct stages of crack propagation. Additionally, the relative error of the reference, Bourdin, and DGCM methods with respect to the skeletonization measurement is shown. As observed, the proposed DGCM yields the smallest relative error. In general, errors are larger for all methods during the initial stage, where crack nucleation and peak force effects are more pronounced. These results demonstrate the effectiveness of the DGCM in accurately estimating the crack area in a 3D context, significantly outperforming the Bourdin correction while avoiding the complexities associated with skeletonization on unstructured meshes.

Table 4.4: Evolution of the crack area and relative error (in parentheses) with respect to the Skeletonization method in the 3D center-cracked specimen.

Correction Method	**Initial Prop.** (mm^2)	**Mid Prop.** (mm^2)	**Final Stage** (mm^2)
Skeletonization	0.00707	0.01493	0.02222
Reference	0.01035 (46.26%)	0.02051 (37.36%)	0.03057 (37.63%)
Bourdin	0.00862 (21.88%)	0.01709 (14.47%)	0.02548 (14.69%)
DGCM	0.00752 (6.24%)	0.01515 (1.45%)	0.02278 (2.54%)

4.7.2 Modified compact tension specimen

This section validates the proposed correction factor by comparing its performance against the Bourdin and skeletonization methods in a complex scenario involving curvilinear crack paths. The analysis employs the modified compact tension (CT) specimen with internal voids as presented in Section 3.7, using the same material and simulation parameters for validation.

Three configurations are analyzed: the standard CT specimen without additional holes (Specimen 1) and two modified specimens with varying initial crack positions. For Specimen 1, the initial crack is centered ($H = 0.60W$), resulting in a symmetric configuration. The other two configurations are Specimen 2 ($H = 0.56W$) and Specimen 4 ($H = 0.64W$). All simulations are performed under plane strain conditions with a specimen thickness of $B = 0.08W$.

The boundary conditions, illustrated in Figure 3.18, involve constraining the lower half of the bottom loading hole in all directions and applying a distributed vertical force to the upper half of the top loading hole. Following the analysis in [17], a length scale parameter of $l = 0.0025W = 0.1$ mm is used with a mesh resolution of $l/h = 2.5$. The energy-controlled solver is employed with constants $c_1 = 1.0$ kN/mm and $c_2 = 1.0$ (dimensionless).

For Specimen 1, Figure 4.13(a) compares the correction factors obtained using the Bourdin, skeletonization, and the proposed DGCM methods, while Figure 4.13(b) presents the corresponding force-displacement curves. The uncorrected simulation yields a final crack length of 48.65 mm and a peak force of 21.31 kN. Applying the corrections significantly modifies these values: the Bourdin method results in 41.88 mm and 19.45 kN, whereas the skeletonization and DGCM methods provide much closer estimates of 39.99 mm (16.96 kN) and 40.06 mm (17.21 kN), respectively.

Turning to Specimen 2, the correction factors and force-displacement responses are depicted in Figures 4.14(a) and 4.14(b), respectively. In the uncorrected simulation, the final crack length reaches 23.96 mm with a peak force of 19.77 kN. While the Bourdin correction adjusts these values to 21.30 mm and 18.05 kN, the skeletonization and DGCM methods yield even smaller and more consistent estimates: 20.35 mm (15.41 kN) and 19.90 mm (15.70 kN), respectively.

Finally, for Specimen 4, the results are depicted in Figures 4.15(a) and 4.15(b). The uncorrected simulation predicts a final crack length of 33.11 mm and a peak force of 19.87 kN. The Bourdin correction adjusts these values to 28.93 mm and 18.14 kN. Con-

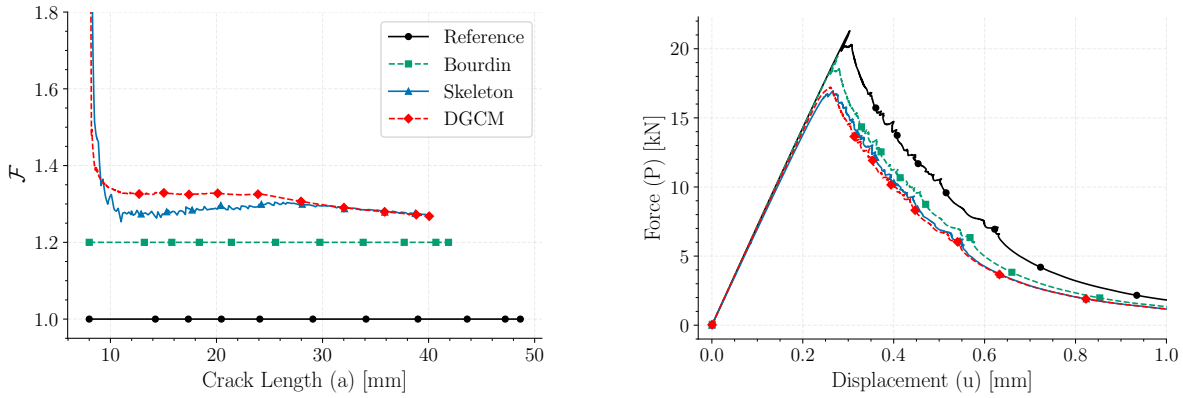

(a) Evolution of correction factors.

(b) Force-displacement response.

Figure 4.13: Specimen 1: (a) Comparison of crack length correction factors from the Bourdin, Skeletonization, and DGCM methods against the uncorrected result. (b) Force-displacement curves corresponding to each correction method.

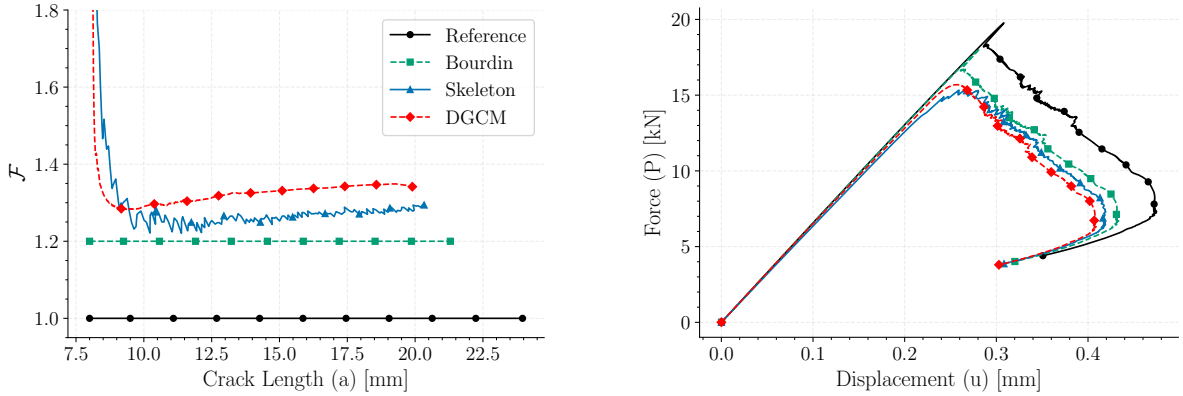

(a) Evolution of correction factors.

(b) Force-displacement response.

Figure 4.14: Specimen 2: (a) Comparison of crack length correction factors from the Bourdin, Skeletonization, and DGCM methods against the uncorrected result. (b) Force-displacement curves corresponding to each correction method.

sistent with the previous cases, the skeletonization and DGCM methods provide closer agreement, yielding corrected lengths of 27.22 mm (15.67 kN) and 26.83 mm (15.87 kN), respectively.

Table 4.5 summarizes the final crack lengths and peak forces for all three specimens, comparing the uncorrected results with those obtained using the Bourdin, skeletonization, and DGCM correction methods.

In all three cases, the uncorrected results exhibit the highest overestimation of the crack length. While the Bourdin correction reduces this overestimation, a significant discrepancy remains. In contrast, both the skeletonization and the proposed DGCM methods yield very similar and more accurate results.

A notable artifact is the presence of a peak force in the uncorrected force-displacement curves, which persists even when the Bourdin correction is applied. This occurs because the Bourdin factor acts as a constant scaling term dependent only on the mesh size and

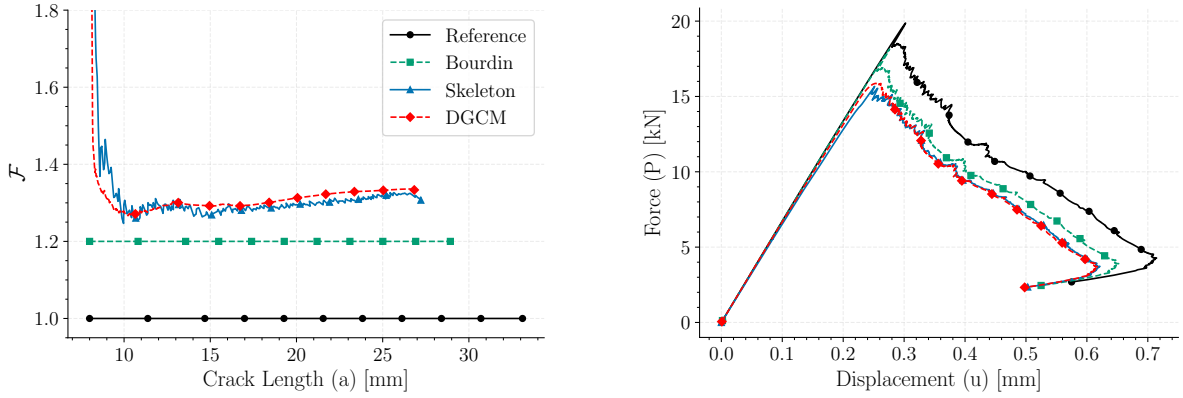

(a) Evolution of correction factors.

(b) Force-displacement response.

Figure 4.15: Specimen 4: (a) Comparison of crack length correction factors from the Bourdin, Skeletonization, and DGCM methods against the uncorrected result. (b) Force-displacement curves corresponding to each correction method.

Table 4.5: Comparison of final crack length (a) and peak force ($P_{\max}$) for the modified compact tension specimens using different correction methods.

Specimen	**Method**	**Crack Length** (mm)	**Peak Force** (kN)
Specimen 1	Uncorrected	48.65	21.31
	Bourdin	41.88	19.45
	Skeletonization	39.99	16.96
	DGCM	40.06	17.21
Specimen 2	Uncorrected	23.96	19.77
	Bourdin	21.30	18.05
	Skeletonization	20.35	15.41
	DGCM	19.90	15.70
Specimen 4	Uncorrected	33.11	19.87
	Bourdin	28.93	18.14
	Skeletonization	27.22	15.67
	DGCM	26.83	15.87

length scale. Conversely, the dynamic correction factors from the skeletonization and DGCM methods effectively eliminate this non-physical peak force. As demonstrated in the previous example, this regularization effect exhibits convergent behavior.

Fatigue assessment of complex compact tension specimens

This section revisits the fatigue analysis of the modified compact-tension specimen, originally presented in Section 3.7 as the decisive benchmark for the proposed fatigue framework. Unlike standard fracture tests, this geometry incorporates internal holes that induce complex, curvilinear crack trajectories, serving as a rigorous stress test for any computational fracture method. In Chapter 3, accurate fatigue life predictions for these specimens relied on the skeletonization technique to correct the inherent crack area overestimation of the phase-field method. Here, it is demonstrated that the DGCM can be effectively

applied to fatigue analysis.

The study focuses on the two configurations that showed consistent experimental agreement in the previous chapter: Specimen 2 ($H = 0.56W$) and Specimen 4 ($H = 0.64W$). In the reference fatigue study, skeletonization proved highly effective, yielding relative cycle-count errors below 4%. When the static, mesh-dependent Bourdin correction is applied instead, these errors increase to 4.72% and 9.53%, respectively, highlighting the limitations of static factors in capturing evolving crack topologies. The dynamic DGCM factor, however, delivers reliable results, with errors of 8.97% for Specimen 2 and a mere 0.60% for Specimen 4. It is crucial to note that these errors are computed using the Paris-law parameters originally calibrated in Chapter 3 specifically for the crack lengths obtained via skeletonization. Consequently, any discrepancy arises partly from the sensitivity of the fatigue model to the specific crack length definition used for calibration, rather than solely from the accuracy of the DGCM itself. Thus, this comparison serves primarily as a relative validation of the DGCM method against the established skeletonization benchmark. Figure 4.16 presents the fatigue life curves (crack length versus cycles) comparing the experimental data with the results obtained using the Bourdin, skeletonization, and DGCM correction methods.

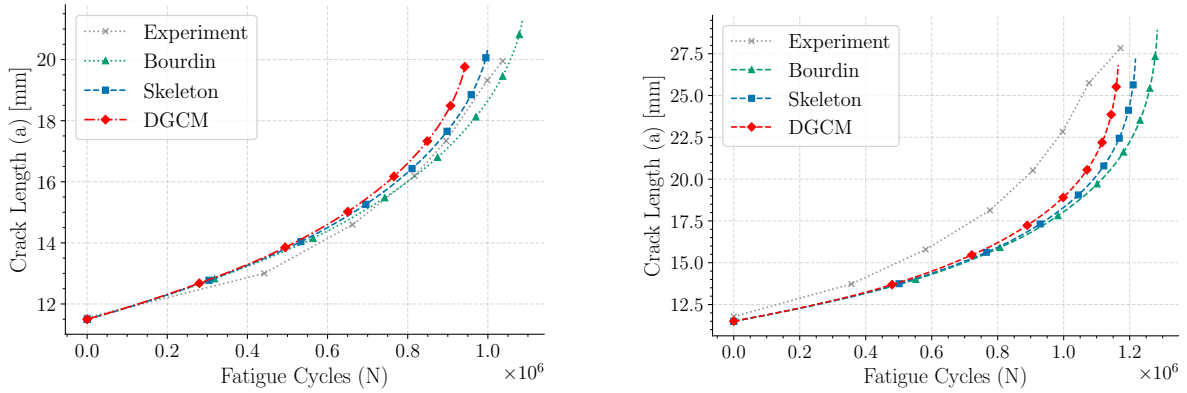

(a) Specimen 2 ($H = 0.56W$). (b) Specimen 4 ($H = 0.64W$).

Figure 4.16: Comparison of fatigue life predictions (crack length vs. number of cycles) for the modified compact tension specimens using different correction methods.

4.8 Extension to general phase-field formulations

Although the derivation presented in this work focuses on the AT2 model, the proposed correction method is applicable to a broader class of phase-field formulations. These models typically share a common structure comprising a phase-field dependent term and a gradient dependent term. They are constructed such that, when the phase-field profile is fully developed and free from boundary effects, the total crack surface energy integrates to 1, and the energy contributions from the phase-field and gradient terms satisfy the equipartition result.

A general form for the crack surface density is given in Eq. (2.18). So following the one-dimensional analysis, the total energy in the absence of numerical artifacts is given by:

$$\Gamma_t(\phi) = \frac{1}{c_0} \int_{-a}^{+a} \left(\frac{1}{l} \alpha(\phi) + l(\phi')^2 \right) dx. \tag{4.23}$$

When strain localization occurs, the phase-field variable artificially saturates to $\phi = 1$ across an element of size h, causing the gradient to vanish locally ($\phi' = 0$). The computed energy, Γ_{sl}, consequently includes an erroneous contribution from this saturated region:

$$\Gamma_{\text{sl}}(\phi) = \Gamma_{\text{t}}(\phi) + \frac{1}{c_0}\int_0^h \frac{1}{l}\alpha(1)\,dx = \Gamma_{\text{t}}(\phi) + \frac{h}{c_0 l}. \tag{4.24}$$

Assuming $\Gamma_{\text{t}} \approx 1$, this leads to a generalized Bourdin-like correction factor of $(1 + \frac{h}{c_0 l})$. This approximation holds when the phase-field has sufficient space to develop without boundary effects. For infinite support models like AT2, this requires $l \to 0$. However, for models with finite support like AT1, this condition is satisfied exactly provided the crack length exceeds the support width.

By relying on the energy equipartition property, a more robust correction can be formulated. Since the gradient term remains unaffected by the saturation artifact, the crack area can be approximated as twice the gradient energy:

$$\Gamma \approx 2\Gamma_{\nabla\phi} = \frac{2}{c_0}\int_\Omega l|\nabla\phi|^2 \mathrm{d}\boldsymbol{x}. \tag{4.25}$$

Consequently, the generalized DGCM factor for any such functional is defined as:

$$\mathcal{F}_{\text{DGCM}} = \frac{1}{2}\left(1 + \frac{1}{l^2}\frac{\int_\Omega \alpha(\phi)\,\mathrm{d}\boldsymbol{x}}{\int_\Omega |\nabla\phi|^2\,\mathrm{d}\boldsymbol{x}}\right). \tag{4.26}$$

4.9 Conclusions

This chapter introduces a novel method for correcting the overestimation of crack area in PFF simulations. Accurate crack measurement is essential for the proper analysis of PFF results, as this overestimation systematically affects the evaluation of key physical quantities such as forces, displacements, and energies.

The proposed correction factor is based on the following key observations:

- In standard finite element implementations of PFF models, a numerical artifact known as strain localization frequently occurs. This effect causes the phase-field variable, ϕ, to artificially saturate at a value of 1 across entire elements along the crack path. Consequently, the energy component dependent on the phase-field variable is significantly overestimated, leading to an inflated measurement of the crack area via the CSDF.
- Crucially, the energy component dependent on the phase-field gradient is not affected in the same way. Within a saturated element, the gradient of the phase field is zero; therefore, this artifact does not introduce an overestimation in the gradient-dependent energy term.
- The theoretical derivation for the phase field model demonstrates that the energy contributions from the phase field and its gradient are equal, provided there is sufficient space for the phase field to develop without interference from boundaries or other cracks. As illustrated with the analytical 1D solution, for an a/l ratio of 5, the error in this equipartition is less than 0.1%. Consequently, the physical crack area can be accurately approximated as twice the gradient-dependent energy. This result forms the basis of the proposed correction factor.

This correction method enables accurate fracture mechanics analysis without an increase in computational cost, as it relies on energy quantities already computed during the simulation. It is directly applicable to three-dimensional simulations, avoiding the need for complex skeletonization algorithms. Furthermore, its definition is independent of the finite element type (e.g., triangles, quadrilaterals, tetrahedra, or hexahedra), although the analyses in this work were conducted using quadrilateral and tetrahedral elements.

It is important to note that both the Bourdin and DGCM corrections are valid only when the length scale parameter is sufficiently small to satisfy the condition of energy equipartition. This requires the crack length to be large enough relative to the length scale to allow the phase-field to develop without interference from boundaries or other cracks. In the context of the Bourdin correction, this is equivalent to ensuring sufficient space for regularization to approach the theoretical infinite-domain solution.

Regarding the peak force artifact observed in uncorrected force-displacement curves, the proposed DGCM effectively mitigates this issue. By dynamically adjusting the correction factor based on the evolving energy distribution, the DGCM eliminates non-physical peaks. It is worth noting that the peak force predicted by this method is generally lower than that of other methods, yielding a more conservative estimate of the maximum load. Convergence studies demonstrate that as the length scale parameter is reduced, the peak force obtained with the proposed correction converges to a stable value. Additionally, the proposed method exhibits less sensitivity to mesh resolution for a constant length scale compared to the Bourdin correction, as the latter depends explicitly on the element size.

Another critical condition is that the mesh resolution must be sufficient to accurately capture the phase-field profile. As established by [15], a ratio of $l/h \geq 2$ is generally recommended for linear elements. The analysis confirms that for this resolution, the error in the CSDF is approximately 1%. While this error analysis is based on the one-dimensional case, the strain localization effect—which induces a constant phase-field value of $\phi = 1$ across an entire element—implies that the discretization error is directly related to the symmetric problem analyzed previously. Therefore, the resolution criteria discussed ensure a correct approximation, though extensions to two or three dimensions may introduce additional geometric considerations.

It is also important to note that all simulations in this work were performed using an energy-controlled solver. This approach enables the capture of the full equilibrium path during crack propagation. Furthermore, this algorithm enforces irreversibility globally, ensuring that the sum of the fracture energy components does not decrease. This condition allows for the analysis of strain localization without the constraints of local irreversibility enforcement. While this study traces the equilibrium path, it is worth noting that in standard displacement-controlled schemes, the critical load would correspond to the peak force overshoot discussed herein.

While this work focuses on the widely used AT2 crack surface representation, the methodology can be adapted for other regularized models, such as the AT1 model, as detailed in Section 4.8. For models with finite support like AT1, the application of the correction factor is valid provided the phase-field support is fully developed—that is, when the crack length exceeds the support width of the phase-field. Under these conditions, energy equipartition holds, and the correction factor can be applied.

Chapter 5

THE LATENT VARIABLE PROXIMAL POINT ALGORITHM FOR PHASE-FIELD FRACTURE

In PFF problems, the phase-field variable ϕ is subject to fundamental inequality constraints: the interval constraint ($0 \leq \phi \leq 1$) and the irreversibility of crack growth ($\dot{\phi} \geq 0$). Enforcing these constraints is crucial to ensure the physical realism of the model, but it also introduces significant numerical challenges. This chapter introduces the Latent Variable Proximal Point (LVPP) algorithm as a robust numerical framework for solving PFF problems while effectively handling these constraints.

The LVPP algorithm, presented in [10] and later applied to several problems in [11], provides a general computational strategy for variational problems with inequality constraints. Built on the Bregman proximal point framework [62, 63] and enriched by the introduction of latent variables [10], the LVPP reformulates the inequality-constrained optimization problem into a sequence of saddle-point problems involving latent variables.

The LVPP formulation was primarily applied to phase-field fracture models in [11], considering the AT2 regularization, where the LVPP formulation enforces the lower-bound constraint on the phase-field variable, although the quadratic nature of the AT2 model implicitly prevents values below 0. As a result, its main effect in this setting is to enforce the irreversibility constraint. In this work, the LVPP formulation is also presented for the AT1 and Wu regularizations, in which the lower-bound constraint must be explicitly enforced, while also handling the irreversibility condition.

In this chapter, the LVPP framework is specialized for phase-field fracture to address the boundedness of the damage variable and the irreversibility of crack evolution. A central advantage of this formulation is that the constraints are embedded at the continuum level through the latent-variable mapping, rather than being imposed through auxiliary penalties or ad hoc discrete corrections. Consequently, the method can be implemented in a standard finite element setting and solved with a Newton–Raphson strategy.

Traditional approaches, such as the penalty method, can lead to parameter sensitivity and numerical instabilities and require careful tuning of the penalty parameter [6]. Relative to these methods, the LVPP approach avoids user-defined penalization parameters that may affect the converged solution. History-field approaches [3] enforce irreversibility by

introducing a history field (commonly the running maximum of the tensile or active energy) that replaces the instantaneous active energy in the phase-field evolution equation. This effectively prevents damage healing but acts indirectly and does not explicitly enforce interval bounds on ϕ, so additional bound-preserving measures (for example, penalization) are sometimes required for regularizations such as AT1 or Wu. By contrast, LVPP enforces boundedness and irreversibility directly within the phase-field, preserving the variational structure of the problem. This also makes the framework largely agnostic to the crack surface density functional (CSDF), enabling a unified treatment of models such as AT1 and AT2 without model-specific modifications at the discrete-equation level.

As discussed in previous chapters, the CSDF is a core component of the PFF formulation, governing the approximation of sharp crack surfaces through a continuous phase-field variable. Since this component can be analyzed independently, it provides a natural starting point for introducing the LVPP algorithm, where the primary requirement is the enforcement of the interval constraint on ϕ. After establishing and validating the method for the CSDF, the formulation is extended to the full PFF problem, where both boundedness and irreversibility are enforced.

This chapter is organized as follows. First, Section 5.1 generalizes the CSDF and discusses the necessity of enforcing the interval constraint of the phase-field variable. Section 5.2 briefly introduces the strategies for handling these constraints, followed by a discussion of the standard penalty approach in Section 5.3. The core method is introduced in Section 5.4, detailing the application of the LVPP algorithm to the CSDF. This formulation is validated against analytical solutions in Section 5.4.4. Subsequently, Section 5.5 extends the LVPP framework to the full PFF problem, enforcing the interval constraint of the phase-field variable as well as its irreversibility. Comprehensive numerical benchmarks demonstrating the robustness of the method are presented in Section 5.5.5. Finally, Section 5.6 provides a summary of the results and concluding remarks.

To present the method transparently and assess its validity, the penalty approach is revisited as a reference baseline for comparison. The history-field method presented in Section 2.5.2 imposes irreversibility indirectly via a history field and cannot enforce the interval constraint directly. For this reason, both the penalty approach and the LVPP approach address the phase-field variable directly: although different, both schemes aim to enforce the bounds and irreversibility on the phase-field variable. Figure 5.1 schematically summarizes the workflow adopted in this work, contrasting the traditional penalty strategy with the proposed LVPP framework for both the isolated CSDF (Figure 5.1(a)) and the full PFF problem (Figure 5.1(b)).

5.1 Generalization and interval constraint of the CSDF

As discussed in Section 2.2, the CSDF is a fundamental component of the PFF method, enabling the approximation of sharp crack surfaces through a continuous phase-field variable. While Section 2.2 primarily focused on the AT2 regularization, this section details the general framework encompassing various regularization forms and outlines key considerations for their implementation.

The definition of the CSDF relies on the generic crack surface density function $\gamma(\phi, \nabla\phi)$, as introduced in Eq. (2.18) of Section 2.2. For clarity and ease of reference, the general

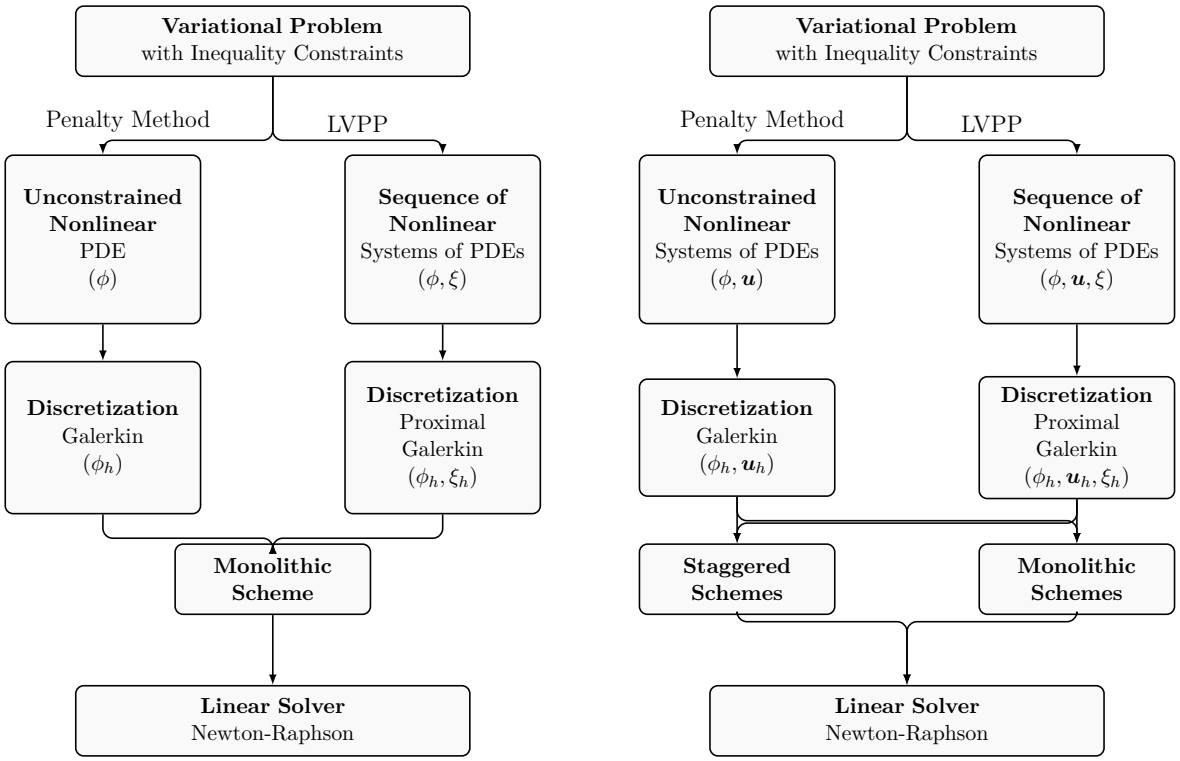

(a) CSDF (b) PFF

Figure 5.1: Solution strategies for (a) the CSDF and (b) the PFF problem. The schematics contrast the traditional penalty method (left branches) with the proposed LVPP algorithm (right branches).

form of the functional in Eq. (2.17) is restated here:

$$\Gamma(\phi) = \int_\Omega \frac{1}{c_0} \left(\frac{\alpha(\phi)}{l} + l|\nabla\phi|^2 \right) \mathrm{d}\boldsymbol{x}, \tag{5.1}$$

where l is the length scale parameter governing the width of the transition zone between no damage ($\phi = 0$) and full damage ($\phi = 1$). The term $\alpha(\phi)$ represents the geometric crack function, which must satisfy the conditions $\alpha(0) = 0$ and $\alpha(1) = 1$, and the normalization constant c_0 is defined as:

$$c_0 := 4 \int_0^1 \sqrt{\alpha(\eta)}\, \mathrm{d}\eta, \tag{5.2}$$

ensuring that the functional accurately recovers the sharp crack surface energy as $l \to 0$.

For the subsequent analysis, it is useful to decompose the functional Eq. (5.1) into two distinct parts: the phase-field energy Γ_ϕ and the gradient energy $\Gamma_{\nabla\phi}$, defined as:

$$\Gamma_\phi(\phi) := \frac{1}{c_0} \int_\Omega \frac{\alpha(\phi)}{l}\, \mathrm{d}\boldsymbol{x}, \tag{5.3}$$

$$\Gamma_{\nabla\phi}(\phi) := \frac{1}{c_0} \int_\Omega l|\nabla\phi|^2\, \mathrm{d}\boldsymbol{x}. \tag{5.4}$$

The equilibrium equation is derived by enforcing the stationarity condition $\delta\Gamma = 0$, leading to the variational form:

$$\Gamma'(\phi) = \int_\Omega \frac{1}{c_0} \left(\frac{\alpha'(\phi)}{l}\delta\phi + 2l\nabla\phi \cdot \nabla\delta\phi \right) \mathrm{d}\boldsymbol{x} = 0. \tag{5.5}$$

The corresponding strong form is given by:

$$\frac{1}{c_0}\left(\frac{\alpha'(\phi)}{l} - 2l\nabla^2\phi\right) = 0 \quad \text{in } \Omega, \tag{5.6}$$

$$\nabla\phi \cdot \boldsymbol{n} = 0 \quad \text{on } \partial\Omega. \tag{5.7}$$

The function $\alpha(\phi)$ can assume various forms. Table 5.1 and Figure 5.2 summarize the specific forms of $\alpha(\phi)$ for the AT2, AT1 (Ambrosio–Tortorelli) [4], and Wu [5, 41] regularizations, which are widely used in PFF analysis. In general, the Wu regularization is combined with specific degradation functions; in this work the focus is on the regularization itself, and it is therefore considered with a quadratic degradation function. For completeness, the double-well potential model is also shown in Figure 5.2(b). The table also provides the normalization constant c_0 as defined in Eq. (5.2).

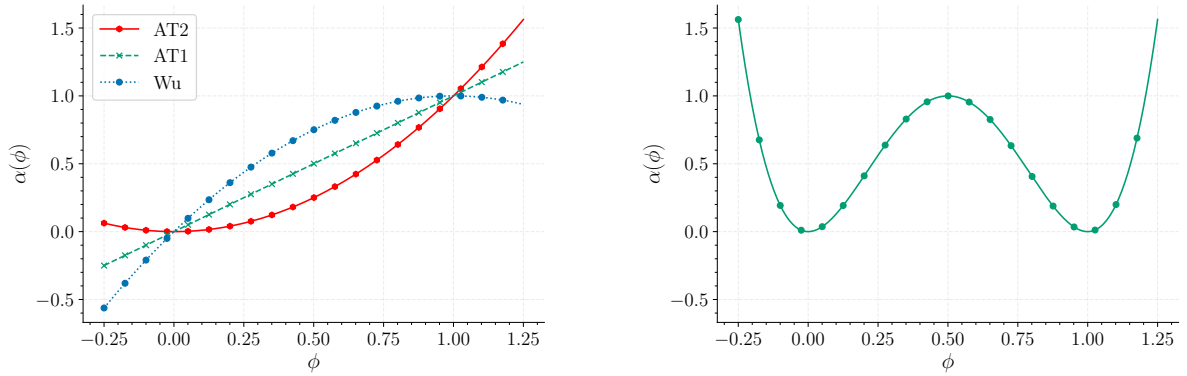

(a) Geometric crack function $\alpha(\phi)$ for the AT2, AT1, and Wu models.

(b) Double-well potential

Figure 5.2: Geometric crack functions $\alpha(\phi)$: (a) AT2, AT1, and Wu models; (b) double-well potential.

Model	$\alpha(\phi)$	$\alpha'(\phi)$	c_0
AT2	ϕ^2	2ϕ	2
AT1	ϕ	1	8/3
Wu	$2\phi - \phi^2$	$2 - 2\phi$	π
Double Well Potential	$16\phi^2(1-\phi)^2$	$32\phi(1-\phi)(1-2\phi)$	8/3

Table 5.1: Geometric crack functions $\alpha(\phi)$, their derivatives $\alpha'(\phi)$, and normalization constants c_0 for the AT2, AT1, Wu, and double-well regularizations.

The regularization functional is central to the phase-field approach, governing the smooth transition from no damage ($\phi = 0$) to full damage ($\phi = 1$). For the model to be physically meaningful, the phase-field variable ϕ must remain strictly within the interval $[0, 1]$.

Regarding the lower bound $\phi \geq 0$, the AT2 model—with its quadratic geometric function $\alpha(\phi) = \phi^2$—naturally satisfies this requirement. The energy is minimized at $\phi = 0$, inherently preventing the phase-field from taking non-physical negative values. In contrast,

the AT1 and Wu models contain terms that render the energy unbounded from below as $\phi \to -\infty$. Consequently, without explicit constraints, numerical minimization can drive ϕ to negative values. Therefore, it is essential to account for both the lower and upper bounds.

5.1.1 Analytical solution of the one-dimensional problem

An analytical study of the CSDF is conducted to investigate the implications of the interval constraints. This section examines the analytical solutions for the various regularization models, providing the motivation for the numerical strategies developed in subsequent sections.

The one-dimensional problem previously analyzed for the AT2 model in Section 2.2.1 is considered: a one-dimensional bar of length $2a$ with a central crack (see Figure 2.4). The crack is represented by a Dirichlet boundary condition $\phi(0) = 1$ at the center, combined with homogeneous Neumann conditions $\phi'(\pm a) = 0$ at the domain boundaries.

This boundary value problem, previously solved for the AT2 model, serves as a benchmark for the AT1 and Wu models. The equilibrium equation for the CSDF (Eq. (5.7)) reduces to the following ordinary differential equation (ODE), which must be solved subject to the physical constraint $0 \leq \phi(x) \leq 1$:

$$\frac{1}{c_0}\left(\frac{\alpha'(\phi(x))}{l} - 2l\phi''(x)\right) = 0 \quad \text{in } \Omega \tag{5.8}$$

$$\phi'(x) = 0 \quad \text{on } \partial\Omega, \tag{5.9}$$

$$0 \leq \phi(x) \leq 1 \quad \forall x \in \Omega. \tag{5.10}$$

Specifically, the governing ODEs for the AT2 model are provided in Eq. (2.25). For the AT1 and Wu models, the specific forms are:

$$\text{AT1:} \quad \frac{1}{2l} - l\phi''(x) = 0, \tag{5.11}$$

$$\text{Wu:} \quad \frac{1}{l}(1 - \phi(x)) - l\phi''(x) = 0. \tag{5.12}$$

For the AT2 model, the quadratic geometric function $\alpha(\phi) = \phi^2$ naturally yields non-negative solutions, making the explicit enforcement of the lower bound redundant in this specific analytical case. Its profile is given by Eq. (2.26), and its derivative by Eq. (2.27).

In contrast, for the AT1 and Wu models, solving the ODEs without constraints can lead to negative values of ϕ. Enforcing the condition $\phi \geq 0$ results in solutions with compact support, provided the domain size a is sufficiently large. The general solutions, accounting for both small and large domains relative to the length scale l, are derived as follows:

For the AT1 model, the phase-field variable $\phi(x)$ and its derivative $\phi'(x)$ are given by:

$$\phi_{\text{AT1}}(x) = \begin{cases} 1 - \frac{a|x|}{2l^2} + \frac{x^2}{4l^2} & \text{if } a < 2l, \\ \left(1 - \frac{|x|}{2l}\right)^2 & \text{if } a \geq 2l \text{ and } |x| < 2l, \\ 0 & \text{if } a \geq 2l \text{ and } |x| \geq 2l. \end{cases} \tag{5.13}$$

$$\phi'_{\mathrm{AT1}}(x) = \begin{cases} \frac{x}{2l^2} - \frac{a\,\mathrm{sgn}(x)}{2l^2} & \text{if } a < 2l, \\ \frac{x}{2l^2} - \frac{\mathrm{sgn}(x)}{l} & \text{if } a \geq 2l \text{ and } |x| < 2l, \\ 0 & \text{if } a \geq 2l \text{ and } |x| \geq 2l. \end{cases} \tag{5.14}$$

Similarly, for the Wu model:

$$\phi_{\mathrm{Wu}}(x) = \begin{cases} 1 & \text{if } a < \frac{\pi l}{2}, \\ 1 - \sin\left(\frac{|x|}{l}\right) & \text{if } a \geq \frac{\pi l}{2} \text{ and } |x| < \frac{\pi l}{2}, \\ 0 & \text{if } a \geq \frac{\pi l}{2} \text{ and } |x| \geq \frac{\pi l}{2}. \end{cases} \tag{5.15}$$

$$\phi'_{\mathrm{Wu}}(x) = \begin{cases} 0 & \text{if } a < \frac{\pi l}{2}, \\ -\frac{\mathrm{sgn}(x)}{l}\cos\left(\frac{|x|}{l}\right) & \text{if } a \geq \frac{\pi l}{2} \text{ and } |x| < \frac{\pi l}{2}, \\ 0 & \text{if } a \geq \frac{\pi l}{2} \text{ and } |x| \geq \frac{\pi l}{2}. \end{cases} \tag{5.16}$$

Substituting these profiles into Eq. (5.1), Eq. (5.3), and Eq. (5.4), the closed-form expressions for the energies are derived.

For the AT1 model:

$$\Gamma_{\mathrm{AT1}} = \begin{cases} \frac{3a}{4l} - \frac{a^3}{16l^3} & \text{if } a < 2l, \\ 1 & \text{if } a \geq 2l. \end{cases} \tag{5.17a}$$

$$\Gamma_{\phi,\mathrm{AT1}} = \begin{cases} \frac{3a}{4l} - \frac{a^3}{8l^3} & \text{if } a < 2l, \\ 1/2 & \text{if } a \geq 2l. \end{cases} \tag{5.17b}$$

$$\Gamma_{\nabla\phi,\mathrm{AT1}} = \begin{cases} \frac{a^3}{16l^3} & \text{if } a < 2l, \\ 1/2 & \text{if } a \geq 2l. \end{cases} \tag{5.17c}$$

For the Wu model:

$$\Gamma_{\mathrm{Wu}} = \begin{cases} \frac{2a}{\pi l} & \text{if } a < \frac{\pi l}{2}, \\ 1 & \text{if } a \geq \frac{\pi l}{2}. \end{cases} \tag{5.18a}$$

$$\Gamma_{\phi,\mathrm{Wu}} = \begin{cases} \frac{2a}{\pi l} & \text{if } a < \frac{\pi l}{2}, \\ 1/2 & \text{if } a \geq \frac{\pi l}{2}. \end{cases} \tag{5.18b}$$

$$\Gamma_{\nabla\phi,\mathrm{Wu}} = \begin{cases} 0 & \text{if } a < \frac{\pi l}{2}, \\ 1/2 & \text{if } a \geq \frac{\pi l}{2}. \end{cases} \tag{5.18c}$$

These general forms for $\phi(x)$ and the resulting energies are summarized in Table 5.2 and Table 5.3, respectively.

It is important to observe that the AT1 and Wu models exhibit compact support when the length scale l is sufficiently small relative to the domain size a. In these cases, ϕ vanishes identically beyond a certain distance from the point where $\phi = 1$, and the energy of the approximated functional exactly matches the sharp crack energy. In contrast, the AT2 model has infinite support; its energy asymptotically approaches the sharp crack energy only as the ratio $a/l \to \infty$. This behavior is illustrated in Figure 5.3, which compares the phase-field profiles and their gradients for all regularization models using a length-scale

Model	$\phi(x)$
AT2	$e^{-\frac{\lvert x\rvert}{l}} + \frac{2\sinh\left(\frac{\lvert x\rvert}{l}\right)}{e^{2a/l}+1}$
AT1	$\left(\frac{x^2}{4l^2} - \frac{\lvert x\rvert}{l} + 1\right) H(2l - \lvert x\rvert) + \left[1 - \frac{a}{2l}\right] \frac{\lvert x\rvert}{l} H(2l - a)$
Wu	$1 - \sin\left(\frac{\lvert x\rvert}{l}\right) H\left(\frac{\pi l}{2} - \lvert x\rvert\right) H\left(a - \frac{\pi l}{2}\right)$

Table 5.2: Analytical solutions for $\phi(x)$ for the AT2, AT1, and Wu models. H denotes the Heaviside step function.

Model	Γ_ϕ	$\Gamma_{\nabla\phi}$
AT2	$\frac{1}{2}\tanh\left(\frac{a}{l}\right) + \frac{1}{2}\frac{a}{l}\left[1 - \tanh^2\left(\frac{a}{l}\right)\right]$	$\frac{1}{2}\tanh\left(\frac{a}{l}\right) - \frac{1}{2}\frac{a}{l}\left[1 - \tanh^2\left(\frac{a}{l}\right)\right]$
AT1	$\frac{1}{2}H(a-2l) + H(2l-a)\left(\frac{-a^3}{8l^3} + \frac{3a}{4l}\right)$	$\frac{1}{2}H(a-2l) + H(2l-a)\frac{a^3}{16l^3}$
Wu	$\frac{1}{2}H(a - l\pi/2) + H(l\pi/2 - a)\frac{2a}{\pi l}$	$\frac{1}{2}H(a - l\pi/2)$

Table 5.3: Analytical expressions for the phase-field energy Γ_ϕ and gradient energy $\Gamma_{\nabla\phi}$ for the AT2, AT1, and Wu models. H denotes the Heaviside step function.

ratio of $l/a = 0.1$. The figure clearly highlights the compact nature of the AT1 and Wu solutions compared with the infinite exponential tail of the AT2 model.

Practically, for the AT2 model, if the ratio a/l is sufficiently large, the boundary discrepancy becomes negligible. As presented in Section 4.5, for $a/l = 5$, the relative error is less than 0.1%, which is generally well within acceptable numerical tolerances.

Table 5.4 summarizes the specific conditions on the ratio a/l under which the one-dimensional energy functional becomes completely independent of boundary effects and precisely equals the exact sharp crack energy. Under these conditions, the following equality rigorously holds for the presented one-dimensional case:

$$G_c \int_\Omega \gamma(\phi, \nabla\phi)\, \mathrm{d}\boldsymbol{x} = G_c \int_{\Gamma_{\text{sharp}}} \mathrm{d}S. \tag{5.19}$$

Model	**Condition for** $\Gamma = 1$
AT2	$a/l \to \infty$
AT1	$a/l \geq 2$
Wu	$a/l \geq \pi/2$

Table 5.4: Conditions on the ratio a/l for the one-dimensional energy functional to be independent of boundary effects and equal to the sharp crack energy.

This indicates that, in an energetic sense, the phase-field regularization functional becomes fully equivalent to the discrete sharp-crack problem. This reinforces the core comparison between the discrete variational fracture problem and the PFF framework presented in Table 2.1, and detailed specifically for the AT2 case in Section 2.2.1.

These properties provide a practical criterion for selecting the length scale parameter l in numerical simulations. By ensuring that the length scale parameter l is sufficiently small relative to the domain dimension a, an accurate energy representation and crack approximation can be achieved without requiring an infinitesimally small l.

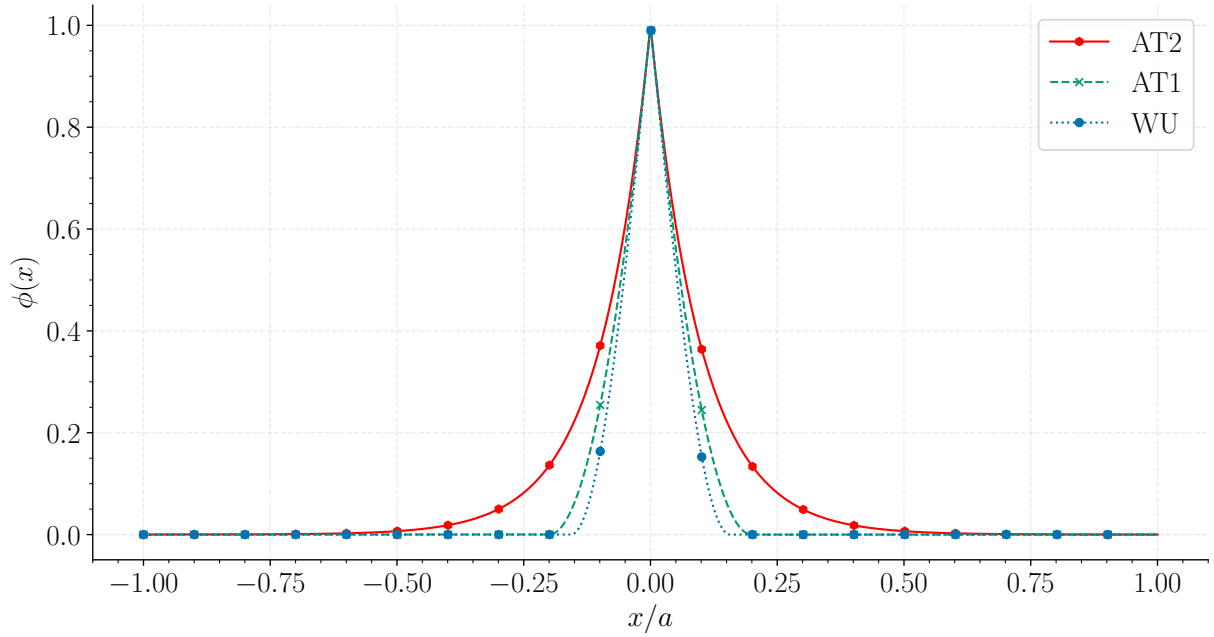

(a) Phase-field

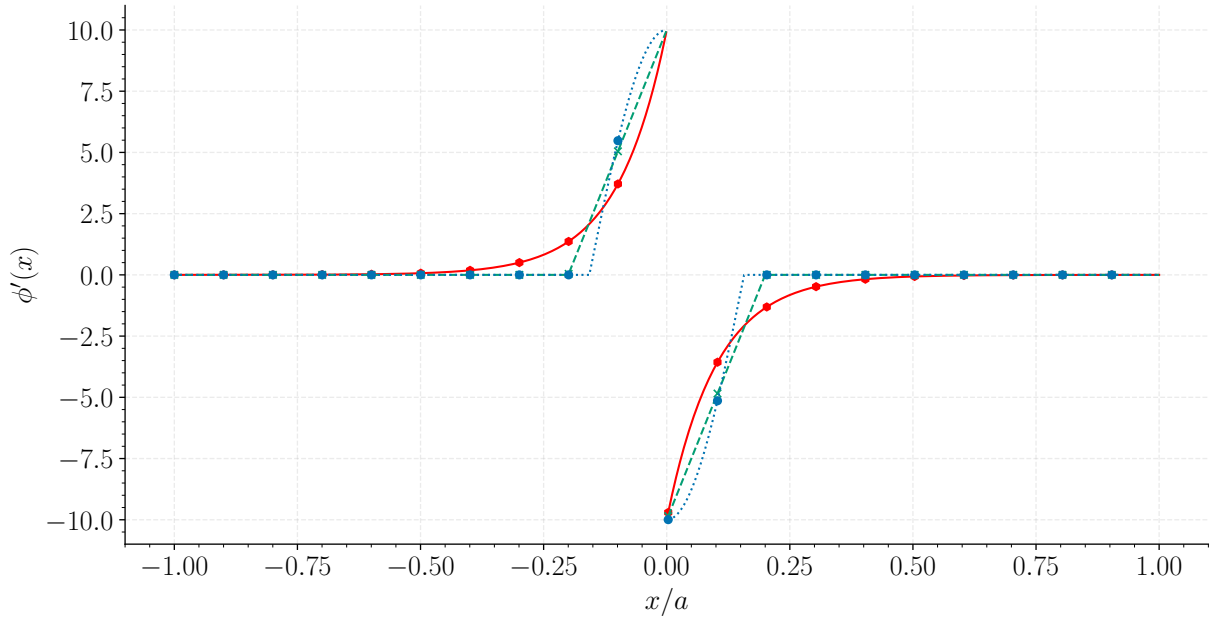

(b) Phase-field gradient

Figure 5.3: Analytical phase-field solutions for the AT2, AT1, and Wu regularization models with $l/a = 0.1$: (a) phase-field profile $\phi(x)$ and (b) gradient $\nabla\phi(x)$. The AT1 and Wu models exhibit compact support, vanishing at a finite distance from the crack, whereas the AT2 model has infinite support.

This principle naturally extends to domains containing multiple cracks, where the interaction distance between cracks can affect the energy representation. In such generalized scenarios, the length-scale parameter must be selected carefully based on the minimum distance between adjacent cracks. This ensures that the distinct energy profile of each crack is represented accurately without artificial overlap, analogous to the way the isolated

domain boundary distance a constrains the single-crack case.

5.2 Handling the interval constraint of the phase-field variable

Having generalized the CSDF, it is evident that enforcing the interval constraint of the phase-field variable is critical for certain regularization models. To address this aspect, two approaches are discussed: the classical penalty method and the LVPP algorithm.

Figure 5.1(a) presents a schematic comparison of these two strategies. The following sections first describe the penalty approach, followed by a detailed presentation of the LVPP method. Initially, the focus is restricted to the CSDF to analyze this fundamental component. Subsequently, the methodology is extended to the PFF problem.

5.3 Penalty approach

A standard technique for enforcing constraints is the penalty method, which transforms the constrained optimization problem into an unconstrained one by penalizing constraint violations. Within the broader PFF framework, it is generally sufficient to explicitly enforce only the lower bound constraint ($\phi \geq 0$). The upper bound ($\phi \leq 1$) is maintained during the crack propagation process, as the degradation naturally prevents the phase-field variable from exceeding the upper bound, as widely observed in the literature. Therefore, only the non-negativity constraint is considered here.

For regularizations in which the lower bound is the primary concern, the constraint is enforced by augmenting the CSDF functional $\Gamma(\phi)$ defined in Eq. (5.1) with a penalty term, resulting in the following penalized functional:

$$\Gamma_{\text{penalty}}(\phi) = \Gamma(\phi) + \frac{\rho}{2} \int_\Omega \langle \phi \rangle_-^2 \, \mathrm{d}\boldsymbol{x}, \tag{5.20}$$

where ρ is a sufficiently large penalty parameter, $\langle \cdot \rangle_-$ denotes the negative Macaulay brackets defined in Eq. (2.8).

The stationarity condition $\delta\Gamma_{\text{penalty}}(\phi) = 0$ leads to the following weak form:

$$\Gamma'_{\text{penalty}}(\phi) := \Gamma'(\phi) + \rho \int_\Omega \langle \phi \rangle_- \, \delta\phi \, \mathrm{d}\boldsymbol{x} = 0. \tag{5.21}$$

where $\Gamma'(\phi)$ is the variational derivative of the original functional $\Gamma(\phi)$, as defined in Eq. (5.5).

The discretization and solution procedure follow standard finite element methods, as presented in Section 2.2.2. The only unknown is the phase-field variable ϕ. A monolithic Newton-Raphson scheme is employed to solve the resulting non-linear system.

The choice of the penalty parameter ρ is crucial. Ideally, ρ should tend to infinity ($\rho \to \infty$) to enforce the constraint exactly; however, this is not practically possible because of numerical limitations. Therefore, it must be chosen sufficiently large to enforce the constraint effectively without causing numerical ill-conditioning.

5.3.1 Analysis of the penalty parameter

Strategies for selecting the penalty parameter ρ have been proposed in the literature, for example in [6], where optimal values are determined as functions of the simulation parameters. However, since the objective here is to highlight the differences between methods and establish a baseline for comparison with the subsequent LVPP approach, a simple sensitivity analysis is conducted to select an appropriate value of ρ for a given mesh and length scale.

For this analysis, a length scale of $l = 0.1$ mm (resulting in a ratio of $l/a = 0.1$) is considered. This ensures a diffuse crack representation with compact support for both AT1 and Wu regularizations models. The domain is discretized using regular elements with a characteristic size of $h = 0.0002$ mm, yielding a highly refined characteristic ratio of $l/h = 500$. This high resolution mitigates mesh dependence, effectively isolating the influence of the penalty parameter.

For the AT1 model, Figure 5.4(a) illustrates the relative error in the total energy Γ as a function of the penalty parameter ρ. Figure 5.4(b) compares the numerical phase-field profiles for three different penalty values with the analytical solution (5.13). It is evident that insufficient penalization results in the phase-field variable violating the physical lower bound.

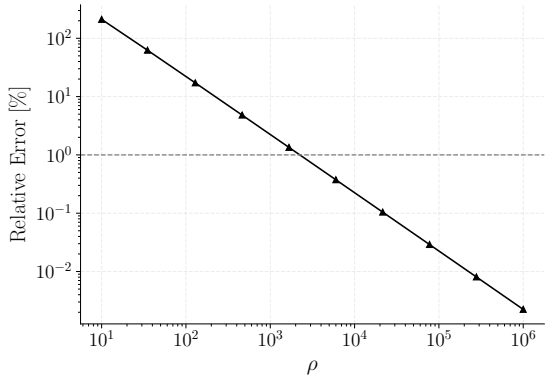

(a) Relative energy error $e_\Gamma = |\Gamma_{\text{num}} - \Gamma_{\text{ana}}|/\Gamma_{\text{ana}}$ vs. penalty parameter ρ.

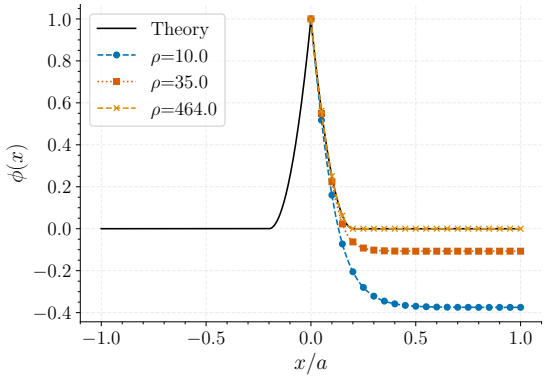

(b) Comparison of phase-field profiles with the analytical solution.

Figure 5.4: Influence of the penalty parameter ρ on phase-field profiles and energy accuracy for the AT1 model.

A similar analysis is performed for the Wu model. Figure 5.5(a) shows the energy error convergence, and Figure 5.5(b) depicts the phase-field profiles for three different penalty values compared with the analytical solution (5.15). Again, low penalty values lead to non-physical solutions.

Based on these results, a penalty parameter of $\rho = 10^6$ for this one-dimensional case yields a relative error below 0.1% for both regularizations.

It is worth noting that for $l/a \geq 0.5$ in the AT1 model, and $l/a \geq 2/\pi$ in the Wu model, boundary effects cause the analytical solution to naturally satisfy $\phi \geq 0$. This renders the penalty term theoretically redundant for this specific one-dimensional isolated example. However, it is essential to consider this constraint when the functional is incorporated

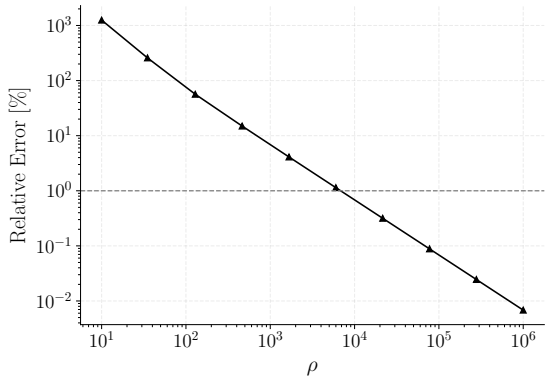

(a) Relative energy error $e_\Gamma = |\Gamma_{\text{num}} - \Gamma_{\text{ana}}| / \Gamma_{\text{ana}}$ vs. penalty parameter ρ.

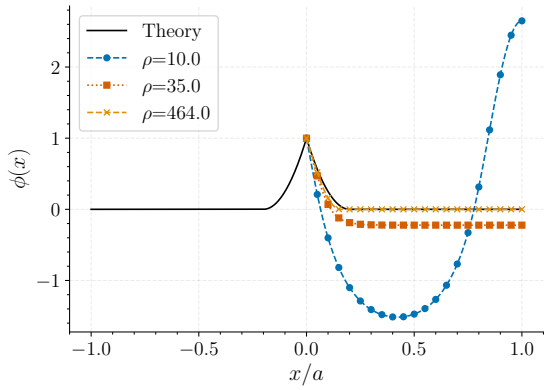

(b) Comparison of phase-field profiles with the analytical solution.

Figure 5.5: Influence of the penalty parameter ρ on phase-field profiles and energy accuracy for the Wu model.

into the full PFF framework, where complex geometries and evolving boundary conditions necessitate explicit enforcement of non-negativity.

5.4 The LVPP algorithm for the CSDF

This section presents the LVPP formulation specialized to the crack surface density functional (CSDF), where the only primal unknown is the phase-field variable ϕ. The objective is to enforce the interval constraint on ϕ through a latent-variable proximal construction, without introducing displacement unknowns in this stage.

For the CSDF problem, the constrained minimization can be written as follows: find ϕ such that

$$\phi = \arg\, min_{\phi \in K} \Gamma(\phi), \tag{5.22}$$

subject to the admissibility constraint $\phi \in K$. Here, K denotes the interval-constrained feasible set for the CSDF. Instead of treating this constrained problem directly, the LVPP strategy uses a Bregman proximal-point sequence [63]. At iteration k, the subproblem reads: find ϕ_k such that

$$\phi_k = \arg\, min_{\phi_k \in K} \left[\Gamma(\phi_k) + \frac{1}{\beta_k} \int_\Omega D_R(\phi_k, \phi_{k-1})\, \mathrm{d}\Omega \right] \text{ for } k = 1, 2, \ldots, \tag{5.23}$$

where β_k is a suitably chosen sequence of positive real numbers. As the iteration index k increases, this sequence is expected to converge to the solution given by Eq. (5.22). The iteration is formulated at the continuum level, yielding weak-form PDEs that can be discretized and solved numerically.

The key regularization term is the Bregman divergence induced by a Legendre function R:

$$D_R(\phi_k, \phi_{k-1}) = R(\phi_k) - R(\phi_{k-1}) - R'(\phi_{k-1})(\phi_k - \phi_{k-1}). \tag{5.24}$$

For the present CSDF case, this term regularizes each iterate while preserving the bound-constrained structure at the variational level, consistent with the LVPP framework in [11].

The method requires a Fréchet differentiable Legendre function R. For box constraints $\phi_{\min} \leq \phi \leq \phi_{\max}$, a convenient choice is the entropic barrier:

$$R(\phi) = (\phi - \phi_{\min}) \ln(\phi - \phi_{\min}) + (\phi_{\max} - \phi) \ln(\phi_{\max} - \phi). \tag{5.25}$$

This choice allows the simultaneous enforcement of both lower and upper bounds within a unique entropic barrier function, ensuring that the phase-field variable remains physically consistent. The derivative of R is

$$R'(\phi) = \ln\left(\frac{\phi - \phi_{\min}}{\phi_{\max} - \phi}\right). \tag{5.26}$$

This mapping enforces the interval constraint by construction. In the standard CSDF case, $\phi_{\min} = 0$ and $\phi_{\max} = 1$, so ϕ remains in $[0, 1]$.

In the notation of [11], this CSDF setting corresponds to the specialization $B = \mathrm{id}$ and pointwise bound constraints on ϕ.

Starting from an initial dual variable $(\phi_0, \xi_0) \in V \times W$, the algorithm seeks a pair $(\phi_k, \xi_k) \in V \times W$ at each iteration k that satisfies:

$$\beta_k \Gamma'(\phi_k) + B^* \xi_k = B^* \xi_{k-1}, \tag{5.27}$$

$$B\phi_k - \nabla R^*(\xi_k) = 0. \tag{5.28}$$

where ∇R^* is the corresponding gradient of the convex conjugate, given by:

$$\nabla R^*(\xi) = \frac{\phi_{\min} + \phi_{\max} \exp \xi}{1 + \exp \xi}, \tag{5.29}$$

and $\Gamma'(\phi_k)$ denotes the variational derivative given by equation (5.5).

In the context of this work, the constraints are pointwise bounds on the phase-field variable, which implies $B = \mathrm{id}$. However, the framework is sufficiently general to handle more complex constraints involving gradients ($B = \nabla$), Hessians, or trace operators, among others.

5.4.1 The sequence of PDEs

For $K = \{\phi \mid 0 \leq \phi \leq 1\}$, the constrained CSDF problem is recast as a two-field LVPP system in (ϕ_k, ξ_k) at each proximal iteration. The pair R and ∇R^* in Eqs. (5.25)–(5.29) provides the constraint-consistent coupling.

Taking the first variation of Eq. (5.23) gives: find $\phi_k \in \mathcal{S}_\phi$ such that for all $\delta\phi \in \mathcal{W}_\phi$,

$$\Gamma'(\phi_k; \delta\phi) + \beta_k^{-1} \int_\Omega [R'(\phi_k) - R'(\phi_{k-1})]\, \delta\phi \, \mathrm{d}\Omega = 0. \tag{5.30}$$

Introducing the latent variable

$$\xi := R'(\phi) = \ln\left(\frac{\phi - \phi_{\min}}{\phi_{\max} - \phi}\right), \tag{5.31}$$

gives a smooth two-field weak formulation.

The weak form of the unconstrained sub-problem at iteration k reads:

$$\beta_k \int_\Omega \frac{1}{c_0}\left(\frac{\alpha'(\phi_k)}{l}\delta\phi + 2l\nabla\phi_k \cdot \nabla\delta\phi\right) \mathrm{d}\boldsymbol{x} + \int_\Omega (\xi_k - \xi_{k-1})\delta\phi \,\mathrm{d}\boldsymbol{x} = 0, \tag{5.32}$$

$$\int_\Omega \left(\phi_k - \frac{\exp\xi_k}{1+\exp\xi_k}\right)\delta\xi \,\mathrm{d}\boldsymbol{x} = 0, \tag{5.33}$$

where the proximal parameter β_k is updated adaptively to accelerate convergence, although theoretical convergence is guaranteed even for a fixed value.

The corresponding strong form of the PDE system is:

$$\beta_k \frac{1}{c_0}\left(\frac{\alpha'(\phi_k)}{l} - 2l\Delta\phi_k\right) + \xi_k - \xi_{k-1} = 0 \qquad \text{in } \Omega, \tag{5.34}$$

$$\phi_k - \frac{\exp\xi_k}{1+\exp\xi_k} = 0 \qquad \text{in } \Omega. \tag{5.35}$$

$$\nabla\phi_k \cdot \boldsymbol{n} = \boldsymbol{0} \quad \text{on } \partial\Omega. \tag{5.36}$$

This system is solved iteratively until convergence. The adaptive update of the proximal parameter β_k is crucial for efficient numerical performance. In the following section, the numerical frameworks will be presented to address these aspects.

Since the phase-field and latent variables are directly related via Eq. (5.29), a closed-form expression for ξ can analytically be derived. Rearranging this relationship yields:

$$\xi = \ln\left(\frac{\phi}{1-\phi}\right). \tag{5.37}$$

The mapping between ϕ and ξ is illustrated in Figure 5.6. This relationship effectively transforms the bounded interval $\phi \in (0,1)$ into the unbounded domain $\xi \in (-\infty, \infty)$. Specifically, ξ diverges to $-\infty$ as $\phi \to 0$ and to $+\infty$ as $\phi \to 1$.

5.4.2 Proximal Galerkin

Once the LVPP formulation is established, the resulting PDEs are discretized using the FEM. This discretization, referred to as the Proximal Galerkin method [10], extends the standard Galerkin approach to accommodate the latent variable framework. A primary advantage of this methodology is that it avoids discretizing the feasible inequality set K directly, and no special treatment is required for the spatial discretization of the latent variable ξ.

To clearly define the numerical framework, the functional settings for the CSDF are first specified. The problem depends on both the phase-field variable ϕ and the latent variable ξ. The feasible continuous set for the phase-field variable is:

$$K_{\mathrm{CSDF}} = \left\{\phi \in H^1_{\bar{\phi}}(\Omega) \;\middle|\; 0 \le \phi \le 1 \text{ a.e. in } \Omega\right\}, \tag{5.38}$$

where $H^1_{\bar{\phi}}(\Omega) = \{v \in H^1(\Omega) \mid v = \bar{\phi} \text{ on } \partial\Omega_\phi\}$ enforces the strongly imposed Dirichlet boundary conditions on the phase-field. The latent variable ξ is naturally sought in $L^2(\Omega)$, as its governing formulation does not involve spatial derivatives.

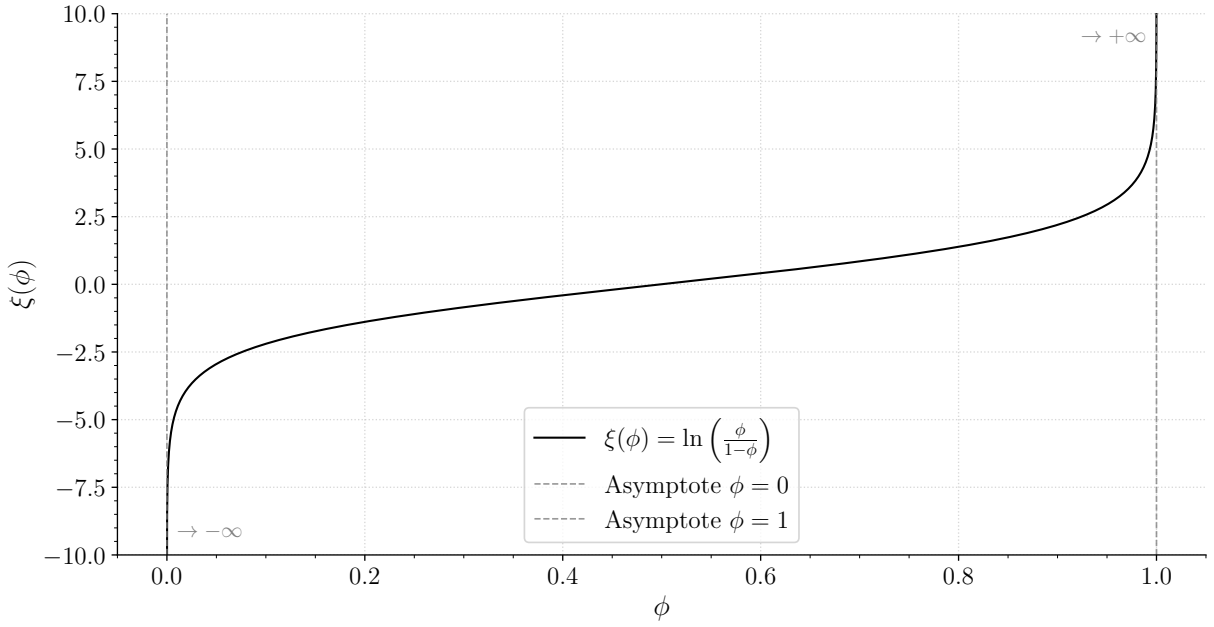

Figure 5.6: Mapping between the phase-field variable ϕ and the latent variable ξ. The transformation maps the physical bounds $[0, 1]$ to the unconstrained real line $(-\infty, \infty)$.

The sequence of PDEs is then discretized using the standard Galerkin FEM. The same set of nodal shape functions N_a is employed to approximate all fields over the domain Ω. Let $\mathcal{T}_h$ be a partition of the domain Ω into elements K_h. The finite element space V_h, composed of continuous functions that are piecewise polynomials of degree p on each element, is defined as:

$$V_h = \left\{ v \in C^0(\Omega) \mid v|_{K_h} \in P_p(K_h) \quad \forall K_h \in \mathcal{T}_h \right\}. \tag{5.39}$$

In this work, linear finite elements are assumed throughout, setting $p = 1$.

The field approximations and their corresponding variations take the standard form:

$$\phi_h(\boldsymbol{x}) = \sum_{a=1}^{n_{\text{node}}} N_a(\boldsymbol{x})\phi_a, \quad \delta\phi_h(\boldsymbol{x}) = \sum_{a=1}^{n_{\text{node}}} N_a(\boldsymbol{x})\delta\phi_a, \tag{5.40}$$

$$\xi_h(\boldsymbol{x}) = \sum_{a=1}^{n_{\text{node}}} N_a(\boldsymbol{x})\xi_a, \quad \delta\xi_h(\boldsymbol{x}) = \sum_{a=1}^{n_{\text{node}}} N_a(\boldsymbol{x})\delta\xi_a. \tag{5.41}$$

The discretization process yields a system of nonlinear algebraic equations that must be solved iteratively. For the CSDF, the system involves only the phase-field and latent variables, i.e., $\mathbf{X} = \{\phi, \xi\}$. Since the displacement field is not involved here, this system is efficiently resolved using a monolithic Newton-Raphson scheme. At each LVPP iteration, the residual $\boldsymbol{R} = [\boldsymbol{R}^{\phi}, \boldsymbol{R}^{\xi}]^T$ is linearized and solved directly.

5.4.3 Initialization and proximal-parameter update strategy

The proximal parameter β_k plays a crucial role in the convergence of the LVPP algorithm and must be appropriately selected. As discussed in [10], the solution converges for any fixed value of β_k as $k \to \infty$; however, the convergence rate is significantly influenced by

this choice. For the CSDF problem, setting the initial parameter $\beta_0 = c_0 l$ provides robust convergence and, in the analyzed cases, convergence to the analytical solutions. This initial value effectively acts as a normalization factor.

The update strategy for the proximal parameter is based on the number of Newton iterations, as described by [11], denoted here as $\text{iter}_{\phi\xi}$, required to solve the linearized PDE system at each LVPP iteration. This adaptive strategy balances computational efficiency and numerical stability by defining an acceptable iteration window between 4 and 10 iterations:

$$\beta_k \leftarrow \begin{cases} \beta_{k-1}\, r & \text{if } \text{iter}_{\phi\xi} \leq 4, \\ \beta_{k-1} & \text{if } 4 < \text{iter}_{\phi\xi} < 10, \\ \beta_{k-1}/r & \text{if } \text{iter}_{\phi\xi} \geq 10, \end{cases} \tag{5.42}$$

where $r > 1$ is a scaling multiplier. If convergence is considered fast ($\text{iter}_{\phi\xi} \leq 4$), the parameter is reduced to accelerate subsequent LVPP iterations. Conversely, if convergence is considered slow ($\text{iter}_{\phi\xi} \geq 10$), the parameter is increased to improve regularization and convergence robustness in the next iteration.

The stopping criterion for the LVPP iterations is based on monitoring the H^1 norm of the difference between successive phase-field iterates, i.e., $\|\phi_k - \phi_{k-1}\|_{H^1} < \text{tol}_{\text{LVPP}}$, where tol_{LVPP} is a predefined tolerance. This ensures that the global solution has sufficiently stabilized and that further iterations will not yield significant geometrical changes in the phase-field profile.

Regarding the initialization of variables at each time step, the phase-field ϕ, the latent variable ξ_k, and the displacement field $\boldsymbol{u}$ (if considering the PFF problem) are initialized using the converged values from the previous time step. The iterative latent variable ξ_{k-1} is re-initialized to zero at the beginning of each time step to ensure that the LVPP iterations start from a neutral state. The resolution algorithm scheme is summarized in Algorithm 4. Note that this problem is generally analyzed in only one time step; however, for generality and to match the following approach, the algorithm shows the entire time-stepping scheme, where the LVPP iterations are nested within each time step.

5.4.4 Validation and examples

The numerical solutions are validated against the one-dimensional analytical solutions for the AT2, AT1, and Wu models. The convergence relative to the mesh size, as well as for the proximal Galerkin iterations, is analyzed.

Analytical solution for the latent variable

Before presenting the specific numerical validations, analytical insights into the behavior of the latent variable ξ are discussed. In Section 5.1.1, analytical solutions for the phase-field variable ϕ were derived. Since the operative relationship between ϕ and ξ is fully explicit (Eq. (5.37)), the corresponding analytical profiles for the latent variable ξ can be readily obtained.

Figure 5.7 maps the analytical profiles of both ϕ and ξ for the three continuous models. The phase-field variable ϕ clearly exhibits its characteristic fracture distributions: an exponential decay for the AT2 model, and strictly compact support for the AT1 and Wu models. The latent variable ξ intrinsically reflects these geometric behaviors. For the

Algorithm 4 Monolithic LVPP algorithm. This scheme is applied to the CSDF problem; hence, in this case $\phi_{\text{prev}} = 0$. The algorithm shows the update procedure. The scheme for the monolithic PFF algorithm is analogous; however, in this case the residual also accounts for the displacement variable $\boldsymbol{u}$.

Initialize: $t \leftarrow 0$, $step \leftarrow 0$, T_{final}, Δt
while $t < T_{final}$ **do**
    Update boundary conditions and loading
    Initialize LVPP iteration parameter: $\beta_1 \leftarrow \beta_0$
    Initialize variables: $\phi_0 \leftarrow \phi_{\text{prev}}$, $\xi_{k-1} \leftarrow 0$
    $k \leftarrow 1$, $\|\Delta\phi\| \leftarrow 1.0$
    while $\|\Delta\phi\| > \text{tol}_{\text{LVPP}}$ **do**
        Solve the nonlinear system $\boldsymbol{R}(\phi_k, \xi_k) = \boldsymbol{0}$
            Record number of Newton-Raphson iterations: N_{iter}
        Compute phase-field increment: $\|\Delta\phi\| \leftarrow \|\phi_k - \phi_{k-1}\|$
        Update iterates: $\phi_k \leftarrow \phi_k$, $\xi_k \leftarrow \xi_k$
        Update proximal parameter based on Newton iterations:
        $k \leftarrow k + 1$
    end while
    Update history: $\phi_{\text{prev}} \leftarrow \phi_{k-1}$
    $t \leftarrow t + \Delta t$, $step \leftarrow step + 1$
end while

bounded compact support models (AT1 and Wu), ξ diverges to $-\infty$ exactly at the boundary of the diffuse crack zone where ϕ perfectly vanishes. In contrast, for the unbounded AT2 model, where ϕ decays exponentially but never strictly reaches zero, ξ structurally decreases tightly but remains definitively finite in the far field. Predictably, in all examined scenarios, at the sharp crack center ($x = 0, \phi = 1$), the latent variable diverges to $+\infty$.

Adaptive update of the proximal parameter

Figure 5.8 illustrates the evolution of the phase-field and latent variable profiles across proximal point iterations, considering the proximal update strategy presented in Section 5.4.3. Each proximal iteration corresponds to one solution of the sequence of PDEs (outer loop), which itself requires several nonlinear Newton iterations (inner loop). The adaptive strategy significantly accelerates convergence, particularly during the early iterations.

Different initial values were also investigated, confirming that the initial choice strongly affects performance. Although some values may appear to accelerate convergence, they can lead to convergence toward incorrect solutions. In this study, the initialization $\beta_0 = c_0 l$ consistently converges to the analytical solution for all regularization models (AT2, AT1, Wu), mesh sizes, and length-scale values.

For comparison, the same simulations were repeated with a constant proximal parameter (without adaptive updates). In that case, the number of iterations required to reach the same tolerance increased substantially, typically to 500–600 iterations. This clearly shows the efficiency gain provided by the update strategy for β_k.

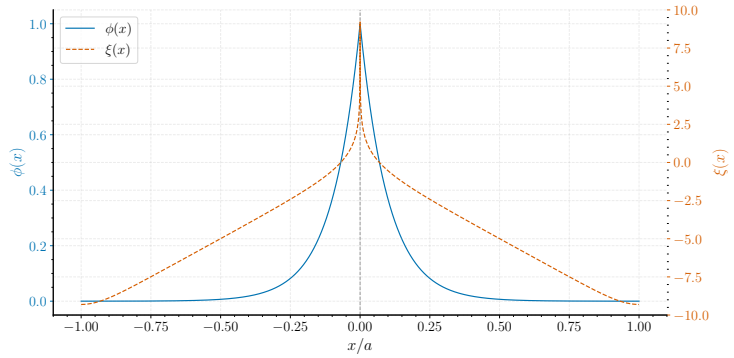

(a) AT2

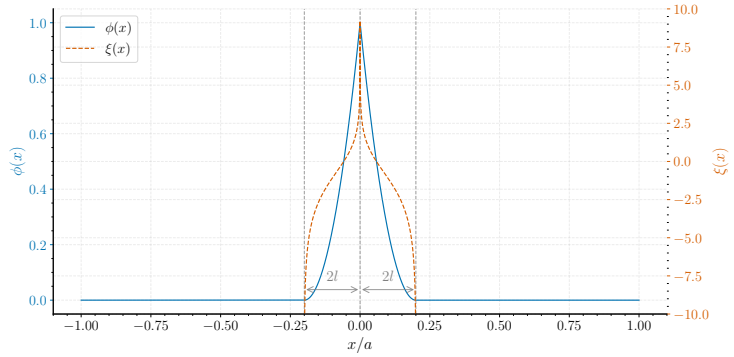

(b) AT1

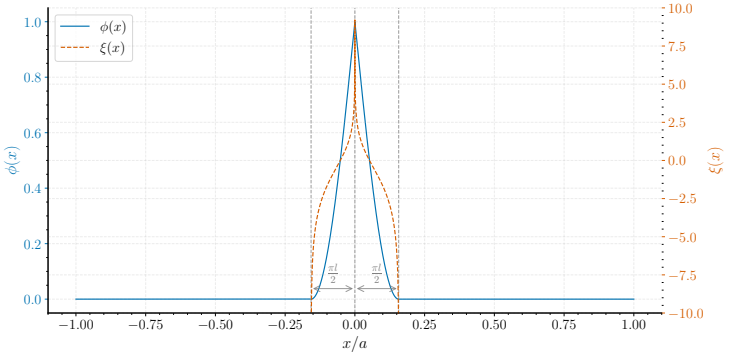

(c) Wu

Figure 5.7: Analytical profiles of the phase-field ϕ and latent variable ξ for different regularizations. (a) AT2 shows infinite support, while (b) AT1 and (c) Wu exhibit compact support with $\xi \to -\infty$ at the compact support boundaries.

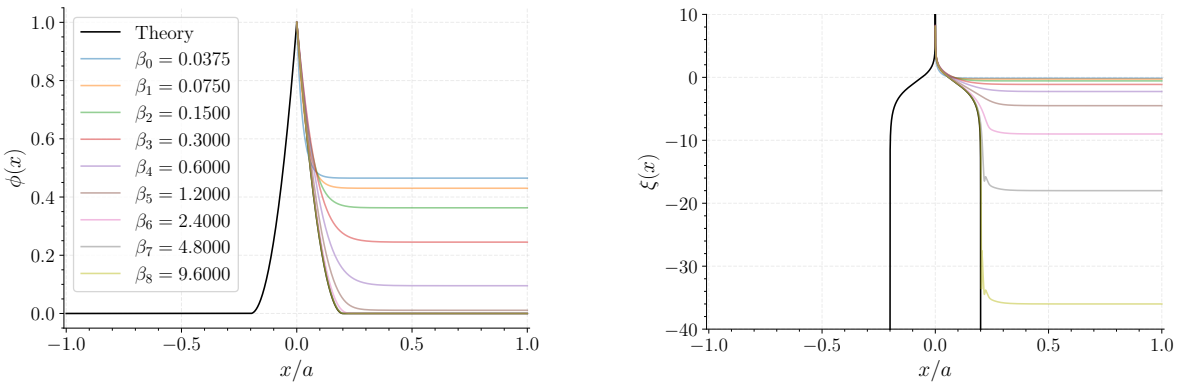

(a) Phase-field variable

(b) Latent variable

Figure 5.8: Proximal point iterations: sequence of PDEs and the update strategy for the proximal parameter β_k. The adaptive update strategy significantly accelerates convergence, especially in the early iterations.

Validation of the phase-field profile and energy

To validate the LVPP algorithm, the one-dimensional bar problem ($a = 1$ mm) introduced in Chapter 2 is revisited. A fine uniform mesh ($h = a/5000$ mm) is used to minimize discretization errors, giving $l/h = 50$ for the smallest length scale considered ($l = 0.01$ mm). The length scale l is varied in the range $[0.01 \text{ mm}, 2a]$.

Figure 5.9 validates the solver by comparing the Γ energy obtained through numerical simulations with the analytical solutions. Excellent agreement is observed for all three regularization models.

The convergence behavior highlights the theoretical properties of each regularization (Table 5.4). The AT1 and Wu models recover the sharp crack energy when the domain is sufficiently large relative to the length scale ($a/l \geq 2$ for AT1, $a/l \geq \pi/2$ for Wu). In contrast, due to its infinite support, the AT2 model approaches the sharp crack limit only asymptotically as $l \to 0$.

Local accuracy is examined in Figure 5.10, which plots the spatial variation of ϕ and $\nabla\phi$. The numerical solutions correctly capture the specific geometric shapes—exponential (AT2), quadratic (AT1), and sinusoidal (Wu). Most importantly, the LVPP method rigorously enforces the physical bounds $\phi \in [0, 1]$ without the need for penalty parameters, preventing the non-physical negative values often observed in unconstrained formulations of the AT1 and Wu models.

Comparing the numerical and analytical profiles of the latent variable ξ (Figure 5.11) provides further validation. The LVPP algorithm accurately captures the distribution of the underlying latent variable, confirming the method's robustness beyond the primary phase-field variable.

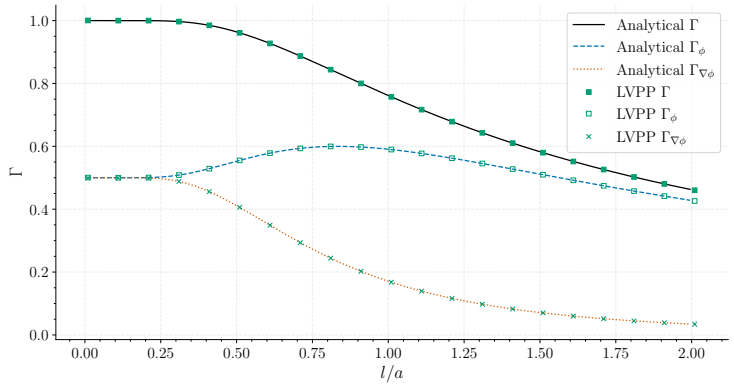

(a) AT2

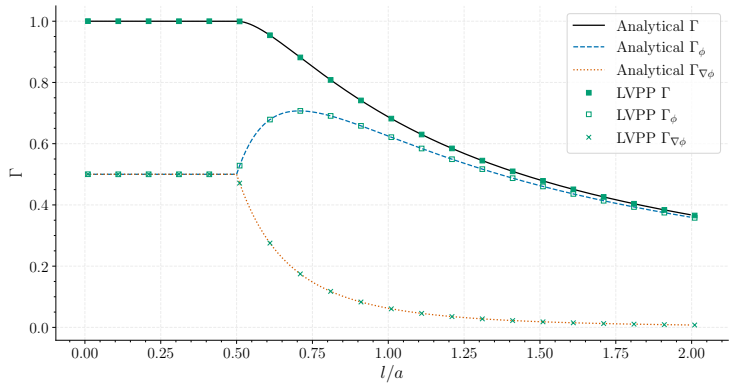

(b) AT1

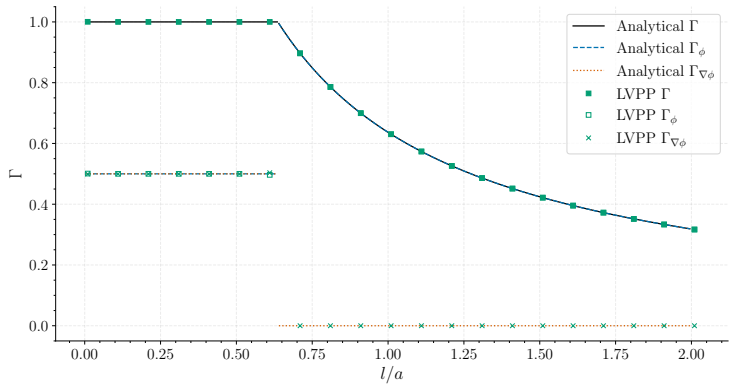

(c) Wu

Figure 5.9: Comparison of the normalized energy Γ as a function of the length scale parameter l for the AT1, AT2, and Wu models. The numerical results obtained via the LVPP method show excellent agreement with the analytical solutions.

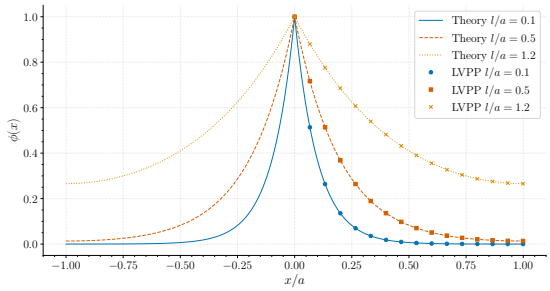

(a) AT2: Phase-field

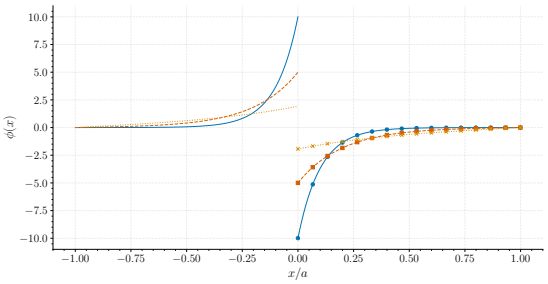

(b) AT2: Gradient

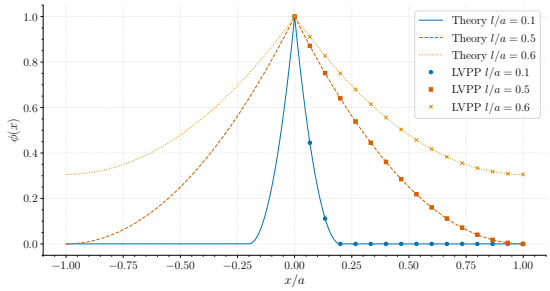

(c) AT1: Phase-field

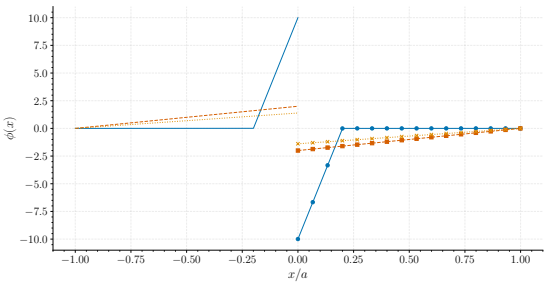

(d) AT1: Gradient

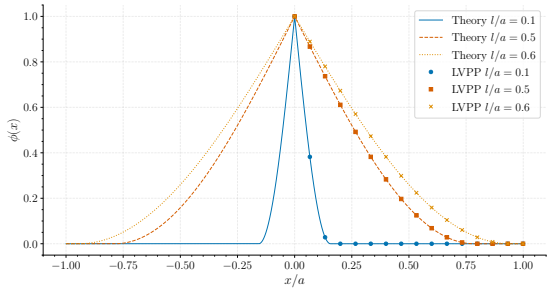

(e) Wu: Phase-field

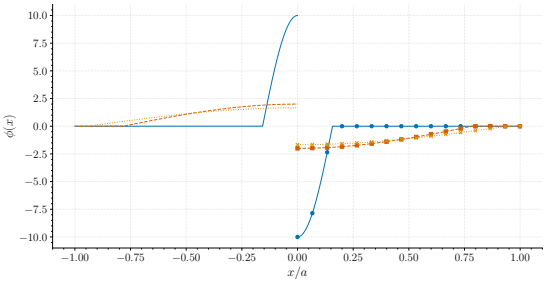

(f) Wu: Gradient

Figure 5.10: Comparison of numerical and analytical solutions for the AT2, AT1, and Wu models using LVPP. Left column: phase-field profiles $\phi(x)$ for various length scales l. Right column: gradients $\nabla\phi(x)$. The results highlight the distinct regularization shapes and compact support properties of the AT1 and Wu models compared to AT2.

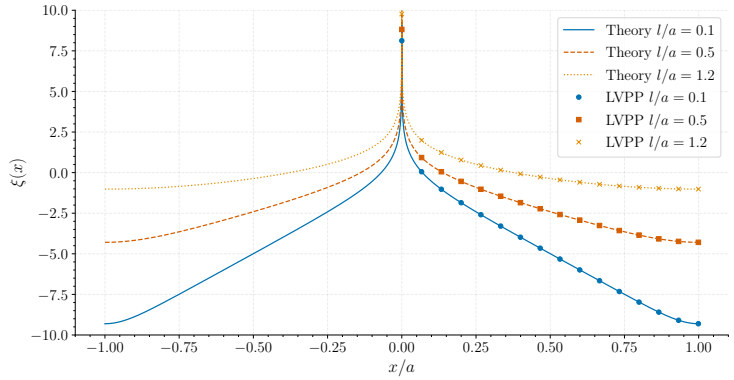

(a) AT2 Model (analytical vs. numerical)

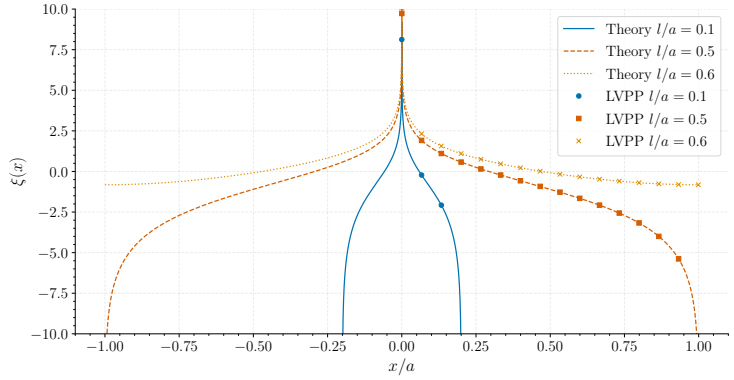

(b) AT1 Model (analytical vs. numerical)

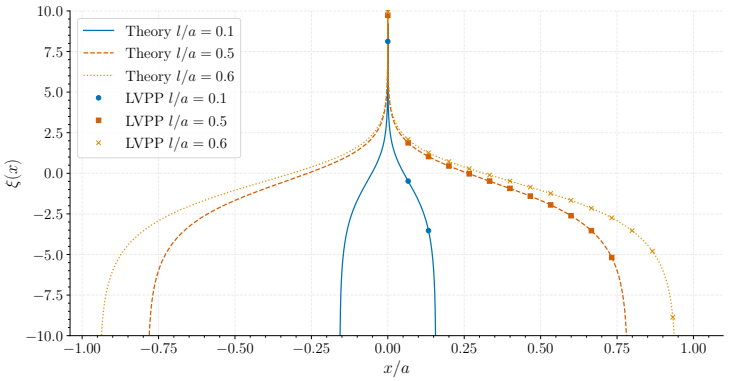

(c) Wu Model (analytical vs. numerical)

Figure 5.11: Comparison of numerical and analytical solutions for the AT2, AT1, and Wu models using LVPP. The rows correspond to each model, showing the latent variable ξ profiles, obtained through numerical simulations and analytical solutions.

Convergence analysis

Accurate phase-field representation relies on sufficient mesh resolution to resolve the diffuse crack interface. As discussed in Section 2.2.2 and by [3], a minimum ratio of $l/h > 2$ is typically recommended when using linear finite elements for the AT2 regularization. In this section, focus is placed on the convergence properties of the proximal Galerkin method using standard linear elements for the AT2, AT1, and Wu models.

Figure 5.12 presents the relative error in the computed energy as a function of the mesh density ratio l/h. Consistent with established literature, a resolution of $l/h \approx 2$ yields a total relative error of approximately 1% for the AT2 model. Similarly, for the AT1 and Wu models, the error at this resolution varies between 0.5% and 1%, confirming that this discretization level is adequate for all considered functionals.

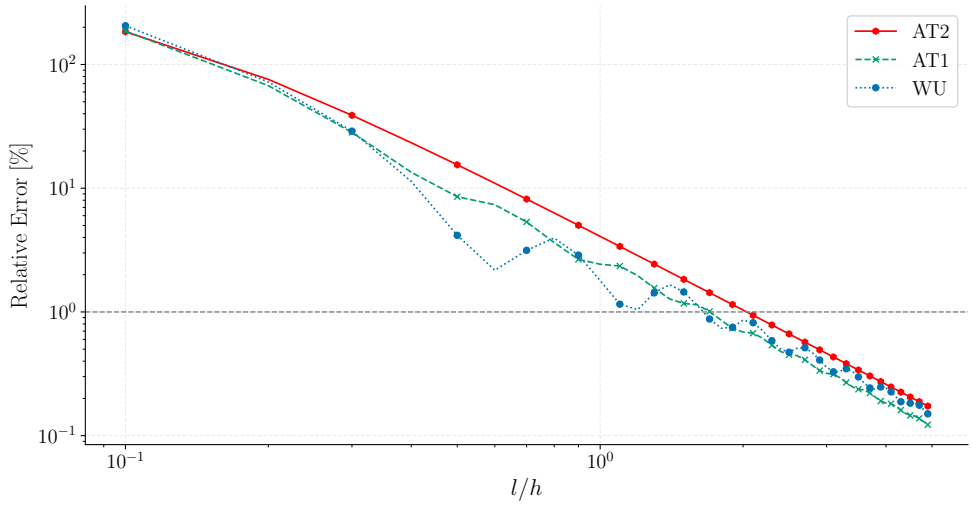

Figure 5.12: Sensitivity of the numerically computed crack surface energy Γ to the mesh size. The relative error is shown as a function of the effective resolution l/h using linear finite elements.

The CSDF analysis establishes the main ingredients of the LVPP framework: the latent-variable mapping, the proximal update strategy, and the finite-element implementation. In the full PFF setting, these ingredients are retained. The extension introduces only two essential changes: coupling with the displacement field and a time-dependent lower bound, $\phi_{\text{prev}} \leq \phi \leq 1$, to enforce irreversibility.

5.5 The LVPP algorithm for PFF

This section extends the LVPP algorithm to the full PFF problem (right branch in Figure 5.1(b)). For comparison, the penalty-based route is summarized in Chapter 2.

The key requirement is unchanged: the phase-field must remain bounded and irreversible. To satisfy this in the coupled setting, the same Legendre function (Eq. (5.25)) and conjugate map (Eq. (5.29)) used in the CSDF are retained, while the lower bound is updated in time.

Accordingly, the feasible set at each step is $\phi_{\text{prev}} \leq \phi \leq 1$, where ϕ_{prev} is the converged phase-field from the previous step.

5.5.1 The sequence of PDEs

For the coupled PFF problem, the total potential energy functional involves both the displacement field $\boldsymbol{u}$ and the phase-field ϕ. The inequality constraints apply exclusively to the phase-field ϕ. Consequently, the latent variable ξ is introduced to handle the constraints on ϕ. At each time step n, the feasible set is defined as $K_n = \{\phi \mid \phi_{\text{prev}} \leq \phi \leq 1\}$. The LVPP algorithm then replaces the constrained minimization problem with a sequence of unconstrained saddle-point problems. At each iteration k, the weak form of the system is given by:

$$\int_\Omega \left[g(\phi_k)\boldsymbol{\sigma}_a(\boldsymbol{\epsilon}(\boldsymbol{u}_k)) + \boldsymbol{\sigma}_b(\boldsymbol{\epsilon}(\boldsymbol{u}_k))\right] : \boldsymbol{\epsilon}(\delta\boldsymbol{u})\,\mathrm{d}\boldsymbol{x} - \int_\Omega \boldsymbol{f}\cdot\delta\boldsymbol{u}\,\mathrm{d}\boldsymbol{x} - \int_{\partial\Omega}\boldsymbol{t}\cdot\delta\boldsymbol{u}\,\mathrm{d}S = 0, \tag{5.43}$$

$$\beta_k\left[\int_\Omega g'(\phi_k)\psi_a(\boldsymbol{\epsilon}(\boldsymbol{u}_k))\delta\phi\,\mathrm{d}\boldsymbol{x} + \frac{G_c}{c_0}\int_\Omega\left(\frac{\alpha'(\phi_k)}{l}\delta\phi + 2l\nabla\phi_k\cdot\nabla\delta\phi\right)\mathrm{d}\boldsymbol{x}\right] + \int_\Omega(\xi_k - \xi_{k-1})\delta\phi\,\mathrm{d}\boldsymbol{x} = 0, \tag{5.44}$$

$$\int_\Omega\left(\phi_k - \frac{\phi_{\text{prev}} + \exp\xi_k}{1+\exp\xi_k}\right)\delta\psi\,\mathrm{d}\boldsymbol{x} = 0. \tag{5.45}$$

Eqs. (5.43)–(5.45) constitute a coupled system of nonlinear PDEs for the unknowns $(\boldsymbol{u}_k, \phi_k, \xi_k)$.

The corresponding strong form equations are given by:

$$\nabla\cdot[g(\phi_k)\boldsymbol{\sigma_a}(\boldsymbol{\epsilon}(\boldsymbol{u}_k)) + \boldsymbol{\sigma_b}(\boldsymbol{\epsilon}(\boldsymbol{u}_k))] + \boldsymbol{f} = \boldsymbol{0} \quad \text{in}\Omega, \tag{5.46}$$

$$\beta_k\left[g'(\phi_k)\,\psi_a(\boldsymbol{\epsilon}(\boldsymbol{u}_k)) + \frac{G_c}{c_0}\left(\frac{\alpha'(\phi_k)}{l} - 2l\Delta\phi_k\right)\right] = 0 \quad \text{in } \Omega, \tag{5.47}$$

$$\phi_k - \frac{\phi_{\text{prev}} + \exp\xi_k}{1+\exp\xi_k} = 0 \quad \text{in } \Omega, \tag{5.48}$$

$$[g(\phi_k)\boldsymbol{\sigma_a}(\boldsymbol{\epsilon}(\boldsymbol{u}_k)) + \boldsymbol{\sigma_b}(\boldsymbol{\epsilon}(\boldsymbol{u}_k))]\cdot\boldsymbol{n} = \boldsymbol{t} \quad \text{on } \partial\Omega_{\boldsymbol{t}}, \tag{5.49}$$

$$\nabla\phi_k\cdot\boldsymbol{n} = \boldsymbol{0} \quad \text{on } \partial\Omega. \tag{5.50}$$

As detailed in Section 5.4, the bound constraints are enforced via a transformation between the physical phase-field variable ϕ and the unconstrained latent variable ξ. To satisfy the irreversibility condition, the lower bound of the feasible set is dynamically updated at each

time step based on the solution from the previous time step (ϕ_{prev}). The transformation becomes:

$$\xi = \ln\left(\frac{\phi - \phi_{\text{prev}}}{1 - \phi}\right). \tag{5.51}$$

This mapping ensures that ϕ remains strictly within the interval $[\phi_{\text{prev}}, 1]$. As illustrated in Figure 5.13, the function maps the feasible physical range to the real line $(-\infty, \infty)$. As damage accumulates ($\phi_{\text{prev}} > 0$), the left vertical asymptote shifts, so the lower bound of the feasible set is automatically updated. This handles automatically and pointwise the irreversibility condition, as well as the interval constraint of the phase-field variable.

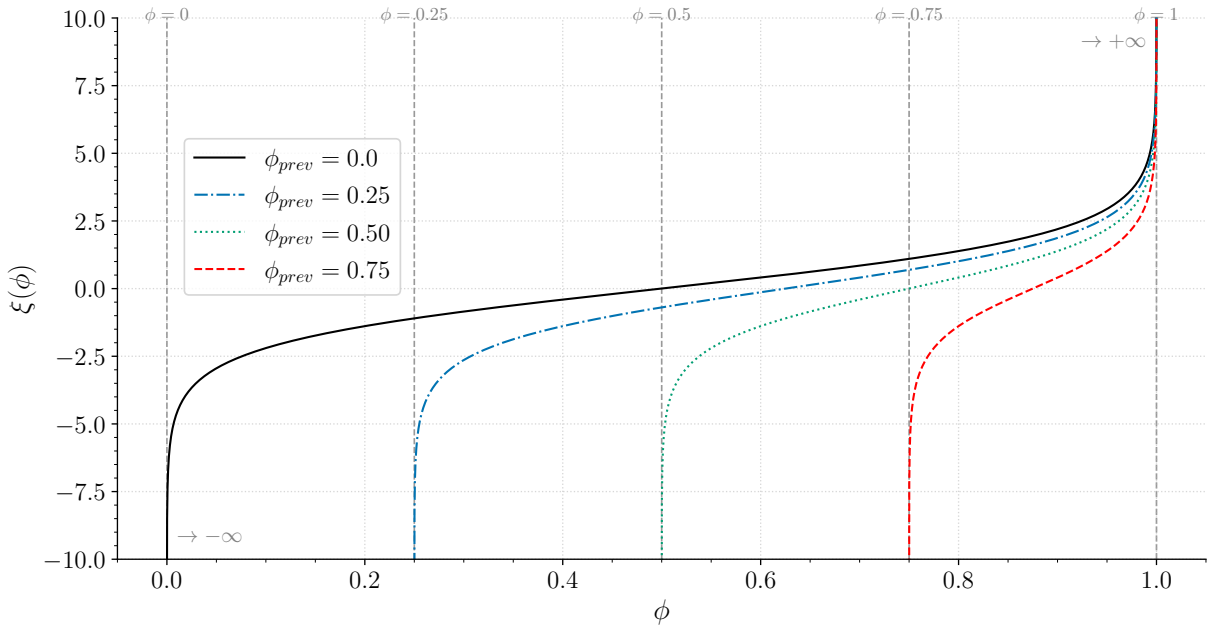

Figure 5.13: Mapping between the phase-field variable ϕ and the latent variable ξ for different history states ϕ_{prev}. The transformation dynamically maps the updated physical bounds $[\phi_{\text{prev}}, 1]$ to the unconstrained real line, ensuring irreversibility.

5.5.2 Proximal Galerkin

Following the methodology described in Section 5.4.2, the sequence of PDEs is discretized using the Proximal Galerkin FEM [10]. A key benefit of this approach, as previously mentioned, is that it circumvents the direct discretization of the feasible set and requires no special treatment for the latent variable space.

The functional settings for the coupled PFF problem are:

$$K_{\text{PFF}} = \left\{(\boldsymbol{u}, \phi) \in H^1_{\boldsymbol{g}}(\Omega; \mathbb{R}^d) \times H^1(\Omega) \;\middle|\; \phi_{\text{prev}} \leq \phi \leq 1 \text{ a.e. in } \Omega\right\}, \tag{5.52}$$

where $H^1_{\boldsymbol{g}}$ enforces Dirichlet boundary conditions on $\boldsymbol{u}$. The phase-field ϕ is sought in $H^1(\Omega)$, while the latent variable ξ in $L^2(\Omega)$.

Standard linear finite elements are employed to approximate all fields $(\boldsymbol{u}, \phi, \xi)$. Accord-

ingly, the discretized fields and their variations are interpolated as:

$$\boldsymbol{u}_h(\boldsymbol{x}) = \sum_{a=1}^{n_{\text{node}}} N_a(\boldsymbol{x})\boldsymbol{u}_a, \quad \delta\boldsymbol{u}_h(\boldsymbol{x}) = \sum_{a=1}^{n_{\text{node}}} N_a(\boldsymbol{x})\delta\boldsymbol{u}_a, \tag{5.53}$$

$$\phi_h(\boldsymbol{x}) = \sum_{a=1}^{n_{\text{node}}} N_a(\boldsymbol{x})\phi_a, \quad \delta\phi_h(\boldsymbol{x}) = \sum_{a=1}^{n_{\text{node}}} N_a(\boldsymbol{x})\delta\phi_a, \tag{5.54}$$

$$\xi_h(\boldsymbol{x}) = \sum_{a=1}^{n_{\text{node}}} N_a(\boldsymbol{x})\xi_a, \quad \delta\xi_h(\boldsymbol{x}) = \sum_{a=1}^{n_{\text{node}}} N_a(\boldsymbol{x})\delta\xi_a. \tag{5.55}$$

Substituting these approximations into the weak forms results in a system of nonlinear algebraic equations. Requiring the variations to be arbitrary implies that the residual vectors must vanish at each node a. The resulting residuals depend on the problem being solved.

5.5.3 Initialization and proximal-parameter update strategy

For the coupled PFF problem, a strategy similar to the one presented in Section 5.4.3 for the CSDF problem is employed. However, in this case, the critical energy release rate parameter G_c is also incorporated, setting $\beta_0 = c_0 l/G_c$. In both cases, the initial value of β_0 essentially serves as a normalization factor to keep the $\alpha(\phi)$ term within a consistent order of magnitude. Regarding the update strategy, the same adaptive scheme based on Newton iterations is applied.

As the PFF problem is solved incrementally over time, the field initialization must be carefully handled. At the beginning of each time step update, the phase-field, latent, and displacement variables (ϕ_k, ξ_k, and $\boldsymbol{u}_k$) are initialized using the converged values from the previous time step. In contrast, the iterative latent variable ξ_{k-1} is re-initialized to zero at the beginning of a new time step. This ensures that the fresh LVPP sequence begins from an unbiased neutral state. Neglecting this reset condition invariably leads to non-physical solutions.

5.5.4 Solution schemes

The discretized system yields a set of nonlinear algebraic equations. Due to the non-convexity of the PFF energy functional, the solution strategy is critical. The LVPP framework is versatile and can be adapted to both monolithic (Section 2.6.2) or staggered (Section 2.6.3) schemes.

Monolithic scheme

In the monolithic approach, the coupled system for $\boldsymbol{u}_k, \phi_k, \xi_k$ is solved simultaneously. The irreversibility is handled by updating the lower bound $\phi_{\min} = \phi_{\text{prev}}$ at the end of each time step. The methodology is synthesized in Algorithm 4.

Staggered scheme

Alternatively, a staggered (operator-split) scheme can be employed, following the same fundamental structure presented in Chapter 2 (specifically Section 2.6.3). The primary distinction here is that while the displacement sub-problem is solved identically to standard

PFF staggered schemes, the phase-field sub-problem incorporates the Proximal Galerkin framework. Consequently, this inner staggered step solves a coupled nonlinear subsystem for both the phase-field ϕ and the latent variable ξ to strictly enforce the bound constraints. The full procedure for the Staggered scheme is summarized sequentially in Algorithm 5, and its corresponding logic flow is visually mapped out in Figure 5.14.

Algorithm 5 Staggered LVPP solver (k_{stg} denotes staggered iterations; k denotes proximal Galerkin (inner LVPP) iterations)

Initialize: $t \leftarrow 0$, $step \leftarrow 0$, initial fields $\boldsymbol{u}_0, \phi_0$. Set $\phi_{\text{prev}} \leftarrow \phi_0$.
Set: $\text{tol}_{\text{LVPP}} \leftarrow 10^{-8}$
while $t < T_{final}$ **do**
    $t \leftarrow t + \Delta t$, $step \leftarrow step + 1$
    Update boundary conditions and loading
    Initialize staggered iteration: $k_{stg} \leftarrow 0$
    Set $\boldsymbol{u}_0 \leftarrow \boldsymbol{u}_{n-1}$, $\phi_0 \leftarrow \phi_{n-1}$
    while $(k_{stg} < k_{stg,min}) \vee$ staggered convergence not satisfied **do**
        $k_{stg} \leftarrow k_{stg} + 1$
        1. Displacement Solve:
        Given $\phi_{k_{stg}-1}$, find $\boldsymbol{u}_{k_{stg}}$ such that $\boldsymbol{R}^{\boldsymbol{u}}(\boldsymbol{u}_{k_{stg}}; \phi_{k_{stg}-1}) = \boldsymbol{0}$
        2. Phase-Field Solve (LVPP):
        Initialize $\beta_1 \leftarrow \beta_0$, $\|\Delta\phi\| \leftarrow 1.0$, $k \leftarrow 1$
        Initialize inner loop fields: $\phi_0 \leftarrow \phi_{n-1}$, $\xi_{k-1} \leftarrow 0$
        while $\|\Delta\phi\| > \text{tol}_{\text{LVPP}}$ **do**
            Solve combined system for (ϕ_k, ξ_k) given $\boldsymbol{u}_{k_{stg}}$
            Record number of Newton-Raphson iterations: N_{iter}
            Compute phase-field increment: $\|\Delta\phi\| \leftarrow \|\phi_k - \phi_{k-1}\|$
            Update iterates: $\phi_k \leftarrow \phi_k$, $\xi_k \leftarrow \xi_k$
            Update proximal parameter β_{k+1} based on Newton iterations N_{iter}
        end while
        Update phase-field estimate: $\phi_{k_{stg}} \leftarrow \phi_{k-1}$
        Check staggered convergence (see Section 2.6.3)
    end while
    Update solutions: $\boldsymbol{u}_n \leftarrow \boldsymbol{u}_{k_{stg}}$, $\phi_n \leftarrow \phi_{k_{stg}}$
    Update history field for next step: $\phi_{\text{prev}} \leftarrow \phi_n$
end while

The convergence of the staggered scheme is typically monitored using criteria such as the norm of the solution increment between staggered iterations, a fixed number of staggered iterations, or the proposed initial residual criterion presented in Section 2.6.3.

5.5.5 Validation and examples

This section validates the proximal Galerkin LVPP framework for the full PFF problem through four benchmarks. The one-element case verifies implementation details against analytical solutions for AT2, AT1, and Wu regularizations. The single-edge notched tension test assesses performance in a standard 2D benchmark and compares LVPP with the penalty approach. The compact specimen under loading–unloading–reloading further tests irreversibility and interval enforcement beyond the one-dimensional setting. Finally, the L-shaped panel demonstrates applicability to anisotropic PFF models. Unless otherwise stated, all analyses assume plane strain and unit thickness.

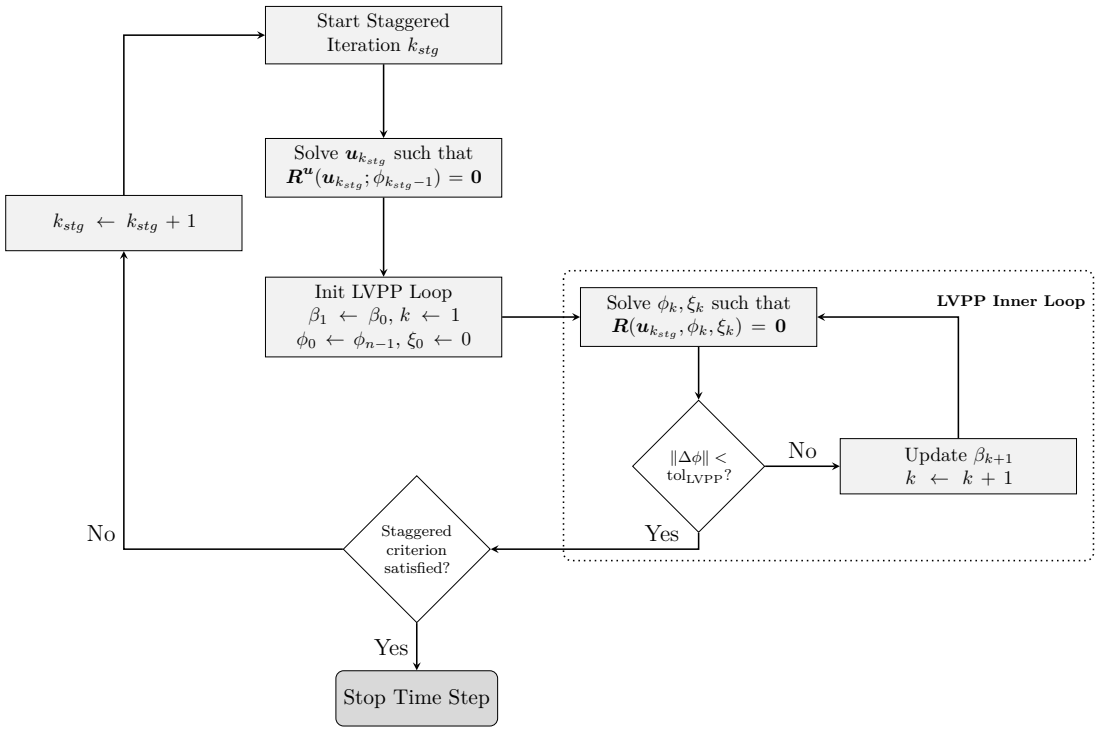

Figure 5.14: Flowchart of the staggered solution scheme incorporating the inner LVPP loop for the PFF problem (k_{stg} denotes staggered iterations; k denotes proximal Galerkin (inner LVPP) iterations).

One-element local damage model

To validate the numerical implementation, the one-element problem presented in Section 2.7.1 is considered. In this case, the solutions for the crack surface density functions —namely the AT2, AT1, and Wu models—are analyzed.

First, the analytical solutions for the phase-field variable and stresses are derived. Assuming a degradation function $g(\phi) = (1-\phi)^2$, the governing equations are:

$$\nabla \cdot \Big[(1-\phi)^2 \boldsymbol{\sigma_a}(\boldsymbol{\epsilon}(\boldsymbol{u})) + \boldsymbol{\sigma_b}(\boldsymbol{\epsilon}(\boldsymbol{u}))\Big] = \mathbf{0} \quad \text{in } \Omega, \tag{5.56}$$

$$-2(1-\phi)\,\psi_a(\boldsymbol{\epsilon}(\boldsymbol{u})) + \frac{G_c}{c_0}\left(\frac{\alpha'(\phi)}{l} \cancel{-2l\Delta\phi}\right) = 0 \quad \text{in } \Omega. \tag{5.57}$$

Since the gradient term vanishes for this single-element example, as explained in Section 2.7.1, the phase-field variable solely acts as a function of the respective positive strain energy, which in turn depends on the strains and displacements.

As shown in Section 2.7.1, the analytical solution for the phase-field variable of the AT2 model is given by Eq. (2.76). For the AT2 model, the phase-field variable is inherently positive since ψ_a is non-negative. Additionally, the denominator is always greater than the numerator, ensuring that ϕ is strictly bounded within the $[0, 1]$ range. Therefore, no special considerations are needed to enforce the bounds of the phase-field variable.

For the AT1 model, the relevant geometric crack function is $\alpha(\phi) = \phi$, and the associated constant is $c_0 = 8/3$. By setting the gradient term to zero and solving for ϕ, the following

expression is obtained:

$$\phi = \frac{2\psi_a(\boldsymbol{\epsilon}(\boldsymbol{u})) - \frac{3}{8}\frac{G_c}{l}}{2\psi_a(\boldsymbol{\epsilon}(\boldsymbol{u}))} = 1 - \frac{\frac{3}{8}\frac{G_c}{l}}{2\psi_a(\boldsymbol{\epsilon}(\boldsymbol{u}))}. \tag{5.58}$$

To ensure the phase-field variable remains within physical bounds ($[0, 1]$), the solution must be suitably constrained. The expression for ϕ is well-defined only when the denominator is strictly positive ($\psi_a > 0$). Moreover, for ϕ to be non-negative, the condition $2\psi_a(\boldsymbol{\epsilon}(\boldsymbol{u})) \geq \frac{3}{8}\frac{G_c}{l}$ must be satisfied. This implies that damage initiates solely when the strain energy density ψ_a reaches a critical threshold. Below this threshold, the material remains fully intact ($\phi = 0$). Applying these restrictions, the constrained solution is formulated as:

$$\phi_{\text{AT1}} = \max\left(0, \frac{2\psi_a(\boldsymbol{\epsilon}(\boldsymbol{u})) - \frac{3}{8}\frac{G_c}{l}}{2\psi_a(\boldsymbol{\epsilon}(\boldsymbol{u}))}\right). \tag{5.59}$$

Note that the upper bound constraint, $\phi \leq 1$, is inherently satisfied by this expression.

For the Wu model, the geometric crack function is $\alpha(\phi) = 2\phi - \phi^2$, with the scaling constant $c_0 = \pi$. Following a similar mathematical derivation, the unconstrained phase-field variable emerges as:

$$\phi = \frac{\psi_a(\boldsymbol{\epsilon}(\boldsymbol{u})) - \frac{G_c}{\pi l}}{\psi_a(\boldsymbol{\epsilon}(\boldsymbol{u}))}. \tag{5.60}$$

In this case, the condition for a non-negative phase field is $\psi_a(\boldsymbol{\epsilon}(\boldsymbol{u})) \geq \frac{G_c}{\pi l}$. If this energy criterion is not met, the variable is simply set to zero. Thus, the physically constrained solution reads:

$$\phi_{\text{Wu}} = \max\left(0, \frac{\psi_a(\boldsymbol{\epsilon}(\boldsymbol{u})) - \frac{G_c}{\pi l}}{\psi_a(\boldsymbol{\epsilon}(\boldsymbol{u}))}\right). \tag{5.61}$$

As with the AT1 model, the upper physical limit ($\phi \leq 1$) is inherently satisfied.

The analytical solutions derived above do not inherently account for damage irreversibility, meaning ϕ could theoretically decrease during unloading. This fundamental condition is enforced numerically by tracking the maximum history value of ϕ over time:

$$\phi_t = \max\left(\phi, \phi_{t-1}\right). \tag{5.62}$$

The effective stress is then calculated using Eq. (2.79).

To verify the proper local enforcement of the irreversibility condition within the proximal Galerkin framework, a cyclic loading-unloading case is examined using the displacement profile shown in Figure 2.13. An initial monotonic load is applied up to a maximum displacement of 0.015 mm, followed by unloading back to 0.0 mm, and subsequent reloading to 0.03 mm. The PFF does not consider an energy split for this case, so the isotropic formulation is considered. For this case, the simulations have been performed with the monolithic and staggered schemes, resulting in the same solutions as expected; thus, the results indicated with LVPP refer to both schemes. The corresponding results for the AT2, AT1, and Wu formulations are presented collectively in Figure 5.15.

During the unloading phase, the phase-field variable remains completely constant, ensuring that the phase-field does not heal—fully consistent with the irreversibility constraint. Upon reloading, damage evolution resumes only after the strain exceeds its previously attained maximum limit. Consequently, the force-displacement curves trace distinct paths

during unloading and reloading, reflecting the permanent energy dissipation from accumulated damage.

In all evaluated cases, the numerical outputs obtained from the finite element simulations exhibit excellent agreement with the mathematically derived analytic solutions, thoroughly validating the correctness of the implemented formulation.

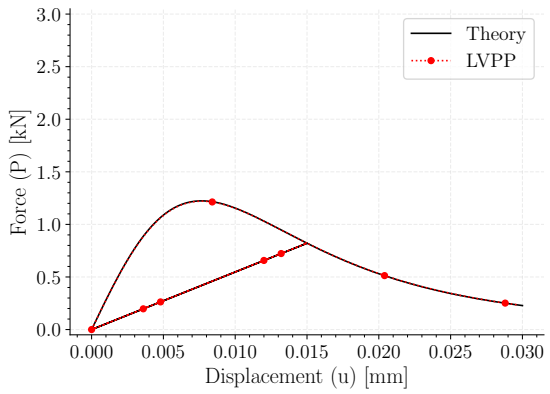

(a) Force vs. displacement - AT2

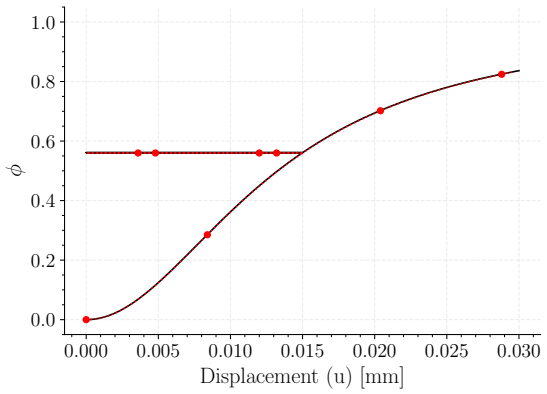

(b) ϕ vs. displacement - AT2

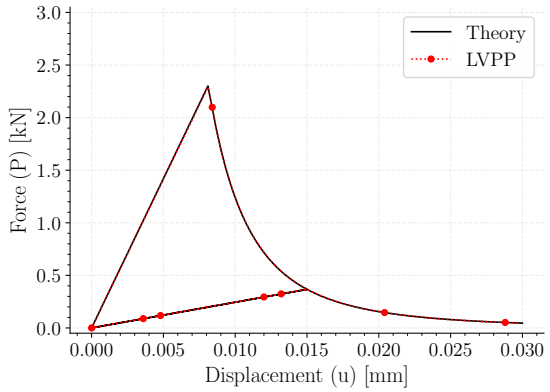

(c) Force vs. displacement - AT1

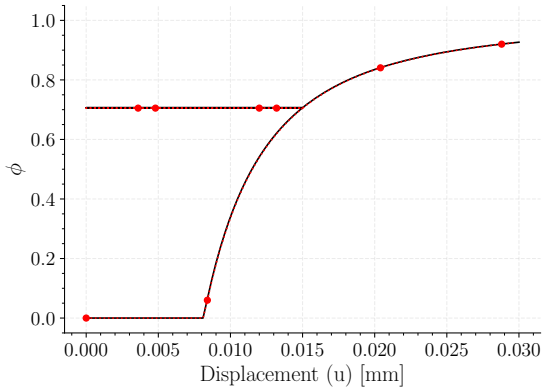

(d) ϕ vs. displacement - AT1

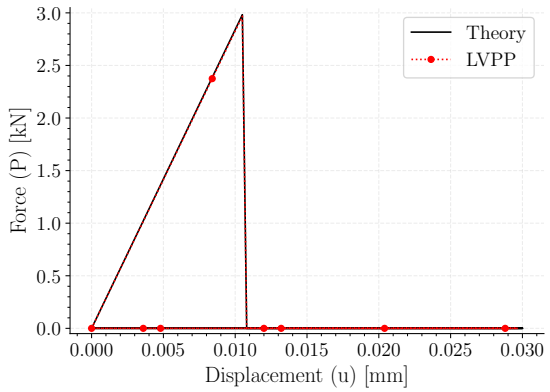

(e) Force vs. displacement - Wu

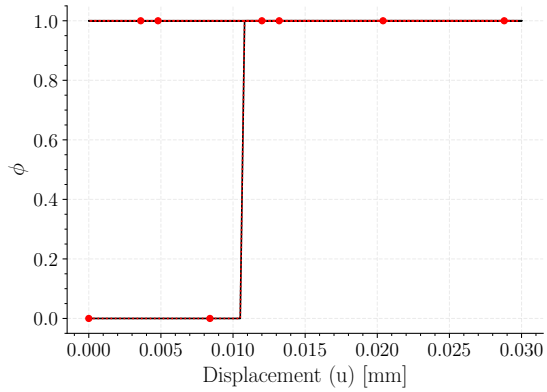

(f) ϕ vs. displacement - Wu

Figure 5.15: One-element local damage model validation. Comparison of reaction force vs. applied displacement (left column) and phase-field variable evolution vs. applied displacement (right column) for the AT2 (top row), AT1 (middle row), and Wu (bottom row) models. Numerical results show excellent agreement with the analytical solutions.

This section also serves as an additional verification benchmark relating to the latent

variable. The mapping between the phase-field variable ϕ and the latent variable ξ is governed by Eq. (5.51). Given that the phase-field variable remains constant over the uniform domain in this single-element experimental setup, the gradient term invariably vanishes, rendering the sub-problem strictly local. Consequently, the associated latent variable is also spatially uniform due to its direct mapping to ϕ. Figure 5.16 illustrates the evolution of ξ across sequential simulation steps for the AT2, AT1, and Wu regularization methods. Although the analytical solution is not explicitly plotted in the figure, the numerical results coincide perfectly with the analytical predictions, such that the plotted results refer indistinguishably to both the numerical and analytical solutions.

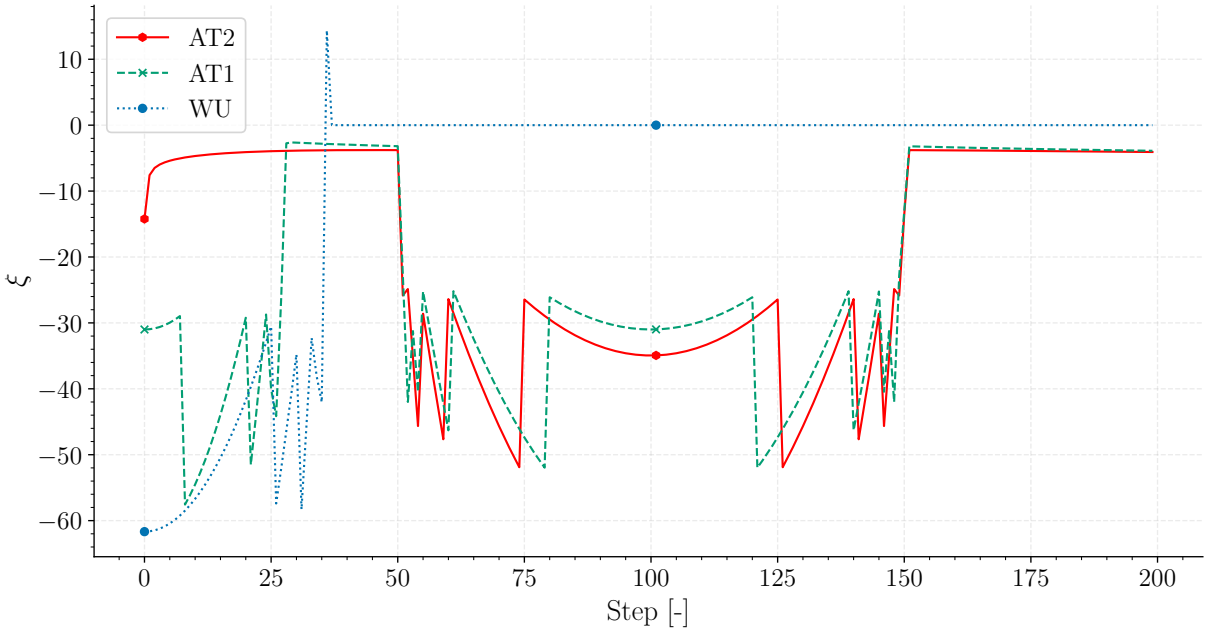

Figure 5.16: Evolution of the latent variable ξ as a function of the simulation steps for the AT2, AT1, and Wu models.

Single edge notched tension test

This section revisits the single edge notched tension test, a standard benchmark problem detailed in Section 2.7.2. The geometric configuration and boundary conditions are identical to those presented in Figure 2.20. The specimen consists of a square plate with a horizontal notch extending from the left edge to the center. The bottom edge is fully constrained, while a vertical displacement is applied to the top edge.

The material properties are consistent with the values listed in Table 2.6: Young's modulus $E = 210\,\mathrm{kN/mm^2}$, Poisson's ratio $\nu = 0.3$, and critical energy release rate $G_c = 0.0027\,\mathrm{kN/mm}$. A length scale parameter of $l = 0.015\,\mathrm{mm}$ is used. The domain is discretized using quadrilateral elements with local refinement in the expected crack path, as shown in Figure 2.21. The effective element size in the refined zone is $h = 0.002\,\mathrm{mm}$, yielding a resolution ratio of $l/h = 7.5$. For this case, the isotropic formulation is considered.

The performance of the proposed LVPP formulation with a staggered scheme is evaluated for the AT2, AT1, and Wu regularizations and compared with the standard staggered

scheme with penalty enforcement described in Section 2.6.3.

The mechanical response and crack evolution are analyzed as a function of the applied displacement. Figure 5.17 provides a comparative assessment of the LVPP algorithm against the standard staggered penalty scheme for the AT2, AT1, and Wu regularization models. The left column displays the reaction force-displacement curves. The results demonstrate excellent agreement between the two methods across all models, confirming that the LVPP formulation correctly captures the global mechanical response. The right column illustrates the evolution of the crack area. Here, distinctions between the methods become apparent. While the LVPP algorithm strictly enforces the physical bounds $0 \leq \phi \leq 1$, the penalty approach exhibits slight deviations, particularly for the AT1 and Wu models (Figures 5.17(c) and 5.17(f)). In these cases, the penalty method allows for small negative values of the energy functional—a non-physical artifact resulting from the violation of the lower bound constraint ($\phi < 0$) due to the finite nature of the penalty parameter. In contrast, the LVPP method rigorously maintains the constraints within solver tolerance, preventing such numerical inconsistencies.

Figure 5.18 compares the reaction force-displacement curves for the AT2, AT1, and Wu regularizations using the LVPP framework. As shown, the AT2 model does not exhibit purely linear elastic behavior initially; damage initiates as soon as strain energy is present and is distributed throughout the domain due to the infinite support of the regularization. In contrast, the AT1 and Wu models exhibit an initial linear elastic response.

Figure 5.19 illustrates the distribution of the phase-field variable ϕ and the latent variable ξ at the load step immediately following the peak force. The phase-field profiles are consistent across all three models, although the width may differ slightly due to the regularization and strain localization effects. The latent variable distribution highlights the different mechanisms of constraint enforcement. These plots are intended for a qualitative comparison, so the color maps should be interpreted as qualitative indicators. For the AT2 model, since the lower bound $\phi \geq 0$ is naturally satisfied, ξ primarily enforces irreversibility. Because the loading is monotonic and crack propagation occurs in a single step, the irreversibility effect is negligible; consequently, the latent variable has a minor or limited influence. In contrast, for the AT1 and Wu models, there is a significant difference in the latent variable distribution, due to the enforcement of the lower bound. In these cases, ξ takes large negative values (approaching negative infinity) as ϕ approaches zero, indicating that the latent variable enforces the non-negativity constraint to prevent unphysical negative values of ϕ. This is directly related to the compact support of these regularization models. This contrast underscores the importance of the LVPP framework in ensuring physically consistent solutions across different regularization models. This behavior, as noted, is directly related to the analytical solution of the CSDF presented in Figure 5.7.

5.5.6 Standard compact tension test specimen

In this section, the objective is to evaluate how the irreversibility condition is enforced on the phase-field variable. As previously discussed, the current implementation of the LVPP framework is displacement-controlled and therefore cannot capture snap-back behavior. For this reason, a compact tension specimen is selected, since crack propagation remains stable under displacement control and is therefore well suited for validation. Because tensile stresses dominate this configuration, as in the previous example, an isotropic

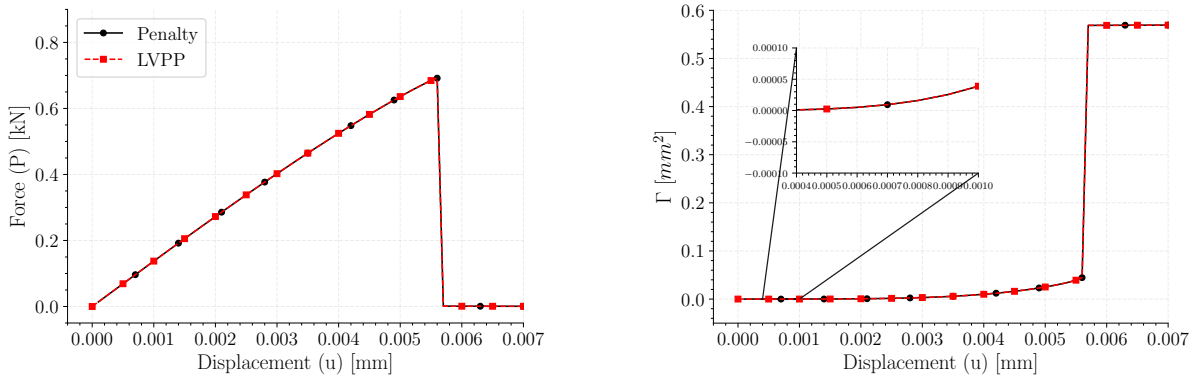

(a) AT2 — Reaction force

(b) AT2 — Crack area

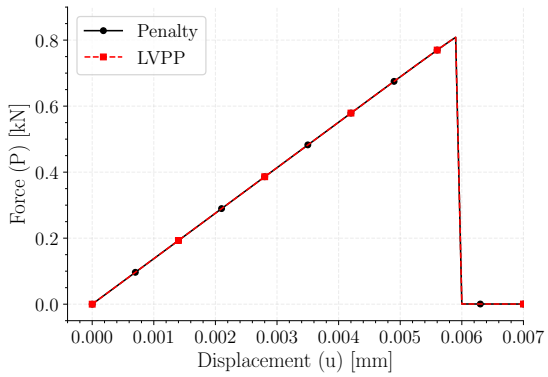

(c) AT1 — Reaction force

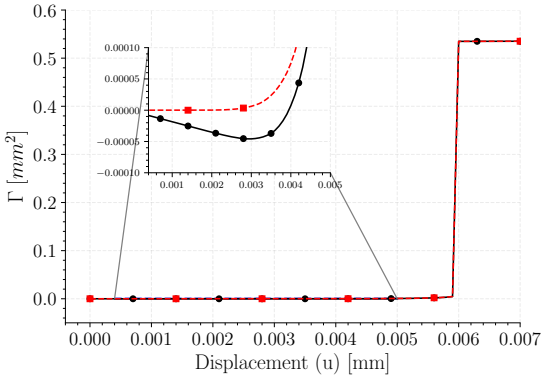

(d) AT1 — Crack area

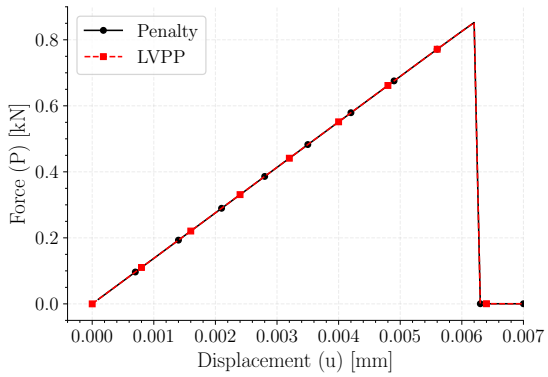

(e) Wu — Reaction force

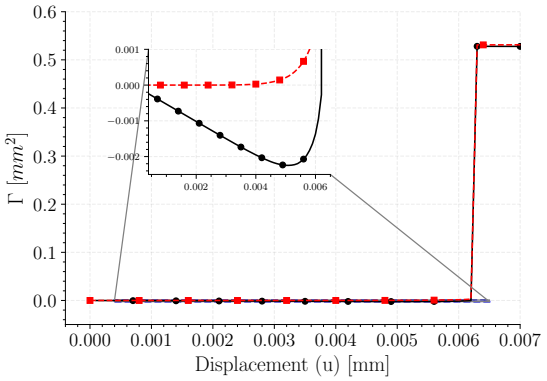

(f) Wu — Crack area

Figure 5.17: Comparison of the LVPP algorithm (solid lines) and the penalty approach (dashed lines) for the single edge notched tension test. The results are organized by regularization model: (a,b) AT2, (c,d) AT1, and (e,f) Wu. Left column: Reaction force vs. displacement. Right column: Evolution of the crack surface energy Γ. Note the fictitious negative energy values in the penalty approach for AT1 and Wu models.

phase-field model is used. The complete geometry and boundary conditions are shown in Figure 5.20. The specimen dimensions coincide with those presented previously in section 3.7; however, in this case the initial crack length is set to $0.5W$. The boundary conditions consider the bottom hole fully constrained, while the top hole is constrained in the horizontal direction and subjected to an imposed vertical displacement.

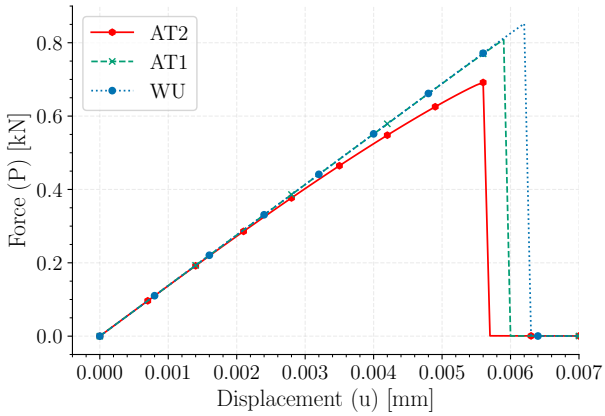

Figure 5.18: Comparison of reaction force versus displacement curves for the AT2, AT1, and Wu regularization models using the proposed LVPP algorithm.

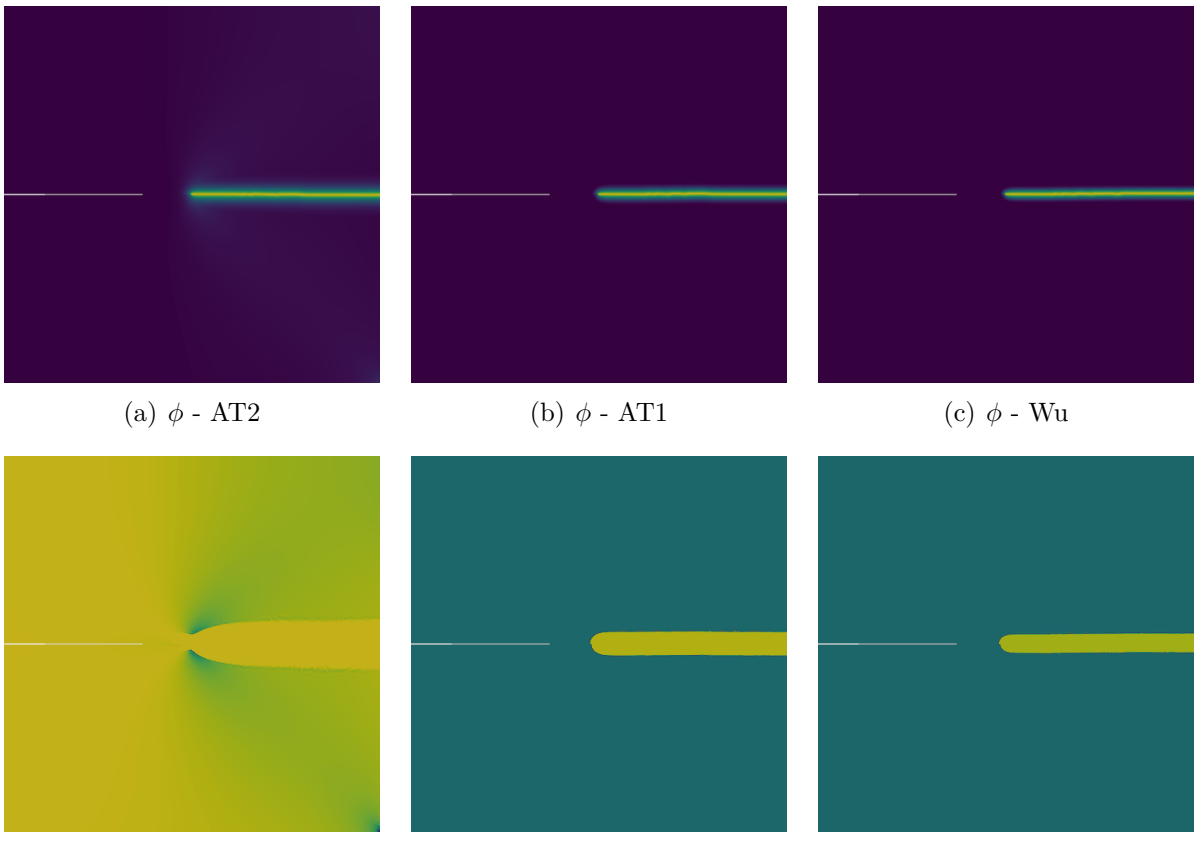

(a) ϕ - AT2 (b) ϕ - AT1 (c) ϕ - Wu

(d) ξ - AT2 (e) ξ - AT1 (f) ξ - Wu

Figure 5.19: Field distributions for the single edge notched tension test. Top row: phase-field variable ϕ. Bottom row: latent variable ξ. Columns (left to right): AT2, AT1, and Wu results.

The same material properties as those presented previously in Table 3.7 are used: Young's modulus $E = 211\,\text{kN/mm}^2$, Poisson's ratio $\nu = 0.3$, and critical energy release rate $G_c = 0.073\,\text{kN/mm}$. A length scale parameter of $l = 0.75\,\text{mm}$ is selected.

The mesh used for the finite element analysis is shown in Figure 5.21. The domain is discretized using quadrilateral elements with local refinement around the expected crack

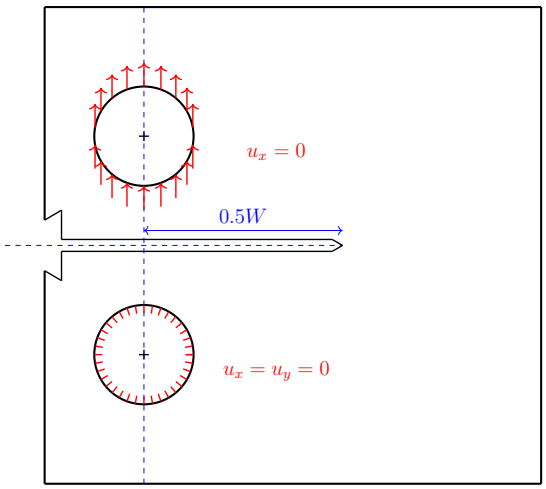

Figure 5.20: Configuration of the compact tension specimen. All the dimensions coincide with the specimen presented in 3.17, except for the initial crack length as shown relative to the specimen width $W = 40.0$ mm. Boundary conditions, labeled in red, indicate: the bottom loading hole is constrained in all directions (fixed support), while the top loading hole is constrained in the horizontal direction with vertical displacement applied to the entire top circle.

path. The refined zone has an effective element size of $h = 0.1\,\text{mm}$, resulting in a ratio of $l/h = 7.5$ which provides sufficient resolution to capture the damage evolution.

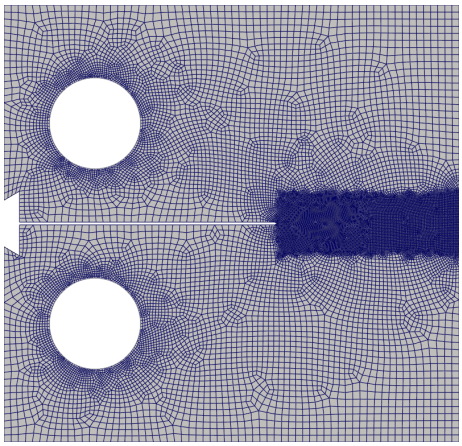

Figure 5.21: Representative finite-element mesh (local refinement at the re-entrant corner). The refined zone uses $h = 0.1\,\text{mm}$.

The specimen is subjected to a loading–unloading–reloading cycle, as shown in Figure 5.22. The vertical displacement is applied in increments of $\Delta u = 10^{-3}\,\text{mm}$, following a history designed to induce crack propagation during the initial loading phase, followed by unloading to verify that damage does not heal, and finally reloading to observe the re-initiation of crack growth. In this case, the staggered scheme is employed, with a staggered termination criterion based on the initial residual criterion described in 2.6.3. To reduce computational cost, a tolerance of 10^{-3} is used. The simulation is performed for the AT2, AT1, and Wu regularization models.

Figure 5.23(a) shows the reaction force versus applied displacement. The response follows

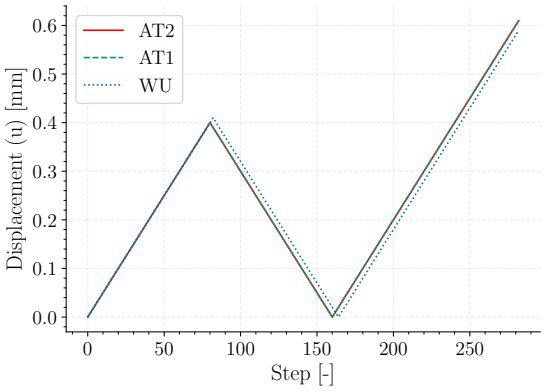

Figure 5.22: Imposed vertical displacement history for the compact tension test, designed to induce a cycle of crack propagation, unloading, and reloading.

the expected pattern for this benchmark: an initial linear-elastic regime, a peak load, and progressive softening as the crack grows. The unloading–reloading branches clearly show irreversible behavior (no crack healing). Figure 5.23(b) presents the evolution of crack area. During unloading, the crack area remains constant for all regularization models, confirming correct enforcement of irreversibility by the LVPP framework. Upon reloading, crack growth resumes once the previous maximum loading state is exceeded. Overall, the results are consistent across the regularizations, supporting the robustness of the method.

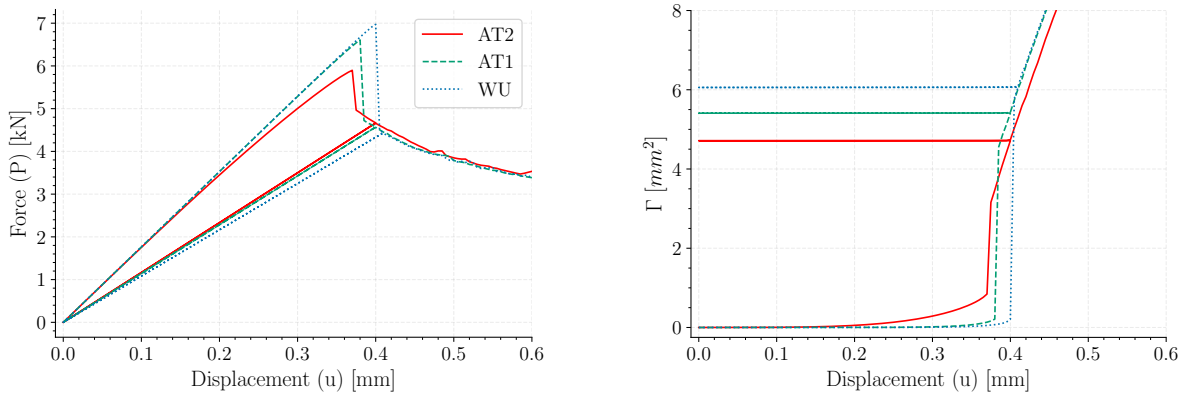

(a) Force vs. applied displacement

(b) Crack area vs. applied displacement

Figure 5.23: Compact tension test response for the AT2, AT1, and Wu models: reaction force vs. applied displacement and crack area vs. applied displacement.

Figure 5.24 shows the phase-field distribution at the end of the unloading phase for the three regularization models.

L-shaped panel test

To evaluate the capability of the LVPP framework in a more complex setting, the L-shaped panel test is analyzed. This benchmark problem, widely recognized in the fracture mechanics literature [48, 64], follows the same loading–unloading–reloading procedure introduced in the compact tension test. In this case, however, the model employs the AT1 regularization combined with the spectral decomposition to account for tension-compression

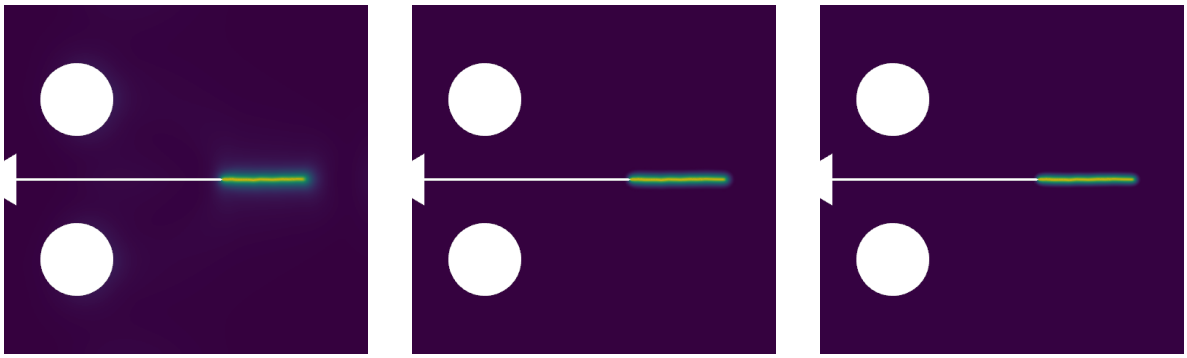

(a) AT2 (b) AT1 (c) Wu

Figure 5.24: Phase-field distribution at the end of the unloading phase for the compact tension test.

asymmetry.

The problem formulation mirrors the setup presented in [48, 64]. The geometry and boundary conditions are depicted in Figure 5.25. The specimen consists of an L-shaped domain where the bottom edge is fully constrained. A vertical displacement is applied to a region extending 30 mm from the right edge of the horizontal arm.

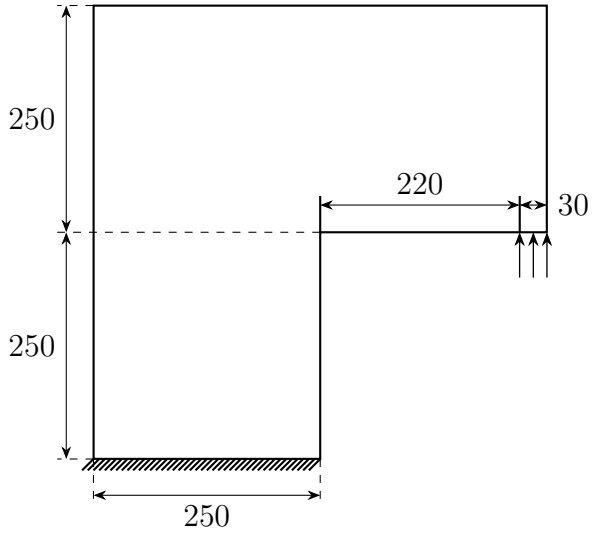

Figure 5.25: L-shaped panel test: geometry, dimensions, and boundary conditions.

The material parameters are listed in Table 5.5. A length scale parameter of $l = 2.5\,\text{mm}$ is adopted. The finite element mesh used for the simulation is illustrated in Figure 5.26; it features local refinement at the re-entrant corner where crack nucleation is expected, with an element size of $h = 1.0\,\text{mm}$ in the refined zone, resulting in a resolution ratio of $l/h = 2.5$. The staggered scheme is used for this simulation, and the maximum number of staggered iterations is set to 100, which is reached for all time steps once the crack has initially propagated.

The displacement is imposed in increments of $10^{-3}\,\text{mm}$, using the same loading scheme shown in Figure 5.27.

Figure 5.28(a) shows the reaction force versus applied displacement. The response follows

Table 5.5: Material parameters for the L-shaped panel test.

Parameter	**Symbol**	**Value**
Young's modulus	E	$25.85\,\mathrm{kN/mm^2}$
Poisson's ratio	ν	0.18
Critical energy release rate	G_c	$8.9 \times 10^{-5}\,\mathrm{kN/mm}$
Length scale parameter	l	2.5 mm
Element size (refined zone)	h	1.0 mm

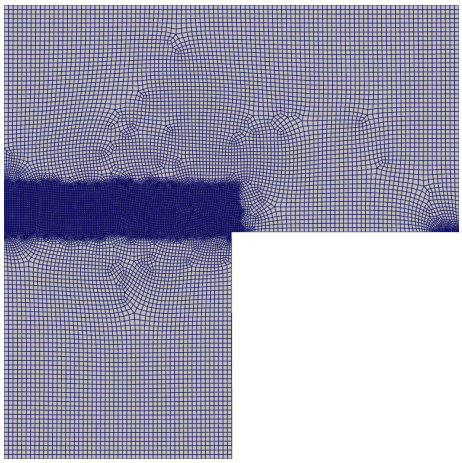

Figure 5.26: Representative finite-element mesh (local refinement at the re-entrant corner). The refined zone uses $h = 1.0\,\mathrm{mm}$.

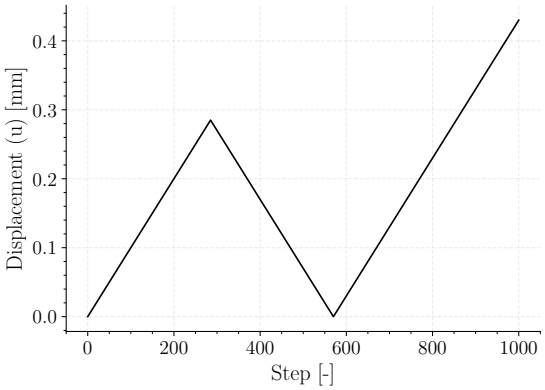

Figure 5.27: Imposed vertical displacement history for the L-shaped panel test, designed to induce a cycle of crack propagation, unloading, and reloading.

the expected pattern for this benchmark: an initial linear-elastic regime, a peak load, and progressive softening as the crack grows. The unloading–reloading branches illustrate that damage is irreversible (no healing). Figure 5.28(b) presents the crack area evolution as a function of the applied displacement; here again, when unloading occurs, the damage remains constant until the reloading phase surpasses the previous maximum.

Figure 5.29 displays the spatial distribution of the phase-field variable ϕ at different stages of the simulation. Initially, the phase-field variable corresponds to the intact state ($\phi = 0$) across the domain. As displacement is applied, the crack propagates; Step 275 shows the crack state prior to unloading. The loading process continues until Step 285, at

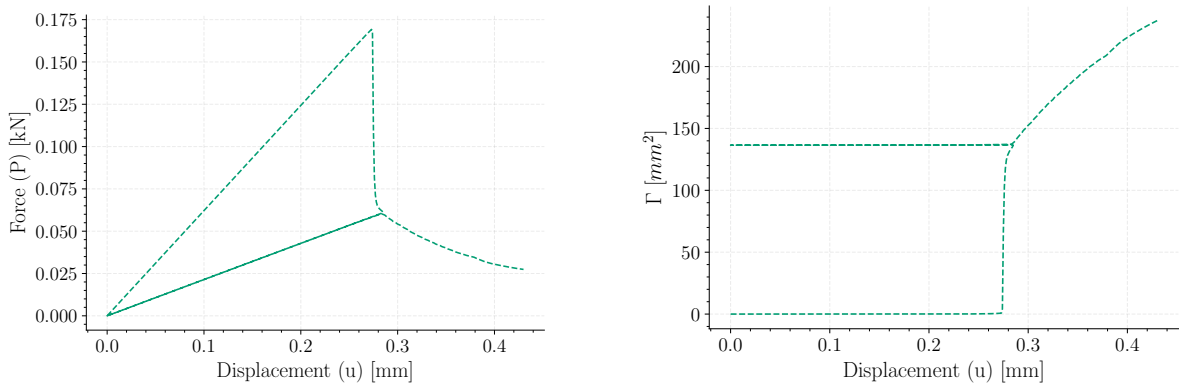

(a) Reaction force vs. applied displacement.

(b) Crack length vs. applied displacement.

Figure 5.28: L-shaped panel test results. (a) Reaction force vs. applied displacement. (b) Crack area vs. applied displacement.

which point the unloading phase begins. The simulation proceeds through the unloading sequence until Step 570. As expected, the damage profile remains constant during this unloading period, confirming the irreversibility of the fracture process. Following this, the loading is reapplied. The crack remains stationary until Step 855, when the applied displacement exceeds the previous maximum. Beyond this point, crack propagation resumes. Step 1000 shows the final phase-field distribution at the end of the simulation.

5.6 Conclusions

In this chapter, the LVPP algorithm was introduced and validated as a robust numerical framework for both isolated CSDFs and fully coupled PFF models with inequality constraints. By reformulating the variational inequality as a sequence of unconstrained saddle-point problems with an entropic barrier, the method enforces the interval constraint of the phase-field variable ($0 \leq \phi \leq 1$) and the irreversibility condition ($\dot{\phi} \geq 0$).

This methodology addresses a key bottleneck in compact-support regularizations (such as AT1 and Wu), where parameter-dependent approaches often fail to maintain physically admissible phase-field values.

The main contributions and findings of this study can be summarized as follows:

1. The LVPP method provides a unified, theoretically sound approach to enforcing inequality constraints across a variety of crack surface density functionals. It inherently guarantees that the damage state does not heal during mechanical unloading in the full PFF context, and that the phase-field rigorously stays within exact physical limits for the independent CSDF problem.

2. The application of the LVPP algorithm within a finite element framework—termed the Proximal Galerkin method—does not require specialized spatial discretization techniques for the feasible constraint set, nor for the latent variable. This enables straightforward implementation into general-purpose finite element codes using standard linear elements without adding computational complexity.

3. Compared to traditional penalty methods, the LVPP approach entirely eliminates

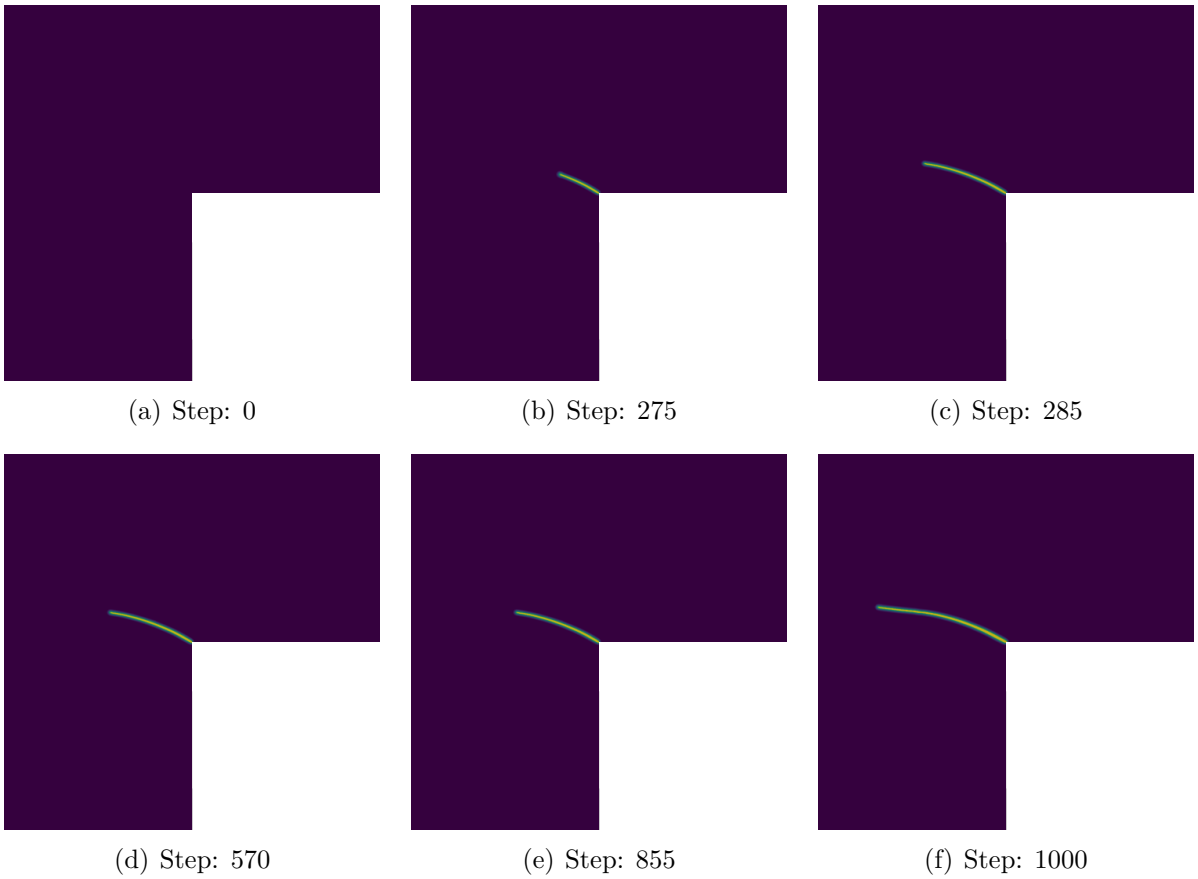

(a) Step: 0 (b) Step: 275 (c) Step: 285

(d) Step: 570 (e) Step: 855 (f) Step: 1000

Figure 5.29: Phase-field (ϕ) snapshots for the L-shaped panel test, for different steps of the simulations.

the need for arbitrary, problem-dependent tuning of penalty parameters for either the bounding CSDF limits or the mechanistic PFF irreversibility criteria. It natively satisfies the mathematical constraints within standard solver tolerances, circumventing the numerical instabilities and non-physical negative energy states often induced by finite penalization limits.

4. The mathematical formulation was validated against one-dimensional analytical solutions for bounded (AT1, Wu) and unbounded (AT2) regularization profiles. The Proximal Galerkin results showed excellent agreement with analytical predictions for both the phase-field variable and the dual latent variable.

5. An adaptive update strategy for the proximal parameter (β_k) was proposed and verified. With $\beta_0 = c_0 l$ for CSDF and $\beta_0 = c_0 l/G_c$ for PFF, the simulations converged to analytical solutions in the one-dimensional CSDF and one-element PFF tests. For cases without closed-form solutions, the results were consistent with those obtained using the penalization approach.

6. The framework's capabilities were effectively demonstrated in realistic physical scenarios, including the single-edge notched tension test and the cyclic L-shaped panel test. The method accurately captured local damage patterns, global mechanical responses, and strict damage irreversibility over extensive unloading–reloading cycles.

7. Regarding the non-convexity of the PFF problem, the LVPP method can be imple-

mented in both monolithic and staggered schemes. Similar behavior to standard methods has been observed, as presented in Section 2.6.2 and Section 2.6.3. The staggered scheme provides a robust solution strategy, but careful attention must be paid to convergence criteria and tolerances.

8. In the PFF framework, the solution procedure involves time steps with staggered iterations at each step. For the mechanics equation, a Newton-Raphson scheme is used with multiple iterations. Similarly, the phase-field equation requires resolving the sequence of PDEs associated with the LVPP, each solved within a Newton-Raphson scheme. This computationally expensive process requires careful attention to tolerances, convergence criteria, and the maximum number of iterations for each sub-problem. Future research will focus on optimizing procedures for the proximal Galerkin method to reduce the number of iterations.

When applying the LVPP framework directly to the fully coupled mechanics of fracture, the displacement field does not involve inequality restrictions; therefore, the latent variable is exclusively bound to the scalar damage variable. With a standard staggered framework, the algorithm captures the expected structural behavior seamlessly.

Notably, when assessing the models' varying mechanical capacities, the AT1 and Wu regularizations predictably exhibit higher peak load thresholds compared to the AT2 model due to their bounded regularization properties.

In conclusion, the proposed LVPP methodology offers a parameter-free and practical tool for fracture analysis. By combining standard PFF discretizations with a latent-variable optimization framework, it addresses the main challenges associated with bounded regularizations and irreversible behavior, and provides a reliable approach for modeling physically consistent crack propagation in complex engineering materials.

An important observation regarding the work presented in this chapter is that its organization closely follows the chronological sequence of its development. Since the LVPP algorithm is directly applied to the phase-field variable, the formulation is first analyzed and validated for the CSDF alone.

Chapter 6

PHASEFIELDX: A COMPUTATIONAL FRAMEWORK FOR PHASE-FIELD FRACTURE

The development of robust and efficient software is a cornerstone of this research, underpinning the scientific contributions of this thesis. A key outcome is the creation of **PhaseFieldX**, an open-source computational framework designed to implement, verify, and analyze PFF models and their corresponding ingredients, such as the elasticity problem and crack surface representation. The significance and quality of this software have been recognized through its peer-reviewed publication in the *Journal of Open Source Software* (JOSS) [38], an open-access journal that ensures research software meets high standards of scientific rigor, usability, and reproducibility.

Reproducibility and transparency are central to modern computational science. By releasing PhaseFieldX under the MIT license and providing comprehensive documentation and examples, this work enables the community to independently verify all numerical results presented in this thesis. The open-source nature of PhaseFieldX not only facilitates the reproduction of results but also encourages further development and critical scrutiny, in line with the principles of Open Science.

Developing a custom computational framework, rather than relying on commercial or black-box software, provides full control over algorithmic implementation and enables rigorous testing of new methods. This approach allows for detailed analysis, rapid prototyping, and the direct translation of theoretical advances into practical tools. As a result, PhaseFieldX serves both as the primary platform for the studies in this dissertation and as a foundation for future research in phase-field modeling. It is worth noting that other in-house tools, such as Iris, were also utilized during the realization of this thesis for implementing and testing specific problems. However, the aim of this chapter is to present a general overview of the motivation and structure of the PhaseFieldX software. For more detailed information about PhaseFieldX, readers are encouraged to consult the GitHub repository [65] and its accompanying documentation, where the code encompasses detailed explanations and numerous examples.

To ensure scientific reliability, the software is accompanied by a suite of analytical benchmarks, validation tests, and example problems. These resources are designed to help users understand, verify, and extend the implemented models. The following sections detail the motivation, design philosophy, structure, and validation strategy of PhaseFieldX, highlighting its role in supporting the findings and reproducibility of this thesis.

This chapter is organized as follows. Section 6.1 presents the structure and modular philosophy of the developed software. Section 6.2 discusses benchmarking and validation procedures. Section 6.3 introduces the PhaseFieldX package, highlighting its features and architecture. Finally, the chapter concludes with a summary and outlook.

6.1 Software development structure

Before developing a complete software package, or even simple scripts, it is essential to define a clear structure and development plan, bearing in mind the final objectives. This planning phase is crucial for ensuring that the process is efficient, organized, and aligned with the intended purpose.

The software development strategy in this thesis mirrors the learning path required to understand PFF models. Since PFF problems are based on the coupling of elasticity and Crack Surface Density Functionals (CSDFs), the development process was structured to address these components sequentially:

1. **Elasticity Problems:** Implementation and verification of standard elasticity.
2. **Phase-Field Functionals:** Implementation of CSDFs (e.g., AT1, AT2, Wu), corresponding to the formulations discussed in Chapter 2 and Chapter 5.
3. **Coupled Fracture Models:** Integration of the previous two components into a complete fracture mechanics framework, following the governing equations presented in Section 2.4.

Additionally, the program structure incorporates other developed submodules, including schemes for handling different anisotropic formulations (see Section 2.1.2) and a module containing various degradation functions. The software architecture is designed so that modifications—such as implementing a new anisotropic model, degradation function, or stagger termination criteria—can be performed easily and integrated seamlessly with other parts of the code.

Regarding the correction method for crack area overestimation introduced in Chapter 4, it is important to note that this relies on a single correction array $\mathcal{F}$, which is also applicable to other quantities. This approach simplifies explanation, documentation, implementation, and testing. It also facilitates the post-processing of results with different methods using a consistent framework.

This approach allows for a modular design where each component is developed, tested, and validated independently before integration. This modularity facilitates the localization of errors in both theoretical formulations and numerical implementations, and allows for the evaluation of limitations in specific models.

Consequently, the structure of **PhaseFieldX** is highly determined by this modular philosophy, following the approach summarized in Figure 2.1. It is designed to be extensible,

allowing users to easily add new degradation functions, energy splits, or solver algorithms without altering the core structure.

The structure of this thesis is directly aligned with the documentation and organization of the PhaseFieldX package. This approach ensures that the theoretical developments are seamlessly connected to their numerical implementation, facilitating both reproducibility and a deeper comprehension of the underlying mechanics.

6.2 Benchmarking and validation

A critical aspect of software development is the creation of rigorous benchmarking and validation examples. These examples serve a dual purpose: they test the implementation of the models and provide a reference for users to understand how to set up simulations. To ensure that the code solves the equations correctly and represents the physical reality, problems with known analytical solutions are prioritized. These analytical benchmarks offer valuable insight into the model's behavior, facilitating a deeper understanding of the underlying physics. Furthermore, they serve as the primary test cases, as the numerical implementation can be directly compared against the analytical solution. This comparison allows for verification either by matching the results exactly within machine precision or by demonstrating appropriate convergence rates with mesh refinement.

6.2.1 Phase-field CSDFs

As presented in previous chapters, the CSDF is central to the phase-field model. Different formulations, such as the AT1, AT2, and Wu models, have been implemented. An analysis has been performed for each regularization, starting with the standard AT2 case and extending to the AT1 and Wu models.

In all cases, a one-dimensional boundary value problem is considered, for which analytical solutions can be derived. In Section 2.2.1, the one-dimensional problem and its analytical solution are presented for the AT2 model. Similar procedures have been followed for the AT1 and Wu models (see Chapter 5), where inequality constraints due to the boundedness of the phase-field variable must be explicitly handled. These analytical benchmarks serve as a basis to understand the behavior of each regularization and to validate their numerical implementation in **PhaseFieldX**.

6.2.2 Elasticity solvers

The elasticity solver is a fundamental component of the framework. To validate its implementation, several benchmark problems with known analytical solutions are included, such as simple tension, compression, and shear tests. These problems are also used to verify the proposed anisotropic formulations.

Before analyzing the full coupled problem, it is essential to evaluate its components. The elastic energy is typically defined as:

$$\Psi_{\text{isotropic}}(\boldsymbol{u}) = \int_{\Omega} \psi(\boldsymbol{\epsilon}(\boldsymbol{u}))\,\mathrm{d}\boldsymbol{x} - \mathcal{E}_{\text{ext}}(\boldsymbol{u}), \tag{6.1}$$

which represents the standard isotropic case.

For anisotropic phase-field formulations (as presented in Section 2.1.2), the energy is split into active (tensile) and inactive (compressive) parts:

$$\Psi_{\text{anisotropic}}(\boldsymbol{u}) = \int_{\Omega} \left[\psi_a(\boldsymbol{\epsilon}(\boldsymbol{u})) + \psi_b(\boldsymbol{\epsilon}(\boldsymbol{u}))\right] \, \mathrm{d}\boldsymbol{x} - \mathcal{E}_{\text{ext}}(\boldsymbol{u}), \tag{6.2}$$

with the corresponding weak form:

$$\int_{\Omega} \left[\boldsymbol{\sigma_a}(\boldsymbol{\epsilon}(\boldsymbol{u})) + \boldsymbol{\sigma_b}(\boldsymbol{\epsilon}(\boldsymbol{u}))\right] : \boldsymbol{\epsilon}(\delta\boldsymbol{u}) \, \mathrm{d}\boldsymbol{x} - \int_{\partial\Omega_t} \boldsymbol{t} \cdot \delta\boldsymbol{u} \, \mathrm{d}S = 0. \tag{6.3}$$

Validating that $\psi = \psi_a + \psi_b$ and checking that the stress responses match the standard isotropic case (in the absence of damage) provides a robust benchmark for the anisotropic elasticity implementation.

6.2.3 PFF model validation

Once the basic ingredients—elasticity and CSDFs—are validated, the complete PFF model is analyzed. Validation requires considering isotropic and anisotropic models, different degradation functions, various numerical algorithms (staggered vs. monolithic), and irreversibility constraints.

Although obtaining analytical solutions for the coupled evolution problem is challenging, two main strategies are used for validation:

1. **Single-element tests:** Presented in Section 2.7.1 and Section 2.7.1, these tests verify the constitutive updates and the correct implementation of energy splits and irreversibility on a fundamental level. Furthermore, they have been used to validate the implementation of the PFF problem within the LVPP algorithm (see Chapter 5).
2. **LEFM comparison:** For complex crack propagation problems, results are compared with LEFM predictions. While exact analytical solutions for arbitrary geometries are in general not available, LEFM provides accurate predictions for critical loads and initial crack paths, serving as a standard for validation. This comparison is particularly relevant for the fatigue extension (see Chapter 3), where LEFM principles are integrated with PFF.

6.3 PhaseFieldX

Leveraging the robust capabilities of FEniCSx [66, 67, 68, 69], a renowned finite element framework for solving partial differential equations, the PhaseFieldX package enables efficient and accurate numerical simulations related to phase-field models. It supports a broad range of applications, including PFF, solidification, and other complex material phenomena, making it an invaluable resource for researchers and engineers in materials science.

PhaseFieldX is a leading open-source package for phase-field modeling, particularly in the absence of commercial solutions that directly support PFF simulations. PhaseFieldX integrates the latest advancements in phase-field research, offering fatigue simulation capabilities (as derived in Chapter 3) in a user-friendly, ready-to-use package. By simplifying access to cutting-edge methods, it lowers barriers to adoption and enables researchers to focus on scientific discovery without the challenges of bespoke modeling.

The source code of the framework is publicly available on GitHub [65], where a link to the project documentation is also provided.

6.3.1 Code structure and testing

To ensure code quality and maintainability, the PhaseFieldX repository follows a structured organization. The codebase is divided into distinct modules, separating the core package logic from the user interface and application examples. This separation of concerns facilitates isolated testing and easier extensibility.

The reliability of the software is safeguarded by a comprehensive testing suite, which is integral to the development workflow. This suite includes testing at multiple levels to verify the correctness of individual functions and classes, ensure that different modules function correctly in concert, and run benchmark problems to prevent experimental regressions.

To automate this process, Continuous Integration (CI) workflows are employed. Upon every update to the repository, these workflows automatically build the documentation and execute the full test suite across different environments. This guarantees that the software remains stable and reliable for the scientific community.

The platform's modular design empowers users to customize parameters such as degradation functions, energy-splitting schemes, and solver strategies, allowing a wide range of configurations for PFF and fatigue studies (refer to Chapter 3 for details on the fatigue solvers). This flexibility encourages innovation and experimentation, making **PhaseFieldX** an ideal tool for reliable simulations and collaborative development. Researchers can contribute to its evolution, creating a dynamic ecosystem that advances understanding of complex material behaviors and drives scientific progress. The PhaseFieldX logo (see Figure 6.1) is inspired by the hyperbolic tangent function and the characteristic profile of the AT2 phase-field regularization, visually relating the symbol to the underlying phase-field fracture model.

Figure 6.1: PhaseFieldX logo.

The software is based on the FEniCSx project [66]. Consequently, it inherits all the advanced capabilities of this platform. A key advantage of this foundation is the seamless integration with the PETSc library (Portable, Extensible Toolkit for Scientific Computation). This connection grants access to a powerful suite of scalable linear and non-linear solvers, including direct solvers (LU decomposition), iterative methods with advanced preconditioners (e.g., algebraic multigrid, incomplete Cholesky), and robust line search algorithms tailored for non-linear problems. Consequently, simulations can be essentially parallelized out-of-the-box, allowing for efficient scaling from personal laptops to high-performance computing clusters. Furthermore, the installation procedure for the entire

framework is straightforward, leveraging modern package managers such as Conda or Docker containers to ensure a consistent and reproducible environment across different operating systems.

Key features of **PhaseFieldX** include:

- **Energy splits:** The software implements both standard isotropic and anisotropic formulations for the strain energy density, such as the spectral decomposition and the volumetric-deviatoric decomposition (as discussed in Section 2.1.2).
- **Regularization Models:** Regarding the crack surface density function, the software supports the AT1, AT2, and Wu models (see Chapter 2).
- **Degradation Functions:** It is possible to consider different degradation functions, such as quadratic, cubic, or quasi-linear functions.
- **Solution Algorithms:** The software permits the use of both staggered and monolithic schemes, including the energy-controlled solver (in variational or non-variational forms, see Chapter 3) and LVPP algorithms like the proximal Galerkin method (see Chapter 5).
- **Irreversibility:** To enforce the irreversibility condition of the fracture field, different approaches have been implemented, such as the history field approach, the penalization approach, and the previously mentioned LVPP-based approach.

By selecting the desired models in the input file, a large number of configurations regarding physical models and numerical strategies can be simulated. This modularity ensures that the basis of the PFF problem—elasticity, crack surface density, and the coupled functional—can be analyzed both individually and collectively, facilitating code maintainability and extensibility.

6.4 Outlook on PhaseFieldX and FEniCSx integration

The framework has been designed to easily incorporate additional advanced features. Some capabilities that have been initially tested or are prepared for integration include:

- **Heterogeneous materials:** Consideration of domains with different material properties in each region, such as varying Young's modulus, Poisson's ratio, or fracture toughness.
- **Periodic boundary conditions:** Implementation of periodic boundary conditions using multi-point constraints (MPC) via the `dolfinx_mpc` package [70].
- **Custom constitutive models:** Integration of user-defined constitutive laws, leveraging the flexibility of the `fenicsx_constitutive_models` package [71].
- **Adaptive mesh refinement:** Support for dynamic mesh adaptation to resolve localized features efficiently.
- **Multi-physics coupling:** Extension of the model to consider thermal effects, hydrogen embrittlement, or other coupled physical phenomena.

Although not presented in this thesis, the **PhaseFieldX** package includes an implemen-

tation of cycle-by-cycle fatigue simulation following the approach presented by [19]. Additionally, initial implementations of the Allen-Cahn and Cahn-Hilliard equations are available for phase-field modeling of solidification and related phenomena. These features facilitate the extension of the package to other problem domains, such as phase transformation, topology optimization, and other physical processes that can be modeled using phase-field methods.

6.5 Conclusions

This chapter has presented the computational framework developed during this thesis, culminating in the creation of the open-source software **PhaseFieldX**. By addressing the critical need for transparent and reproducible research tools in computational mechanics, this work not only supports the findings of this thesis but also provides a valuable resource for the broader scientific community.

The modular architecture of **PhaseFieldX**, built upon the advanced FEniCSx package, allows for the flexible implementation of diverse PFF models, ranging from standard isotropic formulations to complex anisotropic energy decompositions and novel solution algorithms. The rigorous validation process, encompassing analytical benchmarks and established numerical tests, ensures the reliability and accuracy of the implemented methods.

This software serves as the foundation for the numerical examples and scientific contributions presented in the subsequent chapters. By making the source code, documentation, and specific simulation scripts openly available, this thesis adheres to the principles of Open Science, facilitating the verification of results and encouraging future collaborative developments in the field of PFF modeling.

Chapter 7

CONCLUSIONS AND FUTURE WORK

This final chapter summarizes the main findings and contributions of this thesis. First, the general conclusions drawn from the development and validation of phase-field fracture models are presented. Subsequently, potential lines of future research are outlined to extend the capabilities of the proposed framework. Finally, the scientific contributions derived from this work, including publications and software development, are listed.

7.1 General conclusions

The PFF method presents significant advantages for simulating fracture behavior, as it eliminates the need for explicit tracking of the crack surface. This allows for the natural handling of complex topological changes, such as crack branching and merging, within a standard finite element framework. However, several critical aspects must be addressed to ensure reliable and physically meaningful results. The accuracy of the PFF method relies heavily on the interaction between the elastic energy and the CSDF.

Regarding the CSDF, a key parameter governing the diffuse regularization is the length scale l, which controls the width of the regularized crack profile. It has been demonstrated that for the approximation of surface energy to be accurate, l must be sufficiently small relative to the domain boundaries and potential crack path to be energetically equivalent to the discontinuous or sharp crack case. Specifically, for models with finite support such as AT1 or Wu, the energetic approximation becomes exact if the phase-field profile has sufficient space to fully develop. In contrast, for the AT2 model, which lacks compact support, the approximation is asymptotically exact only as $l \to 0$. Nevertheless, for practical purposes, if the length scale is at least 5 times smaller than the domain boundaries or other geometric features, the error remains within acceptable limits. Importantly, this aspect can be quantified exactly through the one-dimensional analytical solution, allowing for precise control and evaluation of the results to ensure their validity.

Regarding the finite element solution of the CSDF, it is important to ensure that the mesh is sufficiently refined to properly capture the phase-field profile and, consequently, the diffuse energy equivalent to the discrete case. As presented for linear elements across all regularization models, the phase-field profile is captured with a relative error in the total

energy approximation of less than 1% for ratios of $l/h > 2$, where h is the characteristic element size. However, it is preferred to use more conservative ratios.

While the regularization of the crack surface is the core strength of PFF, it also introduces numerical artifacts when the CSDF is analyzed as a component of the PFF model. A primary issue identified is the strain localization effect, where the phase-field variable artificially saturates to a value of 1 across entire finite elements, at least for linear elements. This phenomenon leads to a systematic overestimation of the crack area, distorting global quantities such as the force-displacement response, which is essential for evaluating fracture behavior. To address this, several correction factors exist, such as the Bourdin factor or the skeleton algorithm. In this thesis, the new Double Gradient Correction Method (DGCM) has been proposed and validated. Based on the principle of energy equipartition observed in the 1D analytical solution, this method corrects the crack area calculation by relying on the gradient-dependent energy term. As demonstrated in the one-dimensional solution, this term is equivalent to the phase-field energy term when the length scale ratio with respect to boundaries is sufficiently small. Crucially, it is not sensitive to localization artifacts, so this method approximates the true area as twice the gradient-based energy component. The DGCM has proven to be a robust, mesh-independent definition that allows for accurate fracture energy measurements even in the presence of localization, applicable to any type of element and dimension. This aspect can be quantified and its convergence evaluated; it has been observed that refining the mesh reduces the effect. While a ratio of $l/h \approx 2$ is sufficient to capture the crack profile, the strain localization effect requires a higher ratio to be eliminated. Therefore, for computational efficiency, the most effective approach is to evaluate the convergence of this ratio to properly account for these solutions.

Another aspect presented is the presence of the peak force effect, characterized by a peak in the force-displacement curve that is not present in the discrete case. This is related to the nucleation of the phase-field fracture. In cases where the initial crack is included in the mesh, a peak force is observed. In a displacement-controlled system, the maximum force will correspond to this peak force, as the solver is unable to recover the snap-back behavior. Consequently, equilibrium algorithms capable of tracking the complete evolution of the crack are necessary to capture the entire equilibrium path, including snap-back behavior. This allows for the evaluation and consideration of this aspect when analyzing results.

The energy solvers have been presented in variational and non-variational forms, demonstrating that although the results given by the simulation are equivalent, some relations must be considered during post-processing.

Extending the PFF method to high-cycle fatigue typically incurs a prohibitive computational cost due to the need for cycle-by-cycle simulations. This thesis has introduced a novel fatigue framework that bridges the gap between PFF and classical LEFM. By deriving the compliance derivative with respect to the crack area, directly from a single monotonic PFF simulation, the proposed method allows for the integration of Paris' law without simulating individual cycles. This approach simplifies the parametrization of the model and drastically reduces the computational expense, enabling the prediction of fatigue life and crack paths in complex geometries efficiently. To correctly perform and evaluate this aspect, the dimension of the length scale parameter with respect to the boundaries and other cracks, its ability to handle the diffuse representation, and the evaluation of the strain localization effect must be carefully considered.

A critical challenge in phase-field modeling, particularly for AT1 and Wu regularizations, is the robust enforcement of physical constraints, namely the boundedness of the phase-field variable ($0 \leq \phi \leq 1$) and the irreversibility of damage. In the literature, the history field method is commonly used to handle irreversibility, but it does not address boundedness; thus, additional specialized treatments must be included. Furthermore, this formulation breaks the variational structure of the PFF problem. Another approach is the penalty method, which can handle both irreversibility and boundedness within the same framework by transforming the inequality problem into a penalized unconstrained one. However, this thesis has demonstrated that the Latent Variable Proximal Point (LVPP) algorithm offers a superior alternative to traditional penalty methods. By rewriting the variational inequality as a sequence of saddle-point problems, the LVPP method avoids the ill-conditioning and parameter sensitivity associated with penalty parameters. The results confirm that this approach allows for the efficient use of Proximal Galerkin discretizations, effectively handling the constraints of all phase-field regularizations. Regarding the solution scheme, similar challenges due to the non-convexity of the functional have been encountered; consequently, the method has been presented within both monolithic and staggered schemes. Additionally, the implementation of this method is straightforward in most general finite element solvers, as the latent variable is discretized in the same manner as the other fields.

Regarding the tolerance criteria of the staggered scheme, a new method has been proposed based on the first residual of the Newton-Raphson solvers. This criterion allows for the analysis of the staggered scheme in a manner equivalent to the monolithic case, providing a clear and exact metric to evaluate convergence. Although this criterion is rigorous, less restrictive tolerances have also been used to avoid excessive computational costs, provided that the approximation error is well-understood and controlled.

Finally, the reliability of these numerical methods is underpinned by their implementation in the open-source package **PhaseFieldX**. This package follows a modular design aligned with the PFF problem structure, providing clarity and facilitating the implementation of new functionalities. It also includes the numerous analytical solutions presented in this thesis as benchmarks and automated tests for verification.

7.2 Main results

The primary quantitative findings and methodological advancements derived from this research are summarized as follows:

- **Modular framework for PFF:** The Phase-Field Fracture problem has been successfully structured into distinct, modular components—Elastic Energy, Crack Surface Density Function (CSDF), Degradation Function, and Solution Scheme. This separation clarifies the complexity of the method, highlighting that while the CSDF (e.g., AT1 vs. AT2) dictates the diffuse crack topology and convergence properties, the Solution Scheme (e.g., Monolithic vs. Staggered, variational vs. non-variational) governs the numerical stability and efficiency.
- **Crack area correction:** A new robust correction method, the Double Gradient Correction Method (DGCM), was developed derived from the energy equipartition principle. It was proven that this method eliminates the systematic overestimation of crack area caused by strain localization artifacts, providing a mesh-independent

measurement of fracture energy (approximated as twice the gradient-based energy component).

- **Fatigue framework efficiency:** The proposed energy-controlled fatigue framework was validated to rigorously link PFF with LEFM. By extracting the compliance derivative ($\mathrm{d}C/\mathrm{d}a$) directly from a single monotonic simulation, the method allows for the integration of Paris' law (or NASGRO) without the prohibitive cost of cycle-by-cycle simulations.
- **Constraint enforcement via LVPP:** The Latent Variable Proximal Point (LVPP) algorithm was successfully applied to phase-field fracture. It demonstrated superior robustness compared to penalty methods in enforcing the physical constraints of boundedness ($0 \leq \phi \leq 1$) and irreversibility, particularly for models with finite support (AT1, Wu), while maintaining the variational structure of the problem.
- **PhaseFieldX package:** All proposed methodologies have been implemented in the open-source package **PhaseFieldX**. This package ensures the reproducibility of results and facilitates the adoption of advanced phase-field techniques by the broader scientific community.

7.3 Future research lines

Based on the findings of this thesis, several promising avenues for future research have been identified.

The proposed fatigue framework has been analyzed in cases where only one crack is present. So future work will be to consider multiple cracks and their interaction, which is a common scenario in real-world applications.

Regarding **advanced fatigue models and 3D extensions**, the proposed energy-controlled framework presents a straightforward path for expanding into three-dimensional problems. Furthermore, while the current implementation relies on Paris' law, the methodology inherently supports more sophisticated fatigue models, such as the NASGRO equation [72]. Widely utilized in aerospace applications, the NASGRO equation captures the full sigmoidal range of crack growth rates, from the near-threshold region ΔK_{th} to the critical instability limit K_{c}. Conveniently, this critical limit can be directly derived from the compliance derivative ($\mathrm{d}C/\mathrm{d}a$) provided by the proposed PFF computations. The equation also explicitly accounts for mean stress effects (the R-ratio) and crack closure through an opening function f:

$$\frac{\mathrm{d}a}{\mathrm{d}N} = C\left[\left(\frac{1-f}{1-R}\right)\Delta K\right]^{n} \frac{\left(1-\frac{\Delta K_{\mathrm{th}}}{\Delta K}\right)^{p}}{\left(1-\frac{K_{\max}}{K_{\mathrm{crit}}}\right)^{q}}, \tag{7.1}$$

where C, n, p, and q are empirically derived material constants. By substituting the standard power-law relationship with the NASGRO formulation—or other similarly advanced crack growth laws—highly complex fatigue phenomena can be evaluated while maintaining the computational efficiency of the single quasi-static phase-field simulation.

The methodologies presented in this thesis establish a rigorous framework for verifying phase-field fracture simulations. By carefully considering the length scale parameter in relation to the mesh size and domain boundaries, as well as accounting for strain localization and peak force effects using energetic crack solvers, the convergence and accuracy of the

solution can be systematically evaluated. However, a significant remaining challenge lies in assessing the correctness of the predicted crack path. Therefore, related to **crack directionality in fatigue**, it is essential to define and analyze complex crack propagation using established criteria, potentially incorporating explicit crack directionality criteria into the energetic PFF formulation.

Related to this aspect and the different phase-field regularizations, it has been observed that in the AT2 model, once the strain energy increases, damage appears, producing a non-linear relationship between force and displacement. Previous analysis has shown that this effect is mitigated as the length scale parameter approaches zero. In contrast, the AT1 and Wu regularizations exhibit a linear force-displacement relation prior to failure. This provides insight into capturing linear behavior for any length scale value. Additionally, these models offer the advantage of easily quantifying the dimension of the length scale due to their compact support. Although these models present several challenges due to the imposition of boundedness, it has been demonstrated that the LVPP algorithm effectively handles this aspect, as well as irreversibility. Based on this, a promising future direction is the extension of energetic solvers within the LVPP framework to incorporate AT1 and Wu regularizations, potentially handling the irreversibility constraint in a local sense rather than the global sense currently employed. This would enable more robust fatigue analysis.

Regarding the **mitigation of numerical artifacts**, the LVPP algorithm has been analyzed and developed within the finite element framework using the Proximal Galerkin method. However, the LVPP algorithm is formulated for a continuous model, where the corresponding sequence of PDEs can be solved using other numerical methods, such as finite differences or Fast Fourier Transforms (FFT). A direct avenue for future development is the derivation of this methodology for FFT-based solvers, which could offer significant advantages—as well as distinct limitations—particularly for homogenization problems and microstructure analysis.

It has been observed that a major cause of the high computational cost in PFF simulations is the requirement that the length scale parameter be orders of magnitude larger than the mesh size, in order to accurately capture the crack profile and reduce strain localization effects. Based on standard PFF element resolution rules where elements must be smaller than the length scale, $l/h > 2$ for certain regularization models, strain localization effects often necessitate a more refined mesh. Therefore, it is crucial to investigate the root causes of these localization artifacts and develop strategies to avoid them. For instance, the AT1 regularization corresponds to an analytical solution that is quadratic and contains a Heaviside function. This suggests that investigating quadratic spaces, potentially enriched with Heaviside functions, could allow for the exact capture of the phase-field profile without numerical error. Similarly, within an FFT framework, the Wu regularization is particularly relevant as its analytical profile depends on a sine function and also incorporates a Heaviside function. This directly supports the need for **mixed or enriched discretizations**, designing specific regularizations tailored to specific numerical methods to extract maximum performance and capture theoretical solutions with minimal numerical error. Conversely, designing new numerical methods capable of capturing existing regularizations without error is equally promising.

A preliminary exploration of these enriched discretizations has been conducted, comparing standard linear elements with quadratic elements and enriched linear elements with

bubble functions for the convergence analysis of the CSDF presented in 2.2.2 for the AT2 model or in 5.4.4 for the AT1 model. For a length scale of $l = 0.1$ mm, Figure 7.1 compares the convergence of the relative energy error for the AT2 (Figure 7.1(a)) and AT1 (Figure 7.1(b)) regularization models. In the case of the AT1 model, predicting the regularized domain results in convergence curves that exhibit oscillations. These fluctuations arise from the finite nature of its support and the effect of the Heaviside function: as the mesh is uniformly refined, the boundary of the active damage zone ($\phi > 0$) intersects elements discretely, causing small jumps in the integrated energy.

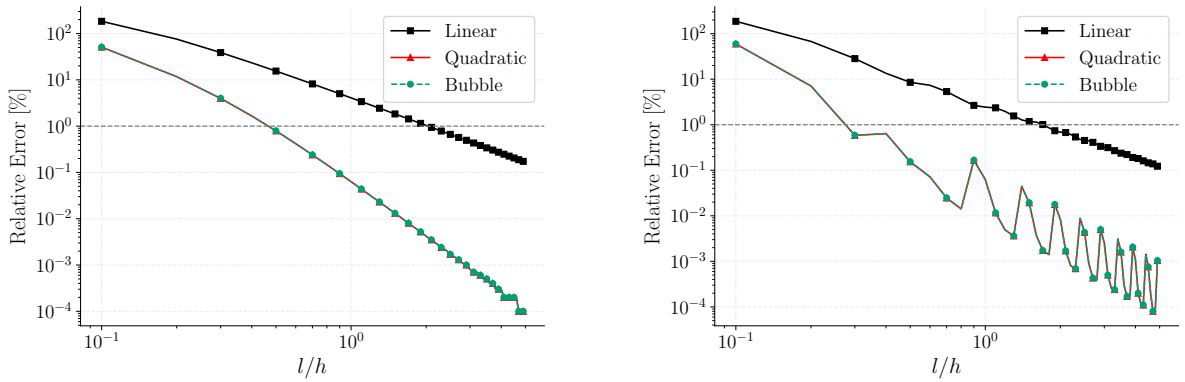

(a) AT2 (b) AT1

Figure 7.1: Relative energy error as a function of mesh size h for $l = 0.1$ mm, comparing the (a) AT2 and (b) AT1 regularization models. The theoretical energy is used as the reference.

To isolate this effect, Figure 7.2 presents the convergence for the AT1 model with a larger length scale of $l = 0.5$ mm. In this configuration, the crack support coincides perfectly with the domain boundaries ($2l = 1.0$ mm), effectively deactivating the Heaviside function's discontinuity within the element interiors. Because of this, the discrete energy jumps are eliminated. Crucially, since the analytical profile of the AT1 model is fundamentally quadratic in this regime, the higher-order quadratic and bubble-enriched finite elements are capable of capturing the solution exactly, yielding effectively zero numerical error. Thus, under these ideal conditions, only the linear approximation continues to present an error. These initial findings underscore the potential value of pursuing specialized element formulations tailored to specific regularizations to efficiently mitigate localization and integration artifacts in future work.

Finally, regarding the LVPP method, the introduction of the latent variable provides new insights into the solution, offering an alternative representation of the phase-field. Investigating numerical spaces capable of capturing this latent variable is of interest. Furthermore, given that the definition of the Legendre transform is not unique, exploring alternative Legendre functions that might be perfectly captured by specific function spaces could lead to more efficient solvers.

Additionally, within the Proximal Galerkin formulation of the LVPP, a critical aspect involves the proximal parameter β, which controls the convergence of the method. While it has been shown that the method is robust across a wide range of values, further investigation into the optimal selection of this parameter could lead to improved convergence rates and computational efficiency.

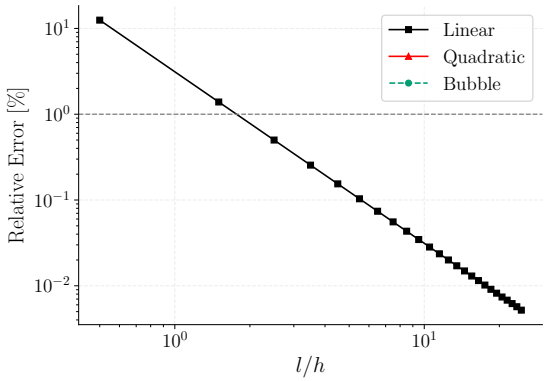

Figure 7.2: Comparison of the relative error in the total energy for linear, quadratic, and bubble-enriched elements for the AT1 model with $l = 0.5$ mm.

From a software perspective, since PhaseFieldX is built upon the FEniCSx ecosystem, there are significant opportunities for extension:

- Implementation of periodic boundary conditions for homogenization and microstructure analysis.
- Extension to complex material behaviors, including plasticity, viscoelasticity, and user-defined constitutive models.
- Integration of automatic adaptive mesh refinement to optimize computational resources dynamically near the crack tip.

7.4 Scientific contributions

The research conducted in this thesis has resulted in several scientific publications covering phase-field fracture modeling, numerical methods, and software development. These contributions are listed below:

1. M. Castillón. "PhaseFieldX: An Open-Source Framework for Advanced Phase-Field Simulations". *Journal of Open Source Software*, 10(108), 7307, 2025.
   DOI: https://doi.org/10.21105/joss.07307
2. M. Castillón, I. Romero, and J. Segurado. "A phase-field approach to fatigue analysis: Bridging theory and simulation". *International Journal of Fatigue*, 205, 109397, 2026.
   DOI: https://doi.org/10.1016/j.ijfatigue.2025.109397
3. M. Castillón, J. Segurado and I. Romero. "A Correction Method for Crack Area Overestimation in Phase-Field Fracture". (Submitted).
   Arxiv: https://arxiv.org/abs/2605.03731
4. M. Castillón, B. Khara, J.S. Dokken, T. M. Surowiec, B. Keith, and Y. Bazilevs. "Proximal Galerkin for Phase-Field Fracture". (Submitted).
   Arxiv: https://arxiv.org/abs/2604.26210

All solvers and methodologies presented in these publications are implemented in the **PhaseFieldX** package, ensuring that the research is reproducible and accessible to the scientific community. Furthermore, the simulations and specific input files related to each

publication have been made available in dedicated repositories. To facilitate the understanding of the methodologies and simulations, a dedicated webpage has been created for each publication. The publications derived from this thesis integrate the scientific article with the corresponding open-source software, documentation, and examples.

A key advantage of this methodology is the simultaneous execution of these workflows. This integrated approach ensures that software development and research writing evolve in tandem, resulting in a more productive and robust research process.

Additionally, the research developed during this PhD thesis has been presented at the following scientific conferences:

1. M. Castillón, J. Segurado, and I. Romero. "Una formulación de elementos finitos incompatibles para la representación mejorada de soluciones en problemas de campo de fase: aplicación a la fractura regularizada". *Congreso del Grupo Español de Fractura 2024 (GEF 2024)*, Palma de Mallorca, Spain, March 6-8, 2024.
2. M. Castillón, J. Segurado, and I. Romero. "An incompatible finite element formulation for enhanced representation of solutions in phase-field problems: application to regularized fracture". *International Conference on Computational Mechanics (GIMC-GMA 2024)*, Madrid, Spain, May 29-31, 2024.
3. M. Castillón, J. Segurado, and I. Romero. "Enriched discretizations for accurate phase field models with sharp interfaces: applications to fracture". *Congress on Numerical Methods in Engineering 2024 (CMN 2024)*, University of Aveiro, Portugal, September 4-6, 2024.
4. J. Segurado, M. Castillón, and I. Romero. "Un modelo de propagación de grietas en fatiga basado en fractura por phase-field". *Congreso del Grupo Español de Fractura 2024 (GEF 2026)*, Aranjuez, Spain, March 11-13, 2026.

Finally, it is worth mentioning that a substantial part of one year was dedicated to a collaborative project with an external company, focusing on the development and analysis of fatigue within phase-field simulations.

Bibliography

[1] G.A. Francfort and J.-J. Marigo. "Revisiting brittle fracture as an energy minimization problem". In: *Journal of the Mechanics and Physics of Solids* 46.8 (1998), pp. 1319–1342. DOI: 10.1016/S0022-5096(98)00034-9.

[2] B. Bourdin, G.A. Francfort, and J.-J. Marigo. "Numerical experiments in revisited brittle fracture". In: *Journal of the Mechanics and Physics of Solids* 48.4 (2000), pp. 797–826. DOI: 10.1016/S0022-5096(99)00028-9.

[3] C. Miehe, M. Hofacker, and F. Welschinger. "A phase field model for rate-independent crack propagation: Robust algorithmic implementation based on operator splits". In: *Computer Methods in Applied Mechanics and Engineering* 199.45 (2010), pp. 2765–2778. DOI: 10.1016/j.cma.2010.04.011.

[4] L. Ambrosio and V.M. Tortorelli. "Approximation of functional depending on jumps by elliptic functional via t-convergence". In: *Communications on Pure and Applied Mathematics* 43.8 (1990), pp. 999–1036. DOI: 10.1002/cpa.3160430805.

[5] J.-Y. Wu. "A unified phase-field theory for the mechanics of damage and quasi-brittle failure". In: *Journal of the Mechanics and Physics of Solids* 103 (2017), pp. 72–99. DOI: 10.1016/j.jmps.2017.03.015.

[6] T. Gerasimov and L. De Lorenzis. "On penalization in variational phase-field models of brittle fracture". In: *Computer Methods in Applied Mechanics and Engineering* 354 (2019), pp. 990–1026. DOI: 10.1016/j.cma.2019.05.038.

[7] J.-Y. Wu, V.P. Nguyen, C.T. Nguyen, D. Sutula, S. Sinaie, and S.P.A. Bordas. "Chapter One - Phase-field modeling of fracture". In: ed. by S.P.A. Bordas and D.S. Balint. Vol. 53. Advances in Applied Mechanics. Elsevier, 2020, pp. 1–183. DOI: 10.1016/bs.aams.2019.08.001.

[8] C. Kuhn, A. Schlüter, and R. Müller. "On degradation functions in phase field fracture models". In: *Computational Materials Science* 108 (2015). Selected Articles from Phase-field Method 2014 International Seminar, pp. 374–384. DOI: 10.1016/j.commatsci.2015.05.034.

[9] H. Amor, J.-J. Marigo, and C. Maurini. "Regularized formulation of the variational brittle fracture with unilateral contact: Numerical experiments". In: *Journal of the Mechanics and Physics of Solids* 57.8 (2009), pp. 1209–1229. DOI: 10.1016/j.jmps.2009.04.011.

[10] B. Keith and T.M. Surowiec. "Proximal Galerkin: A Structure-Preserving Finite Element Method for Pointwise Bound Constraints". In: *Foundations of Computational Mathematics* (Nov. 20, 2024). DOI: 10.1007/s10208-024-09681-8.

[11] J.S. Dokken, P.E. Farrell, B. Keith, I.P.A. Papadopoulos, and T.M. Surowiec. "The latent variable proximal point algorithm for variational problems with inequality constraints". In: *Computer Methods in Applied Mechanics and Engineering* 445 (2025), p. 118181. DOI: 10.1016/j.cma.2025.118181.

[12] R. Bharali, S. Goswami, C. Anitescu, and T. Rabczuk. "A robust monolithic solver for phase-field fracture integrated with fracture energy based arc-length method and under-relaxation". In: *Computer Methods in Applied Mechanics and Engineering* 394 (2022), p. 114927. DOI: 10.1016/j.cma.2022.114927.

[13] J. Zambrano, S. Toro, P.J. Sánchez, F.P. Duda, C.G. Méndez, and A.E. Huespe. "An arc-length control technique for solving quasi-static fracture problems with phase field models and a staggered scheme". In: *Computational Mechanics* 73.4 (2024), pp. 751–772. DOI: 10.1007/s00466-023-02388-7.

[14] P. Aranda and J. Segurado. "A crack-length control technique for phase-field fracture in FFT homogenization". In: *International Journal for Numerical Methods in Engineering* 126.2 (2025), e7664. DOI: 10.1002/nme.7664.

[15] C. Miehe, F. Welschinger, and M. Hofacker. "Thermodynamically consistent phase-field models of fracture: Variational principles and multi-field FE implementations". In: *International Journal for Numerical Methods in Engineering* 83.10 (2010), pp. 1273–1311. DOI: 10.1002/nme.2861.

[16] G. Molnár, A. Doitrand, A. Jaccon, B. Prabel, and A. Gravouil. "Thermodynamically consistent linear-gradient damage model in Abaqus". In: *Engineering Fracture Mechanics* 266 (2022), p. 108390. DOI: 10.1016/j.engfracmech.2022.108390.

[17] M. Castillón, I. Romero, and J. Segurado. "A phase-field approach to fatigue analysis: Bridging theory and simulation". In: *International Journal of Fatigue* 205 (2026), p. 109397. DOI: 10.1016/j.ijfatigue.2025.109397.

[18] L. Greco, A. Patton, M. Negri, A. Marengo, U. Perego, and A. Reali. "Higher order phase-field modeling of brittle fracture via isogeometric analysis". In: *Engineering with Computers* 40.6 (2024), pp. 3541–3560. DOI: 10.1007/s00366-024-01949-5.

[19] P. Carrara, M. Ambati, R. Alessi, and L. De Lorenzis. "A framework to model the fatigue behavior of brittle materials based on a variational phase-field approach". In: *Computer Methods in Applied Mechanics and Engineering* 361 (2020), p. 112731. DOI: 10.1016/j.cma.2019.112731.

[20] K. Seleš, F. Aldakheel, Z. Tonković, J. Sorić, and P. Wriggers. "A general phase-field model for fatigue failure in brittle and ductile solids". In: *Computational Mechanics* 67.5 (2021), pp. 1431–1452. DOI: 10.1007/s00466-021-01996-5.

[21] A. Golahmar, C. F. Niordson, and E. Martínez-Pañeda. "A phase field model for high-cycle fatigue: Total-life analysis". In: *International Journal of Fatigue* 170 (2023), p. 107558. DOI: 10.1016/j.ijfatigue.2023.107558.

[22] C. Schreiber, C. Kuhn, R. Müller, and T. Zohdi. "A phase field modeling approach of cyclic fatigue crack growth". In: *International Journal of Fracture* 225.1 (2020), pp. 89–100. DOI: 10.1007/s10704-020-00468-w.

[23] A. Mesgarnejad, A. Imanian, and A. Karma. "Phase-field models for fatigue crack growth". In: *Theoretical and Applied Fracture Mechanics* 103 (2019), p. 102282. DOI: 10.1016/j.tafmec.2019.102282.

[24] J. Heinzmann, P. Carrara, M. Ambati, A.M. Mirzaei, and L. De Lorenzis. "An adaptive acceleration scheme for phase-field fatigue computations". In: *Computational Mechanics* (Oct. 12, 2024). DOI: 10.1007/s00466-024-02551-8.

[25] P. K. Kristensen, A. Golahmar, E. Martínez-Pañeda, and C. F. Niordson. "Accelerated high-cycle phase field fatigue predictions". In: *European Journal of Mechanics - A/Solids* 100 (2023), p. 104991. DOI: 10.1016/j.euromechsol.2023.104991.

[26] H.D. Huynh, M.N. Nguyen, G. Cusatis, S. Tanaka, and T.Q. Bui. "A polygonal XFEM with new numerical integration for linear elastic fracture mechanics".

In: *Engineering Fracture Mechanics* 213 (2019), pp. 241–263. DOI: 10.1016/j.engfracmech.2019.04.002.

[27] R. Branco, F.V. Antunes, and J.D. Costa. "A review on 3D-FE adaptive remeshing techniques for crack growth modelling". In: *Engineering Fracture Mechanics* 141 (2015), pp. 170–195. DOI: 10.1016/j.engfracmech.2015.05.023.

[28] C. Wang, K. Pereira, D. Wang, A. Zinovev, D. Terentyev, and M. Abdel Wahab. "Fretting fatigue crack propagation under out-of-phase loading conditions using extended maximum tangential stress criterion". In: *Tribology International* 187 (2023), p. 108738. DOI: 10.1016/j.triboint.2023.108738.

[29] C. Hou, X. Jin, X. Fan, R. Xu, and Z. Wang. "A generalized maximum energy release rate criterion for mixed mode fracture analysis of brittle and quasi-brittle materials". In: *Theoretical and Applied Fracture Mechanics* 100 (2019), pp. 78–85. DOI: 10.1016/j.tafmec.2018.12.015.

[30] G. Molnár and A. Gravouil. "2D and 3D Abaqus implementation of a robust staggered phase-field solution for modeling brittle fracture". In: *Finite Elements in Analysis and Design* 130 (2017), pp. 27–38. DOI: 10.1016/j.finel.2017.03.002.

[31] K. Seleš, T. Lesičar, Z. Tonković, and J. Sorić. "A residual control staggered solution scheme for the phase-field modeling of brittle fracture". In: *Engineering Fracture Mechanics* 205 (2019), pp. 370–386. DOI: 10.1016/j.engfracmech.2018.09.027.

[32] Y. Navidtehrani, C. Betegón, and E. Martínez-Pañeda. "A simple and robust Abaqus implementation of the phase field fracture method". In: *Applications in Engineering Science* 6 (2021), p. 100050. DOI: 10.1016/j.apples.2021.100050.

[33] G. Hu. *RACCOON: A parallel finite-element code specialized in phase-field for fracture*. 2019.

[34] H. Hirshikesh, S. Natarajan, and R. K. Annabattula. "A FEniCS implementation of the phase field method for quasi-static brittle fracture". In: *Frontiers of Structural and Civil Engineering* 13.2 (2019), pp. 380–396. DOI: 10.1007/s11709-018-0471-9.

[35] S.A. Silber and M. Karttunen. "SymPhas—General Purpose Software for Phase-Field, Phase-Field Crystal, and Reaction-Diffusion Simulations". In: *Advanced Theory and Simulations* 5.1 (2022), p. 2100351. DOI: 10.1002/adts.202100351.

[36] M. Tegeler, O. Shchyglo, R. Kamachali, A. Monas, I. Steinbach, and G. Sutmann. "Parallel multiphase field simulations with OpenPhase". In: *Computer Physics Communications* 215 (2017), pp. 173–187. DOI: 10.1016/j.cpc.2017.01.023.

[37] S. DeWitt, S. Rudraraju, D. Montiel, W. Beck Andrews, and K. Thornton. "PRISMS-PF: A general framework for phase-field modeling with a matrix-free finite element method". In: *npj Computational Materials* 6.1 (2020), p. 29. DOI: 10.1038/s41524-020-0298-5.

[38] M. Castillón. "PhaseFieldX: An Open-Source Framework for Advanced Phase-Field Simulations". In: *Journal of Open Source Software* 10.108 (2025), p. 7307. DOI: 10.21105/joss.07307.

[39] M. Castillón, J. Segurado, and I. Romero. *A Correction Method for Crack Area Overestimation in Phase-Field Fracture*. 2026. arXiv: 2605.03731 [cond-mat.mtrl-sci].

[40] M. Castillón, B. Khara, J. S. Dokken, T. M. Surowiec, B. Keith, and Y. Bazilevs. *Proximal Galerkin for Phase Field Fracture*. 2026. arXiv: 2604.26210 [math.NA].

[41] J.-Y. Wu, V.P. Nguyen, C.T. Nguyen, D. Sutula, S. Sinaie, and S.P.A. Bordas. "Chapter One - Phase-field modeling of fracture". In: *Advances in Applied Mechanics*. Ed. by S.P.A. Bordas and D.S. Balint. Vol. 53. Elsevier, 2020, pp. 1–183. DOI: 10.1016/bs.aams.2019.08.001.

[42] A. Karma, D.A. Kessler, and H. Levine. "Phase-Field Model of Mode III Dynamic Fracture". In: *Phys. Rev. Lett.* 87 (4 July 2001), p. 045501. DOI: 10.1103/PhysRevLett.87.045501.

[43] C. Miehe. "Comparison of two algorithms for the computation of fourth-order isotropic tensor functions". In: *Computers & Structures* 66.1 (1998), pp. 37–43. DOI: 10.1016/S0045-7949(97)00073-4.

[44] C. Steinke, J. Storm, and M. Kaliske. "Energetically motivated crack orientation vector for phase-field fracture with a directional split". In: *International Journal of Fracture* 237.1 (Sept. 2022), pp. 15–46. DOI: 10.1007/s10704-022-00633-3.

[45] A. M. Fajardo Lacave, F. Vicentini, F. Welschinger, and L. De Lorenzis. "A variational phase-field model for anisotropic fracture accounting for multiple cohesive lengths". In: *Journal of the Mechanics and Physics of Solids* 212 (2026), p. 106585. DOI: 10.1016/j.jmps.2026.106585.

[46] T. J. R. Hughes. *The finite element method*. Englewood Cliffs, New Jersey: Prentice-Hall Inc., 1987.

[47] A. Ern and J. L. Guermond. *Theory and practice of finite elements*. Springer, 2004.

[48] M. Ambati, T. Gerasimov, and L. De Lorenzis. "A review on phase-field models of brittle fracture and a new fast hybrid formulation". In: *Computational Mechanics* 55.2 (Feb. 2015), pp. 383–405. DOI: 10.1007/s00466-014-1109-y.

[49] H. Amor, J.-J. Marigo, and C. Maurini. "Regularized formulation of the variational brittle fracture with unilateral contact: Numerical experiments". In: *Journal of the Mechanics and Physics of Solids* 57.8 (2009), pp. 1209–1229. DOI: 10.1016/j.jmps.2009.04.011.

[50] M.J. Borden, C.V. Verhoosel, M.A. Scott, T.J.R. Hughes, and C.M. Landis. "A phase-field description of dynamic brittle fracture". In: *Computer Methods in Applied Mechanics and Engineering* 217-220 (2012), pp. 77–95. DOI: 10.1016/j.cma.2012.01.008.

[51] B. Bourdin, G.A. Francfort, and J.-J. Marigo. "The Variational Approach to Fracture". In: *Journal of Elasticity* 91.1 (2008), pp. 5–148. DOI: 10.1007/s10659-007-9107-3.

[52] S. van der Walt, J.L. Schönberger, J. Nunez-Iglesias, F. Boulogne, J.D. Warner, N. Yager, E. Gouillart, T. Yu, and the scikit-image contributors. "scikit-image: image processing in Python". In: *PeerJ* 2 (2014), e453. DOI: 10.7717/peerj.453.

[53] T.Y. Zhang and C.Y. Suen. "A fast parallel algorithm for thinning digital patterns". In: *Communications of the ACM* 27.3 (1984), pp. 236–239. DOI: 10.1145/357994.358023.

[54] M. Manav, R. Molinaro, S. Mishra, and L. De Lorenzis. "Phase-field modeling of fracture with physics-informed deep learning". In: *Computer Methods in Applied Mechanics and Engineering* 429 (2024), p. 117104. DOI: 10.1016/j.cma.2024.117104.

[55] H. Tada. *The Stress Analysis of Cracks Handbook, Third Edition*. ASME Press, 2000.

[56] D. Wagner, M.J. Garcia, A. Montoya, and H. Millwater. "A finite element-based adaptive energy response function method for 2D curvilinear progressive fracture". In: *International Journal of Fatigue* 127 (2019), pp. 229–245. DOI: 10.1016/j.ijfatigue.2019.05.036.

[57] D. Wagner. "A finite element-based adaptive energy response function method for curvilinear progressive fracture". PhD thesis. United States – Texas: The University of Texas at San Antonio, 2018, p. 181.

[58] G.J. Pataky, H. Sehitoglu, and H.J. Maier. "High temperature fatigue crack growth of Haynes 230". In: *Materials Characterization* 75 (2013), pp. 69–78. DOI: 10.1016/j.matchar.2012.09.012.

[59] A.M. Alshoaibi. "Fatigue Crack Growth Analysis under Constant Amplitude Loading Using Finite Element Method". In: *Materials* 15.8 (2022). DOI: 10.3390/ma15082937.

[60] T.L. Anderson. *Fracture Mechanics: Fundamentals and Applications, Third Edition*. Taylor & Francis, 2005.

[61] H. Xin, J.A.F.O. Correia, and M. Veljkovic. "Three-dimensional fatigue crack propagation simulation using extended finite element methods for steel grades S355 and S690 considering mean stress effects". In: *Engineering Structures* 227 (2021), p. 111414. DOI: 10.1016/j.engstruct.2020.111414.

[62] G. Chen and M. Teboulle. "Convergence analysis of a proximal-like minimization algorithm using Bregman functions". In: *SIAM Journal on Optimization* 3.3 (1993), pp. 538–543. DOI: 10.1137/0803026.

[63] M. Teboulle. "A simplified view of first order methods for optimization". In: *Mathematical Programming* 170.1 (2018), pp. 67–96. DOI: 10.1007/s10107-018-1284-2.

[64] A. Muixí, O. Marco, A. Rodríguez-Ferran, and S. Fernández-Méndez. "A combined XFEM phase-field computational model for crack growth without remeshing". In: *Computational Mechanics* 67.1 (2021), pp. 231–249. DOI: 10.1007/s00466-020-01929-8.

[65] M. Castillón. *PhaseFieldX*. https://github.com/CastillonMiguel/phasefieldx. GitHub repository. 2025.

[66] I.A. Baratta, J.P. Dean, J.S. Dokken, M. Habera, J.S. Hale, C.N. Richardson, M.E. Rognes, M.W. Scroggs, N. Sime, and G.N. Wells. *DOLFINx: the next generation FEniCS problem solving environment*. 2023. DOI: 10.5281/zenodo.10447666.

[67] M.W. Scroggs, J.S. Dokken, C.N. Richardson, and G.N. Wells. "Construction of arbitrary order finite element degree-of-freedom maps on polygonal and polyhedral cell meshes". In: *ACM Transactions on Mathematical Software* 48.2 (2022), 18:1–18:23. DOI: 10.1145/3524456.

[68] M.W. Scroggs, I.A. Baratta, C.N. Richardson, and G.N. Wells. "Basix: a runtime finite element basis evaluation library". In: *Journal of Open Source Software* 7.73 (2022), p. 3982. DOI: 10.21105/joss.03982.

[69] M.S. Alnaes, A. Logg, K.B. Ølgaard, M.E. Rognes, and G.N. Wells. "Unified Form Language: A domain-specific language for weak formulations of partial differential equations". In: *ACM Transactions on Mathematical Software* 40 (2014). DOI: 10.1145/2566630.

[70] J.S. Dokken. *DOLFINx-MPC*. Software, version 0.10.0, released 2025-10-20. 2025.

[71] S.M. Rosenbusch, P. Diercks, V. Kindrachuk, and J.F. Unger. "Integrating custom constitutive models into FEniCSx: A versatile approach and case studies". In: *Advances in Engineering Software* 206 (2025), p. 103922. DOI: 10.1016/j.advengsoft.2025.103922.

[72] S.R. Mettu, V. Shivakumar, J. Beek, F. Yeh, L.C. Williams, R.G. Forman, J.J. McMahon, and J.C. Newman. "NASGRO 3.0: A Software for Analyzing Aging Aircraft". In: JSC-22267A. Houston, Texas, 1995.